

**Biologically-inspired selective filters**

by

**Laura K. Maguire**

B.S., Harvey Mudd College, 2013

A thesis submitted to the  
Faculty of the Graduate School of the  
University of Colorado in partial fulfillment  
of the requirements for the degree of  
Doctor of Philosophy  
Department of Physics  
2019

This thesis entitled:  
Biologically-inspired selective filters  
written by Laura K. Maguire  
has been approved for the Department of Physics

---

Assistant Professor Loren Hough

---

Professor Attendant Rank Matthew Glaser

Date \_\_\_\_\_

The final copy of this thesis has been examined by the signatories, and we find that both the content and the form meet acceptable presentation standards of scholarly work in the above mentioned discipline.

Maguire, Laura K. (Ph.D., Physics)

Biologically-inspired selective filters

Thesis directed by Assistant Professor Loren Hough

Selective biofilters are essential to life, controlling the transport of proteins, nucleic acids, and other macromolecules. Of particular interest are filters that require rapid motion or high flux of proteins that must still bind targets with high specificity. Despite the apparent competition between these two attributes, many selective materials exist which leverage binding interactions to fulfill both requirements. In this work, we investigate the mechanisms by which such filters function through both modeling and experiment, using the nuclear pore, a well-studied example of selective transport, as inspiration. The nuclear pore, a channel lined with intrinsically disordered FG nucleoporins, permits a high flux of transport factor proteins and their cargoes while suppressing transport of proteins that cannot bind to the FG nucleoporins. We developed a minimal model of nuclear transport that relies on the bound-state mobility of the Nup-transport factor complex for selectivity. This model reproduces the experimentally-observed properties of the nuclear pore and demonstrates that bound-state diffusion can arise from transient, multivalent binding and binding to flexible, dynamic tethers. We then designed tunable hydrogel mimics of the nuclear pore for use in measuring bound-state diffusion and testing the predictions of our model. Fluorescence microscopy demonstrated that our mimics display non-zero bound diffusion. Both the model and experimental system are sufficiently general that their principles can be applied to a wide variety of selective biomaterials.

Dedicated in remembrance of J. Chance Crompton:  
irreplaceable friend, extraordinary scientist, greatly missed.

## Acknowledgements

First, deep thanks to my advisor Loren Hough, who demonstrates that it's possible to combine expertise in physics, biology, theory, and experiment with truly supportive mentorship. Loren's guidance and enthusiasm kept this project going, and I have gained immensely in both knowledge and skills along the way. Meredith Betterton often acted as an unofficial advisor, and I greatly appreciate her talent for getting me un-stuck and moving forward. Valuable ideas and advice also came from the rest of my committee: Matt Glaser, Noel Clark, and Franck Vernerey.

Many people made significant contributions to this project before and during my time on it. My thanks go to Eric Verbeke, undergraduate extraordinaire, for his insights, dedication, and cloning skills. Nate Crossette and Katie Rainey contributed much time and thought to the hydrogel designs. Andrea Egan and Nick Bax laid the groundwork for this project. I had the pleasure of mentoring Sophie Reskin and Elena Arroyo while they did excellent work on FG Nup aggregation. Help also came from Scott Tilden, Taylor Moon, Lucrezia Cester, Paul Marchando, and Christopher Lawton.

Years of advice and assistance came from current and former labmates Allison Holt, Jeffre Allen, Nabanita Das, Maria Pagratis, Amanda Hollar, and Bart Black. Thanks go to close collaborator Mike Stefferson for his much-needed crash course in computational physics. Special gratitude goes to Kathryn Wall, without whose knowledge, patience, and wisdom I would never have lasted as a physicist learning biochemistry.

I owe a great deal to the CU/NIH Biophysics Training Program and its director Joe Falke, which jumpstarted me into biophysics. Generous hydrogel help came from Sadhana Sharma,

Stephanie Bryant, Ben Fairbanks, Danielle Konetski, and Christopher Bowman. Many thanks to Annette Erbse of the Biochemistry Shared Instruments Pool and Joe Dragavon of the BioFrontiers Advanced Light Microscopy Core. I've quite enjoyed working with Johannes Rudolph and Jyothi Mahadevan on PARP1 diffusion. Thanks also to Jeeseong Hwang and Kim Briggman of NIST.

Last but not least, I am grateful to my family and friends who have supported me unwaveringly throughout this endeavor.

## Contents

### Chapter

<b>1</b>	<b>Introduction</b>	<b>1</b>
1.1	The nuclear pore complex is a unique selective filter . . . . .	1
1.1.1	Intrinsically disordered proteins . . . . .	2
1.1.2	Basics of nuclear transport . . . . .	3
1.1.3	Models of nuclear transport . . . . .	7
1.1.4	Nuclear pore mimics . . . . .	10
1.2	Other selective biofilters . . . . .	12
1.2.1	Drug delivery through mucus barriers . . . . .	13
1.2.2	Diffusion of DNA-binding proteins in the nucleus . . . . .	15
1.2.3	Subcompartments in liquid droplets . . . . .	16
1.3	Project goals and motivation . . . . .	18
1.3.1	Minimal model of selective transport . . . . .	18
1.3.2	Experimental tests of bound-state diffusion in biomaterials . . . . .	19
1.4	Biophysics is beautiful . . . . .	21
<b>2</b>	<b>Modeling bound-state diffusion in selective filters</b>	<b>24</b>
2.1	Simplified model of nuclear transport . . . . .	25
2.1.1	Linear approximation and analytic solution . . . . .	27
2.1.2	Effect of bound-state diffusion constant . . . . .	29

2.1.3	Bound diffusion in the linear model . . . . .	31
2.2	Mechanisms of bound transport factor mobility . . . . .	32
2.2.1	Bound mobility through tethered diffusion . . . . .	32
2.2.2	Bound mobility through inter-chain hopping . . . . .	37
2.3	Fickian and anomalous diffusion . . . . .	41
2.4	Bound diffusion in other biological systems . . . . .	44
2.4.1	DNA damage repair protein recruitment in the nucleus . . . . .	45
2.5	Conclusions . . . . .	47
<b>3</b>	<b>Hydrogel design for protein separation</b>	<b>49</b>
3.1	Hydrogel fabrication . . . . .	50
3.2	Flow chamber fabrication . . . . .	54
3.3	Hydrogel geometries . . . . .	58
3.4	FG Nup peptides . . . . .	60
3.4.1	SSSG negative control . . . . .	62
3.5	Transport factor constructs . . . . .	63
3.5.1	Covalently-tethered NTF2 dimer . . . . .	64
3.5.2	NTF2-GFP . . . . .	64
3.5.3	Nonbinding NTF2 F5R . . . . .	66
3.5.4	Kap121 and GFP-NLS . . . . .	66
3.6	Pore size . . . . .	68
3.7	Porogens . . . . .	70
3.7.1	Alginate nanospheres . . . . .	70
3.7.2	Dextran/dextranase porogen system . . . . .	73
3.8	Polymerization using confocal microscope . . . . .	76
3.9	Dye-labeling and free dye . . . . .	81
3.10	Discussion . . . . .	84

<b>4</b>	<b>Bound diffusion measurements</b>	<b>86</b>
4.1	Experimental parameters . . . . .	87
4.1.1	Nup contour length and valency . . . . .	87
4.1.2	Binding affinity of NTF2 and FSFG . . . . .	87
4.1.3	Quantifying concentration of tethered Nups . . . . .	89
4.1.4	Free diffusion constant . . . . .	90
4.2	Experimental procedures . . . . .	91
4.2.1	Hydrogel preparation . . . . .	91
4.2.2	Influx of transport factor and inert protein . . . . .	92
4.2.3	Fluorescence recovery after photobleaching . . . . .	93
4.3	Analysis of steady-state hydrogel properties . . . . .	94
4.3.1	Gel dimension estimates . . . . .	95
4.3.2	Partition coefficients and fraction of time spent bound . . . . .	96
4.3.3	Bound-diffusion calculation . . . . .	98
4.4	Influx analysis . . . . .	98
4.4.1	Profile analysis . . . . .	100
4.4.2	Accumulation analysis . . . . .	101
4.5	FRAP analysis . . . . .	103
4.5.1	Accounting for photobleaching . . . . .	103
4.5.2	No-exchange solution to diffusion equation . . . . .	104
4.5.3	Fourier series solution to diffusion equation . . . . .	105
4.6	Results . . . . .	113
4.7	Discussion . . . . .	117
<b>5</b>	<b>FG Nup aggregation under crowded conditions</b>	<b>118</b>
5.1	Fluorescence time courses . . . . .	120
5.1.1	Methods . . . . .	121

5.1.2	Results . . . . .	125
5.1.3	Discussion . . . . .	127
5.2	Fluorescence spectra . . . . .	128
5.2.1	Methods . . . . .	128
5.2.2	Results . . . . .	129
5.2.3	Discussion . . . . .	132
5.3	NMR relaxation measurements . . . . .	133
5.3.1	Methods . . . . .	134
5.3.2	Results . . . . .	134
5.3.3	Discussion . . . . .	135
5.4	Conclusions . . . . .	137
<b>6</b>	<b>Conclusions and future directions</b>	<b>138</b>
6.1	Future directions . . . . .	139
<b>Bibliography</b>		<b>142</b>
<b>Appendix</b>		
<b>A</b>	Predicted selectivity of nuclear pore mimics	<b>155</b>
<b>B</b>	Calculation of PEG hydrogel pore size	<b>156</b>
<b>C</b>	Protein expression and purification	<b>158</b>
C.1	Purification of his-tagged protein with metal affinity column . . . . .	158
C.2	Periplasmic matrix removal (PPMR) . . . . .	161
C.3	Lyophilization . . . . .	162
<b>D</b>	Bis-labeling Nup fragments for incorporation into acrylamide hydrogels	<b>163</b>

D.1 Bis-labeling reaction protocol . . . . .	163
D.2 Ellman's reagent assay protocol . . . . .	164
<b>E Hydrogel precursor solutions</b>	<b>166</b>
E.1 PEG hydrogel precursor recipes . . . . .	166
E.2 Acrylamide hydrogel precursor recipes . . . . .	167
<b>F Protein and peptide sequences</b>	<b>169</b>
<b>G Dye-labeling protocols</b>	<b>173</b>
G.1 Labeling NTF2 with fluorescein-NHS . . . . .	173
G.2 Labeling NTF2 with Alexa Fluor 488 - SDP or FSFG with Alexa Fluor 647 - SDP .	174
G.3 Labeling NTF2-cys with Alexa Fluor 488 - maleimide . . . . .	175
<b>H Hydrogel nuclear pore mimic dataset</b>	<b>177</b>
<b>I FG124 aggregation condition p-values</b>	<b>180</b>

## Tables

### Table

2.1	Comparison between flux measurements and model predictions. . . . .	31
2.2	Experimentally-measured parameters for PARP1 bound diffusion. . . . .	48
5.1	Aggregation rates and lag times for all crowding agents. . . . .	125
5.2	Aggregation lifetimes and lag times with varying pH. . . . .	127
A.1	Predicted selectivity of FG Nup hydrogels in previous work. . . . .	155
E.1	PEG hydrogel precursor stocks. . . . .	166
E.2	PEG hydrogel recipes. . . . .	167
E.3	Acrylamide hydrogel precursor stocks. . . . .	167
E.4	Acrylamide hydrogel recipes. . . . .	167
E.5	APS/TEMED crosslinking times. . . . .	168
F.1	Protein and peptide sequences . . . . .	169
I.1	Aggregation rate p-values for all crowding agents. . . . .	180
I.2	Lag time p-values for all crowding agents. . . . .	180
I.3	Aggregation rate p-values for PEG. . . . .	180
I.4	Lag time p-values for PEG. . . . .	181
I.5	Aggregation rate p-values for PVP. . . . .	181
I.6	Lag time p-values for PVP. . . . .	181

## Figures

### Figure

1.1	Nuclear pore complex and FG Nups.	4
1.2	Two important models of nuclear transport.	8
1.3	Effective-potential model of nuclear transport.	9
1.4	Nanoparticle drug delivery through a mucus barrier.	13
1.5	Phase-separated subcompartments of the nucleolus.	16
2.1	Schematics of the nuclear pore complex and model.	26
2.2	Flux and selectivity as a function of bound mobility.	29
2.3	Selectivity in the linear approximation.	30
2.4	Dependence of selectivity on model parameters.	33
2.5	Dependence of absolute flux on model parameters.	34
2.6	Selectivity from tethered diffusion.	36
2.7	Nup contour length and concentration comparison.	37
2.8	Selectivity from inter-chain hopping.	38
2.9	Mean-squared displacement in the hopping simulation.	40
2.10	Effect of Nup contour length and hopping rate on selectivity.	42
2.11	Anomalous diffusion in the hopping simulation.	43
2.12	Bound diffusion in other systems.	44
2.13	Possible bound-diffusion mechanisms of PARP1.	45

3.1	Hydrogels for protein separation. . . . .	51
3.2	Monomers and crosslinkers for PEG and acrylamide hydrogels. . . . .	52
3.3	Photoinitiator properties. . . . .	53
3.4	Photopolymerization with and without photomasks. . . . .	55
3.5	Flow chamber design and geometries. . . . .	55
3.6	Microfluidic sticker fabrication. . . . .	56
3.7	Nup fragments used in nuclear pore mimic experiments. . . . .	60
3.8	SSSG as a nonbinding Nup. . . . .	62
3.9	NTF2 fusion proteins. . . . .	65
3.10	Kap121 and GFP-NLS cargo. . . . .	67
3.11	Partition coefficient as a function of molecular weight. . . . .	69
3.12	Alginate nanospheres as porogens. . . . .	71
3.13	Equilibration of hydrogels after digestion of dextran porogen. . . . .	74
3.14	Dextranase degradation of FSFG. . . . .	75
3.15	Protein accumulation within dextran/dextranase hydrogels. . . . .	75
3.16	Confocal-crosslinked hydrogels. . . . .	77
3.17	Influx plots for confocal-crosslinked hydrogel ring. . . . .	78
3.18	NTF2 binding to confocal-crosslinked FSFG hydrogels. . . . .	79
3.19	Effect of dwell time and loop number on confocal-crosslinked hydrogels. . . . .	80
3.20	Quantifying free dye concentration. . . . .	82
3.21	Comparison of single and double exponential fits for free-dye analysis. . . . .	83
4.1	Isothermal titration calorimetry with NTF2 and FSFG. . . . .	88
4.2	Influx experiments images and accumulation. . . . .	92
4.3	Bright NTF2-F ring surrounding photobleach spot. . . . .	94
4.4	FRAP image series. . . . .	95
4.5	Hydrogel masks with radius and center calculations. . . . .	96

4.6	Partitioning of NTF2 and mCherry into FSFG hydrogel. . . . .	97
4.7	Intensity profiles and accumulation curve from influx experiments. . . . .	99
4.8	Geometry of profile and accumulation model. . . . .	100
4.9	Fits to concentration profiles at a fixed time. . . . .	102
4.10	Fits to concentration profiles at a fixed position. . . . .	103
4.11	Fits to accumulation curves. . . . .	104
4.12	Geometry for Fourier transform solution. . . . .	106
4.13	Reconstruction of initial concentration distribution. . . . .	111
4.14	Heatmap of mode coefficients. . . . .	111
4.15	Fits to recovery curves using Fourier transform solution. . . . .	112
4.16	Partition coefficients and fraction of NTF2 bound. . . . .	113
4.17	FRAP recovery curves. . . . .	114
4.18	Observed diffusion constants and NTF2 bound diffusion. . . . .	116
5.1	Aggregation of FG Nups into amyloid fibrils. . . . .	119
5.2	Sample sigmoid fit to FG124 aggregation timecourse. . . . .	121
5.3	Aggregation rates and lag times for all crowding agents. . . . .	124
5.4	Aggregation rates and lag times for varying PEG and PVP concentrations. . . . .	126
5.5	Chemical structures of PEG and PVP. . . . .	128
5.6	Fluorescence and absorbance of crowders. . . . .	130
5.7	Fluorescence spectra of FSFG, FG124, and phenylalanine. . . . .	131
5.8	FG124 fluorescence in crowded conditions. . . . .	131
5.9	FG124 fluorescence comparison between crowding agents. . . . .	131
5.10	Classes of tryptophan fluorescence. . . . .	133
5.11	Relaxation times of FSFG in crowded conditions. . . . .	135
5.12	Approximate dependence of relaxation times on viscosity. . . . .	136
C.1	Buffers for metal affinity column purifications. . . . .	159

H.1	Parameters for predicted bound diffusion.	177
H.2	No-Nup hydrogel dataset.	178
H.3	FSFG concat-1 hydrogel dataset.	178
H.4	FSFG concat-2 hydrogel dataset.	179

# **Chapter 1**

## **Introduction**

Selective biofilters are found in all manner of living systems and control the motion of proteins, nucleic acids, and other macromolecules. While many operate by size exclusion, permitting only the passage of particles below a size cutoff, more sophisticated filters make use of binding interactions. Of particular interest are filters which require rapid motion or high flux of proteins that must still bind targets with high specificity. The two requirements would seem to be in direct competition, yet there are many examples of these systems. In this work, we investigate the mechanisms by which such filters function through both modeling and experiment, using the nuclear pore, a canonical example of selective transport, as inspiration.

### **1.1 The nuclear pore complex is a unique selective filter**

The nuclear pore complex (NPC) is the filter that regulates all transport between the cell's nucleus and its cytoplasm (Fig. 1.1). It shows unusual selective properties. The nuclear pore prevents significant flux of macromolecules larger than about 30 kDa ( $\sim 5$  nm) [1]. However, a class of proteins known as transport factors carry cargo molecules quite rapidly across the pore, although the complex of transport factor and cargo can be up to 40 nm in size. Far from being a typical size-exclusion filter, therefore, the nuclear pore complex is a highly specific selective barrier which the cell uses to tightly control passage in and out of the nucleus. While the important biochemical components of nuclear transport have been identified, the mechanism of selectivity is

still not well understood. Even though the precise mechanism is under debate, it is clear that the NPC is a fascinating example of the cell leveraging intrinsically disordered proteins to accomplish a unique task.

### 1.1.1     **Intrinsically disordered proteins**

It has been long-standing conventional wisdom among biologists that a protein's folded shape determines its function. Most enzymes and other proteins that were studied had a stable folded configuration, the lowest point on a well-defined folding energy landscape. A protein's conformation provided specific docking points through which it could interact with ligands or other proteins in a "lock-and-key" model.

However, a few decades ago, it became clear that not all proteins have a well-defined ternary or even secondary structure, but rather exist as extended polymer chains. These intrinsically disordered proteins (IDPs) were initially dismissed as nonfunctional, but evidence began to accumulate that they were in fact essential for cellular function, modifying the structure-function paradigm. Their roles and importance are still being understood, as are the unusual mechanisms by which they accomplish their functions without a well-defined structure.

Today, it is estimated that 30% of eukaryotic proteins are disordered or contain significant disordered regions [2]. While there is significant sequence heterogeneity among IDPs, they tend to contain a large proportion of hydrophilic residues, and often have long stretches of low-complexity regions where only a few amino acids are represented. They also often have high net charge.

Some IDPs fold (or partially fold) upon binding with an ordered partner, while others form a "fuzzy" complex that remains disordered. Their advantages over folded proteins may include their plasticity, which enables them to bind many different binding partners. Multivalency, either as one-to-many or many-to-one binding, may also play a role. They may act as hubs that bring together larger complexes. Similarly, IDPs often have high specificity at relatively weak binding strengths [3,4].

While the normal functioning of IDPs is important to the cell, IDPs are also prone to aggre-

gation and are at the root of pathologies such as Alzheimer's, Parkinson's, and prion diseases [5]. Often, normally-disordered proteins aggregate into amyloid fibrils, a stable structure consisting of stacked  $\beta$ -sheets.

IDPs are commonly involved in cell signaling and regulation [3]. Their disordered nature makes them useful as hubs that bring together many other proteins, and as scaffolds that many proteins can bind to at once. IDPs appear to be prevalent in transcriptional regulation, and they are increasingly recognized as playing roles in liquid-liquid phase separation within cells [6]. One of the most fascinating examples of IDP function is in the nuclear pore complex (NPC), a unique selective barrier that regulates all transport between the nucleus and the cytoplasm. The link between disorder and selectivity is not well understood in this case.

### **1.1.2 Basics of nuclear transport**

The nuclear pore complex (NPC) resides in the nuclear envelope of eukaryotes and regulates all macromolecular traffic between the nucleus and cytoplasm (Fig. 1.1). The NPC is one of the largest protein complexes in the cell, at about 60 MDa in yeast and 120 MDa in humans [7]. As the regulator of nucleocytoplasmic transport, the NPC must rapidly and specifically allow the passage of a wide array of macromolecules: transcription factors into the nucleus, and RNA into the cytoplasm. It must also be robust under perturbations and able to accommodate mechanical strain as the nuclear envelope changes shape, as well as during the passage of large cargo. These functions are accomplished through a structure with two major components, both made of proteins known as nucleoporins, or Nups: the scaffold Nups, which form a ringlike complex, and the FG Nups, which are disordered and fill the central channel created by the scaffold Nups (Fig. 1.1).

The nuclear pore itself is formed of scaffold Nups, which are ordered proteins that form ring structures with eightfold symmetry [7,9]. The central channel of the pore is filled with disordered FG Nups. FG Nups typically consist of an ordered domain that anchors them to the wall of the channel and an entirely disordered domain that extends into the channel. As with all Nups, FG Nups have eightfold symmetry in the pore, and some of them are present in much higher copy

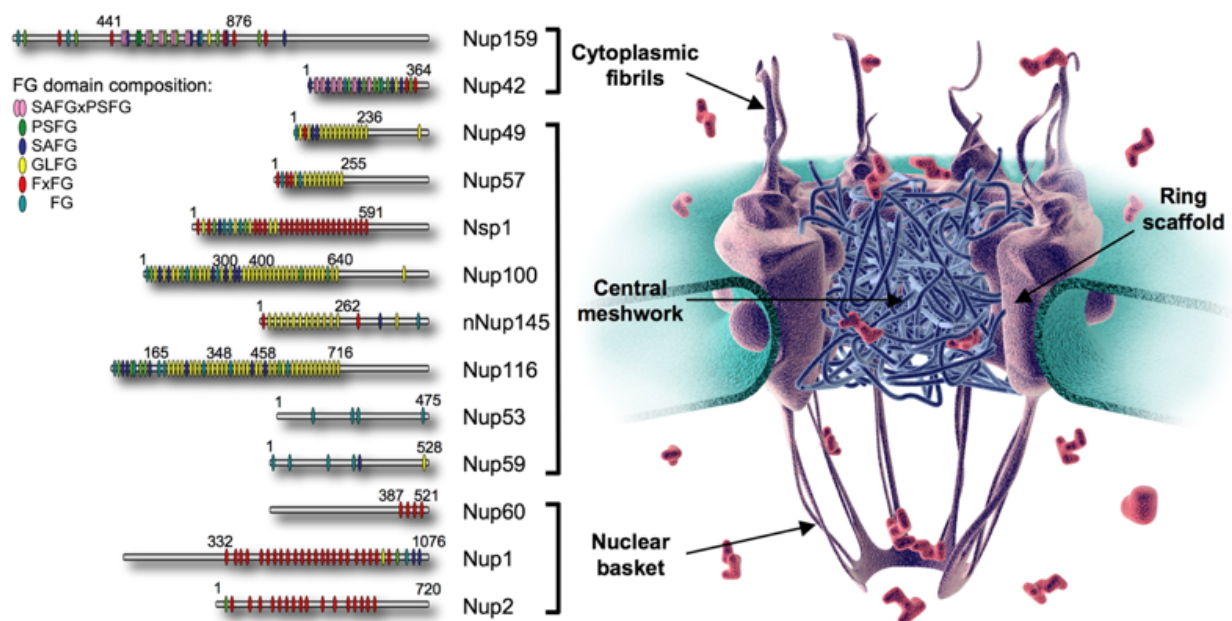


**Figure 1.1:** Nuclear pore complex and FG Nups. The cartoon shows the role of the FG Nups filling the central channel. The left panel shows a schematic of the sequences of important FG Nups and the locations of their FG motifs. Figure adapted from [8].

number. The disordered portion of every FG Nup contains phenylalanine-glycine (FG) motifs which bind to the hydrophobic binding pockets of transport factors. While there are multiple binding motifs, all are short sequences which incorporate an FG repeat; for instance, FSFG, GLFG, and others (Fig. 1.1). Each FG Nup contains tens of FG repeats, leading to a high density of FG repeats within the pore [9, 10].

Since the FG Nups are disordered, most conventional visualization techniques, such as cryogenic electron microscopy and x-ray crystallography, are ineffective. When imaged over time or when several pores are imaged, the averaged results do not show the disordered portion of the FG Nups. Techniques such as NMR and atomic force microscopy (AFM) can help gain insight into their conformational ensembles, as can some superresolution microscopy techniques, though the time and length scales of transport are often prohibitive for any microscopy [11–13]. Early research suggested that the FG Nups formed a central plug or “transporter,” but more recent work suggests that there is no central structure and the central channel is filled instead with highly dynamic disordered proteins [12, 14, 15]. There is some evidence from simulations that the density of the FG Nups, as well as their charge density and hydrophobic properties, are not uniform along either the radial or axial directions [16–18]. This may contribute to selective transport, although the pore still functions without the asymmetric FG Nups [19]. Indeed, the NPC is remarkably robust to FG Nup deletion. Over half of the mass of FG Nups can be removed without eliminating the selectivity barrier [19–22].

Transport factors are ordered proteins that carry cargo through the NPC. While there are various types, they share several features in common, most notably the fact that all known transport factors have more than one hydrophobic binding pocket which binds to FG repeats. Binding affinities between transport factors and FG Nups are surprisingly difficult to measure accurately. Values of the dissociation constant  $K_D$  measured outside of the cellular context are often in the low nanomolar range, implying a binding lifetime which is inconsistent with the experimentally-observed rapid translocation through the nuclear pore [23, 24]. Recent consensus is that binding is much weaker in the cellular environment, with  $K_D$  values between hundreds of micromolar

and millimolar, and with some transport factors additionally being actively released from the pore [25–27]. The extreme binding multivalency of Nup - transport factor interactions adds a further layer of complexity to interpreting affinity data. It is increasingly accepted that the highly transient and multivalent binding of transport factors to FG Nups is key to the combination of high specificity and rapid transport exhibited by the NPC [28].

The karyopherins (Kaps), also known as importins and exportins, are the largest family of transport factors. The approximately twenty different Kaps are responsible for most nucleocytoplasmic transport [29]. Kaps typically consist of multiple HEAT repeats, a helical motif which conveys structural flexibility [30]. Most Kaps bind their cargo directly via a nuclear localization signal (NLS, for nuclear import) or nuclear export signal (NES, for nuclear export). NLS and NES are relatively short amino acid tags found on cargo [31]. However, sometimes the adapter protein importin  $\alpha$  is also needed. In general, Kaps are on the order of 100 kDa in size, well above the passive permeability limit [1]. As discussed below, there is evidence that the presence of Kaps contributes to the selectivity barrier [29, 32–34]. Many Kaps must be actively released from the nuclear pore and from their cargo after transit through hydrolysis of GTP [35, 36].

Unlike the karyopherins, nuclear transport factor 2 (NTF2) does not transport a wide variety of cargo across the NPC. Instead, NTF2 helps maintain the energy gradient needed for transport by carrying the protein RanGDP across the pore [37, 38]. NTF2 is a homodimer whose monomers are 14 kDa and contain at least one FG binding site apiece. Although its small size of 28 kDa is near the 30 kDa cutoff for passive transit through the pore, its flux through the pore is still 30-120 times that of similarly-sized proteins that do not bind to FG Nups [39–41]. NTF2 does not require adapter proteins or active release from the pore. We predominantly use NTF2 as a model transport factor in both the theoretical and experimental work discussed here, because of its simplicity as well as its ease of expression and purification from bacterial cells.

Selective transport requires an energy source, which in the case of the NPC is provided by the Ran cycle. When a transport factor-cargo complex passes from the cytoplasm into the nucleus, it encounters a Ran protein carrying GTP (RanGTP) on the nuclear side, which binds to the

transport factor and displaces the cargo, actively releasing it. Then the transport factor-RanGTP complex can collect a cargo destined for nuclear export, and this ternary complex can diffuse back through the NPC to the cytoplasm. The protein RanGAP then hydrolyzes the RanGTP to RanGDP, breaking the complex into its three original pieces. Ultimately, the energy source for selective nuclear transport comes from the RanGTP-RanGDP gradient between the nucleus and the cytoplasm. This gradient is maintained partially by NTF2, which carries RanGDP through the pore. In the nucleus, RanGDP is returned to its RanGTP state by RanGEF, a protein which is localized to the nucleus [28, 37, 42]. Therefore, even though there is no directionality to NTF2-RanGDP transport, the effect is to replenish the pool of RanGTP in the nucleus. From the perspective of transport, this means that, for many molecules, the process of passing through the pore is itself passive and does not consume energy. The selectivity ultimately arises from concentration gradients maintained by the Ran cycle, but the selection mechanism does not itself require energy input.

One surprising feature of nuclear transport is its sheer speed and volume. The high macromolecular traffic between nucleus and cytoplasm requires high flux through each NPC, of which there are 2000-3000 per human cell [43]. Experiments with permeabilized cells estimate that the total molecular flow through the NPC could be as high as 10-20 MDa per pore per second, corresponding to 100-1000 transport events per pore per second [39]. Experiments focusing particularly on NTF2 report fluxes between 50 and 250 molecules per pore per second [39-41]. Fluxes this high mean a continuously high occupancy of the NPC, estimated at up to 100 karyopherins at once [44]. One reason that individual NPCs can accommodate such high flux is the rapidity with which molecules pass through the pore. A wide range of transport factors and cargo have a dwell time of less than 10 ms in the pore [13, 45-47].

### **1.1.3 Models of nuclear transport**

While the components of nuclear transport are well understood, questions remain regarding the mechanism behind its unusual selective properties. Broadly speaking, two of the most important

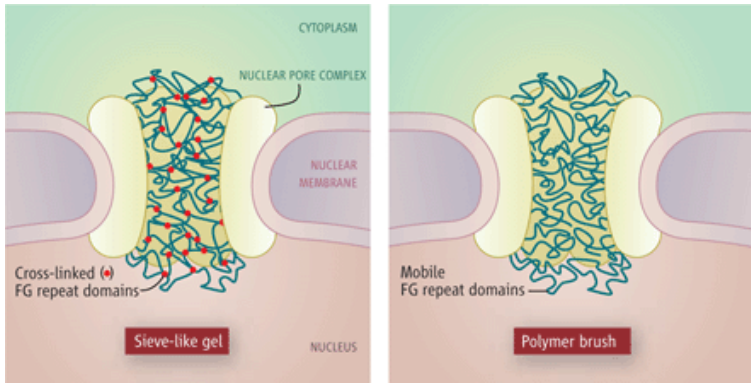


**Figure 1.2:** The two major models of the nuclear pore: the hydrogel (sieve-like gel) and entropic barrier (polymer brush) models. Figure from [48].

theoretical frameworks are the hydrogel model and the entropic barrier model (Fig. 1.2). Both are supported by some experimental results and challenged by others, and they are not mutually exclusive. More recent work suggests that the environment of the nuclear pore is somewhere between these two extremes.

The hydrogel model posits that the FG Nups within the nuclear pore are transiently crosslinked at their FG repeats into a hydrogel-like structure. Inert proteins are prevented from passing through the pore due to the small mesh size, while transport factors carrying cargo can bind to the FG repeats, disrupting the hydrogel and moving through the pore. This view of the nuclear pore is supported by experiments showing that the disordered domain of the FG Nup Nsp1 aggregates into a hydrogel when purified into buffer [49]. These hydrogels show strong selectivity for import of transport factors and their cargo over inert proteins, demonstrating binding between the aggregated FG Nups and the transport factors [50–52]. Theoretical models of diffusion through a transiently-crosslinked hydrogel show selective properties [39,53,54]. However, while nuclear pore mimics which consist of aggregated FG Nups display highly selective entry of transport factors, they do not permit the exit of transport factors over timescales consistent with transport [50, 51]. Furthermore, some Nups which aggregate in buffer remain disordered in the cellular environment [11].

Conversely, the entropic barrier model supposes that FG Nups instead act as polymer brushes within the pore. In this view, inert proteins are prevented from entering the pore due to the entropic penalty they would incur by restricting the possible conformations of the Nups. However, the change in free energy upon a transport factor binding to a Nup offsets the entropic penalty

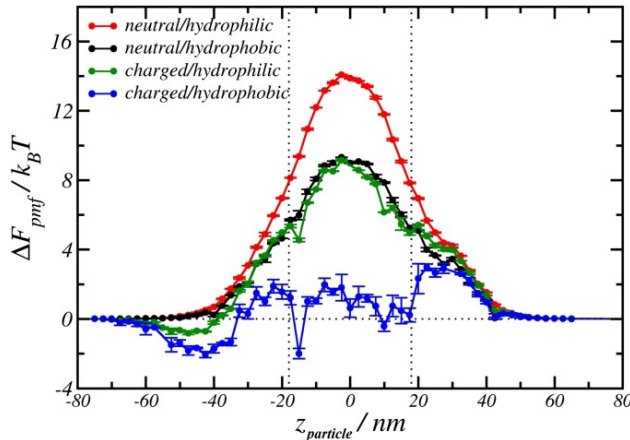


**Figure 1.3:** Example of effective-potential model of nuclear transport. Figure shows a simulated free-energy landscape for a variety of possible transport factors as a function of position within the nuclear pore. Figure from [18].

and allows transport factors and their cargo to pass [55, 56]. Evidence for this view comes from a number of studies in which single layers of FG Nups are grafted onto a surface and their extension monitored as transport factors are titrated on and off the surface [57–59]. Layer height tends to change non-monotonically as transport factors are added, suggesting that the presence of transport factors affects the selectivity of the nuclear pore.

More generally, FG Nups exist on a continuum of “cohesiveness,” ranging from Nups (or portions of Nups) which do not aggregate under any physiological conditions to ones which do so readily [11]. A Nup’s cohesiveness depends on its charge, length, and hydrophobicity. Many simulations of the nuclear pore aim to understand the role of Nup cohesiveness in transport [18, 54, 60, 61]. A relatively common method of modeling transport is to computationally reduce the problem to that of a transport factor diffusing in a one-dimensional effective potential representing its interactions with Nups (Fig 1.3) [1, 18, 62, 63]. These models predict selective transport while being highly dependent on the precise details of Nup composition and location within the nuclear pore. These models also do not presuppose that either the hydrogel or entropic brush model is fully correct, but allow for a mixture of cohesive and non-cohesive Nups.

Apart from the question of FG Nup conformation within the nuclear pore, the role of transport factors themselves in the permeability barrier has been under investigation [29, 32–34]. There is evidence that the presence of karyopherins in the nuclear pore increases its selectivity for transport factors, possibly by establishing “tight-binding” and “weak-binding” subpopulations of Kaps which

compete for binding sites on the Nups [57]. Even nonspecific competition may make the nuclear pore's selectivity barrier more robust as well [64–67]. The precise role of crowding and competition in nuclear pore selectivity is fascinating but as yet unclear.

Relatively few non-computational, quantitative theories of nuclear transport exist. Reaction-diffusion models have been proposed with varying degrees of complexity and different underlying assumptions, but they do not take both binding kinetics and binding site saturation into account [62, 68].

#### **1.1.4 Nuclear pore mimics**

Many strategies have been used in attempts to create nuclear pore mimics which reproduce the selectivity properties of the nuclear pore. These generally fall into two categories: solid-state nanopores grafted with FG Nups, and hydrogels either made entirely of or filled with FG Nups. The hydrogel systems in particular are successful at showing selective entry of transport factors as compared to inert proteins but cannot be used to directly measure the material's selectivity.

Some synthetic nuclear pores recreate the nanopore geometry of the NPC using a perforated membrane which is coated in FG Nups. One such solid-state nuclear pore mimic consisted of the FG domains of Nsp1, Nup98, or Nup153 grafted onto a porous silicon nitride membrane [21, 69]. Translocation events of transport factors or inert proteins through the bare or coated pores can be measured by monitoring the electrical conductance of the pore, which spikes when a protein passes through. The flux of inert proteins drops significantly when the pore is coated with Nups, but that of transport factors remains roughly constant, suggesting selective transport [69]. Another nanopore NPC mimic used pores with diameters ranging from 25 to 100 nm in 15-nm-thick polycarbonate membranes [22]. A portion of the pore was coated in gold to which FG domains of Nsp1 or Nup100 were conjugated. Measurements of flux through these pores showed a maximum of  $\sim 3$ -fold selectivity for NTF2-GST as compared to the similarly-sized inert protein BSA. Similar selectivities were seen for the karyopherin Kap95 with and without cargo. The FG Nup concentration could be tuned by varying the extent of the gold coating; increasing the Nup concentration increased

the selectivity. Solid-state nanopores are the only nuclear pore mimic where selectivity has been directly shown; these selectivities are fairly low relative to that shown by the nuclear pore itself.

One class of hydrogel nuclear pore mimics consists of aggregated FG Nup domains. The FG repeat domain of Nsp1 will spontaneously aggregate into a hydrogel in buffer at physiological pH, as will the GLFG domains of Nup49p and Nup57p [49, 70]. When these hydrogels are challenged with fluorescent transport factors or transport factor - cargo complexes, they show strongly selective influx as compared to inert proteins, with in-gel concentrations reaching 1000 times that of the reservoir surrounding the gel [50]. These hydrogels have amyloid-like characteristics, such as the presence of  $\beta$ -sheets, and they immobilize the FG Nups to a large degree, as shown by fluorescence recovery after photobleaching (FRAP) studies [49, 51]. In addition to transport factors partitioning into the gel, other FG Nup domains become incorporated into the gel when introduced to the surrounding reservoir [49]. Gelation and selective influx are both destroyed by mutating the phenylalanines of the FG motifs to serines, indicating that interactions between FG repeats are necessary for these features [50]. While the selective influx is quite dramatic, direct measurements of diffusion constant or flux through an FG Nup hydrogel have not been made. Appendix A shows the estimated selectivity of several FG Nup hydrogels as predicted by our model described in Chapter 2. Some gels reach predicted selectivities of  $\sim 200$ , within the range observed in the nuclear pore [39–41].

Other nuclear pore mimics also make use of hydrogels, but incorporate FG Nups as only one component of the gel rather than its entirety. One such hydrogel was composed of a portion of the FG domain of Nsp1 fused to a domain that forms pentamers [52]. A fluorescent cargo targeted by Kap95 showed strong selective influx into these hydrogels, though equilibration was not achieved over the timescale of the experiments. The length of the FG Nup fragment used was varied so as to contain one, two, or six FSFG motifs, and the extent of binding of the transport factor-cargo complex to the gel was shown to depend on the number of binding motifs used. Predicted selectivities of these hydrogels are also shown in Appendix A.

Other hydrogel nuclear pore mimics used an inert hydrogel as a scaffold to which fragments

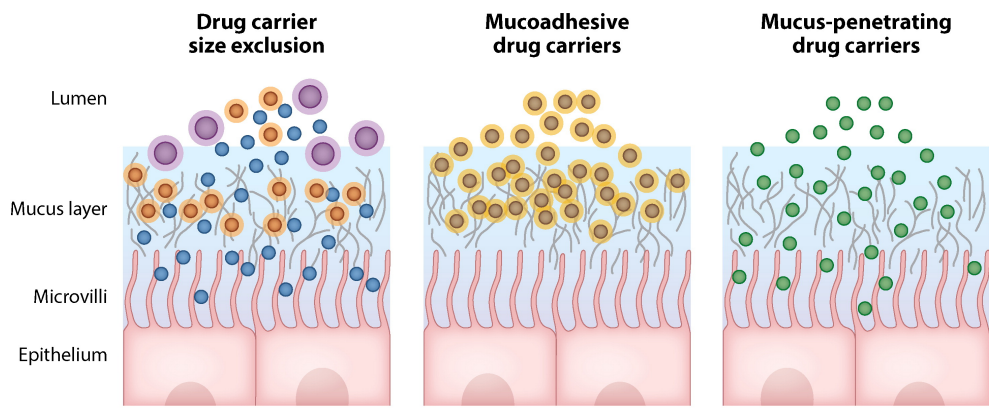
of FG Nups or other disordered peptides were tethered. Selective influx of the transport factor fusion protein GFP-Kap95 was shown for an acrylamide hydrogel containing high concentrations (250-400 mM) of stand-alone FSFG motifs, not incorporated into a longer peptide [71]. Increasing the concentration of FSFG anchored to the hydrogel increased the partitioning of GFP-Kap95 into the gel, but the influx was relatively low given the high concentration of FSFG motifs in the hydrogel. Other hydrogel mimics used engineered peptides with similar properties as those of FG Nups but not derived from them [68]. These were tethered to a PEG hydrogel and bound a fluorescent antibody (approximately 150 kDa) with varying affinity. The influx of antibody into the hydrogels showed a non-monotonic dependence on affinity, with an optimal dissociation constant  $K_D \approx 30 \mu\text{M}$ . FRAP measurements confirmed that binding antibodies diffused more slowly in the gel than did inert control proteins.

An interesting preliminary work demonstrated the use of DNA origami to mimic the scaffold of the nuclear pore by assembling DNA into a ring 46 nm in diameter and 14 nm in height, with up to 48 sites for FG Nup attachment [72]. When FG domains of Nsp1 or Nup100 were anchored to the attachment points, AFM confirmed that the Nups filled the center of the ring and remained highly dynamic.

While nuclear pore mimics, especially hydrogel-based mimics, show strong selective influx of transport factors, direct measurements of selectivity have remained largely unavailable.

## 1.2 Other selective biofilters

Selective biofilters exist in many contexts outside of nuclear transport, and they frequently include a common set of elements that are exemplified by the nuclear pore. In particular, cells often need proteins to move rapidly within a cellular compartment but still possess high binding specificity. This is often accomplished with intrinsically disordered proteins that interact transiently and multivalently with their binding partners. In the crowded environment of the cell or extracellular matrix, nonspecific binding can immobilize proteins, hindering selective motion, unless those proteins are able to continue diffusing while bound, a feature which we argue is key to the selective



 Carlson TL, et al. 2018.  
Annu. Rev. Biomed. Eng. 20:197–220

**Figure 1.4:** Nanoparticle drug delivery through a mucus barrier. Particles which are too large cannot pass the size-exclusion barrier. Mucoadhesive particles penetrate the mucus layer but are trapped by binding interactions. Inert mucus-penetrating particles have a much higher diffusion constant in mucus. Figure adapted from [73, 74].

transport of the NPC as well as the biofilters discussed here. The following section presents three particular examples of selectivity in biological systems, from widely disparate areas, which bear striking similarities to the selectivity of the nuclear pore. In the remainder of this work, we model selective transport using a minimal set of characteristics that, while inspired by the nuclear pore, apply to the systems described here as well.

### 1.2.1 Drug delivery through mucus barriers

One medically-important selective biological barrier is the mucus which lines organs such as the lungs, nose, and stomach. In particular, lung mucus presents a barrier to delivery of inhaled medication. If nanoparticles containing drugs for diseases such as asthma and lung cancer could be inhaled and taken up by lung cells, doses could be lower, as the uptake would be more targeted [73, 75]. However, lungs are coated by a layer of mucus intended to prevent foreign objects from reaching the lung cells. In order to deliver nanoparticles to lung cells, they must be engineered to pass the selective mucus barrier.

Mucus consists predominantly of disordered glycoproteins known as mucins, though other components such as lipids are present as well [76]. These entangled mucins present multiple barriers

to nanoparticles, as shown in Fig. 1.4. First, large particles are excluded due to the 150-350 nm average pore size of mucus gels [77, 78]. Second, even particles which are small enough to enter the mucus layer often bind to mucins. In fact, mucoadhesive particles (MAPs) have been specifically engineered on the principle that increasing the nanoparticle's lifetime within the mucus will lead to more efficient drug delivery [79]. However, diffusion of MAPs is often so slow that they do not penetrate beyond the edge of the mucus layer. Furthermore, mucus gradually replaces itself on clearing timescales which vary depending on the type of mucus. Nanoparticles in the outermost region may be cleared more rapidly than those which diffuse deeply into the mucus layer; however, the extent to which mucus clearance depends on depth within the layer is uncertain [80–82].

Another approach for nanoparticle delivery through the lung mucus barrier makes use of small, inert particles which minimize nonspecific interactions with mucins. These mucus-penetrating particles (MPPs) are typically coated in PEG or another inert polymer [75, 83]. MPPs can reach much higher diffusion constants in mucus than can MAPs [78, 84–86]. For instance, 200-500 nm particles coated in PEG had a diffusion constant in mucus thousands of times higher than similarly-sized uncoated particles [78]. PEG-coated nanoparticles under 300 nm are retained in mouse lungs 2-3 times longer than uncoated particles [75]. These results suggest that drug delivery through the mucus barrier may be improved by minimizing binding interactions with mucins.

The selective barrier of lung mucus bears similarities to the selectivity of the nuclear pore in that it consists of disordered proteins which bind to particles impinging on the barrier. However, in the case of mucus, binding inhibits the flux of particles through the selective filter, while binding enhances the flux of transport factors through the nuclear pore. A better understanding of the role of binding and bound diffusion in a selective filter such as the nuclear pore could suggest novel strategies for nanoparticle delivery through lung mucus. Perhaps binding can be used in a way that enhances nanoparticle flux over that of inert particles, improving drug delivery through mucus barriers.

### 1.2.2 Diffusion of DNA-binding proteins in the nucleus

Principles of selectivity appear in biological systems beyond straightforward filtering. In particular, transient binding and bound-state diffusion are important to DNA targeting in the nucleus by transcription factors and DNA damage repair proteins. A protein diffusing in the cell's nucleus has many of the same constraints and capabilities as a transport factor passing through the nuclear pore: it is surrounded by a high concentration of flexible tethers to which it binds transiently. Just as this situation leads, counterintuitively, to high flux of transport factors through the nuclear pore, DNA-targeting proteins find their specific targets much more rapidly than would be naively predicted [87]. For example, the zinc-finger transcription factor Egr-1 appears to locate its target DNA within a few minutes of arriving in the nucleus, despite observed micromolar affinities for nonspecific DNA sequences [88].

Solutions to this “needle in the haystack” challenge resemble possible mechanisms of bound diffusion in the nuclear pore complex. In particular, it is widely accepted that the search for targets is made more rapid through facilitated diffusion, involving proteins sliding along strands of DNA. However, the optimal time spent in a one-dimensional search as opposed to a free three-dimensional search is unclear; as is the effectiveness of sliding as opposed to multiple, rapid binding and unbinding events [89]. This mechanism is reminiscent of both the sliding mechanism predicted in some transport factors and of the effect of diffusion while bound to a flexible tether [90]. Additionally, transfer of a multivalent transcription factor between two strands of chromatin, a mechanism known as intersegmental hopping, can increase the protein’s search space similarly to the multivalent inter-Nup hopping that is available to transport factors [91, 92]. Finally, transient binding plays an important role in the search for DNA targets. This speed-stability paradox reflects the fact that, like in the nuclear pore, proteins must bind very weakly to their DNA tethers to avoid becoming immobile. Unlike nuclear transport, however, DNA-binding proteins must bind more tightly to their targets upon reaching them [88, 93].

A case in point, further discussed in Sec. 2.4.1, is that of poly(ADP-ribose) polymerase 1

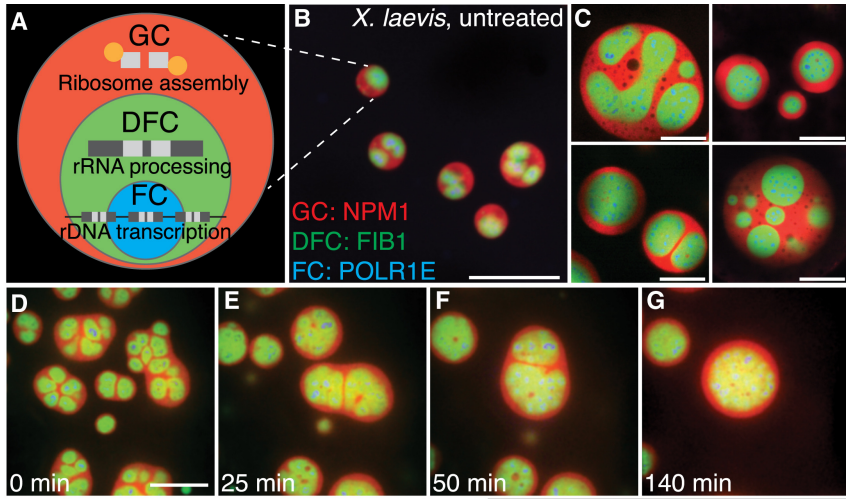


**Figure 1.5:** Phase-separated subcompartments of a *Xenopus* nucleolus. (A) Schematic of subcompartments. (B)-(C) Fluorescence microscopy image of nucleoli with subcompartments in red, green, and blue. (D)-(G) Time-course showing dissolution of compartments after actin disruption. Figure adapted from [97].

(PARP1), a DNA damage repair protein which rapidly localizes to sites of DNA damage. PARP1 binds damaged DNA with low nanomolar affinities, and appears to bind undamaged DNA only a few orders of magnitude more weakly [94]. Given that there are up to 5 mM nonspecific DNA binding sites in the nucleus, the speed with which PARP1 diffuses ( $\sim$  10 times slower than in buffer) is remarkable [88]. PARP1 contains multiple DNA-binding sites, and an inter-strand hopping mechanism has recently been demonstrated, which may explain its rapid diffusion [95]. However, removal of that mechanism only moderately slows the recruitment of PARP1 to sites of DNA damage, suggesting that a further mechanism of bound-state diffusion is necessary [96]. The principles of selective nuclear transport may help to explain the rapid motion of PARP1, along with other DNA damage repair proteins and transcription factors.

### 1.2.3 Subcompartments in liquid droplets

Features of nuclear transport such as highly-concentrated disordered proteins and bound-state diffusion also appear in liquid-liquid phase separated droplets. Liquid-liquid phase separation as a driving force for the formation of membraneless organelles is rapidly gaining prominence. It is becoming clearer that many cellular functions are regulated through the separation of mixtures into phases rich in various proteins and other cellular components. Membraneless organelles include nucleoli, which aid in processing ribosomal DNA genes within the nucleus, and RNA granules, which

help sort mRNA [6, 98].

Liquid-liquid phase separation typically occurs for mixtures containing IDPs with multivalent interactions, described as “sticker” and “spacer” regions, similar to the hydrophobic FG repeats and hydrophilic linker regions in FG Nups [99]. For example, the disordered protein FUS, widely studied for its phase separation behavior, consists of interacting regions rich in tyrosine and arginine separated by linkers enriched in glycine and serine [100]. Dense liquid phases are highly concentrated, but the proteins that compose them remain mobile. There are subcompartments of varying composition within some membraneless organelles, which may be due to liquid-liquid phase separation. Nucleoli contain multiple subcompartments which are thought to perform distinct functions (Fig. 1.5) [97, 101, 102], while RNA granules have recently also been shown to have a core-shell structure [98, 103].

Much of the current work on liquid-liquid phase separation in subcompartments of membraneless organelles is focused on simply identifying the components of the compartments [102]. Discussion of their purpose and mechanisms is still quite speculative. However, it seems plausible that one function of these compartments is to selectively concentrate enzymes or other proteins to increase reaction rates. RNA bodies in particular are known to sort and sequester mRNA [98]. As such, the presence of disordered, multivalent proteins may not simply be necessary for the formation of phase separated droplets, but could potentially assist in selectively filtering the components of the subcompartments. If nuclear transport is a guide, binding partners of the IDPs which form the outermost phase might have a higher flux into the inner compartments than nonbinding proteins. Additionally, in the context of bound-state diffusion, liquid droplets represent maximal bound diffusion, as binding to an IDP in solution will not appreciably slow the diffusion of the binding partner. While these possibilities will not be testable for some time, phase-separated membraneless organelles may prove to be a fascinating application of selective biofiltering.

### 1.3 Project goals and motivation

All of the systems described above involve the rapid flux of proteins which still bind highly selectively to their environment. We wondered whether there were simple features, such as such as transient, multivalent binding to flexible, dynamic tethers, that could explain this apparent paradox. We approached the problem through both modeling and experiment and identified a common key parameter in the form of bound-state diffusion. While the theory and experimental setup were based on nuclear transport, both platforms are general enough to apply to a number of selective biofilters.

#### 1.3.1 Minimal model of selective transport

Despite the complexity of nuclear transport, many components can be removed or approximated without eliminating its unusual selective properties. For example, Nups which are asymmetrically distributed along the axis of the nuclear pore can be removed, as can a large fraction of Nups overall, without destroying selectivity [19–22]. And though many transport factors require active release from the pore (i.e. energy consumption), others, such as NTF2, do not; selectivity is not therefore dependent on active release. We decided to model the pore in order to answer the question: What are the minimum requirements for selective transport?

In the course of creating the model, we found that one possible set of minimum requirements is quite simple indeed. The model discussed in Chapter 2 not only dispenses with non-uniformly distributed Nups and facilitated release, but also with nonspecific crowding, Kap-centric control of the nuclear pore, the Ran cycle, and even the nanopore geometry. Instead, the pore is treated as a bulk material of finite thickness with an artificially-imposed concentration gradient to drive flux across it. Competition for binding sites is retained in the form of binding site saturation, but even without this feature we see selective flux across the barrier. Our model fundamentally contains only diffusion and binding of transport factors to Nups - an extremely streamlined depiction of nuclear transport, and one that can even be treated semi-analytically.

The simplicity of our model made the key parameter clear: we could not reproduce the selectivity of the nuclear pore without allowing bound-state diffusion, that is, assuming that bound Nup - transport factor complexes were mobile within the pore. Bound diffusion provides a possible answer to the paradox of nuclear transport, resulting in a higher flux of transport factors, which bind to Nups, than inert proteins which do not. In our model, this straightforward mechanism alone gave rise to the decidedly unintuitive behavior of the nuclear pore.

Having identified bound-state diffusion as an important parameter for selective filters, we investigated possible methods of bound diffusion within the nuclear pore. Two possibilities emerged from basic, well-accepted facts of nuclear transport: tethered diffusion arising from the disordered, flexible nature of the Nups, and inter-chain hopping of the transport factor due to its binding multivalency. Upon investigation, both mechanisms can plausibly provide the high bound diffusion constant needed to reproduce the selectivity of the nuclear pore.

While this model was inspired by nuclear transport, it ultimately relies on only a few key properties of the system. With this model, we predict that selective transport will occur where there is bound-state diffusion, which can be readily obtained if flexible IDPs are present for tethered diffusion, or if highly transient, multivalent binding allows for motion from one site to another while remaining bound. The systems described above in Sec. 1.2 fall into this category, as likely do many others. Furthermore, these principles might guide artificial selective biofilters with novel rapid, highly-selective properties.

### **1.3.2 Experimental tests of bound-state diffusion in biomaterials**

After developing a minimal model of selectivity, we began designing a synthetic biofilter with which to experimentally probe the effects of bound-state diffusion. The model itself is sufficiently general to apply to a wide range of filters, giving us some freedom in designing a material to test its predictions. We chose to use the nuclear pore as inspiration for this material because its key components are so well known, if not well understood. In order to capture the key features of selectivity, we designed hydrogels containing peptide tethers derived from FG Nups. The transport

factor NTF2 served as a test protein whose diffusion we could compare with a similarly-sized but nonbinding control protein. These hydrogel nuclear pore mimics display the mechanisms that lead to selective transport in our model: flexible, dynamic tethers which can transiently bind to transport factors, along with multivalent transport factors which can “hop” between peptide chains without fully unbinding. We predicted that these features would be sufficient for bound-state diffusion of the transport factor within the hydrogel.

As with the theoretical model, many of the NPC-specific details, such as the nanopore structure and Ran gradient, were omitted. A bulk material was used instead of nanopores because our model should apply equally well to both, and a macroscopic hydrogel is much easier to study. We quickly realized that hydrogels are a challenging system to use for protein separation. The nuclear pore mimics have a rigorous set of competing constraints: for example, the hydrogel should be in mechanical equilibrium and homogeneous, while still well-sealed to a flow chamber so that proteins cannot bypass the gel. Chapter 3 documents the design of the hydrogel nuclear pore mimics. Many modifications intended to improve the diffusion properties and reproducibility of the hydrogels proved unsuitable for our needs. However, we eventually produced a biomaterial that can be used to measure bound diffusion, while also developing more general guidelines for designing hydrogels that are useful for protein separation.

The resulting bound-state diffusion measurements are presented in Chapter 4. Fluorescence recovery after photobleaching (FRAP) was used to determine the effective diffusion constants of both NTF2 and an inert protein, from which the bound diffusion constant was calculated. The data analysis ultimately required a two-dimensional Fourier series solution to the diffusion equation, resulting in a set of data-processing scripts which describe the FRAP recovery curves while the proteins are undergoing equilibration between the hydrogel and a reservoir. We measured a non-zero bound diffusion constant that is consistent with the predictions of our model and tested the effect of varying Nup length on bound-state diffusion. Our results indicate that these nuclear-pore-inspired hydrogels can be used to probe the effect of our model’s parameters on bound diffusion.

While bound diffusion is a key parameter in our selectivity model, the aggregation state of

the Nups could also affect selectivity. Aggregated Nups will be less dynamic and will effectively act as shorter tethers, limiting bound diffusion. In Chapter 5, we probed the aggregation behavior of an FG-Nup-derived peptide in several crowded conditions. Using a fluorescent amyloid assay, we identified significant differences in the aggregation dynamics in the presence of different crowding agents, including poly(ethylene glycol) (PEG) and polyvinylpyrrolidone (PVP), two inert polymers that are widely presumed to be interchangeable as crowders. We followed this aggregation assay with NMR and fluorimetry studies in order to investigate the nature of the changes. The results suggest that the presence of an aromatic ring in PVP may interact with the phenylalanines in the FG motifs of the peptide, changing its local chemical environment and therefore its aggregation behavior.

Although a true hydrogel-based selective biofilter proved challenging to design, our nuclear-pore-inspired material can be used to measure the bound-state diffusion of proteins. This parameter is likely important to a variety of problems involving rapid transport of highly-selective proteins. Both the model and biomaterials developed here could be used to investigate these systems more generally in the future. This work suggests that bound-state diffusion, particularly when resulting from transient, multivalent binding, may explain a number of unusual biological filters.

#### **1.4 Biophysics is beautiful**

Even beyond the ample practical reasons to study the nuclear pore, nuclear transport is a fascinating process, full of counterintuitive results and apparent paradoxes. The nuclear pore is at once an incredibly intricate nano-machine and surprisingly robust to perturbation. Passage through the nuclear pore is carefully controlled by complex cellular processes, yet the mechanism of selectivity itself does not require energy input. Nuclear transport can enhance the flux of transport factors hundreds of times over that of inert proteins using a mechanism that conventionally *reduces* protein mobility.

Where the NPC is not apparently self-contradictory, it is a picture of extremes. FG Nups are not only disordered, many show virtually no signs of secondary structure whatsoever and do not

order appreciably upon binding transport factors. Nup - transport factor binding is extreme on many axes: the affinity, likely in the millimolar range, is weak enough that most biochemists would characterize it as nonspecific binding, yet it permits a high flux through the pore. At the same time, the on-rate is ultrafast, bounded by the physical diffusion limit rather than chemical considerations. Finally, with dozens of FG motifs along the length of each Nup, and multiple binding pockets on each transport factor, Nup - transport factor binding is dizzyingly multivalent. It is perhaps no wonder that measurements of the binding affinity have historically spanned six orders of magnitude; at this level of multivalency, even the notion of “binding affinity” itself becomes difficult to define. In almost every respect, the binding interactions which underpin selective transport are as far removed as possible from textbook protein-protein interactions. The nuclear pore is a fundamentally *weird* system and deserves to be studied purely for the joy of discovering how something so unusual operates.

Furthermore, the details of nuclear transport are all but invisible even to the most cutting-edge biochemical techniques. The timescale of transport is too fast, the size too small, and the disordered Nups too dynamic to permit direct visualization of transport. This is a system which practically demands to be studied using nontraditional, interdisciplinary methods.

There is value in approaching the nuclear pore specifically from the perspective of physics. Biophysics as a field experiences constant tension between the need to account for the incredible complexity of any living system and the drive to reduce it to its smallest, tidiest set of component parts. As a physicist, I take deep satisfaction from applying a broad and simple theory to a complicated system and still getting meaningful results. All of the messy intractable details are of course ultimately necessary for life to exist, but if a big, sweeping, absurdly simple, underlying principle can explain even 50% of a complex system, that’s beautiful. Such opportunities abound in biophysics, from fruit flies which right themselves after mid-flight perturbation, to the scaling of barbs in cat tongues, to how cucumber tendrils coil and overwind, to the nuclear pore complex and more [104–106]. Sometimes it’s worthwhile to apply basic physical theories to ridiculously complicated things which they manifestly cannot fully explain - valuable practical advances frequently

arise from surprisingly slender foundations.

Whether viewed through a practical, intellectual, or aesthetic lens, there is much to be gained from the study of nuclear transport and, more broadly, of binding and diffusion in selective biofilters. Certainly I have found that, despite the setbacks and disappointments which accompany all research, I have never been able to describe my work to others without becoming truly enthusiastic yet again.

## Chapter 2

### Modeling bound-state diffusion in selective filters

The nuclear pore complex (NPC) is an unusual selective biofilter whose precise mechanism of selectivity is not well understood. In particular, an apparent paradox arises from the fact that transport factors, which bind to FG Nups within the pore, have a much higher flux through the pore than inert, nonbinding proteins. This fact is surprising, given that binding must necessarily slow the passage of a transport factor through the pore. We wanted to understand how binding increases flux through the nuclear pore and other similar selective biofilters.

To that end, we developed a simple mathematical model of selective transport inspired by the nuclear pore. While the model is based on nuclear transport, it is general enough that it can be applied to a wide range of biological systems and synthetic biofilters. Unlike most existing quantitative models of nuclear transport, which reduce transport to diffusion in a single one-dimensional effective potential, this model does not require simulations or a precise accounting of the locations and composition of Nups along the pore axis [1, 18, 59, 63, 107]. It is equally applicable to bulk materials and to nanopores. A few other first-principles models of the pore have been developed using similar differential equations but making different assumptions about boundary conditions and binding equilibrium [62, 68]. Our model is the only one we know of to explicitly include both binding kinetics and binding site saturation.

The primary surprising result of our model was the importance of bound-state diffusion for selectivity. No selective filtering was possible if the transport factor - Nup complex was immobile, regardless of the other parameters. However, if bound diffusion within the pore was permitted,

the selective flux of transport factor through the pore as compared to that of an inert protein approached that measured experimentally. These results suggest that bound-state diffusion is a key parameter to selective transport within the nuclear pore and perhaps to a number of other biofilters as well.

The work in this chapter was a collaboration between myself and Mike Stefferson under the direction of Loren Hough. Mike contributed significantly to developing the model and wrote the numerical simulations in both the linear and non-linear cases.

## 2.1 Simplified model of nuclear transport

Nuclear transport is quite complex, but its unusual selective properties can be modeled much more simply than can the entirety of transport. A major goal of our model was to reproduce the selectivity of the nuclear pore in most straightforward way possible. To that end, we made many simplifying assumptions. The nuclear pore was treated as a one-dimensional selective membrane uniformly filled with Nups. While the nuclear pore itself has a non-uniform, asymmetric distribution of Nups along its axis, as well as variation in the FG motif density along its radius, its selectivity remains intact when the asymmetric Nups are removed. In fact, a significant fraction of Nups can be removed without destroying selectivity [19–22]. The possibility of a wide capture area outside the pore was also neglected [108], leaving a simplified system as shown in Fig. 2.1A.

Many transport factors require active release from the pore and from their cargo [24, 35, 61, 109]. To avoid the complications of facilitated release, we focused on the diffusion of Nuclear Transport Factor 2 (NTF2) through the selective barrier. NTF2 leaves the pore without consuming energy. While it is on the cusp of the passive diffusion limit at 30 kDa, its flux through the pore is 30-120 times higher than that of a similarly-sized non-binding protein [61, 62]. The small size of NTF2 is also a benefit in that it is significantly smaller ( $\sim 5$  nm) than the depth of the nuclear pore ( $\sim 100$  nm), meaning that our approximation of the pore as a bulk material is appropriate.

Our model also assumed that the rate-limiting step of nuclear transport is motion within the pore, not entry or exit. In single-molecule measurements, most of the transport time is spent in a

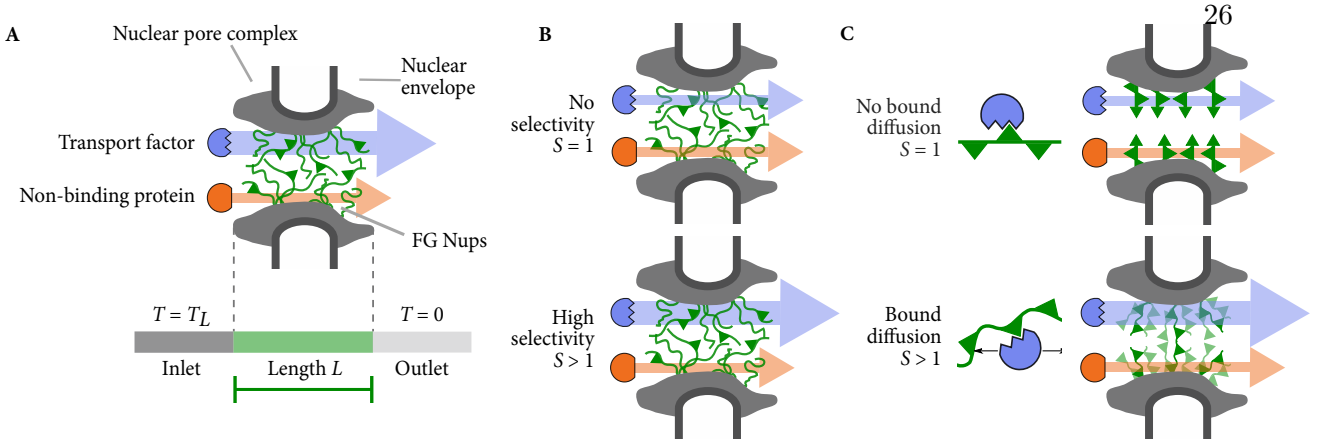


**Figure 2.1:** Schematics of the nuclear pore complex and model. (A) The nuclear pore complex (gray) is filled with FG Nups (green polymers) that selectively pass transport factors that bind to FG Nups (blue) while blocking nonbinding proteins (red). The central channel of the pore has length  $L$ . Protein concentration is high on the left (inlet) and low on the right (outlet). (B) Selectivity quantifies the degree of selective transport through the pore. A non-selective pore with  $S = 1$  has the same flux for a transport factor as for a non-binding protein (top). A selective pore with  $S > 1$  has a larger flux for a transport factor than a non-binding protein (bottom). (C) The bound diffusion coefficient quantifies the mobility of a bound transport factor. A transport factor may be immobile (top) or mobile (bottom) when bound.

random walk within the central channel, supporting this assumption [63, 110].

We considered a channel of length  $L$  separating two reservoirs and filled homogeneously with Nups (Fig. 2.1A). A concentration difference was imposed between the two reservoirs in order to drive flux. Within the channel were free transport factor (concentration  $T$ ), free FG Nups ( $N$ ), and bound transport factor-FG Nup complex ( $C$ ), with total Nup concentration  $N_t = N + C$ . Transport factor diffusion within the channel ( $0 < x < L$ ) was described by the reaction-diffusion equations

$$\frac{\partial T}{\partial t} = -k_{on}TN + k_{off}C + D_F \frac{\partial^2 T}{\partial x^2}, \quad (2.1)$$

$$\frac{\partial C}{\partial t} = k_{on}TN - k_{off}C + D_B \frac{\partial^2 C}{\partial x^2}. \quad (2.2)$$

Transport factor - Nup interactions had on-rate constant  $k_{on}$ , off-rate  $k_{off}$ , and dissociation constant  $K_D = k_{off}/k_{on}$ . We included competition between transport factors for FG binding sites by allowing the concentration of free Nups  $N$  to vary [1]. The diffusion constants of free ( $D_F$ ) and bound ( $D_B$ ) transport factors were spatially constant. The fixed reservoir transport factor concentrations were  $T_0$  (inlet, left) and 0 (outlet, right).

The flux of transport factor out of the pore is  $J = -D_F \partial T / \partial x|_{x=L}$ . We defined a figure of merit, selectivity, to describe the steady-state enhancement in transport factor flux over that of a non-binding protein (Fig. 2.1B). Selectivity is defined as

$$S = \frac{J_{\text{binding}}(t \rightarrow \infty)}{J_{\text{non-binding}}(t \rightarrow \infty)}. \quad (2.3)$$

Mike Stefferson developed code that numerically integrated the full, nonlinear reaction-diffusion equations and calculated selectivity [111].

### 2.1.1 Linear approximation and analytic solution

Experimental evidence suggests that the flux of transport factors within the pore is linearly related to their concentration [67, 112]. This would imply that few of the Nup binding motifs are occupied, so that  $C \ll N$ . In this case, the concentration  $N$  of unbound Nups is approximately equal to the total Nup concentration  $N_t$ . Letting  $N \approx N_t$  linearizes the reaction-diffusion equations (Eqns. 2.1 and 2.2), at which point they can be solved analytically. The solution was developed by Loren Hough and Mike Stefferson and is presented here. A similar system was solved in the linear case by [68]. The full nonlinear numerical solution was used in all other sections unless noted otherwise.

The analytic solution for flux can be directly derived in the linear case. For ease of calculation, we reverse the concentration gradient used in the nonlinear model, so that  $T(0) = 0$  and  $T(L) = T_0$ , allowing us to calculate flux at  $x = 0$ . The reaction-diffusion equations at steady state in the linear limit  $N \approx N_t$  are

$$0 = -k_{\text{on}}N_tT + k_{\text{off}}C + D_F \frac{\partial^2 T}{\partial x^2}, \quad (2.4)$$

$$0 = k_{\text{on}}N_tT - k_{\text{off}}C + D_B \frac{\partial^2 C}{\partial x^2}. \quad (2.5)$$

The change of variables  $C = C_x + N_t K_A T$  (where  $K_A = k_{\text{on}}/k_{\text{off}} = 1/K_D$ ) yields

$$0 = k_{\text{off}}C_x + D_F \frac{\partial^2 T}{\partial x^2} \quad (2.6)$$

$$0 = -k_{\text{off}}C_x + D_B \frac{\partial^2 C_x}{\partial x^2} + N_t K_A D_B \frac{\partial^2 T}{\partial x^2}. \quad (2.7)$$

Substituting  $C_x(x) = -\frac{D_F}{k_{\text{off}}}\partial^2T/\partial x^2$  makes Eqn. 2.7 into a fourth-order ODE

$$\lambda^2 \frac{\partial^2 T}{\partial x^2} = \frac{\partial^4 T}{\partial x^4}, \quad (2.8)$$

where  $\lambda^2 = k_{\text{off}}(D_F + N_t K_A D_B)/(D_F D_B)$ . Solutions to this equation have the form

$$T(x) = b + mx + fe^{\lambda x} + ge^{-\lambda x}$$

where  $b$ ,  $m$ ,  $f$  and  $g$  are constants fixed by four boundary conditions: free transport factor concentration is fixed at the edges of the pore, with  $T(0) = 0$ ,  $T(L) = T_0$ . No flux of bound transport factor into or out of the pore occurs, giving  $\partial C/\partial x|_{x=0} = 0$ ,  $\partial C/\partial x|_{x=L} = 0$ . The constants of integration are

$$b = -(f + g), \quad (2.9)$$

$$m = \frac{T_0 \lambda (\zeta - (D_F/k_{\text{off}})\lambda^2) (e^{L\lambda} + 1)}{2\zeta - 2\zeta e^{L\lambda} + L\zeta\lambda - (D_F/k_{\text{off}})L\lambda^3 - (D_F/k_{\text{off}})L\lambda^3 e^{L\lambda} + L\zeta\lambda e^{L\lambda}}, \quad (2.10)$$

$$f = -\frac{\zeta m}{\lambda (\zeta - (D_F/k_{\text{off}})\lambda^2) (e^{L\lambda} + 1)}, \quad (2.11)$$

$$g = \frac{\zeta m + f\zeta\lambda - (D_F/k_{\text{off}})f\lambda^3}{\zeta\lambda - (D_F/k_{\text{off}})\lambda^3}. \quad (2.12)$$

where  $\zeta = N_t/K_D$ . This leads to a concentration profile of bound transport factors

$$C(x) = \zeta \left( b + mx + fe^{\lambda x} + ge^{-\lambda x} \right) - (D_F\lambda^2/k_{\text{off}}) \left( ge^{-\lambda x} + fe^{\lambda x} \right). \quad (2.13)$$

To determine the selectivity, we calculate the steady-state flux out of the pore  $J = -D_F \partial T / \partial x|_{x=0}$ , giving

$$J = -D_F(m + \lambda f - \lambda g) \quad (2.14)$$

$$J = \frac{T_0(D_F^2/k_{\text{off}})\lambda^3 (e^{L\lambda} + 1)}{2\zeta - 2\zeta e^{L\lambda} + L\zeta\lambda - (D_F/k_{\text{off}})L\lambda^3 - (D_F/k_{\text{off}})L\lambda^3 e^{L\lambda} + L\zeta\lambda e^{L\lambda}} \quad (2.15)$$

The dependence on  $D_B$  enters through  $\lambda$ . For a non-binding particle,  $C(x) = 0$ ,  $T = T_0 x/L$ , and

$$J_n = -\frac{D_F T_0}{L}. \quad (2.16)$$

The selectivity  $J/J_n$  is then independent of  $T_0$  in the linear approximation (Fig. 2.3).

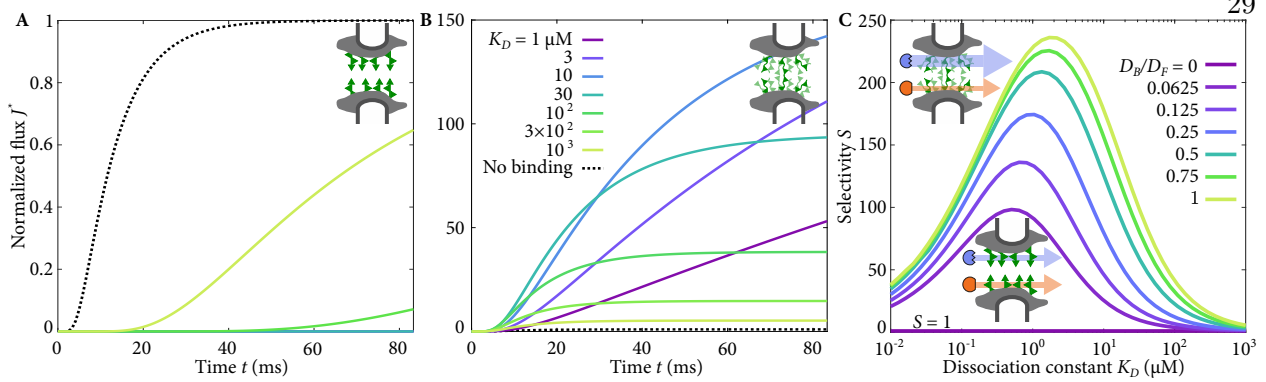


**Figure 2.2:** Flux through the pore and selectivity for transport factors with varying bound mobility. (A) Flux as a function of time when transport factors are immobile while bound, with varying binding affinity as in (B). (B) Flux as a function of time when transport factors are mobile while bound with  $D_B = D_F$ , with varying binding affinity. (C) Selectivity as a function of dissociation constant with varying bound diffusion coefficient.

### 2.1.2 Effect of bound-state diffusion constant

When the selectivity is calculated for the full nonlinear equations, bound-state mobility is immediately obvious as the key parameter. We were unable to create a selective material if the bound diffusion constant  $D_B$  was set to zero, i.e. if the Nup-transport factor complex was immobile while bound. In those cases, the steady-state flux of transport factor and inert protein was identical regardless of the values chosen for  $k_{\text{on}}$  or  $k_{\text{off}}$ , giving a selectivity of  $S = 1$ . The transient flux ratio did depend on binding kinetics, as shown in Fig. 2.2A and B. As would be expected, the transient flux of transport factor out of the material was suppressed relative to that of the inert protein while a subpopulation of the transport factor filled binding sites throughout the material. Once binding equilibrium has been established, however, the immobile population of bound transport factors cannot contribute to the flux out of the pore, and the steady-state flux of binding and non-binding proteins is identical in the absence of bound diffusion.

However, when bound-state mobility is allowed and  $D_B > 0$ , the system's selectivity can greatly increase, as shown in Figure 2.2C. The transient response is dramatically different as well. Now transport factor flux very rapidly outpaces that of inert protein. It should be noted that the timescale for equilibration is similar to the dwell time observed experimentally for NTF2 in the

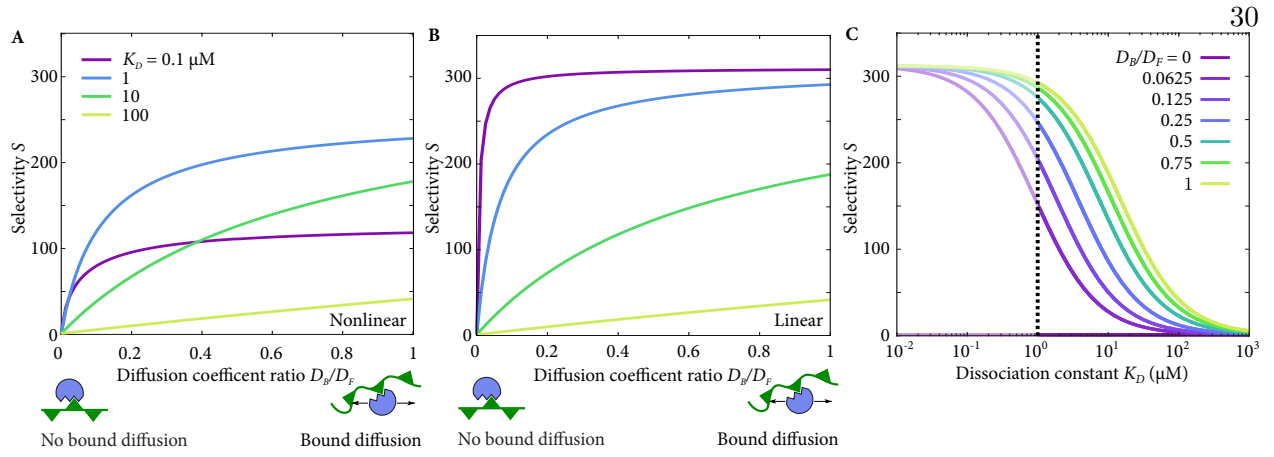


**Figure 2.3:** (A, B) Selectivity as a function of diffusion coefficient ratio, with varying dissociation constant, in the full nonlinear model (A) or in the linear approximation (B). (C) Selectivity as a function of dissociation constant, with varying diffusion coefficient ratio, in the linear approximation. The region to the left of the dotted line is non-physical; the full nonlinear solution should be used there instead.

nuclear pore, approximately 10 ms.

In order to create these plots, we used the FG-filled pore length  $L = 100 \text{ nm}$  [113, 114]. Total FG Nup concentration was determined from an estimate of the number of transport factor binding sites (800), and the volume of a cylinder of diameter 60 nm and length  $L$ . We also need an estimate of the free diffusion constant of NTF2 moving within the nuclear pore. This value has not been directly measured, but it was estimated at  $D_F = 0.12 \mu\text{m}^2/\text{s}$  using a similar value for a non-binding protein [39]. As would be expected, this diffusion constant is smaller than that of a karyopherin in the nucleus, which has been estimated at  $D_F = 1 \mu\text{m}^2/\text{s}$  [115]. In order to estimate the concentration gradient between nucleus and cytoplasm, we need to know the concentration of transport factor just inside the cytoplasmic side of the nuclear pore. There will be an energy barrier to any protein entering the pore because of the entropic penalty of the Nups. We estimate this barrier is approximately  $1.5 k_B T$  for an NTF2-sized molecule [1]. We estimate the cytoplasmic concentration of NTF2 is  $5 \mu\text{M}$ . Then  $T_0 = 5 \times e^{-1.5} \mu\text{M} = 1 \mu\text{M}$ .

Experimental evidence suggests that the on-rate constant of Nup-transport factor binding is diffusion-limited, with  $k_{\text{on}} = 10^{-3} \mu\text{M}^{-1} \mu\text{s}^{-1}$  [11, 26]. The off-rate is given by  $k_{\text{off}} = k_{\text{on}} K_D$ . Measured values of the dissociation constant  $K_D$  span several orders of magnitude, between ap-

proximately between 10 nM and 1 mM [1, 23–27, 59]; therefore the off-rate constant is not well-determined. Figure 2.6B and C show the bound diffusion constant and selectivity for a range of  $K_D$  values spanning those measured experimentally, with a fixed, diffusion-limited on-rate. Throughout this work, we consider a wide range of dissociation constants.

This model provides a straightforward method of predicting the selectivity of various other hydrogel nuclear pore mimics [50–52, 70]. A table of predicted selectivity is provided in Appendix A.

Using the above parameters along with a non-negligible bound diffusion constant, selectivity can approach the values seen in experimental measurements (Table 2.1). The interplay between binding kinetics and diffusion leads to an optimal dissociation constant near 1  $\mu\text{M}$  for maximum selectivity (Figure 2.2C). Selectivity decreases for high  $K_D$  because binding is too weak to significantly increase transport factor concentration in the pore. For low  $K_D$ , tight binding causes the concentration of bound complexes to become approximately constant across the pore, eliminating the concentration gradient needed to provide flux across the pore.

### 2.1.3 Bound diffusion in the linear model

In the linear approximation described in Sec. 2.1.1, bound diffusion plays a similar role as in the full nonlinear model. By definition, the Nup binding sites don't saturate in the linear model. This leads to a plateau in the selectivity at tighter binding, rather than a peak (Fig 2.3). However,

**Table 2.1:** Comparison between experimental results for NTF2 and GFP ( a similarly-sized non-binding protein) and model predictions. Flux is measured in units of molecules per pore per second.

Method	Cell type	Species	Flux	Selectivity	Notes
OSTR	<i>Xenopus</i>	NTF2	91–123	24–37	[40]
		GFP	3.3–3.8		
OSTR	<i>Xenopus</i>	NTF2	47.3	43	[41]
		GFP	1.1		
Permeabilized cells	HeLa	NTF2	250	125	[39]
		GFP	2		
Model	–	Binding	2–480	1–240	This work
		Non-binding	2		

the linear model becomes non-physical for  $K_D < N_t$ , denoted by the dotted line in Fig. 2.3C.

The role of individual parameters can be more easily investigated using the linear approximation. Figure 2.4 illustrates the effect on selectivity of varying the on-rate constant, total FG Nup concentration, free diffusion constant, and pore length. Figure 2.5 does the same for the absolute flux of transport factor through the pore. These results show that increasing the on-rate constant or the total Nup concentration results in both higher selectivity and transport factor flux, a conclusion which is supported by the fact that these values are maximized within the nuclear pore [11, 26]. However, there is a trade-off between selectivity and flux for the pore length and free diffusion constant. Increasing pore length or decreasing free diffusion constant makes the pore more selective but lowers the absolute flux of transport factor.

## 2.2 Mechanisms of bound transport factor mobility

The importance of bound diffusion to selectivity in our model raises the question of how transport factor- Nup complexes might diffuse within the pore. The following sections describe two possible mechanisms of bound-state diffusion within the nuclear pore: tethered diffusion and inter-chain hopping due to binding multivalency. Both mechanisms rely only on well-established properties of Nups and transport factors. Our results suggest that each mechanism could contribute significant selectivity.

### 2.2.1 Bound mobility through tethered diffusion

One possible mechanism of bound-state diffusion within the nuclear pore is tethered diffusion. FG Nups, as disordered proteins, are flexible and highly dynamic [8, 11, 116, 117]. It is not clear whether they form polymer brushes or crosslinked hydrogels within the nuclear pore, but in either case tethered diffusion remains a viable mechanism of bound diffusion. In the case of a polymer brush, one end of an FG Nup is anchored to the NPC scaffold, but the other end is free, affording mobility to a bound transport factor. If FG Nups are crosslinked, the effective length of the flexible tether will be shorter, but the same principle of tethered diffusion will apply.

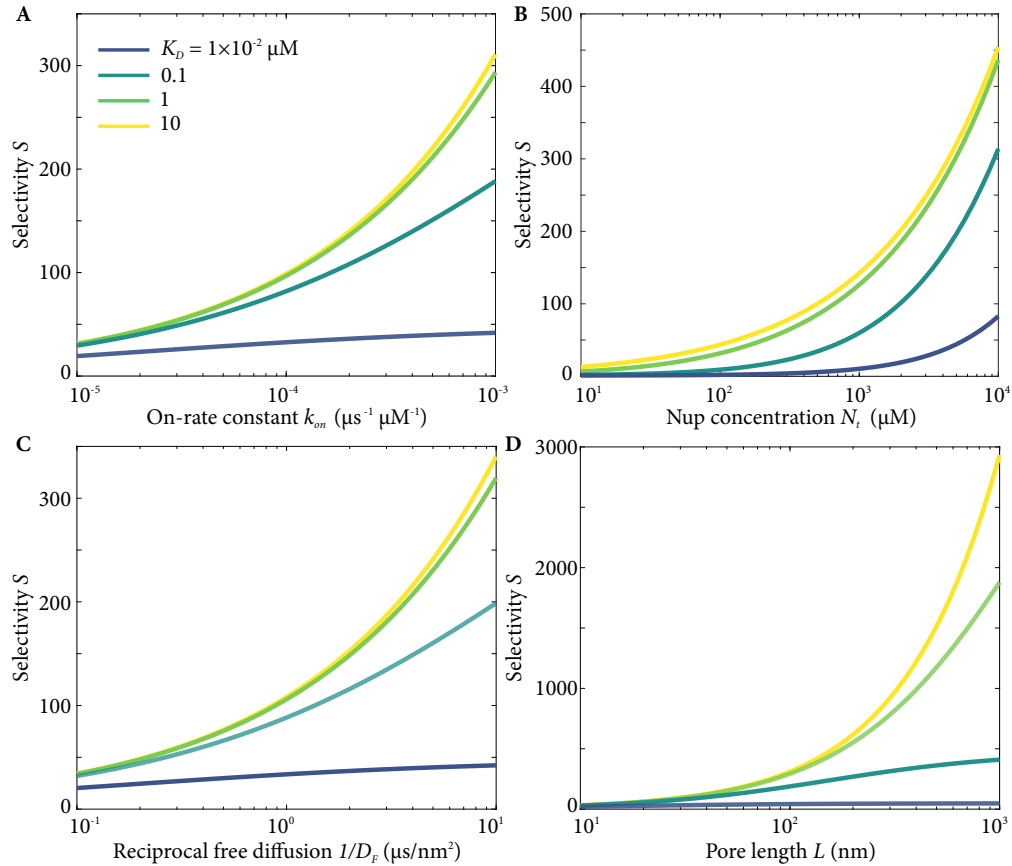


**Figure 2.4:** Dependence of selectivity on variation of individual parameters: (A) on-rate constant, (B) total FG Nup concentration, (C) inverse of the free diffusion coefficient, and (D) pore length, with varying dissociation constant. All values calculated using the linear solution to the binding-diffusion equations. Bound diffusion coefficient is  $D_B = 0.1D_F$ . Other parameters fixed at values described in the text.

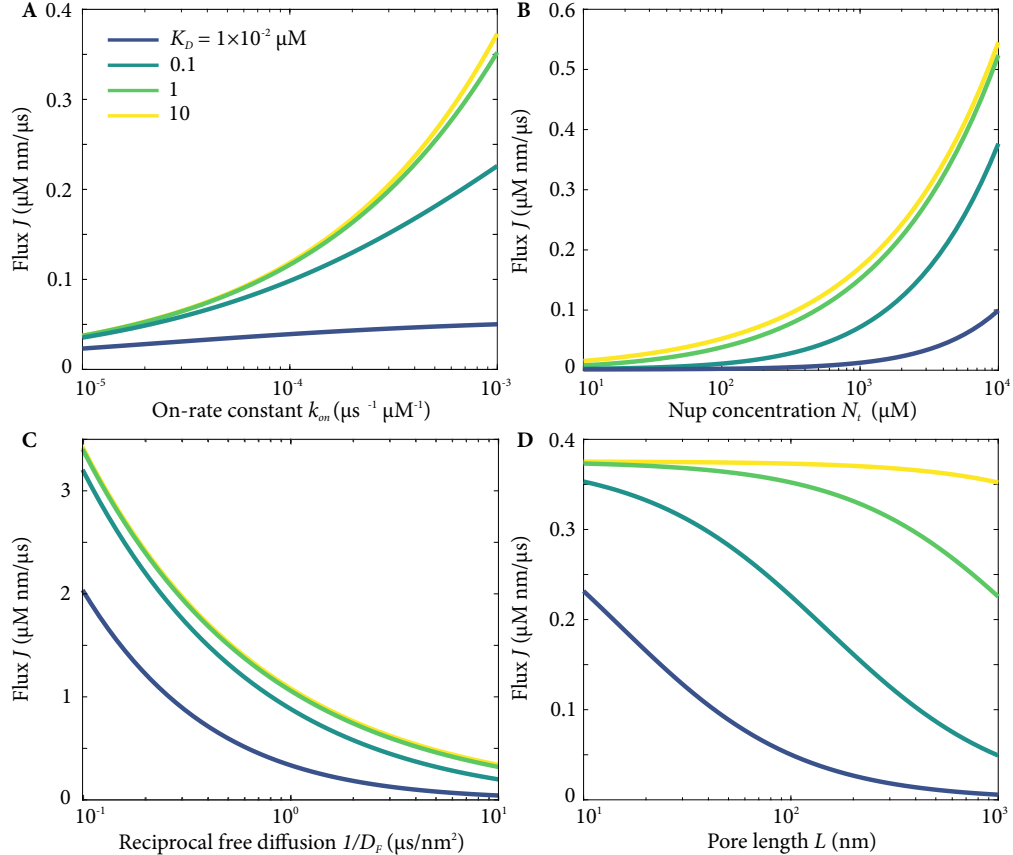


**Figure 2.5:** Dependence of flux on variation of individual parameters: (A) on-rate constant, (B) total FG Nup concentration  $N_t$ , (C) inverse of the free diffusion coefficient, and (D) pore length, with varying dissociation constant. All values calculated using the linear solution to the binding-diffusion equations. Bound diffusion coefficient is  $D_B = 0.1D_F$ . Other parameters fixed at values described in the text.

Flexible polymers behave as entropic springs [118] if they are not highly stretched. Therefore, a bound transport factor diffuses while attached to a spring-like tether, which can be represented as diffusion in a harmonic potential well (Fig. 2.6A). The width of the harmonic well is related to the length of the flexible domain. The effective length is the full FG Nup length if the FG Nups are not crosslinked, while the effective length is reduced if they are crosslinked or entangled [39].

In order to calculate the bound diffusion coefficient of the transport factors, an averaging procedure is followed. The diffusion is assumed to be Fickian, which is a reasonably good though not perfect assumption. (See discussion in Sec. 2.3.) In the Fickian diffusion case, the diffusion coefficient is proportional to mean-squared displacement (MSD) divided by time. We calculate the mean binding lifetime  $\tau$  and the MSD corresponding to this “typical” binding event of duration  $\tau$  and divide them.

To begin, note that the duration of a binding event follows the exponential distribution

$$\rho(t) = \exp(-t/\tau)/\tau, \quad (2.17)$$

where  $\tau = 1/k_{\text{off}}$  is the mean binding lifetime.

Next, the probability density of the position of a bound transport factor is

$$P(x,t) = e^{-\frac{x^2}{2\alpha(t)}} / \sqrt{2\pi\alpha(t)}, \quad (2.18)$$

$$\alpha(t) = (1 - e^{-2kD_F\beta t})/(k\beta) \quad (2.19)$$

where  $k$  is the spring constant of the FG Nup tether and  $1/\beta = k_B T$  is the thermal energy [119].

The center of the well is set at  $x = 0$ .

The MSD of the transport factor as a function of time is calculated, as any expected value, with the integral

$$\langle x^2(t) \rangle = \int_{-\infty}^{\infty} P(x,t)x^2 dx = \alpha(t). \quad (2.20)$$

Finally, the typical transport factor MSD during a binding event can be determined by evaluating

$$\overline{\langle x^2 \rangle} = \int_0^{\infty} \rho(t') \langle x^2(t') \rangle dt' = \frac{2D_F L_c \ell_p}{L_c \ell_p k_{\text{off}} + 3D_F}. \quad (2.21)$$

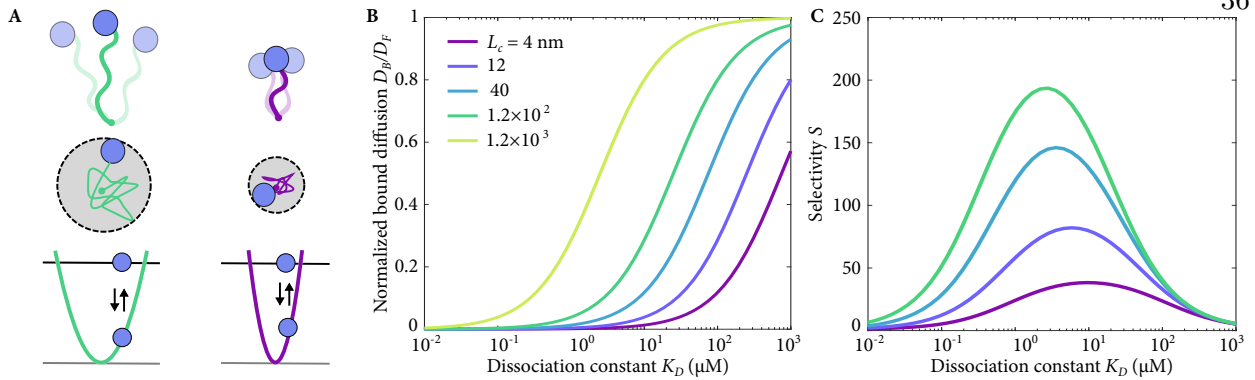


**Figure 2.6:** (A) Schematic of the flexible tether model of bound-state diffusion. FG Nups are treated as entropic springs that constrain the motion of transport factors to a greater (top and center left, longer Nup) or lesser (top and center right, shorter Nup) extent, which corresponds to changing the width of the harmonic potential well (lower). (B) Ratio of bound to free diffusion coefficient as a function of dissociation constant, with varying polymer length, in the tethered-diffusion model. (C) Selectivity as a function of  $K_D$ , with varying polymer length, in the tethered-diffusion model. Selectivity calculated by Mike Stefferson.

Here we assume that the spring constant is that of a worm-like chain polymer  $k = 3/(2\beta L_c \ell_p)$ , where  $L_c$  is the contour length and  $\ell_p$  the persistence length [118].

Combining these results, the one-dimensional bound diffusion coefficient is

$$D_B \approx \frac{\overline{\langle x^2 \rangle}}{2\tau} = \frac{D_F L_c \ell_p k_{\text{off}}}{L_c \ell_p k_{\text{off}} + 3D_F} = \frac{D_F}{1 + 3\frac{D_F}{D_P}}. \quad (2.22)$$

Here  $D_P \equiv L_c \ell_p k_{\text{off}}$  controls the bound-state diffusion coefficient: higher  $D_P$  corresponds to a lower constraint of the transport factor by the tether and greater bound mobility. Bound mobility increases with increasing chain length and persistence length, or decreasing binding lifetime. When  $D_P$  is large ( $D_F/D_P \ll 1$ ),  $D_B$  approaches  $D_F$ , since the long chains barely affect transport factor motion during the short binding event. For small  $D_P$  ( $D_F/D_P \gg 1$ ), transport factor motion is inhibited by a short tether, giving  $D_B \approx D_P/3 \ll D_F$ .

Physiological values can be estimated for all of the relevant parameters. Disordered proteins are relatively flexible, with persistence lengths around  $\ell_p \approx 1 \text{ nm}$  [120]. The contour lengths of the disordered regions of FG Nups are in the range  $L_c \approx 100\text{--}280 \text{ nm}$  (250–700 amino acids long [8] with a contour length of approximately 0.4 nm per amino acid).

Using these parameters, along with those described in earlier sections, Mike Stefferson calculated the selectivity due to tethered diffusion for several tether lengths (Fig. 2.6C). Selectivity was

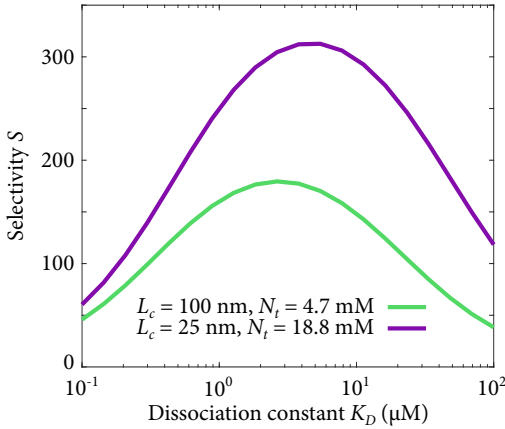


**Figure 2.7:** Selectivity as a function of dissociation constant in the tethered diffusion model, varying Nup contour length  $L_c$  and total Nup concentration  $N_t$ . The product  $L_c N_t$  is held constant.

also calculated for two values of the total Nup concentration  $N_t$ , mimicking the possible effect of Nup crosslinking within the pore (Fig 2.7). The product of contour length and Nup concentration  $L_c N_t$  was held constant, and selectivity was calculated for a long Nup length of 100 nm as well as a shorter length of 25 nm, reflecting the possibility of crosslinking. Corresponding total Nup concentrations of 4.7 and 18.8 nm, respectively, were determined from an estimate of the number of transport factor binding sites (800), and the volume of a cylinder of diameter 60 nm and length  $L = 100$  nm.

Using these realistic parameters, selectivity can reach 200-300, a large flux enhancement for transport factors over nonbinding proteins.

### 2.2.2 Bound mobility through inter-chain hopping

Another possible mechanism of bound-state diffusion is inter-chain hopping enabled by multivalent binding interactions. All known transport factors have at least two hydrophobic binding pockets which bind to FG motifs, and some have many more [57]. FG Nups in turn each possess many FG motifs, leading to a highly multivalent binding interaction. This feature allows a transport factor to bind to multiple Nups at once, moving between them with a hand-over-hand or sliding motion without ever fully unbinding [64, 90]. While binding to multiple FG motifs on the same Nup will not lead to bound diffusion, inter-chain hopping will cause the origin site of tethered transport factor diffusion to move with time. In order to understand the effect of hopping on the

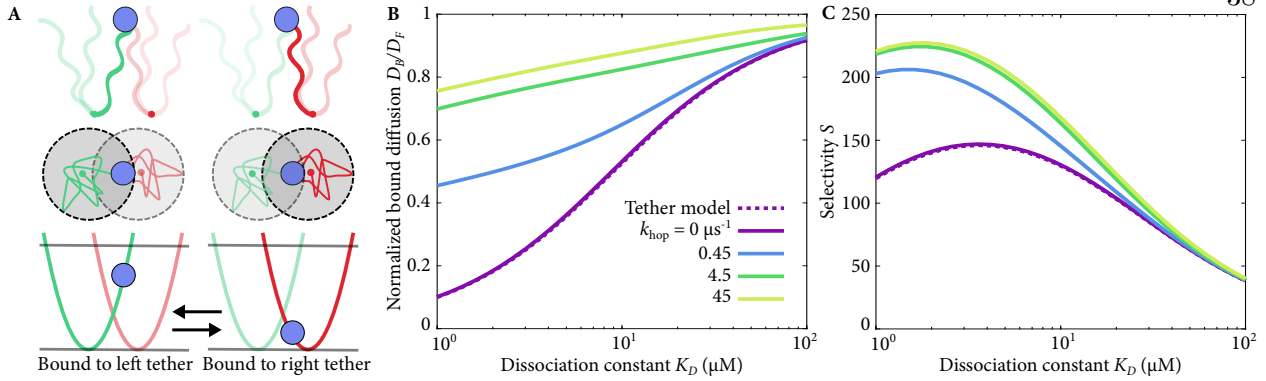


**Figure 2.8:** (A) Schematic of the inter-chain hopping model of bound-state diffusion. FG Nups are treated as entropic springs that constrain the motion of transport factors, and inter-chain hopping allows a transport factor to move from one FG Nup (top and center left, green Nup) to another (top and center right, red Nup) without unbinding, which corresponds to switching from one harmonic potential well to another (lower). (B) Ratio of bound to free diffusion coefficient as a function of dissociation constant, with varying hopping rate in the inter-chain hopping model. (C) Selectivity as a function of  $K_D$  with varying hopping rate. FG Nup contour length  $L_c = 40 \text{ nm}$  in (B, C).

overall bound diffusion constant, we model a transport factor that undergoes tethered diffusion when bound to an FG Nup and hops between neighboring, randomly distributed tethers (Fig. 2.8).

In our simulation of transport factor motion with hopping between FG Nups while bound, we represented each FG Nup as an entropic spring (i.e. as a harmonic potential well). Well positions were randomly chosen from a uniform distribution, with the exception that we always placed one well at the starting position of the transport factor. The transport factor started the simulation bound to this FG Nup, and remained bound throughout the simulation. While bound to one FG Nup, the transport factor diffused within the harmonic well representing that FG Nup. We recorded the position and mean-squared displacement of the transport factor from its starting location, which we then used to determine a bound diffusion coefficient, as described in more detail below. The transport factor could hop between tethers by changing which well it moved in.

The source code of the hopping simulation is available at <https://github.com/LauraMaguire/hoppingSim>.

### 2.2.2.1 Diffusion in a potential well

The transport factor moved in the harmonic potential of the FG Nup according to Brownian dynamics. At each timestep, the transport factor position was updated using a force-dependent diffusive step [121].

$$x(t + \delta t) = x(t) + \frac{F}{\Gamma} \delta t + \delta x, \quad (2.23)$$

where  $F$  is the force acting on the transport factor,  $\Gamma$  is the drag coefficient,  $\delta t$  is the timestep, and  $\delta x$  is a random Brownian step drawn from a Gaussian distribution with variance  $\sigma^2 = 2D\delta t$ . The drag coefficient of a spherical particle at low Reynolds number is given by Stokes' Law as  $\Gamma = 6\pi\eta r$ , where  $\eta$  is the fluid's viscosity and  $r$  is the sphere's radius. This result can be combined with the Einstein relation  $D = k_B T / (6\pi\eta r)$  to give

$$\Gamma = \frac{k_B T}{D}. \quad (2.24)$$

The force is  $F = -k\Delta x$ , where  $k$  is the spring constant of the FG Nup and  $\Delta x$  is the displacement of the transport factor from the Nup attachment point. We model the FG Nup as a worm-like-chain at small extension, so that  $k = 3k_B T / (2\ell_p L_c)$ , where  $\ell_p$  is the tether persistence length and  $L_c$  is the contour length. Then

$$x(t + \delta t) = x(t) - \frac{3D\Delta x \delta t}{2\ell_p L_c} + \delta x = x(t) - DK\Delta x \delta t + \delta x, \quad (2.25)$$

where  $K$  is the normalized spring constant  $K = k/k_B T = 3/(2\ell_p L_c)$ .

### 2.2.2.2 Hopping probability

We designed the hopping probability  $P_{\text{hop}}$  in order to satisfy the principle of detailed balance. During every iteration of the simulation, we picked an FG Nup at random from a list of the  $M$  Nups near enough to have a reasonable probability of hopping. Transport factor hopping to the new FG Nup was attempted with success probability

$$P_{\text{hop}} = r_{\text{hop}} M \delta t e^{-\Delta G/2}. \quad (2.26)$$

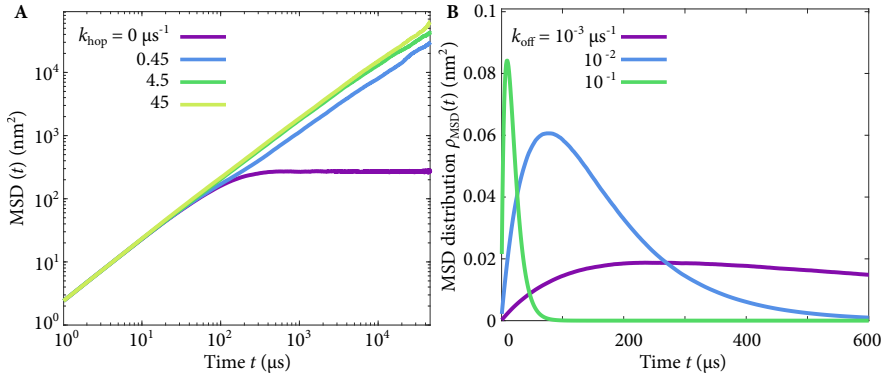


**Figure 2.9:** (A) Examples of mean-squared displacement (MSD) of a simulated transport factor in the inter-chain hopping model, with varying hopping rate. (B) Examples of MSD distributions  $\rho_{\text{MSD}}(t)$  used in estimating the diffusion coefficient, with varying unbinding rate. Tethers have 40 nm contour length; other parameters are as discussed in the text.

Here the base hopping rate  $r_{\text{hop}}$  is a dimensionless input parameter, and the change in free energy (in units of  $k_B T$ ) between the current Nup and the proposed new Nup is

$$\Delta G = \frac{1}{2}K(x - x_{\text{new}})^2 - \frac{1}{2}K(x - x_{\text{cur}})^2, \quad (2.27)$$

where  $K$  is the normalized spring constant,  $x$  is the particle's current position,  $x_{\text{cur}}$  is the anchor location of the Nup to which the particle is currently bound, and  $x_{\text{new}}$  is the anchor location of the proposed new Nup. Note that when a hop succeeds, the energy landscape changes to that of the new Nup, but the transport factor's position does not change during the hop. There is no upper bound on  $P_{\text{hop}}$ , but we adjusted the timestep to ensure that  $P_{\text{hop}}$  was greater than unity no more than 0.5% of the time that a hop was attempted.

### 2.2.2.3 Mean-squared displacement and diffusion coefficient calculation

We ran each simulation for  $10^7$  time steps with  $\delta t = 0.01 \mu\text{s}$ , and recorded the transport factor's position every 100 time steps. We calculated the mean-squared displacement  $\langle x^2 \rangle$  (MSD) of the transport factor and averaged it over 100 runs (Fig. 2.9A). We then computed

$$\rho_{\text{MSD}}(t) = \langle x^2(t) \rangle \rho(k_{\text{off}}, t) = k_{\text{off}} \langle x^2(t) \rangle e^{-k_{\text{off}} t}, \quad (2.28)$$

as shown in Fig. 2.9B and numerically integrated the distribution over all times  $t > 0$ . We determined the bound diffusion coefficient from the typical MSD-per-binding-event  $\overline{\langle x^2 \rangle}$  using

$$D_B = \frac{k_{\text{off}} \overline{\langle x^2 \rangle}}{2}. \quad (2.29)$$

Here, the factor of 1/2 is appropriate because we consider a one-dimensional random walk.

#### 2.2.2.4 Bound diffusion and selectivity from hopping simulation

Upon calculating the bound diffusion constant using the hopping simulation described above, it was clear that inter-chain hopping could lead to a relatively large bound diffusion constant, with a corresponding increase in selectivity (Figs. 2.8, 2.10). In the limit of a hopping rate of zero, the tethered-diffusion-only result is recovered, as anticipated. Hopping most enhances selectivity when the Nup length or dissociation constant are small. This is the regime where tethered diffusion is limited, corresponding to crosslinked Nups within the nuclear pore. If the pore is highly crosslinked, binding multivalency may be essential to selectivity.

### 2.3 Fickian and anomalous diffusion

A particle whose mean-squared displacement is proportional to time ( $\langle x^2(t) \rangle \propto t$ ) is said to be undergoing normal or Fickian diffusion. This is generally the case for a freely-diffusing particle with no driving forces acting upon it. Anomalous diffusion is the more general case where  $\langle x^2(t) \rangle \propto t^\alpha$ . When  $\alpha > 1$ , the motion is superdiffusive;  $\alpha < 1$  is the subdiffusive regime, typically caused by confined diffusion or binding.

Throughout this analysis, we have assumed that all proteins are experiencing Fickian diffusion. For inert, nonbinding proteins, this is true provided we neglect any steric confinement from the presence of the FG Nups. Additionally, transport factors should show normal diffusion over timescales much longer than their binding lifetime. However, binding interactions will result in slightly subdiffusive motion on shorter timescales.

In order to quantify the extent of anomalous diffusion, we ran a modified version of the

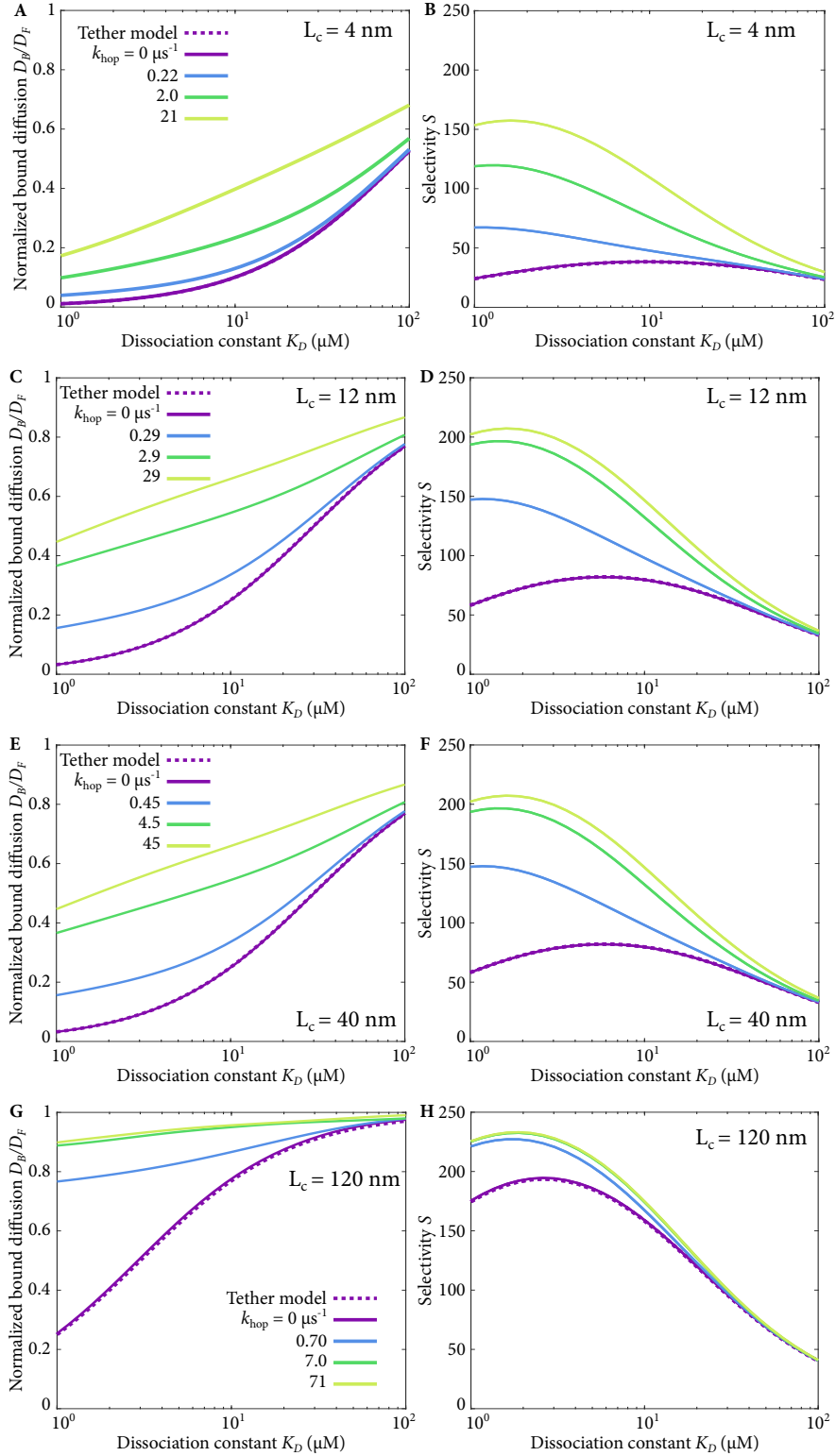


**Figure 2.10:** Bound diffusion and selectivity as a function of dissociation constant, with varying hopping rate for FG Nups with (A,B)  $L_c = 4 \text{ nm}$ ; (C,D)  $L_c = 12 \text{ nm}$ ; (E,F)  $L_c = 40 \text{ nm}$ ; (G,H)  $L_c = 120 \text{ nm}$ .

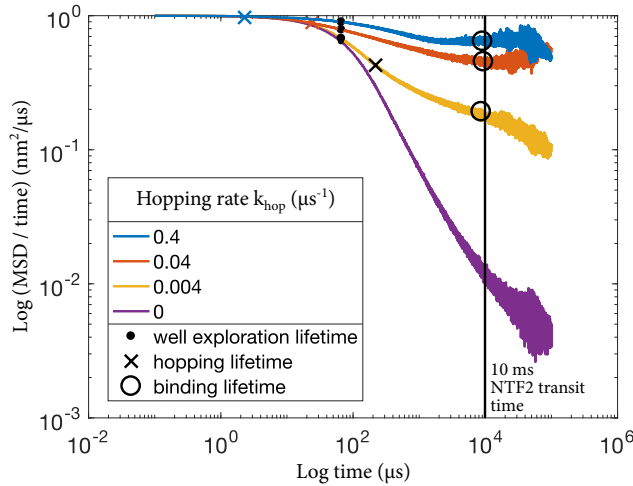


**Figure 2.11:** Anomalous diffusion of transport factors at several hopping rates. The hopping, binding, and well-exploration lifetimes are also shown where applicable. NTF2 transit time (10 ms) is indicated with a vertical line.

hopping simulation described in Sec. 2.2.2 in which the transport factor was not solely limited to hopping but also able to entirely unbind from and rebind to Nups with rates  $k_{\text{off}}$  and  $k_{\text{on}}$  respectively. The resulting MSD  $\langle x^2(t) \rangle$  can then be used to investigate anomalous diffusion. Figure 2.11 is a log-log plot of  $\langle x^2(t) \rangle/t$  vs time  $t$ , generated using a script created by Mike Stefferson [111]. In such a plot, a horizontal asymptote indicates Fickian diffusion, while a non-zero slope  $m$  indicates anomalous diffusion with  $m = \alpha - 1$ .

Figure 2.11 shows several hopping rates. When the transport factor is not able to hop between Nups, diffusion remains anomalous until well past the binding lifetime  $1/k_{\text{off}}$  (not shown). Larger hopping rates cause diffusion to become Fickian over shorter timescales. The hopping lifetime  $1/k_{\text{hop}}$  is shown for each nonzero hopping rate, as well as the binding lifetime ( $k_{\text{off}} = 10^{-4} \mu\text{s}^{-1}$  in all cases). The time to explore the potential well caused by binding to Nups is also shown. The vertical line marks the experimentally-measured time for NTF2 to pass through the nuclear pore,  $t_{\text{NTF2}} = 10 \text{ ms}$ .

The anomalous diffusion plot indicates that the diffusion of transport factors is not entirely Fickian, but that shorter binding lifetimes and higher hopping rates lead to less anomalous diffusion. Most hopping rates used in the simulation are high enough that diffusion is Fickian over the timescale of NTF2 transport.

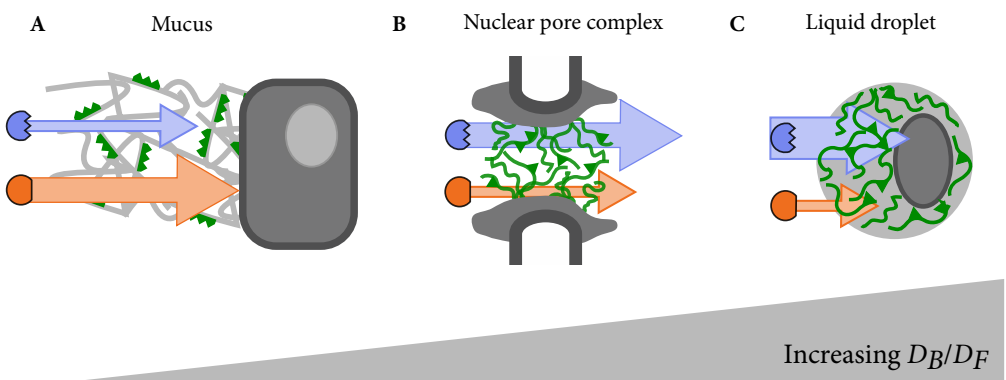


**Figure 2.12:** Possible effect of bound diffusion on other biological systems, ordered by increasing bound diffusion constant.

## 2.4 Bound diffusion in other biological systems

While the above model was inspired by nuclear transport, it is sufficiently general that it can be applied to other biological systems as well, as described in more detail in Chapter 1. A variety of selective filters exist *in vivo*, and bound-state diffusion could be relevant to many of them. Our model predicts that higher bound diffusion will lead to higher selectivity in biofilters.

Figure 2.12 shows three biofilters ordered by increasing bound-to-free diffusion ratio ( $D_B/D_F$ ). Mucus, such as the mucus which lines the lungs, permits very little bound diffusion of particles that bind to it. Research in targeted drug delivery to lung cells has observed that inert nanoparticles may be more effective at penetrating the mucus barrier than binding particles [76]. This observation agrees with the prediction that binding will only enhance transport if bound diffusion occurs. On the other hand, Fig 2.12C depicts a system with maximal bound-state diffusion: a phase-separated liquid droplet. Such a droplet, consisting of a phase rich in an intrinsically disordered protein, may be used in order to concentrate binding partners and speed up reactions within the cell [6, 97]. In this case, complexes of intrinsically disordered proteins and their binding partners would have approximately the same diffusion constant as free binding partners ( $D_B/D_F \approx 1$ ), leading to high selectivity for binding partners to pass to the center of the droplet.

Systems other than filters may make use of principles found in our model as well. For example, the bacteria *Staphylococcus aureus*, responsible for many antibiotic-resistant infections in hospitals,

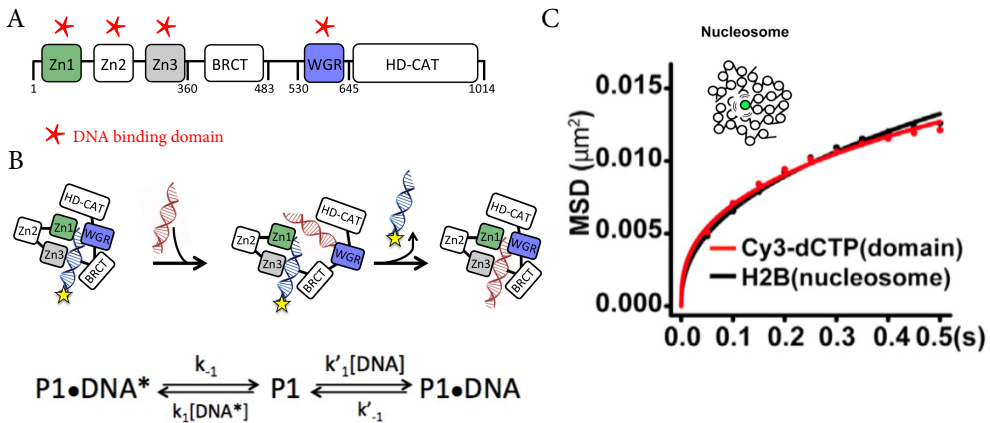


**Figure 2.13:** PARP1 and its possible mechanisms of bound diffusion. (A) Schematic of PARP1 structure showing its four DNA-binding domains [95]. (B) “Monkey-bar” inter-strand hopping mechanism cartoon and reaction showing on- and off- rates for binding a second strand of DNA and subsequently releasing the first [95]. (C) Mean-squared displacement of a nucleosome bound to chromatin, corresponding to a spring constant on the order of  $10^{-4}$  pN/nm. Figure adapted from [123].

can exhibit resistance to the antibiotic vancomycin by constantly building and shedding its cell wall, to which vancomycin binds [122]. Our model predicts that such a strategy should keep the vancomycin flux through the cell wall from reaching steady-state, in the transient regime where the flux of a binding molecule is suppressed (Fig. 2.2). The targeting of the DNA damage repair protein PARP1 to appropriate sites in the nucleus, described below, is another potential application of binding and diffusion principles.

#### 2.4.1 DNA damage repair protein recruitment in the nucleus

Poly(ADP-ribose) polymerase 1 (PARP1) is a protein which assists in DNA damage repair. As discussed in Sec. 1.2.2, PARP1 must rapidly diffuse to and bind sites of damage, a task made difficult by the large amounts of intact chromatin within the nucleus. PARP1 binds to damaged DNA with a low-nanomolar dissociation constant and appears to bind intact DNA only a few orders of magnitude more weakly [94, 95]. Given the millimolar concentration of potential binding sites in the nucleus, it is thought that virtually all PARP1 is bound. Therefore, the rapid migration of PARP1 to damaged DNA is dependent on bound-state mobility.

The mechanisms of PARP1’s bound diffusion may be similar to those used by the nuclear

pore. First, PARP1 binds DNA multivalently. It possesses four DNA binding domains, though some may work in tandem (Fig. 2.13A). PARP1 binds to nonspecific DNA sequences, meaning that a strand of DNA also has many binding sites along its length, reminiscent of the numerous FG motifs of Nups. The high degree of multivalency suggests that inter-strand hopping may be important to PARP1 bound diffusion, as transport factor hopping may be to nuclear transport. In fact, Johannes Rudolph, Jyothi Mahadevan, and Karolin Luger have recently demonstrated the existence of a multivalent “monkey-bar” mechanism equivalent to inter-chain hopping between DNA strands [95]. However, disruption of this mechanism reduces PARP1 diffusion only twofold, suggesting that there are more methods of bound diffusion available to PARP1 [96].

First, we investigated whether the already-identified “monkey bar” hopping mechanism could produce bound diffusion in agreement with experimental measurements. Analytic models of hopping are complicated and difficult to apply to PARP1 [68], but a highly-simplified model can be used to estimate the maximum expected contribution to bound diffusion from hopping. Using the reaction scheme described in Fig. 2.13B, assume PARP1 takes a “step” of its own size whenever a second strand of DNA binds. The bound diffusion constant would then be on the order of

$$D_B \sim R^2 k_{on,2} N_t$$

where  $R$  is the size of PARP1 and  $k_{on,2}$  is the on-rate constant for binding a second strand of DNA. Using the parameters given in Table 2.2, we have  $D_B \approx 10 \mu\text{m}^2/\text{s}$ . This is a naive calculation of the upper limit on the bound diffusion constant that we could expect from inter-strand hopping. This calculation is of the same order of magnitude as the observed diffusion constant of  $\sim 3 \mu\text{m}^2/\text{s}$ , suggesting that hopping can indeed produce the diffusion seen in the nucleus.

Next, we examined the feasibility of an additional possible mechanism of bound-state diffusion: tethered diffusion from the thermal motion of chromatin. Several studies suggest that chromatin is flexible and dynamic, with nucleosomes moving 50 nm over 30 ms in mammalian cells [123, 126–128]. A representative MSD plot is shown in Fig. 2.13C. Treating the nucleosome as a particle bound irreversibly to a flexible tether, the MSD shown corresponds to a chromatin

spring constant of approximately  $5 \times 10^{-4}$  pN/nm. This data can be combined with the values given in Table 2.2 to give a predicted bound diffusion constant using the tethered-diffusion equation identified earlier in this chapter:

$$D_B = \frac{D_F}{1 + \frac{2D_F k}{k_B T k_{\text{off}}}} \quad (2.30)$$

where the thermal energy is  $k_B T \approx 4.1$  pN nm at room temperature. The predicted bound diffusion constant is  $3.6 \mu\text{m}^2/\text{s}$ , which is consistent with the experimentally-observed value of  $\sim 3 \mu\text{m}^2/\text{s}$  [96].

Using these order-of-magnitude calculations, either tethered diffusion or hopping could provide enough bound-state mobility to explain the rapid diffusion of PARP1 to sites of DNA damage within the nucleus. It may be thanks to either tethered diffusion or additional hopping that PARP1 retains significant mobility even when its “monkey-bar” hopping mechanism is removed. It would be interesting to experimentally test for the presence of tethered diffusion.

## 2.5 Conclusions

In the above chapter, we have developed a simple model of selective nuclear transport which may apply more broadly to other biofilters as well. Surprisingly, this simple model can reproduce the high selectivity of the nuclear pore. The diffusion coefficient of the bound complex proved to be the most important factor in predicting selectivity. In order to test the predictions of our model, we next began developing nuclear-pore-inspired biofilters to investigate the effect of bound-state diffusion on protein separation *in vitro*.

**Table 2.2:** Experimentally-measured parameters for PARP1 bound diffusion.

Parameter	Lower estimate	Upper estimate	Notes
On-rate constant $k_{on}$	$10^9 \text{ M}^{-1} \text{ s}^{-1}$	—	Diffusion limit, [95]
On-rate constant for binding 2nd strand $k_{on,2}$	$0.043 \times 10^{-9} \text{ nM}^{-1} \text{ s}^{-1}$	—	[95]
Off-rate constant, $k_{off}$ , damaged DNA	—	$10 \text{ s}^{-1}$	Upper bound, [95]
Off-rate constant, $k_{off}$ , intact DNA	$10^3 \text{ s}^{-1}$	—	Calculated from $K_D$ measurements, Johannes Rudolph.
Intact DNA binding site concentration $N_t$	$100 \mu\text{M}$	$10 \text{ mM}$	Varies depending on how unique binding sites are counted.
Chromatin spring constant $k$	$5 \times 10^{-4} \text{ pN/nm}$	$0.65 \text{ pN/nm}$	[123, 125]
PARP1 size $R$	5 nm	—	PDB 1UK1 structure
Bound diffusion constant $D_B$	$3 \mu\text{m}^2/\text{s}$	—	[96]
Free diffusion constant $D_F$	—	$30 \mu\text{m}^2/\text{s}$	Upper bound based on diffusion in buffer, Johannes Rudolph.

## Chapter 3

### Hydrogel design for protein separation

In order to test the predictions of our bound-state diffusion model of selectivity, we needed to develop a biomaterial that could support bound diffusion and be used to test selectivity. We decided to focus on making a material that mimics the environment of the nuclear pore.

One of the advantages of the bound-state diffusion model is that it does not rely on the geometry of the selective material. As long as the dimensions of the material are significantly larger than the protein diffusing through it, there is no practical difference between a nanoscale cylindrical pore and a macroscale bulk material. For ease of fabrication and testing, we opted to design a bulk material for protein separation.

A hydrogel substrate was chosen as the basis of the nuclear pore mimic. Hydrogels are versatile materials, many of which are bio-compatible, whose properties can often be easily tuned. We used a hydrogel substrate to provide an inert scaffold to which fragments of FG Nups were conjugated. Like Nups in the nuclear pore, these Nups were conjugated to the hydrogel at one end and free at the other, providing a mechanism of tethered bound diffusion. The properties of these Nups, such as their length, number of transport factor binding motifs, and propensity towards aggregation, can be easily varied in order to test how these properties impact bound-state diffusion and thus protein selectivity.

This hydrogel model is a simple way to make a material to explore the effects of bound diffusion on protein separation. While it is inspired by the nuclear pore, the goal is not to directly reproduce the mechanism of nucleocytoplasmic transport. Instead, we hoped to show that bound-

state diffusion was measurable and controllable in a biomaterial, paving the way for molecular filters that might make use of this principle.

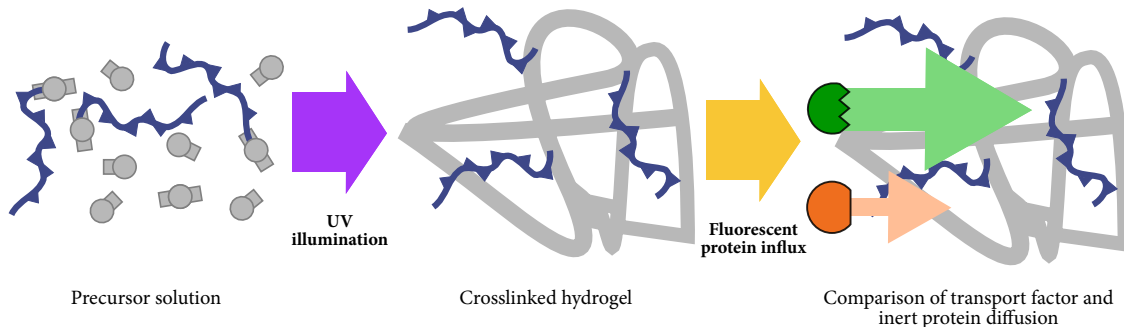
Over the course of making these materials, we ran into several significant roadblocks. Although hydrogels with a wide range of properties have been well-studied, gels suitable for protein separation are less common. They require an intermediate pore size, large enough that the diffusion of a protein is not significantly hindered by the presence of the hydrogel meshwork, but small enough that the Nup peptides often encounter the protein as it diffuses. This average pore size of 5-20 nm is difficult to produce, though much smaller and much larger pores are easy to make. The problem of pore size is made more difficult by the need to create a well-sealed hydrogel barrier in order to separate proteins; such a barrier must necessarily be confined and therefore unable to swell to its equilibrium size. The creation of a hydrogel for selective protein separation poses many stringent requirements, often in competition with each other. This chapter describes the setbacks we faced and the progress we have made towards creating a hydrogel-based biomaterial suitable for selective separation of proteins.

### 3.1 Hydrogel fabrication

A wide range of hydrogels systems have been well-studied. Many are not suitable for the addition of proteins, but both PEG and acrylamide hydrogels, among others, can be crosslinked in an aqueous solution that does not harm proteins. We used both PEG and acrylamide hydrogels in our diffusion experiments. Thanks to Stephanie Bryant, Sadhana Sharma, Christopher Bowman, Danielle Konetski, and Benjamin Fairbanks for their help as we learned to make these hydrogels.

Whether using PEG or acrylamide, the basic hydrogel fabrication procedure was the same (Fig. 3.1). First, a precursor solution was mixed, which contained the hydrogel monomer, a crosslinker, a radical generator, and the Nup fragment, labeled with a reactive group at one end that would conjugate it to the hydrogel. The radical generator was almost always a photoinitiator, which caused the precursor solution to crosslink when exposed to UV illumination. In a few cases, a chemical initiator was used, in which case the precursor solution crosslinked 10-30 minutes after

**Figure 3.1:** Overview of hydrogel fabrication and fluorescent protein influx. A precursor solution is mixed, containing hydrogel monomers, crosslinkers, a photoinitiator, and the Nup fragment. Upon exposure to UV light, the precursor solution crosslinks, and one end of each Nup is conjugated to the hydrogel. The diffusion of a fluorescently-tagged transport factor can then be compared to that of a similarly-sized inert fluorescent protein.



mixing. By the end of the polymerization process, the hydrogel contained Nup fragments tethered to the gel at one end, mimicking the arrangement of Nups in the nuclear pore and providing a mechanism of tethered bound diffusion for transport factors but not for nonbinding inert proteins. The diffusion of both types of protein within the hydrogel could then be quantified using fluorescence microscopy. Detailed protocols and precursor solution recipes are reported in Appendix E.

There were four major components to the precursor solution: monomers, crosslinkers, initiators, and Nup fragments. To an extent, these components can be tuned independently of each other. Bisacrylamide or PEG-diacrylate crosslinkers must be used with acrylamide monomers, and PEG-dithiol crosslinkers with PEG-norbornene monomers, but the initiators and Nup fragments can be varied. There are many variations on crosslinker length as well, leading to a wide variety of possible hydrogels even using a relatively small set of components.

The PEG hydrogels were made using 20 kDa 8-armed PEG-norbornene monomers (synthesized by the Bryant lab and Nathan Crossette) and either a 1 kDa or 8 kDa PEG-dithiol crosslinker (Sigma) (Fig. 3.2). To conjugate the Nup fragment to the PEG hydrogels, a C-terminal cysteine was added to the peptide. Both the crosslinker and Nup fragment made use of Michael-thiol “click” chemistry [129] [130].

The acrylamide hydrogels used an acrylamide monomer and bisacrylamide crosslinker (Bio-

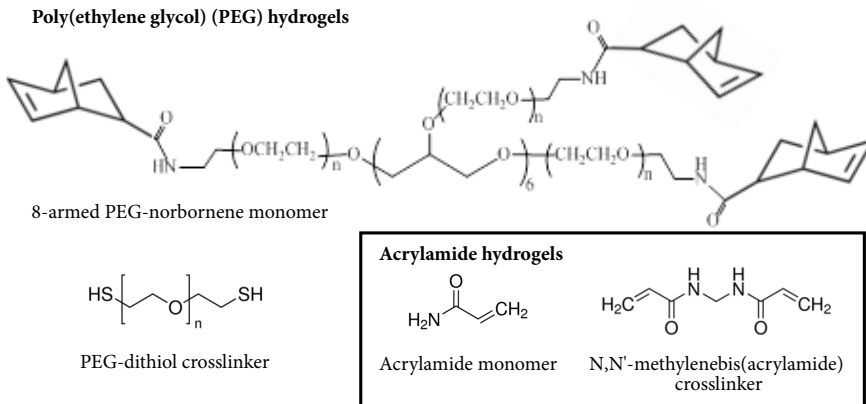


**Figure 3.2:** Chemical structures of monomers and crosslinkers for PEG and acrylamide hydrogels. The total molecular weight of the 8-armed PEG-norbornene was 20 kDa, and either a 1 kDa or 8 kDa PEG dithiol crosslinker was used. Structures from Sigma and CreativePEGWorks.

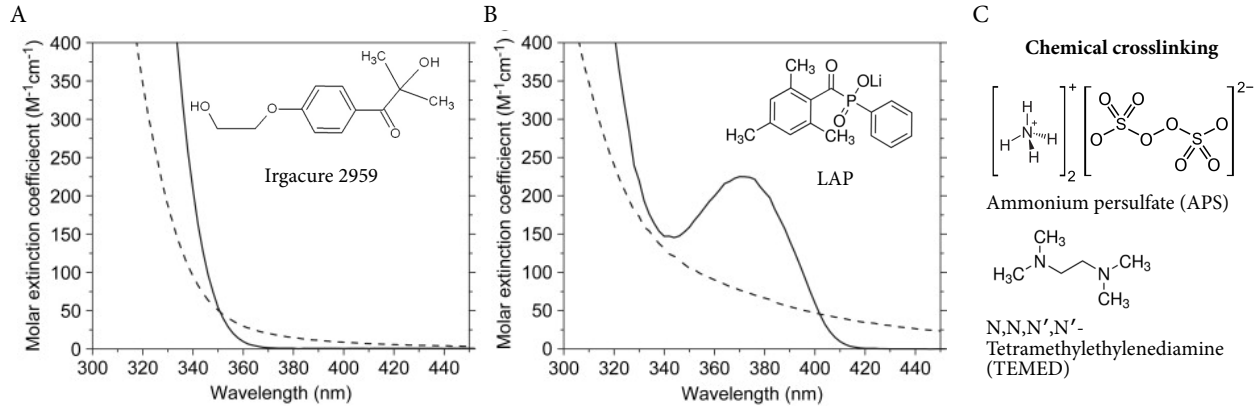
Rad) (Fig. 3.2). An additional step was needed to prepare the Nup fragment for tethering to the hydrogel: either bisacrylamide or 700-Da PEG-diacrylate (Sigma) was conjugated to the terminal cysteine (see Appendix D).

Regardless of the monomers and crosslinkers used, a radical generator is needed to initiate polymerization. We used either a photoinitiator, activated by UV light, or a chemical initiator system which began polymerization upon its addition to the precursor solution. Both systems have advantages: Photoinitiators are useful for patterned polymerization using photomasks and allow the precursor to be mixed prior to polymerization, while chemical crosslinkers do not require careful protection from light. We nearly always used a photoinitiator.

Two photoinitiators were tested: 1-[4-(2-hydroxyethoxy)-phenyl]-2-hydroxy-2-methyl-1-propane-1-one (commercially known as Irgacure 2959) and lithium phenyl-2,4,6-trimethylbenzoylphosphinate (LAP). Figure 3.3 shows the absorption spectra of each photoinitiator and that of its cleavage products [131]. LAP has an absorbance peak in the near-IR / violet range, is highly water-soluble, and is more effective at crosslinking, so it was used most of the time. However, due to its absorbance in the visible range, care must be taken to protect solutions containing LAP from ambient light wherever possible. Our LAP was synthesized by the Bryant lab, but it is now commercially available from Sigma as well.

An APS/TEMED chemical crosslinking system was occasionally used in place of the photoinitiator. Large numbers of hydrogels can be polymerized at once in this way, without the need

**Figure 3.3:** Absorption spectra of (A) Irgacure 2959 and (B) LAP (solid lines) and with that of their cleavage products (dotted lines) [131]. (C) Chemical structures of the APS/TEMED crosslinking system. Structures from Sigma.



for a large area of uniform UV illumination. Figure 3.3C gives the chemical structure of ammonium persulfate (APS) and N,N,N,N-tetramethylethylenediamine (TEMED). APS is the radical generator, and TEMED accelerates the radical formation. The time to polymerize can be controlled by adjusting the concentration of both components (Appendix E).

It should be noted that the presence of oxygen inhibits all the initiators discussed above. Precursor solutions were degassed for 10 minutes before use in a vacuum desiccator and polymerized no more than 10 minutes after degassing.

When a photoinitiator was used, the hydrogels were polymerized using UV illumination at either 365 nm (ThorLabs M365LP1 mounted LED) or 405 nm (laser on Nikon A1R confocal microscope) inside flow chambers as described in Sec. 3.2. The typical intensity of the LED was 220 mW/cm<sup>2</sup> and the typical crosslinking time 30 s. Depending on the situation, photomasks were used to selectively expose regions of precursor to UV, or entire droplets of precursor solution were polymerized in an otherwise-empty chamber (Fig. 3.4). After crosslinking, hydrogels were rinsed with 10-100 times their volume with buffer and allowed to soak in fresh buffer solution overnight at 4°C in order to approach swelling equilibrium and remove any remaining precursor solution.

Following the buffer soak, typically a fluorescent solution of proteins was added to the gels. Usually this consisted of a transport factor (typically Nuclear Transport Factor 2, or NTF2) and a

similarly-sized inert protein (typically the red fluorescent protein mCherry). A standard experiment consisted of a 4x or 10x magnification video of the hydrogel, reservoir chamber, and (sometimes) an outlet/inner reservoir which slowly accumulated protein that passed through and exited the gel. Experiments ranged from 1-24 hours, with 2 hours being the most common. Typical data produced was a plot of accumulation in the inner reservoir or hydrogel over the course of the experiment, as well as a concentration profile through the gel and inner reservoir. Experiments are described in greater detail in Chapter 4.

### 3.2 Flow chamber fabrication

The hydrogels were usually crosslinked in microfluidic flow chambers as shown in Fig. 3.5A. The thin chambers ensured that the top and bottom of the gel were sealed, so that transport factors and inert proteins could enter the gel only by diffusing into it. The small chamber size also reduced the quantity of transport factor and inert protein solution needed. Finally, the chambers were designed to be easily mounted on a microscope stage for recording experiments.

The basic flow chamber design consisted of an acrylic slide, patterned spacer or gasket, and coverslip, stacked and sealed together. Ports were almost always drilled in the plastic slide before chamber assembly, in order to allow the chamber to be filled and emptied. Several methods of fabricating the gaskets and ports were tested in order to optimize the watertightness and longevity of the chambers as well as the ease of fabrication and re-use.

In particular, several materials were attempted for the gasket that determined the height and shape of the chamber. The simplest was double-stick tape, which could be used as a single width or cut into shape with a razor. The double-stick tape chambers were thin ( $70\ \mu\text{m}$  per tape layer), of reliable thickness, and quick to make. However, they often leaked or dried over the course of several hours. Since many experiments take several days from preparation to finish, double-stick tape chambers were not usually not sufficient.

Norland Optical Adhesive (NOA), a liquid adhesive which cures upon exposure to UV, was used in another style of flow chamber. Thin semi-cured NOA layers can be molded and used as

**Figure 3.4:** Procedure for photopolymerization with (A) or without (B) a photomask. (A) A flow chamber is filled with precursor solution. The photomask is placed to hide all areas that should not be crosslinked, and the chamber is exposed to UV illumination. Excess precursor solution is removed with a buffer rinse. (B) Microliter droplets of precursor solution are pipetted onto the slide surface before the chamber is assembled. After assembly, the chamber is exposed to UV illumination. The chamber is then filled with buffer.

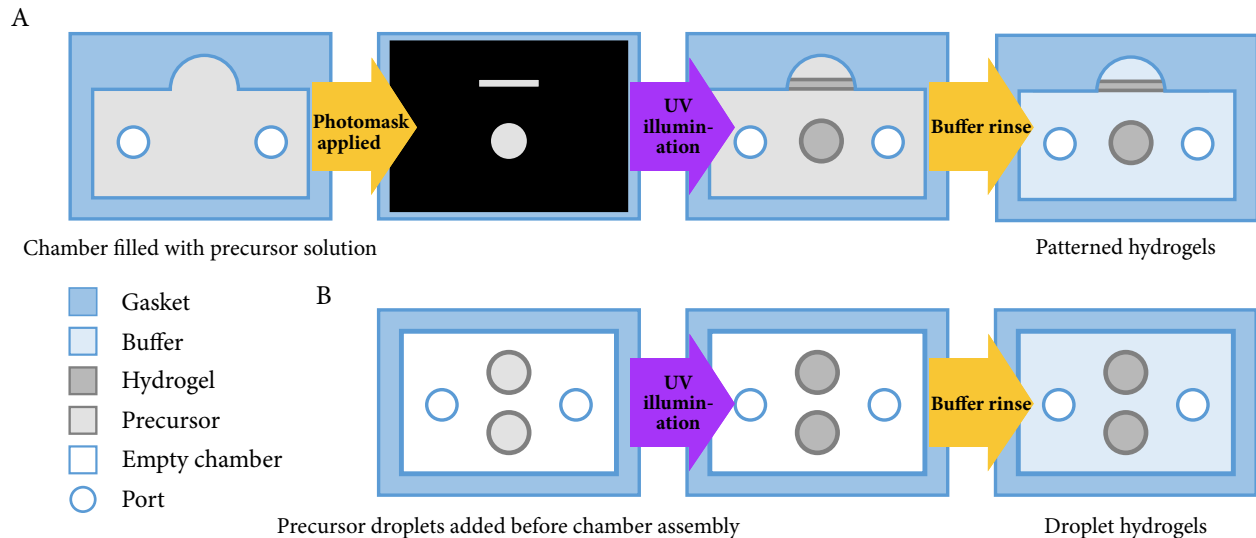


**Figure 3.5:** Flow chamber design and geometries. (A) Schematic of the most common flow chamber, showing slide, coverslip, gasket, ports, and hydrogels. (B)-(G) Common hydrogel geometries.

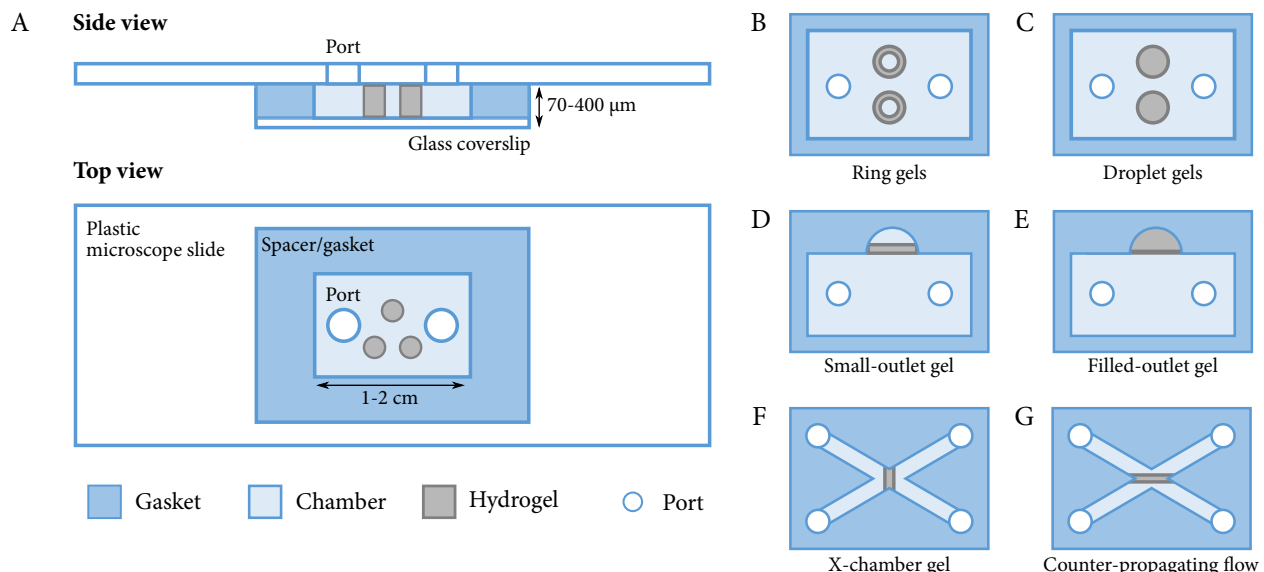
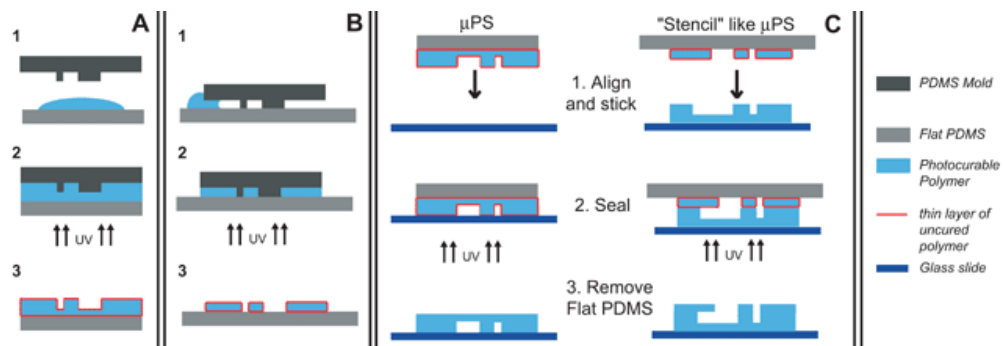


**Figure 3.6:** Microfluidic sticker fabrication from [132]. (A) A PDMS mold is used to shape an NOA droplet on a flat slide. The NOA is briefly cured but retains a sticky surface. (B) NOA can also be wicked into a PDMS mold. (C) The NOA sticker is placed onto a permanent surface, sealed, and cured entirely.



“stickers” to build flow chambers [132, 133]. This procedure is outlined in Fig. 3.6 and relies on the inhibition of curing by oxygen. A droplet of NOA is sandwiched between a glass coverslip and a PDMS mold, which is permeable to oxygen. The NOA is briefly (approximately 3 seconds at 220 mW/cm<sup>2</sup>) cured, though a thin layer remains uncured due to the presence of oxygen at the adhesive’s surface. The PDMS mold is carefully peeled away, and the coverslip with NOA sticker is attached to the slide and sealed. The NOA is then fully cured and the chamber rinsed with ethanol to remove any uncured NOA remaining. Rather than applying NOA directly to the mold, as shown in Fig. 3.6A, it is also possible to seal the mold to the coverslip and wick NOA into the hollows (Fig. 3.6B). This method is more error-prone and time-consuming but results in a flow chamber with glass on the top surface instead of NOA. Proteins are often less inclined to stick to the glass surface than to NOA.

PDMS molds for the NOA stickers were made with 0.5-mm resolution using a Silhouette Cameo craft cutter. After creating a template with the craft cutter’s software, the design was cut into a layer of packing tape that had been carefully applied to a large glass slide. The unwanted tape was peeled away using a razor and tweezers, leaving a depression where the chamber would eventually sit, and the slide used as the reverse-mold for a PDMS mold.

NOA-chambers are much more resistant to drying than double-stick-tape chambers, and can withstand the largest pressure and most rapid flow of any chambers tested. On the other hand,

they are significantly more difficult to make and cannot be re-used. For most experiments, where rapid flow is not necessary, PDMS gaskets were the most useful. Chambers made with PDMS gaskets are thicker (100-400  $\mu\text{m}$ ) than the other varieties and their thickness is not as reproducible, but they are easy to reuse, often last several days without drying out, and are quick to assemble.

PDMS gaskets were made by preparing the volume of PDMS mixture needed to create a layer of a given thickness in a standard Petri dish. Once the PDMS had been thoroughly mixed, degassed, and spread evenly across the dish, it was cured for an hour at 70°C and cut into shape with a razor. Measurement with a micrometer indicated that the nominally 400- $\mu\text{m}$ -thick PDMS film had an error of no more than 10%. This thickness proved to be optimal for sealing to both the acrylic slide and glass coverslip, as well as easily reusable after thorough cleaning with ethanol.

While plasma-bonding the PDMS to the glass was tested, it proved unreliable. As long as the chamber was not subjected to high pressures, an adequate seal formed without additional treatment if all materials were cleaned with ethanol and dried with house air before use. Likewise, we attempted to silanate the glass in order to bond the hydrogel more securely to the top and bottom chamber surfaces, but it was not needed. The gels sealed well to the chamber as long as they were in contact with the surfaces while crosslinking. However, crosslinking the hydrogels on PDMS and then transferring them to the chamber resulted in a poor seal. In consequence, almost all experiments were run using gels that had been crosslinked inside a chamber.

The ports were another point of concern for the watertightness of the chambers. If liquid needed to be flowed through a chamber at an appreciable speed, short lengths of PEEK tubing were superglued into the ports and fitted with Tygon tubing, which was then attached to a blunt-tipped syringe. For sufficiently gentle flows, however, ports were left simply as holes in the plastic slide and the chamber filled by pipette. After the chamber was filled, PEEK tubing ports were sealed with parafilm, and holes were sealed with a flat slab of clean PDMS.

Finally, portless thin chambers were used occasionally, such as for attempting fluorescence recovery after photobleaching (FRAP) using a confocal microscope. To make these chambers, microliter or smaller droplets of precursor solution containing 6- $\mu\text{m}$  glass spacer beads were placed

on glass slides and covered with a coverslip. The hydrogel was crosslinked and fluorescent protein solution wicked into the chamber. The chamber was sealed with valap (a 1:1:1 ratio of Vaseline, lanolin, and paraffin which easily melts over a burner and re-solidifies rapidly). Such chambers last several hours on the microscope without drying but could not be used for longer experiments.

### 3.3 Hydrogel geometries

Our ultimate goal was testing protein separation by monitoring protein passage into and through a selective material. In order to truly measure selectivity, the accumulation of proteins in an outlet reservoir beyond the test material must be measured, not just influx into the material. Many hydrogel and flow chamber geometries were tested in search of a setup that would allow selectivity, as well as free and bound diffusion, to be directly observed.

The limiting factors were the resolution of patterned hydrogel features, the size and accessibility of the outlets, and the equilibrium swelling of the hydrogels. Attempts to improve one of these factors typically led to worse outcomes for the others. Two major classes of hydrogel geometry emerged: those with an outlet reservoir, and those without. The hydrogels without an outlet reservoir cannot be used to directly measure the gels' selectivity, but diffusion constants for the inert protein and transport factors can still be determined. Chapter 4 details the results of bound-state-diffusion experiments using no-outlet hydrogels.

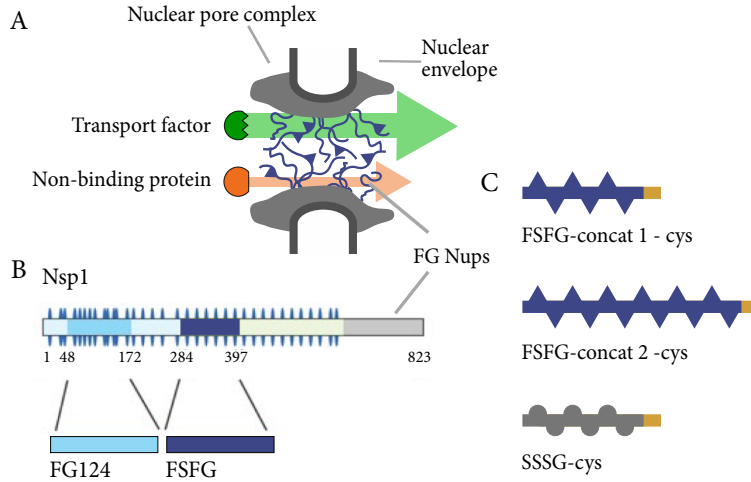
The hydrogel geometries that contained an outlet reservoir are shown in Fig. 3.5B, D, F, and G. Ring-shaped gels (B) provide a small outlet reservoir, which is quick to equilibrate. They were fabricated using a confocal microscope (Sec. 3.8) or using PDMS molds 1-5 mm in diameter. While these rings would have been ideal for selectivity measurements, we were never able to find a procedure that resulted in artifact-free, well-sealed rings.

Fig. 3.5D features a portless outlet reservoir which is much smaller than the inlet. As with the ring gels, these outlets are quick to equilibrate and their precise volume can be calculated, as the entire outlet is in the field of view of a 4x objective. A thin hydrogel bar was polymerized using a photomask, separating the inlet and outlet reservoirs. Without ports in the outlet, the

chamber was soaked in buffer for 24 hours to remove the remaining precursor solution from the outlet. The inlet could then be filled with a fluorescent protein solution and accumulation in the outlet measured over time. Unfortunately, the outlet itself was likely lightly crosslinked, even with careful use of the photomask. See Sec. 3.8 for more evidence of stray crosslinking. Additionally, the hydrogel bars were of irreproducible thickness (50-200  $\mu\text{m}$ ) and swelled or buckled unpredictably. Ultimately, the lack of reproducibility between replicates made this geometry unusable.

Finally, Fig. 3.5F shows an x-shaped chamber with four ports. A thin bar of hydrogel was polymerized at the junction of the arms using a photomask. The inlet and outlet reservoirs are approximately the same size, leading to slow equilibration in the outlet. The precise volume of the outlet is impossible to determine, as the arms are usually partly filled. Additionally, these chambers must be made using NOA stickers, which are difficult to use, and they tend to dry rapidly. The x-chamber geometry is therefore not useful except in specialized situations. A slightly more useful version is the counter-propagating flow chamber shown in Fig. 3.5G. In this version, the hydrogel bar is as long as possible, creating a “hydrogel window” that separates the two arms of the chamber. While this setup was never used to test protein selectivity, in principle a counter-propagating flow can be established using syringe pumps in order to simulate constant concentration in infinite inlet and outlet reservoirs while using a limited amount of material. A similar setup is demonstrated in [133].

The no-outlet hydrogel geometries shown in Fig 3.5C and E are much simpler to make but do not allow for measurement of protein selectivity. Panel E shows a variation on the small-outlet chamber in which the outlet is filled with hydrogel and crosslinked using a photomask. Finally, the droplet gels in panel C were added to the chamber before assembly and crosslinked without a mask (Fig. 3.4B). These are the only hydrogels which were made without a mask, greatly reducing the irreproducible edge effects (also seen in Sec. 3.8). Droplet gels have volumes of 0.5-2  $\mu\text{L}$  and equilibrate 30-kDa proteins in 24-48 hours. While these gels cannot be used to monitor selective transport through and exit from the gel, we can use them to measure the diffusion constants of proteins within the gel and the selective influx of transport factors. Chapter 4 focuses entirely on



**Figure 3.7:** Nup fragments used in nuclear pore mimic experiments. (A) The nuclear pore with FG Nups filling the central channel. (B) The FG Nup Nsp1 shown as a schematic sequence, with FG124 and FSFG fragments noted. (C) Variants of FSFG: FSFG concat 1-cys with 6 FSFG motifs and a C-terminal cysteine; FSFG concat 2-cys, as above but twice as long; SSSG-cys, like FSFG concat 1-cys with the F's mutated to non-binding S's.

droplet hydrogels made in 400- $\mu\text{m}$ -thick PDMS gasket chambers with two PEEK-less ports.

### 3.4 FG Nup peptides

The remaining components of the nuclear pore mimics are the FG Nup fragments which are tethered to the hydrogel scaffold. We chose to use Nsp1 as the basis for our Nup peptides. Like all FG Nups, Nsp1 has an ordered domain which anchors it to the channel wall, and a disordered region containing many FG motifs. As a whole, the disordered region aggregates when isolated in buffer [49, 50].

As shown in Fig. 3.7, we made use of two distinct fragments of Nsp1, denoted FSFG and FG124 [11]. Both are entirely disordered, are approximately 120 amino acids (14 kDa) in length, and contain multiple FG motifs. FSFG is so called because it possesses six FSFG repeats. It is extremely stable and unlikely to aggregate, remaining unaggregated throughout a wide range of buffers, pH values, concentrations, and crowding conditions. As an additional advantage, FSFG can easily be expressed and purified. The other Nup fragment, FG124, contains 8 FG motifs. If not kept in 7M guanidine hydrochloride, FG124 will aggregate over the course of several hours. However, FG124 does not aggregate in the cellular environment, suggesting that Nsp1 itself may not be aggregated in the nuclear pore [11].

Both FSFG and FG124 are expressed in BL21 DE3 Gold cells in the pRSF plasmid, which is

Kan resistant. Each has a C-terminus 6x histidine tag and is purified in potassium transport buffer (PTB; 150 mM KCl, 20 mM HEPES, 2 mM MgCl<sub>2</sub>) using a metal affinity column as described in Appendix C. They are unharmed by lyophilization and resuspension.

We have access to a wide library of FSFG and FG124 variants, few of which I helped to create. Many originate in the Rout lab at Rockefeller University, and others were created by Andrea Egan, Nick Bax, Eric Verbeke, and myself. Appendix F provides the sequence of the most commonly-used Nup variants.

In order to test the effect of Nup length and number of FG motifs, FSFG also exists in concatenated versions: FSFG concat-2 (twice as long as FSFG) and FSFG concat-3 (three times as long). Although both have been expressed and purified in the past, I was only able to express FSFG concat-2. All of these FSFG variants, as well as FG124 and the nonbinding negative control SSSG (Sec. 3.4.1), exist with one or both terminal cysteines as well. The C-terminal cysteine version is the most commonly used, as a cysteine is necessary to tether the Nup fragment to a hydrogel (Sec. 3.1 and Appendix D). It should be noted that ybbR FSFG cys is most commonly used in the nuclear pore mimics. The ybbR tag is intended for site-specific labeling with a fluorophore or other tag but almost always goes unused in the context of FSFG hydrogels [134].

The cysteines in all of the above Nup variants form disulfide bonds very rapidly (within minutes) after being removed from reducing agents. In addition, the Bradford assay is unreliable for these Nup variants due to the relative lack of aromatic residues. A BCA assay should be used instead to quantify protein concentration.

In addition to the commonly-used Nup variants in Table F.1, we have access to several other Nup fragments and mutants. These include shortened versions of FSFG with two or four FSFG motifs, FSFG variants with most but not all binding motifs removed (FSFG mutated to FSYG), the full FG domain of Nsp1, and full-length Nsp1.

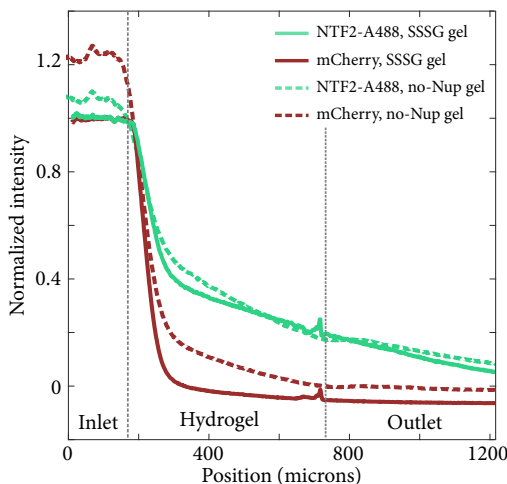


**Figure 3.8:** Comparison of intensity profiles for SSSG and no-Nup (control) gels. Both hydrogels were 10% wt PEG with a 1-kDa PEG dithiol linker. The SSSG gel precursor contained 10 mg/mL SSSG. Inlet reservoir contained 20  $\mu$ M NTF2-Alexa488 and mCherry in PTB. As expected, no binding is seen in either gel.

### 3.4.1 SSSG negative control

The obvious negative control for a Nup-filled hydrogel is a hydrogel containing no Nups. However, it is possible that the presence of FSFG in the precursor solution changes the final gel properties such as pore size, or that nonspecific interactions between the Nup peptide and test proteins alter the behavior of the test proteins. To account for these possibilities, we designed a negative control peptide which is identical to FSFG except that the phenylalanine residues have been mutated to serine (i.e. FSFG goes to SSSG). This mutant does not bind NTF2, as demonstrated by the lack of NTF2 accumulation in hydrogels containing tethered SSSG. Figure 3.8 compares the intensity profile of a 10 wt% PEG hydrogel whose precursor contained 10 mg/mL SSSG to that of a hydrogel with no Nups. The two profiles are quite similar, suggesting that the presence of peptide in the hydrogel does not itself alter the diffusion of NTF2 and mCherry. Following the initial tests, SSSG gels were used periodically to confirm that no-Nup gels continued to serve well as negative controls, but they were not used regularly as controls.

The SSSG peptide was prepared in an identical manner to FSFG: SSSG-cys was his-tagged, inserted into pRSF, and expressed in BL21 DE3 Gold cells. It was purified using a metal affinity column using the same procedure as FSFG variants and had a high yield. As with FSFG, SSSG is stable and non-aggregating over a wide range of conditions.

### 3.5 Transport factor constructs

A wide variety of transport factors exist, specialized for the import and export of particular cargo. Almost all protein separation experiments we performed made use of Nuclear Transport Factor 2 (NTF2). This transport factor is relatively small (28 kDa dimer) and, unlike most other transport factors, does not require active release of cargo after transport. NTF2 transports RanGDP as part of a mechanism which maintains a high RanGTP concentration in the nucleus, necessary for the active release of other protein cargoes (Sec. 1.1.2) [37]. The choice to focus on NTF2 was made for a number of reasons: the lack of facilitated release makes it a simple first choice to study, it is small enough to move reasonably quickly through hydrogels, and it is readily expressed in bacteria and purified.

His-tagged yeast NTF2 in the Kan-resistant plasmid pRSF was expressed in BL21 DE3 Gold cells and purified using the procedure described in Appendix C. When necessary, NTF2 was covalently labeled with fluorescent dyes as described in Appendix G. In addition to wild-type yeast NTF2, several variants were created in order to address shortcomings of NTF2 in the experimental setup. In particular, efforts were made to prevent the presence of any NTF2 monomers and to eliminate the need for dye labeling. Finally, a point mutant of NTF2 was created with the intent of disrupting the binding pocket and providing another non-binding negative control protein to complement mCherry.

Beyond NTF2, we briefly tested the influx of Kap121, a member of the well-studied karyopherin family of transport factors, into hydrogels. Although Kap121 and its fluorescent cargo protein clearly bound to the FSFG in the hydrogel, the pore size remained too small for significant import into the gel.

The remainder of this section provides an overview of the transport factor constructs we created. Much of the cloning work was done by Eric Verbeke and Scott Tilden.

### 3.5.1 Covalently-tethered NTF2 dimer

Despite the work done to increase the hydrogel's average pore size, we often observed that NTF2 and mCherry equilibrated to different extents and on different timescales even in hydrogels containing no Nups or nonbinding Nups. As these proteins are nominally the same size, this implies that they may be interacting differently with the hydrogel substrate, or that they may not be the same size after all. NTF2 is a 28 kDa homodimer whose monomers are 14 kDa. If there exists an appreciable population of NTF2 monomers within the hydrogel, it will equilibrate more rapidly and to a higher concentration than the larger mCherry. The dissociation constant  $K_D$  of mammalian NTF2 is about 1  $\mu\text{M}$  [135]. Assuming this is approximately true for yeast NTF2 as well, there should be very little monomeric NTF2 present at our typical reservoir concentration of 20  $\mu\text{M}$ .

However, we designed a covalently-tethered version of NTF2 to eliminate the possibility of monomerization. This consisted of two NTF2 monomers connected by a flexible amino-acid tether (Fig. 3.9A). Several trial tethers with their length and composition are shown below:

10aa – linker : TSGSGSGSPG

15aa – linker : TSGSPRGSSGSGSPG

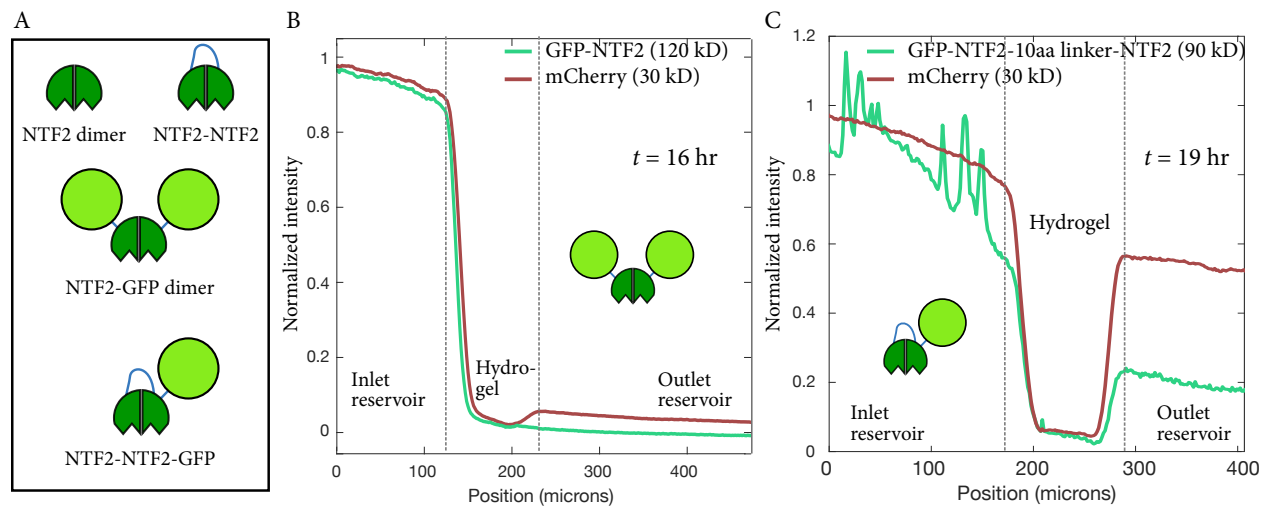
18aa – linker : TSPGLVSRGSGSGSGSPG

Eric Verbeke and Scott Tilden successfully cloned covalently-tethered NTF2 with all three tethers. Unfortunately, no binding was seen when the NTF2 was introduced to an FSFG hydrogel. It is likely that the tether interferes with the binding pockets or dimerization interface.

### 3.5.2 NTF2-GFP

In addition to the potential problem of NTF2 monomerization, the fluorophores that labeled NTF2 were prone to hydrolysis, leaving an unknown amount of free dye in the reservoir mixture. Free dye is indistinguishable from labeled NTF2 in the influx and selectivity experiments, and it is important that free dye not be present in appreciable amounts. This problem is addressed through

**Figure 3.9:** Attempts to create functional NTF2 fusion proteins. (A) Cartoon of various NTF2 constructs: wild-type NTF2 dimer, covalently-tethered NTF2-NTF2, GFP-NTF2, GFP-NTF2-NTF2 (B) Intensity profile for GFP-NTF2 dimer showing no binding to FSFG hydrogel. Hydrogel precursor contained 10 mg/mL FSFG; reservoir solution contained 20  $\mu$ M GFP-NTF2 and mCherry in PTB. (C) Similar experiment as (B) for GFP-NTF2-NTF2.



data processing in Sec. 3.9, but we also approached it by engineering a GFP-NTF2 fusion protein. Such a protein would eliminate the need for dye-labeling the NTF2 and therefore eliminate free dye in the chamber entirely.

However, as GFP is also approximately 30 kDa, the fusion protein is much larger than NTF2 alone. To mitigate this problem, a GFP-NTF2-NTF2 version was also created (Fig. 3.9A). While this is still larger than an NTF2 dimer, it contains only one copy of GFP. Both constructs were inserted into the pET21 plasmid, his-tagged, and expressed in BL21 DE3 Gold cells. They were purified as described in Appendix C, using a cobalt affinity column in PTB and 1:1000 PIC and eluted with 250 mM imidazole, yielding ample protein with moderate degradation products.

Figure 3.9B and C show that neither construct is able to bind to FSFG PEG hydrogels. Again, the binding pockets or dimerization interface may be disrupted by the tethers, or the fusion protein may simply be too large.

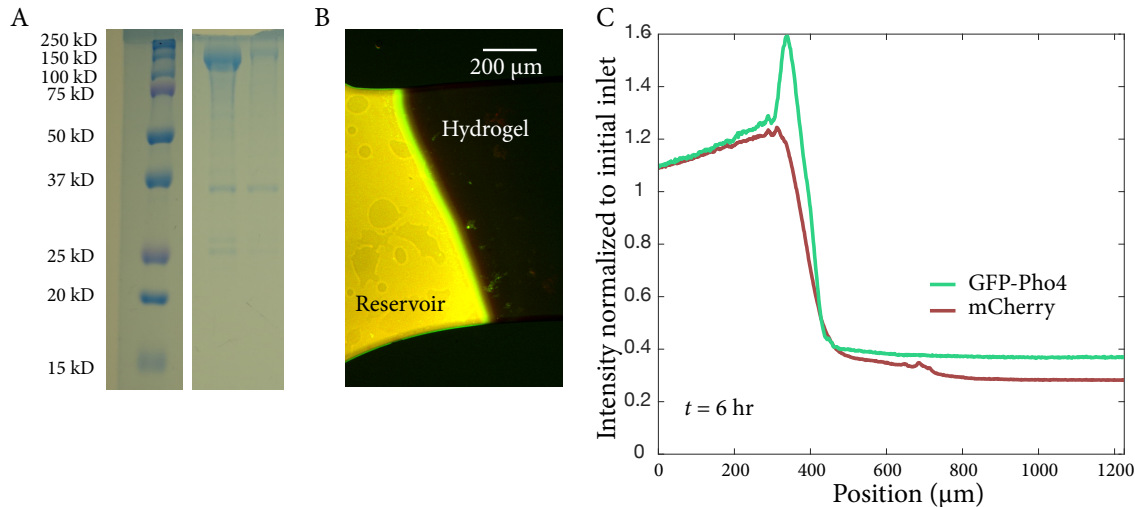
### **3.5.3 Nonbinding NTF2 F5R**

Although mCherry is a similar size as the NTF2 dimer and makes an acceptable negative-control inert protein, it may well interact differently with the hydrogel scaffold than NTF2 does. A better control would be a nonbinding mutant form of NTF2. A W7A point mutant in mammalian NTF2 reduced its affinity for FG Nups [38, 57]. A corresponding mutant in yeast NTF2 is F5R. This mutant was cloned by myself and Scott Tilden, expressed, and purified. Further tests, such as NMR, are needed to verify its binding affinity for FSFG.

### **3.5.4 Kap121 and GFP-NLS**

The karyopherins (Kaps) are a canonical class of transport factors. They transport proteins tagged with nuclear localization signals (NLS) through the nuclear pore. We were interested in testing Kaps because they are widely studied and much larger than NTF2, so selective transport would be more apparent. Eric Verbeke engineered two GFP-NLS constructs: GFP-Spo12 and GFP-Pho4 (Appendix F). These constructs were his-tagged, inserted into pET21b, expressed in

**Figure 3.10:** (A) SDS-PAGE showing ladder and two Kap121 elutions (purified by Chris Lawton), (B) FSFG PEG hydrogel (right) with reservoir (left) containing mCherry, Kap121, and GFP-Pho4. (C) Normalized intensity profiles from hydrogel in (B), showing binding of the Kap121 - GFP-Pho4 complex at the edge of the gel.



BL21 DE3 Gold cells, and purified using a cobalt affinity column as described in Appendix C. Kap121-GST was expressed and purified following [64] and the GST subsequently cleaved with thrombin resin (Fig. 3.10A).

Kap121 binding and influx was tested using a hydrogel made from precursor solution containing 0.05 wt% Irgacure2959, 110 mg/mL 20kD 8-armed PEG-norbornene, 11 mg/mL 1 kDa PEG-dithiol, and 1 mM TCEP in PTB, crosslinked for 2 minutes under the UV LED. After soaking in PTB overnight, 5  $\mu$ M Kap121, 10  $\mu$ M GFP-Pho4, and 100  $\mu$ M mCherry in PTB were added to the inlet reservoir. Selective influx of the Kap121/GFP-Pho4 complex was evident, since the complex accumulated at the edge of the hydrogel (Fig. 3.10B and C). The bright band demonstrates binding of FSFG to Kap121 as well as of Kap121 to GFP-Pho4. Over the course of several hours, the GFP-Pho4 front remained localized at the edge of the gel, likely indicating that the pore size of the hydrogel was too small to accommodate the Kap121/GFP-Pho4 complex. Given the large size of this complex, the pore size was never increased sufficiently for influx into the hydrogels.

### 3.6 Pore size

The perennial difficulty with our hydrogel nuclear pore mimics has been the pore size of the hydrogels. While hydrogels with an average pore size between 10 and 100  $\mu\text{m}$  are well-studied [136], as well as hydrogels with pores under 5 nm, the intermediate-porosity regime which would allow for separation of proteins in the size range 30-150 kDa (typically 5-10 nm) is difficult to reach. We wanted to be confident that any differences in the behavior of transport factor and inert protein were due to their interactions with the Nups, not slight differences in size or interactions with the hydrogel. At the same time, we wanted the anchored Nups to fill a significant portion of the pore. Much of our work on hydrogel design was performed with the aim of achieving a suitable pore size.

Hydrogel swelling in particular has been an obstacle in our search for protein-separating hydrogels. When polymerized from a precursor solution, hydrogels are almost never in mechanical equilibrium. They must be soaked in an aqueous solution until they have swelled and taken up enough water to reach equilibrium. Common methods of estimating pore size rely on the swelling ratio of the gel, i.e. the ratio of the wet to dry gel weight. However, our gels are small enough to make that method impractical, and it is unclear whether a Nup-filled hydrogel that is allowed to swell to equilibrium in buffer will have the same properties as one that is polymerized inside a confined flow chamber. In fact, the repeated but unpredictable buckling and swelling of hydrogels within the flow chambers indicate that our hydrogels do not reach mechanical equilibrium. Despite efforts to improve the swelling ability of our hydrogels, the lack of equilibrium swelling likely contributes to the smaller-than-ideal pore size as well as inconsistency between replicate experiments.

Of the two hydrogel substrates tested, acrylamide gels appear to have a better pore size distribution than PEG gels. An order-of-magnitude calculation estimated 1 nm as the average mesh size of a 10 wt % PEG hydrogel, comparable to or smaller than the 5-nm size of NTF2 (Appendix B). We were not able to lower the weight percent of PEG and still achieve gelation. Overall, 6% w/v acrylamide gels are more mechanically stable and yield more reproducible results than 10% wt PEG gels, the lowest stable percent weight PEG gel we were able to attain. Before

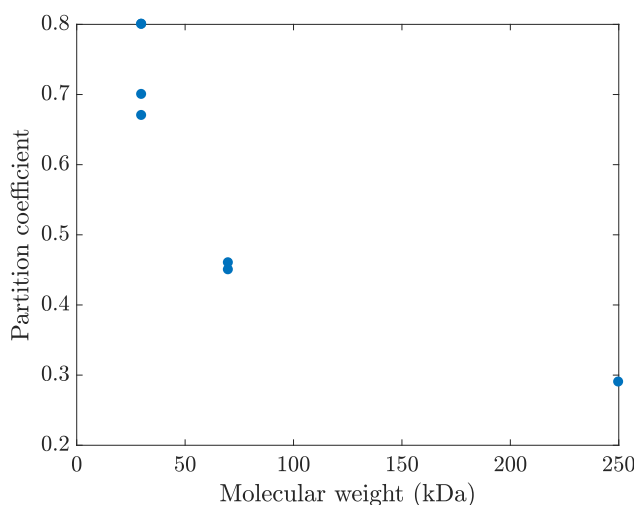


**Figure 3.11:** Equilibrium partition coefficient as a function of macromolecule molecular weight for 6% acrylamide no-Nup hydrogels. NTF2, mCherry and GFP were used as 30-kDa test proteins along with 70-kDa dextran-rhodamine and 250-kDa dextran-fluorescein.

settling on acrylamide hydrogels, we considered several alternative crosslinkers in hopes of creating more mechanically-stable PEG hydrogels that would support larger pores. Most notably, we moved from a 1 kDa PEG dithiol linker to an 8 kDa linker. This change did increase the pore size of the resulting PEG gel, but the gel was mechanically weak and required proportionately more swelling to reach equilibrium, an impossibility inside the flow chamber. DNA oligomers, coiled-coil rationally-designed proteins, and FSFG with both terminal cysteines were also considered as crosslinkers, but none were able to support gelation [137, 138]. Therefore, we turned our attention to acrylamide hydrogels.

Figure 3.11 shows the partition coefficient of equilibrated fluorescent macromolecules as a function of molecular weight for 6% acrylamide gels containing no Nups. The partition coefficient is the ratio of equilibrium concentration within the hydrogel to that in the reservoir outside; a partition coefficient of 1 indicates that the macromolecule's diffusion and equilibration is not impeded at all by the presence of the gel. Although 250 kDa dextran has a low partition coefficient, 30 kDa transport factors and fluorescent proteins have similar partition coefficients around  $\gamma = 0.7$ . The partition coefficient of inert proteins decreases when Nups are tethered to the hydrogel, as they further impede diffusion and equilibration.

The no-Nup hydrogel dataset used in Chapter 4, containing 15 experiments in total, provides another measurement of partition coefficient and diffusion. In this later dataset, both the NTF2

and mCherry partition coefficients are equal to  $0.48 \pm 0.03$ , statistically indistinguishable. It is unclear why this value is lower than that measured in Fig. 3.11. The mean diffusion constant of NTF2 in these gels was  $56 \pm 11 \mu\text{m}^2/\text{s}$ , as compared to  $46 \pm 8 \mu\text{m}^2/\text{s}$  for mCherry. These results indicate that NTF2 and mCherry behave similarly within the hydrogel, suggesting overall a small interaction with the hydrogel scaffold. We deemed this to be acceptable for the NTF2-mCherry pair but did not quantify the diffusion of larger proteins using acrylamide gels.

### 3.7 Porogens

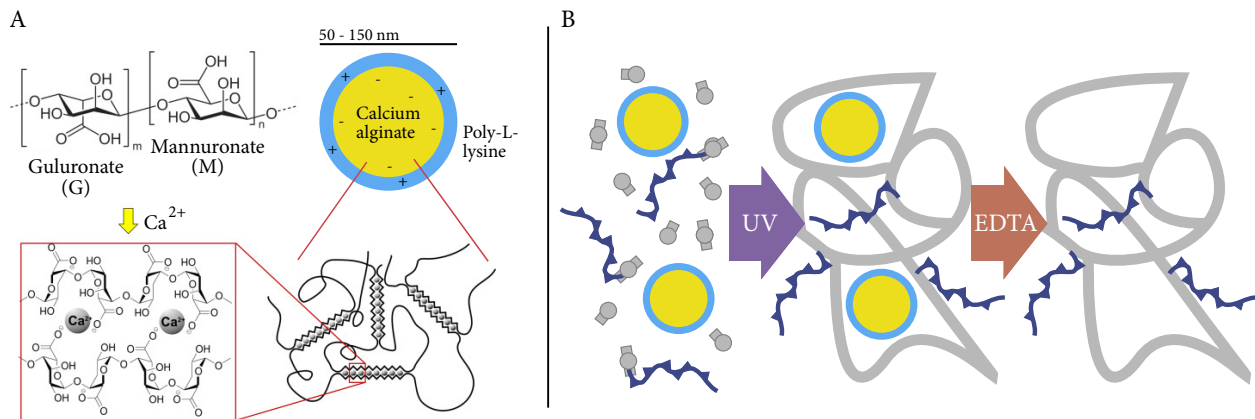
Given the difficulties of increasing the average pore size by changing the hydrogel composition, we investigated the possibility of introducing a porogen into the precursor solution. To be useful, the porogen must be a macromolecule or particle 10-100 nm in diameter that could be evenly distributed throughout the precursor solution and therefore the hydrogel without disrupting polymerization. The porogen must then be digested, dissolved, or otherwise removed from the hydrogel, as it is too large to passively diffuse from the gel on a reasonable timescale. The pores left behind would then increase the overall pore size of the gel as well as potentially allowing the hydrogel network to swell to equilibrium even while confined in a chamber.

Two possible porogens were tried: Alginate nanospheres and high-molecular-weight dextran. Alginate can be polymerized and depolymerized through the addition or removal of calcium ions, and dextran can be digested by dextranase. Although both showed promise, neither was ultimately well-suited to increasing a hydrogel's pore size.

#### 3.7.1 Alginate nanospheres

Alginate is a polysaccharide derived from algae which polymerizes upon addition of calcium ions (Fig. 3.12A). It can be depolymerized by adding EDTA or another chelator to remove the calcium. Alginate salts are available in a number of molecular weights and viscosities, making alginate a promising candidate for a porogen. If alginate nanospheres could be polymerized and added to the hydrogel precursor solution, they could later be removed with EDTA, leaving larger

**Figure 3.12:** Alginate crosslinking from [140]. (A) Alginate is composed of alternating guluronate (G) and mannuronate (M) blocks. Addition of calcium ions leads to an “egg-box” crosslinked structure. Calcium alginate nanospheres are coated with poly-L-lysine [139]. (B) Alginate nanospheres should act as a porogen when added to a hydrogel precursor solution. Removal of the spheres with EDTA should leave larger pores in the crosslinked hydrogel.



pores than would otherwise be present (Fig. 3.12B).

A number of protocols exist for creating alginate microspheres, but fewer are appropriate for nanospheres, which is the scale that is necessary for use as a porogen. I made nanospheres following the method described in [139]. I prepared 10 mL of 0.6 mg/mL alginic acid sodium salt (Sigma, low-viscosity, product number A0628) in water. Even a small amount of sodium alginate added to water creates a viscous solution that requires extensive stirring to dissolve. I used a sonicator with a microtip to sonicate the sodium alginate solution while adding 2 mL of 0.67 mg/mL calcium chloride in water drop-wise. I then stirred the solution on a magnetic stir plate for 30 minutes before adding 2 mL of 0.3 mg/mL poly-L-lysine in water. The solution was then stirred 30 more minutes.

I tested several methods of preparing the nanospheres for addition to the hydrogel precursor solution. First, the nanospheres were left in the solution in which they were made. Second, the nanospheres were spun down out of that solution at 14400g for 10 minutes and immediately resuspended in deionized water. (The pellet becomes more difficult to resuspend if it is not immediately resuspended.) Finally, the nanospheres were lyophilized and resuspended in water. The

resuspended solution remained cloudy even after several days, and so I didn't pursue lyophilizing the nanospheres.

The radius and diffusion coefficients of the both the non-spun and spun nanospheres were determined using a Titan DynaPro dynamic light scattering (DLS) system. The non-spun nanospheres had an average radius of  $170 \pm 10$  nm, with an estimated diffusion constant of  $1.1 \pm 0.1 \mu\text{m}^2/\text{s}$ . The nanospheres that had been spun and resuspended had two populations: almost entirely particles of radius  $210 \pm 10$  nm and diffusion constant  $1.05 \pm 0.06 \mu\text{m}^2/\text{s}$ , and a small number of very large particles. The large particles are probably aggregates from centrifugation.

After measuring the size distribution of the two samples, I added EDTA in an effort to depolymerize the nanospheres. The maximum final EDTA concentration was 25 mM, and the samples were left to sit up to 30 minutes. Re-running the DLS data gave inconclusive results as to the presence or size of remaining particles. The fits did not change much, although the large aggregates appeared to have vanished from the spun sample. It appeared that at least some nanospheres remained.

Next, the nanospheres were added to hydrogel precursor solution, which was then crosslinked. Several nanosphere concentrations were tested before a condition was found in which the nanospheres appeared by eye to resuspend. An approximately 2  $\mu\text{L}$  nanosphere pellet (spun down from 10 mL of solution) was resuspended in a final concentration of 110 mg/mL PEG-norbornene, 90 mg/mL 8 kDa PEG dithiol linker, and 5 mM LAP, all in 50 mM MOPS buffer pH 7.4. The MOPS buffer was chosen because it has no divalent cations (and thus will not interfere with the alginate nanospheres). The isoelectric point of poly-L-lysine is at about pH 5, and the nanospheres should be kept above that pH so their coating remains intact.

However, even these gels were clearly inhomogeneous under 4x magnification. In an attempt to depolymerize the nanospheres, the resulting hydrogels were rinsed with PTB pH 5 (to remove any possible poly-L-lysine coating) and then soaked in 100 mM EDTA for two days. No change was observed under 4x magnification. For comparison, a macroscopic alginate droplet dissolved after 20 minutes in 100 mM EDTA and vortexing. New gels were made and soaked in a pH 5 buffer (to

remove any poly-L-lysine coating) and then in a solution containing 100 mM EDTA and 200 mM sodium citrate. Gels remained cloudy and no change was observed.

Given the difficulty in resuspending and depolymerizing the alginate nanospheres, our focus shifted to developing a dextran/dextranase porogen system.

### 3.7.2 Dextran/dextranase porogen system

Following the alginate nanospheres attempt, we tried creating nanopores using high-molecular-weight (high-MW) dextran. Dextran is a branched, inert polymer that is commercially available at molecular weights up to 250 kDa. We used two sizes as porogens, 70 kDa ( $R_H \approx 10$  nm) and 250 kDa ( $R_H \approx 15$  nm) [141].

As a proof of concept, I made and crosslinked precursor solutions containing 100  $\mu$ M 70 kDa dextran-rhodamine or 250 kDa dextran-fluorescein. The precursor contained 12% acrylamide and 3.3% bisacrylamide in 50 mM sodium acetate (NaOAc) buffer pH 5 as well as 2 mM LAP. The precursor solution was crosslinked as 1- $\mu$ L hydrogels in a 400- $\mu$ m tall PDMS gasket chamber for 20 s using the UV LED. After rinsing with NaOAc buffer, the chamber was filled with a freshly-made solution of 20 mg/mL dextranase (Sigma, D5884, dextranase from *Penicillium sp.*) in NaOAc buffer. The chamber was immediately placed in an Olympus IX-81 widefield microscope's environmental chamber, held at 37°C, and imaged overnight. The fluorescence intensity in the dextranase-treated gels decreased significantly more rapidly than that of gels which contained dextran but were not treated with dextranase (Fig. 3.13). In the case of 70 kDa dextran, the fluorescence reached a steady value (equilibrated, equal to that in the reservoir) in approximately 100 minutes, while the non-treated case wasn't equilibrated after an overnight incubation. For the 250 kDa dextran, both the treated and non-treated gels reached equilibrium in approximately the same amount of time, but the treated gel equilibrated much closer to the reservoir level than the non-treated gel. Both sets of gels indicate that dextranase is able to digest the dextran within the hydrogels, allowing a significant amount of dextran and digest products to leave the gel, as expected.

The next step in attempting this porogen system was recreating the effect in FSFG gels.

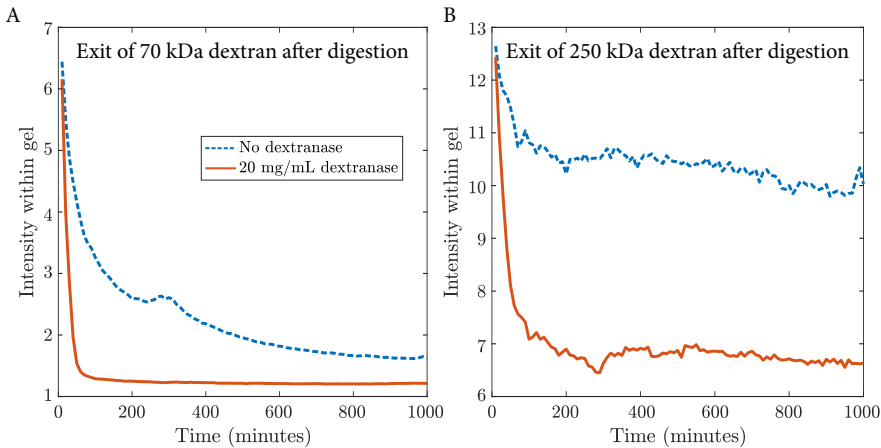


**Figure 3.13:** Exit of fluorescent dextran from hydrogels after dextranase digestion. Hydrogels were made with  $100 \mu\text{M}$  dextran and were treated with  $20 \text{ mg/mL}$  dextranase as described in the text. Fluorescence intensity within the gel approaches equilibrium with the reservoir. Intensity was normalized to initial gel fluorescence.

Unfortunately, it became clear that the dextranase was digesting the FSFG as well as the dextran (Fig. 3.14).

At this point, we stopped trying to use the dextran-dextranase porogen system for FSFG gels. However, we did investigate the effect of dextran-dextranase treatment on the pore size in acrylamide hydrogels without anchored proteins. Contrary to expectations, dextran-dextranase treatment did not increase subsequent diffusion of fluorescent proteins into the treated hydrogels. For these experiments, I used  $200 \text{ kDa}$  non-fluorescent dextran in the acrylamide precursor solution. After the gels (either  $12\%$  or  $6\%$  final acrylamide concentration) were crosslinked, I treated them with  $20 \text{ mg/mL}$  dextranase solution in sodium acetate buffer (freshly made solution) for 2 hours at  $37^\circ\text{C}$  in an incubator. Then I rinsed the gels with buffer and used a syringe pump to flow  $10 \text{ mL}$  of PTB through the chamber over the course of 10 hours. The next day, I challenged the gels with a solution containing  $10 \mu\text{M}$  each immunoglobulin G tagged with Alexa Fluor 488 (IgG-Alexa488,  $150 \text{ kDa}$ ) and mCherry ( $28 \text{ kDa}$ ). I monitored the accumulation of each protein in the gel over time (Fig. 3.15). In both the  $12\%$  and  $6\%$  acrylamide gels, dextran-dextranase treatment did not improve influx of IgG-Alexa488 over corresponding non-treated gels. In  $6\%$  acrylamide gels, the influx of mCherry also remained approximately the same for treated and non-treated gels. This indicates that dextran-dextranase treatment does not significantly increase the pore size in acrylamide hydrogels. This is probably because significant dextran remains in the gel even after dextranase treatment, as suggested by Fig. 3.13.

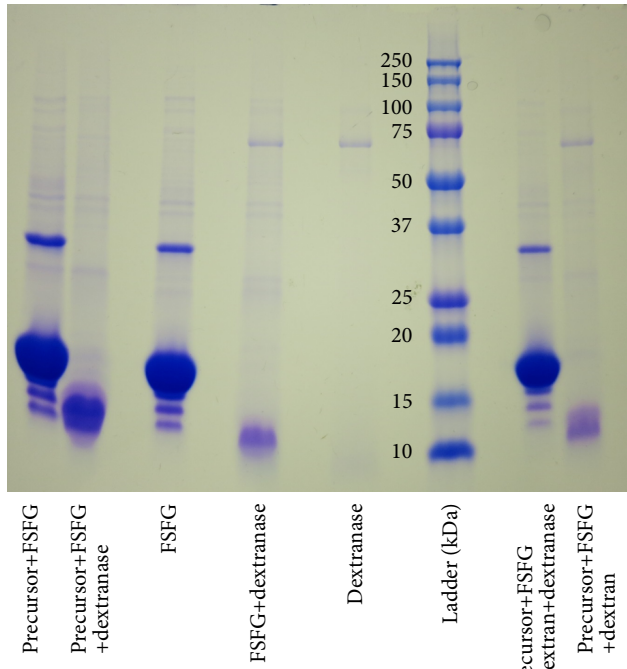


**Figure 3.14:** SDS-PAGE gel demonstrating dextranase digestion of FSFG-cys. Three conditions are shown, with and without dextranase: precursor solution with FSFG, FSFG only, and precursor with FSFG and dextran. In each case, addition of dextranase destroys the FSFG band at 15 kDa and produces bands of smaller degradation products. FSFG-cys dimer bands are visible. Dextranase alone is shown for reference. AnyKD PAGE gel (BioRad), 100 V, 80 minutes.

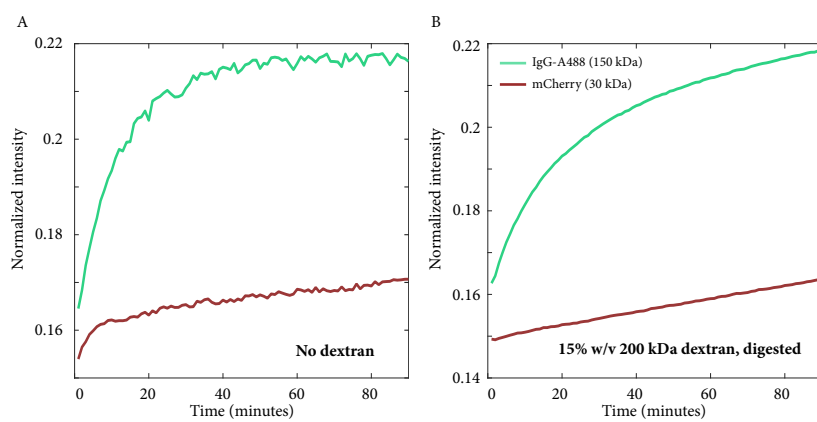


**Figure 3.15:** Protein accumulation within hydrogels made with or without dextran. Reservoirs contained 10  $\mu$ M IgG-Alexa488 and mCherry. (A) Accumulation in a 12% acrylamide hydrogel containing no Nups or dextran. (B) Accumulation in a 12% acrylamide hydrogel containing no Nups, made with 15% w/v 200 kDa dextran, digested for 2 hours at 37°C with 20 mg/mL dextranase.

In conclusion, dextranase is capable of digesting a significant fraction of high-MW dextran within an acrylamide hydrogel. However, a large amount of the dextran still remains in the gel even after an overnight rinse, meaning that dextran-dextranase treatment does not result in noticeably larger pores overall. In addition, the dextranase we used digested the FSFG peptide as well as dextran. Dextran-dextranase treatment is not suitable as a porogen system for our hydrogels.

### 3.8 Polymerization using confocal microscope

Although photomasks are simple to use, they have several drawbacks. As shown in Fig. 3.4, the flow chamber is filled with precursor solution and only a portion is exposed to UV light. The edges of the exposed region tend to behave differently depending on whether they are bounded by air or precursor solution. When using a photomask, the edge of the resulting gel typically shows a dip in transport factor or inert protein concentration when equilibrated, similar to that seen in Fig. 3.19. This dip is undesirable, as it makes fitting to the concentration profiles more difficult and is irreproducible. Additionally, the smallest feature that can be created with a photomask is a bar around 150  $\mu\text{m}$  in thickness with a variability of about 50  $\mu\text{m}$ . Smaller features would permit more rapid outlet equilibration and use less material.

Given the problems that arose using photomasks and a UV LED to make hydrogels, we tested a crosslinking method using a 405 nm laser on a Nikon A1R spinning disc confocal microscope. Once a region of interest has been defined with the Nikon software, the photobleaching setting can be used to selectively expose regions of the field of view to UV light. The precursor solution therefore crosslinks in the region of interest only. This method is similar to that used in [133], but the masking is done using the A1R software instead of a physical mask in the back focal plane.

We were able to “draw” hydrogels of arbitrary shapes using the 10x objective on the confocal along with the 405 nm laser at 100% power. Figure 3.16 shows hollow rings with an outer diameter of about 600  $\mu\text{m}$  and an inner diameter of 500  $\mu\text{m}$ , as well as lines with a width of about 50  $\mu\text{m}$ . In order to crosslink the precursor solution, two raster-scans of the laser across the region of interest were needed, with the longest-allowable dwell time per pixel. (In the microscope settings,

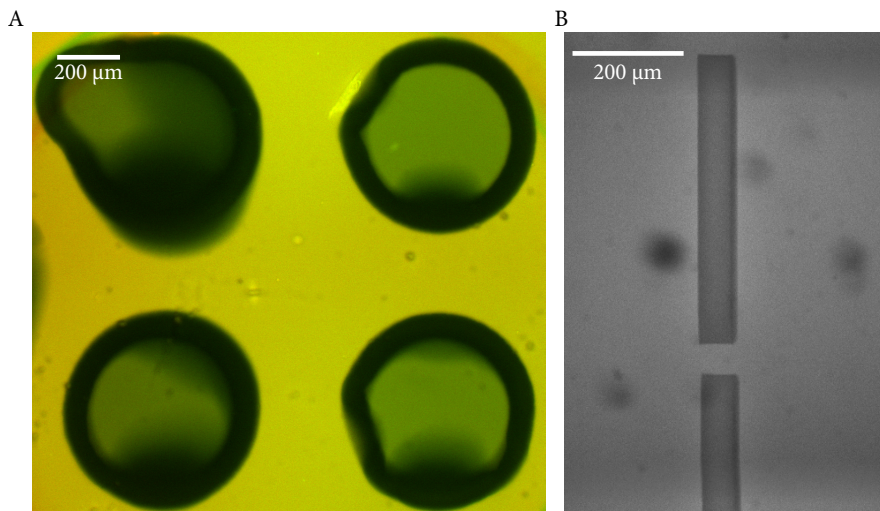


**Figure 3.16:** Image of confocal-crosslinked hydrogels. (A) Ring hydrogels containing no Nups. Reservoir contains 20  $\mu$ M NTF2-A488 and mCherry. (B) Line hydrogels containing FSFG-Alexa647. Reservoir contains precursor solution with FSFG-Alexa647. Photo-bleaching within gel by 405 nm laser is evident.

the shortest dwell time is set as ‘1’ and the longest as ‘1/32’.) The precursor solution contained 0.5 mM LAP, 110 mg/mL 20kDa 8-armed PEG-norbornene, 11 mg/mL 1kDa PEG-dithiol, and 1 mM TCEP in PTB; it was polymerized in 70- $\mu$ m-thick sticky-tape or NOA flow chambers.

Crosslinking with the confocal has several advantages over LED crosslinking. Significantly smaller features are possible using the confocal. 50- $\mu$ m features are consistent and reproducible, and features down to approximately 25  $\mu$ m are possible, in contrast with the effective 100- $\mu$ m lower limit using the LED and photomasks. Additionally, arbitrary shapes, including shapes with inner cavities, are possible using the confocal. Multiple small hydrogels can be created in the same chamber, including hydrogels of varying composition, which are made by removing the excess precursor solution and refilling the chamber with a different solution. Finally, the degree of crosslinking can potentially be varied by changing the photobleaching settings.

The most appealing geometry made possible with confocal crosslinking is the hydrogel ring, as shown in Figs. 3.16 and 3.18. Unlike all other hydrogel-chamber geometries, the inner reservoir is small enough to equilibrate in only a few hours (Fig. 3.17). Ideally, the hydrogel rings could have been used to test selective flux through the NPC mimics, a possibility not offered by other geometries, which are optimized for testing influx into the hydrogels only. Long thin lines can also be written with the confocal by repeatedly moving the field of view and re-crosslinking, overlapping the new segment with the previous. This geometry could be useful in creating counter-propagating

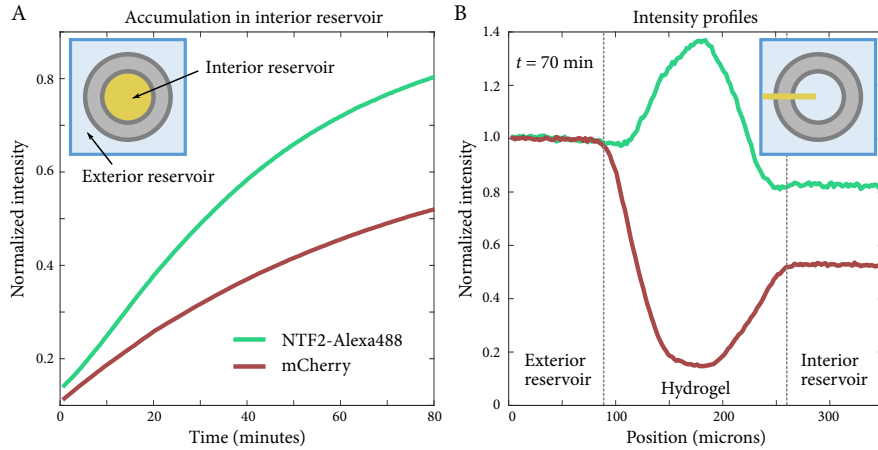


**Figure 3.17:** Sample (A) accumulation and (B) intensity profile plots for a  $50 \mu\text{m}$  thick confocal-crosslinked ring whose precursor contained  $10 \text{ mg/mL}$  FSFG. Intensity normalized to inlet reservoir. Inlet contains  $25 \mu\text{M}$  NTF2-Alexa488 and mCherry in PTB.

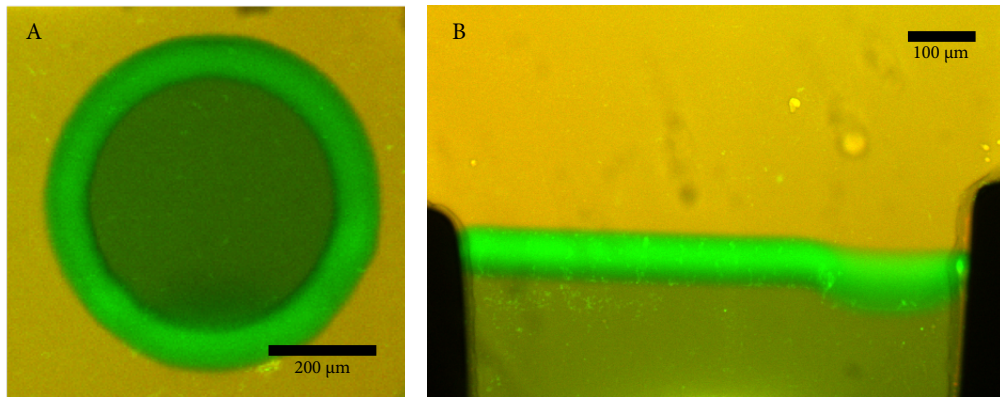
flow chambers with hydrogel windows.

Confocal crosslinking does not damage FSFG, as demonstrated in Fig. 3.18. Hydrogels were made using the precursor solution described above with the addition of  $10 \text{ mg/mL}$  FSFG-cys. After soaking in PTB buffer overnight, a mixture of  $25 \mu\text{m}$  each NTF2-Alexa488 and mCherry was added to the outer reservoir. After two hours of equilibration, the FSFG hydrogels showed a partition coefficient greater than one for NTF2-Alexa488 but smaller than one for mCherry. This indicates that FSFG is anchored into the gel and that NTF2-A488 is able to bind it.

Finally, Norland Optical Adhesive (NOA) can also be crosslinked using this method. Complicated flow chambers can be created, although it is labor-intensive and difficult to remove all of the excess NOA afterwards.

Despite the advantages of confocal crosslinking, several obstacles combined to ultimately make this method unusable for our purposes. The most serious problem was that of stray crosslinking. Areas outside of the defined region of interest were often unpredictably crosslinked, as can be seen in Fig. 3.16. Stray crosslinking outside of the rings is limited by rinsing the gels within 5 minutes of crosslinking, removing any excess precursor solution [133]. However, rinsing the chamber does not remove precursor solution from the ring's inner reservoir. Stray crosslinking in this reservoir is often more difficult to detect and more damaging to the experimental results. Figure 3.18 illustrates the problem: the ring has been equilibrated with NTF2-A488, which has preferentially entered the inner reservoir over mCherry. The concentration of NTF2-Alexa488 is, in fact, higher in

**Figure 3.18:** Images of confocal crosslinked hydrogels whose precursors contained 10 mg/mL FSFG. Reservoirs contain 20  $\mu$ M NTF2-Alexa488 and mCherry. (A) Hydrogel ring, likely with lightly-crosslinked inner reservoir. (B) Hydrogel bar separating large inlet and small outlet.



the inner than the outer reservoir, indicating that there is some low concentration of FSFG available in the inner reservoir for binding to NTF2. As the hydrogel was soaked in buffer overnight after crosslinking, any mobile FSFG remaining from the precursor solution has been removed, meaning that the remaining FSFG is most likely anchored into a lightly-crosslinked hydrogel that fills the inner reservoir. The presence of this gel alters the results of an equilibration experiment by artificially increasing the final NTF2 concentration in the inner reservoir.

With help from Danielle Konetski and Christopher Bowman, we attempted to address the stray crosslinking by adding a photoinhibitor to the precursor solution. The radical inhibitor 2,2,6,6-tetramethylpiperidine 1-oxyl (TEMPO) can be used in aqueous solution to limit crosslinking [129]. We tested the effect of the photoinhibitor using a precursor solution as described above with the addition of 0.5 mM TEMPO. While the edges of the resulting hydrogels became marginally sharper, stray crosslinking was still evident, especially in the interior reservoir.

Another significant problem was swelling and buckling of the hydrogels. Despite the hope that thinner hydrogels would swell and equilibrate more easily, buckling of the rings and lines was pervasive and difficult to predict (Fig. 3.16). Ring hydrogels in particular often developed minor leaks due to buckling. Despite many attempts to improve the swelling problem, the rings ultimately could not be used for selective transport experiments.

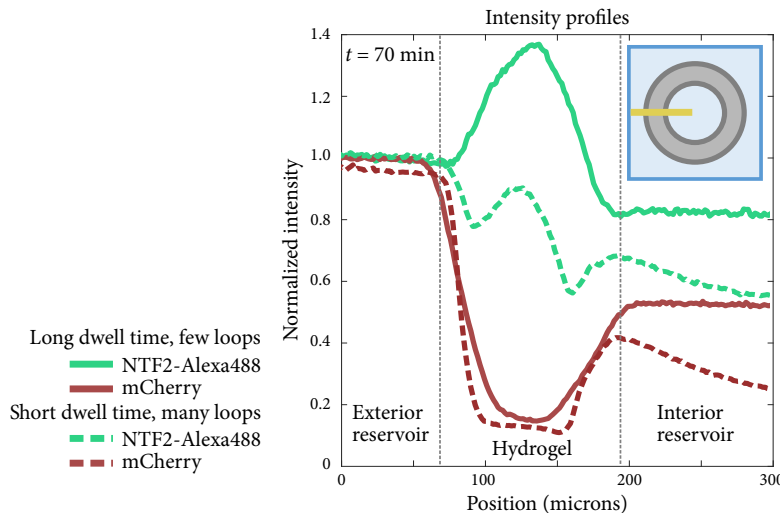


**Figure 3.19:** Effect of dwell time and loop number on edge-dip effect in equilibrated, confocal-crosslinked ring hydrogels. Precursor contained 10 mg/mL FSFG. Reservoirs contain 20  $\mu$ M NTF2-A488 and mCherry in PTB. Intensity profiles are shown for a hydrogel polymerized with  $t_{\text{dwell}} = 1/32$  and two loops (solid lines) and a hydrogel polymerized with  $t_{\text{dwell}} = 1$  and 64 loops.

One interesting feature of confocal crosslinking is the degree of control it affords over the illumination method. In the A1R's photobleaching mode, the 405 nm laser is raster-scanned over each pixel in the field of view. The shutter is toggled in order to illuminate only pixels within the predefined region of interest. The controls permit the laser intensity, dwell time at each pixel, and number of raster scan loops to be varied. The laser intensity was always kept at 100%, but changing the dwell time and loop number had a dramatic effect on the final properties of the hydrogel.

Generally speaking, a longer dwell time at each pixel and a low number of loops gave the best results. Figure 3.19 shows post-equilibration profiles for two hydrogel rings made with different illumination settings. Each gel received the same total illumination time, but in one case the dwell time was reduced 32-fold and the loop number increased by the same factor. In both cases, the hydrogels were soaked in PTB overnight and then challenged with 25  $\mu$ M NTF2-Alexa488 and mCherry. After 70 minutes, sufficient NTF2 had accumulated in the gel to make the differences between gels obvious. The low-dwell-time hydrogel accumulated less NTF2 and displayed noticeable dips in NTF2 accumulation at both its inner and outer edges. The edge-dip is reminiscent of those noted in the gels crosslinked by photomasking and the UV LED. While the cause of the dip is unclear, it may be the result of diffusion of fresh precursor solution into the edge region over the course of the crosslinking process. The fresh precursor then crosslinks, leading to a dense hydrogel edge that excludes NTF2 and mCherry. This hypothesis is consistent with the observation that a

longer dwell time and fewer raster loops largely eliminated the edge dip. With fewer raster loops, there is less opportunity for diffusion of uncrosslinked precursor solution into the gel edge. It should also be noted that the edge dip does not form when an entire droplet of precursor solution is crosslinked with the UV LED (i.e. no mask is used), further supporting the diffusion explanation. In any case, long dwell times and low loop numbers are clearly preferable with confocal crosslinking.

In conclusion, confocal crosslinking has a number of advantages over LED crosslinking, and a corresponding number of obstacles. Despite our desire to test selective transport using small hydrogel rings, we ultimately chose to use a much simpler hydrogel geometry and crosslinking method.

### 3.9 Dye-labeling and free dye

NTF2 must be labeled with a fluorescent dye before it can be used in diffusion experiments. Alexa Fluor 488 or fluorescein have both been used. When photobleaching is needed, as in the case of fluorescence recovery after photobleaching, fluorescein must be used, due to the extreme photostability of Alexa Fluor 488. There are several choices of labeling chemistry, including both NHS and SDP esters, which label the multiple exposed lysines of NTF2, and maleimide, which labels the cysteine of an engineered NTF2-cys. Both labeling chemistries result in bonds that eventually hydrolyze, cleaving the dye from the protein.

Free dye is a significant problem for diffusion experiments, since free dye ( $\sim 1$  kDa) diffuses much faster than dye bound to a protein and is experimentally identical. Non-negligible levels of free dye would give the impression that NTF2 is equilibrating significantly faster than it actually is. With help from Annette Erbse, Eric Verbeke and I tested several protocols to optimize the dye-labeling process and minimize the presence of free dye. We found that the maleimide-labeling chemistry is more stable, but in practice not as efficient as the ester-labeling protocol. Ultimately we chose to use esters for labeling. Detailed protocols are described in Appendix G. Extensive washing during the protein re-purification step is crucial, as is immediate aliquoting and freezing of the labeled protein. Labeled protein should be used within a few days of thawing.

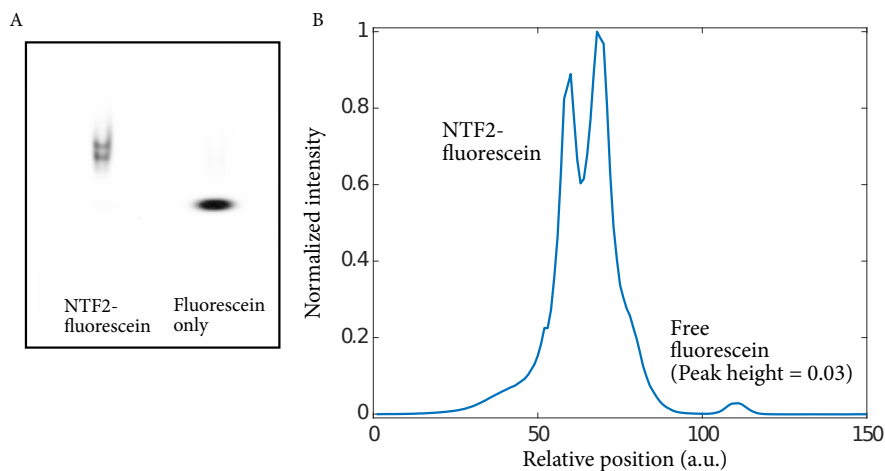


**Figure 3.20:** (A) Fluorescence Typhoon image native PAGE gel containing freshly-labeled NTF2-fluorescein sample and fluorescein sample. Free dye band is too dim to see. NTF2 shows monomer and dimer band. (B) Line scan of NTF2-fluorescein sample. The height of the free dye peak is 3% that of the labeled protein peak.

As soon as possible after a reaction, a BCA is performed to quantify the protein concentration in the labeled sample. Within 24 hours, the labeled protein is aliquoted and frozen. A small sample is thawed and run on a native PAGE gel along with a sample of free dye. The gel is then imaged using a Typhoon fluorescence imager and stained with Coomassie dye. The intensity of each fluorescence band in the labeled protein sample is estimated with a line scan. Figure 3.20 shows a representative batch of labeled protein. Typically, the free dye band is 1-3% the amplitude of the labeled-protein band. Finally, we measure the absorbance of the labeled protein at 494 nm to calculate the concentration of Alexa488. We compare this measurement with the protein measurement from the BCA to calculate a labeling efficiency. Typical labeling efficiencies are 50-70%, lower than the reported values of 90% or more.

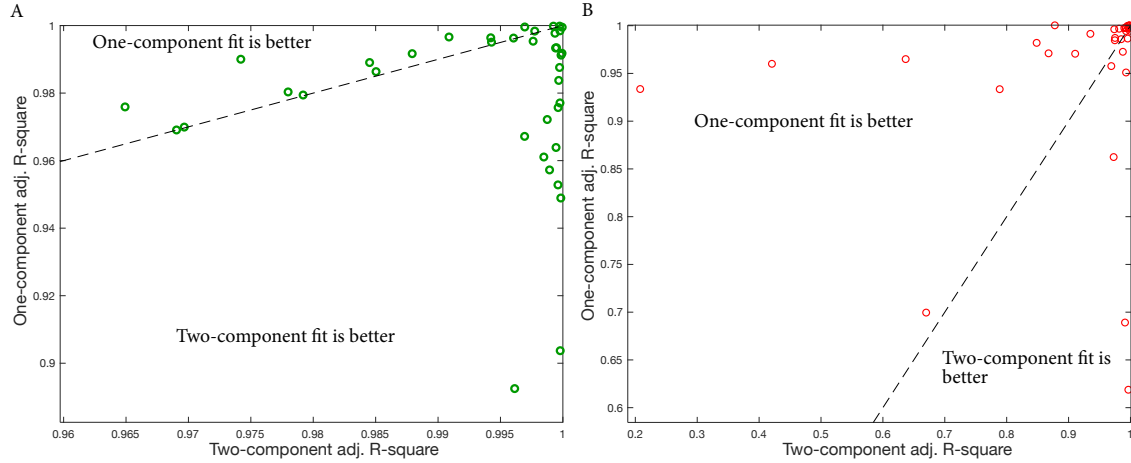
Mathematical analysis also suggests that free dye is minimal when the optimized protocol is used. A large dataset of accumulation curves was fit to either single or double exponentials and the resulting parameters and goodness of fit analyzed. While the accumulation curve should in fact be fit to an error function (Sec. 4.4.1), exponentials were used to simplify the analysis.

If there is no free dye, as in the case of the mCherry accumulation, the accumulated intensity  $I(t)$  can be approximated as

$$I(t) = A_1 \exp(-t/\tau_1) + C \quad (3.1)$$

with some amplitude  $A_1$ , equilibration lifetime  $\tau_1$ , and constant offset  $C$ . In this case, a non-zero

**Figure 3.21:** Comparison of adjusted R-square goodness-of-fit value for one- and two- component exponential fits for (A) NTF2 and (B) mCherry accumulation fits. Dotted line indicates no change between fits. Points in the upper left fit better to a single exponential while points in the lower right fit better to a double exponential.



value of  $C$  is likely due to background fluorescence. If, on the other hand, a sample contains a population of small, free dye molecules as well as large labeled protein, both populations will equilibrate at different rates, leading to an accumulated intensity of

$$I(t) = A_1 \exp(-t/\tau_1) + A_2 \exp(-t/\tau_2) + C \quad (3.2)$$

where each population has an equilibration lifetime as well as an amplitude related to its abundance in the sample.

I fit a collection of 43 accumulation experiments to both Eqns. 3.1 and 3.2. I compared the resulting parameters as well as the adjusted R-square value of each fit. Adding more parameters to the fit will always improve the fit, but the adjusted R-square is intended to account for the effect of adding more parameters to a model. A higher adjusted R-square therefore means a better fit.

The adjusted R-square values did not significantly improve when the mCherry data was fitted to a double instead of a single exponential (Fig. 3.21B). The adjusted R-square values changed by an average of  $-0.04 \pm 0.03$ . In addition, the lifetimes and amplitudes of each component of the two-component fit were apparently uncorrelated. Both results support the fact that there is no free dye in the red channel, since the only fluorescence is coming from mCherry.

On the other hand, the NTF2 fits did result in a noticeably higher (by  $0.019 \pm 0.006$ ) adjusted R-square value on average when the double-exponential fit was used (Fig. 3.21A). Strikingly, the two components sorted themselves into two categories: a low-amplitude, short-lifetime component and a high-amplitude, long-lifetime one. The most straightforward interpretation is that the low-amplitude component is the free dye, which should be present in low amounts and equilibrate much more rapidly than labeled protein, thanks to its small size.

The median amplitude of the free-dye signal was 1.2% that of the labeled-protein signal, using a sample of 43 experiments, a result comparable to that seen in Fig. 3.20. The median free-dye equilibration lifetime was 50 minutes, as compared to approximately 2000 minutes for the labeled-protein lifetime. These results confirm that the new, more stringent dye-labeling protocol is successful in removing almost all free dye from the labeled-protein sample, and that the hydrolysis of the dye is negligible on the time scale of the experiment and enforced shelf life of the labeled protein.

### 3.10 Discussion

We met with many obstacles during the process of creating hydrogels suitable for protein separation. Ultimately, we were forced to compromise on many properties that would be ideal in these gels, such as an average pore size that permits the diffusion of karyopherins and hydrogel geometries which allow direct measurements of selectivity. However, we made significant progress in many areas. Experimental reproducibility improved markedly as the hydrogel precursor recipes were refined and the flow chambers optimized. The flow chambers in particular underwent extensive revision; their final form as used in Chapter 4 was approximately an order of magnitude quicker to fabricate than, and remained watertight over timescales many times longer than, our original design. Strategies were found to minimize the edge effects of polymerization and to control the hydrolysis of dye-labeled proteins. Much of this work is applicable to other questions of protein separation by hydrogels and may be useful in the future.

Perhaps the most important lesson of the design process was the virtue of simplicity. A

number of fairly complex plans for improving the hydrogel properties are described in the above chapter, all of which had a reasonable chance of success but none of which proved workable. Our greatest success came from leveraging the simplest protocols, hydrogel geometries, and experimental conditions. Even without ideal properties, the hydrogel nuclear pore mimics that emerged from this design process are well-suited as a platform for probing bound-state diffusion in biofilters.

## Chapter 4

### Bound diffusion measurements

Bound-state mobility - the ability of a macromolecule to diffuse while binding to its environment - was the key parameter in our simplified model of selective transport in Chapter 2. After several false starts, we designed an experimental system to investigate bound diffusion in biomaterials. This hydrogel nuclear pore mimic, as described in Chapter 3, is inspired by the nuclear pore but does not attempt to exactly reproduce selective nuclear transport. Instead, it is designed to provide a method of measuring the effect of model parameters such as binding valency, tether length, and tether concentration on bound diffusion.

Diffusion of transport factors and inert proteins was measured within the Nup-filled hydrogels using two main methods: by quantifying the influx of these proteins into the hydrogels, and by measuring fluorescence recovery after photobleaching (FRAP) using hydrogels equilibrated with fluorescent proteins. FRAP relies on the gradual redistribution of fluorophores after patterned photobleaching. After a small portion of the hydrogel is bleached, the bleached spot gradually exchanges with the non-bleached fluorophores outside, and the average fluorescence intensity within the bleached spot recovers. The recovery lifetime can be used to determine the fluorophore's diffusion constant, and the final recovered intensity as compared to the intensity outside the bleach spot can be used to determine the mobile fraction of fluorophore. Many models of FRAP exist, including some that take binding into account [142–145]. We made use of several models of varying degrees of complexity.

We calculated bound diffusion constants for NTF2 in hydrogels containing FSFG concat-1

(with six binding motifs) or FSFG concat-2 (12 binding motifs, twice as long as FSFG concat-1) and found non-zero bound diffusion in both cases. Both tether lengths led to bound diffusion that was consistent with that predicted by our tethered-diffusion model.

## 4.1 Experimental parameters

Our reaction-diffusion model of selectivity is controlled by a relatively small number of parameters. Ideally, we would like to vary all of these experimentally in order to verify the model's predictions. In reality, most are highly difficult to alter in a well-controlled way. Of the model's parameters, the contour length  $L_C$  of the tethered Nups is the simplest to control. Varying this contour length will vary the bound diffusion coefficient  $D_B$  according to Eqn. 2.22. This section discusses  $L_C$  and the other experimental parameters used in our hydrogel nuclear pore mimics.

### 4.1.1 Nup contour length and valency

The most straightforward way to vary  $D_B$  is to change the contour length of the Nups that are anchored into the hydrogel. To that end, we compared hydrogels containing the constructs FSFG concat-1 and FSFG concat-2 (Sec. 3.4, Appendix F). These Nup fragments have  $L_C = 50$  nm and 100 nm, respectively. Given the parameters described below, the bound diffusion constant should increase by roughly 40% from FSFG concat-1 to FSFG concat-2. In addition to differing lengths, the FSFG concat-1 and concat-2 differ in their number of binding sites, with six and twelve respectively.

### 4.1.2 Binding affinity of NTF2 and FSFG

Although bound diffusion is the key parameter from our reaction-diffusion model of selectivity, the kinetic parameters of off-rate  $k_{\text{off}}$ , on rate  $k_{\text{on}}$ , and dissociation constant  $K_D = k_{\text{off}}/k_{\text{on}}$  are also important. These parameters are surprisingly difficult to measure, yielding values between 10 nM and 10  $\mu\text{M}$  depending on the experimental conditions. We estimated the dissociation constant for NTF2 and FSFG concat-1 using isothermal titration calorimetry (ITC). The heat of injection

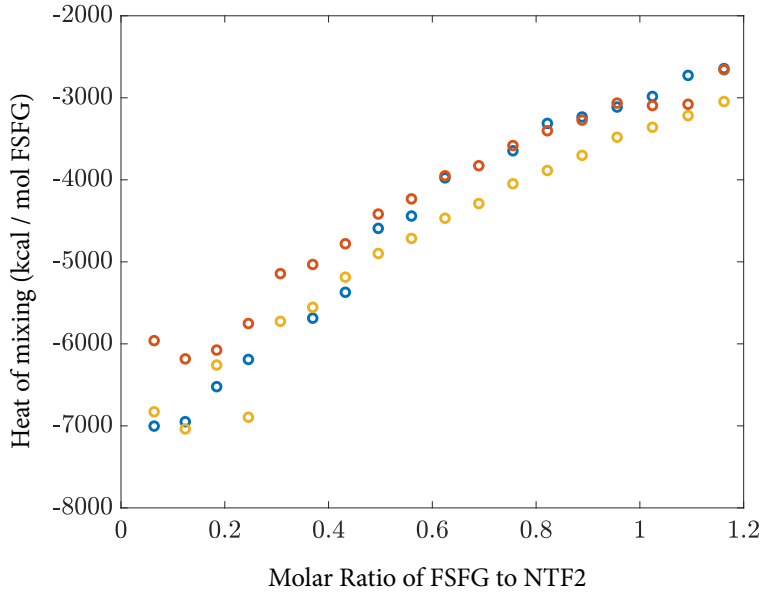


**Figure 4.1:** Isothermal calorimetry titration curve: heat of injection vs. molar ratio of FSFG to NTF2. Fits are questionable but multiple runs suggest  $K_D \approx 200 \mu\text{M}$ .

was recorded as FSFG was titrated into a stock of NTF2. While the resulting titration curves had low signal-to-noise and did not reach saturation, they clearly indicated binding (Fig. 4.1). Simple fits are likely inaccurate, given the high degree of multivalent binding, but may provide an order-of-magnitude estimate of the affinity. Several ITC curves agree on a dissociation constant of  $K_D \approx 200 \mu\text{M}$ , lower than that measured by other studies. Using ITC and NMR, the Rout lab measured a single FSFG motif to bind to NTF2 with  $K_D \approx 4 \text{ mM}$ . Addition of more motifs lowered the  $K_D$  until it reached an asymptotic value just under 1 mM when six motifs or more were present [27]. Similarly weak values of  $K_D \approx 1\text{-}7 \text{ mM}$  per single FSFG motif were predicted through NMR, simulation, and stopped-flow fluorescence anisotropy [26]. Due to the twin difficulties of varying  $K_D$  in a controlled way and accurately measuring its value, we did not attempt to experimentally alter this parameter.

Assuming the tethered Nup concentration to be 1 mg/mL within the hydrogels, we estimate a  $K_D$  of around  $30 \mu\text{M}$  for FSFG concat-1 and  $18 \mu\text{M}$  for FSFG concat-2 using the partition coefficients of NTF2 and mCherry (Sec. 4.3.2). This value is lower than expected and may result from an underestimation of the tethered protein concentration. If instead we use the maximum possible tethered Nup concentration of 10 mg/mL FSFG concat-1 and 20 mg/mL FSFG concat-2, we estimate  $K_D$  of  $300 \pm 80 \mu\text{M}$  for FSFG concat-1 and  $360 \pm 40 \mu\text{M}$  for FSFG concat-2. Ideally,

a transport factor - Nup pair with  $K_D \approx 1 \mu\text{M}$  would have been used to maximize selectivity.

Only the ratio  $K_D/N_t$  is necessary for determining the bound diffusion constant, and it can be estimated using the partitioning of transport factors and inert proteins into the FSFG hydrogels (Sec. 4.3.2). Unsuccessful attempts to vary the dissociation constant included expressing the ubiquitin-associated (UBA) domain of the mRNA exporter Mex67 as a Nup-binding domain in GFP fusion proteins. In principle, varying numbers of this small ( $<10 \text{ kDa}$ ) domain could be added to GFP to explore the effect of varying binding affinity and valency in transport factors. The constructs GFP-UBA, GFP-UBAx2, and GFP-UBAx3 were created by Eric Verbeke, but did not express and/or bind well.

#### 4.1.3 Quantifying concentration of tethered Nups

Another potentially-tunable parameter of the bound-diffusion model is  $N_t$ , the total concentration of tethered Nups. It is straightforward to control the Nup concentration in the hydrogel precursor solution by resuspending a known mass of lyophilized protein. FSFG concentrations up to  $\sim 50 \text{ mg/mL}$  can be resuspended. However, it is much more difficult to determine how much protein was tethered to the hydrogel upon crosslinking.

BCA protein quantitation assays were used to place upper bounds on  $N_t$ . Two methods were attempted: incubating the hydrogel itself in the working reagent, and soaking the hydrogel in a known volume of buffer and testing the concentration of FSFG released. When applying the first method, the hydrogel was first soaked to remove excess precursor solution and thoroughly rinsed. The gel was placed into a 96-well plate and buffer added until the appropriate sample volume was reached. A standard BCA protocol was then followed. Upon incubation with the working reagent, the hydrogels turned purple, as expected. Standard absorption measurements and processing yielded an estimate of  $0.5 \text{ mg/mL}$  tethered FSFG-concat 1; this should be taken as an approximate value only. The second method, that of soaking hydrogels and measuring the FSFG released, placed a similarly-low upper bound on tethered FSFG concentration. Hydrogels made with  $5 \mu\text{L}$  of precursor solution were soaked in  $45 \mu\text{L}$  buffer to equilibrate, diluting any

remaining free FSFG to a tenth of its original value. The buffer was then measured to have a concentration of 1.0 mg/mL FSFG, implying a tethered FSFG concentration of < 1 mg/mL.

The concentration of Nups within the pore may reach 100 mg/mL, depending on how compact the disordered FG Nups are. The low concentration of tethered Nups that we were able to achieve is therefore a major barrier to selectivity. It is likely that the disordered nature of FSFG makes the labeled end less accessible to the hydrogel scaffold than would be the case for an ordered protein. In an effort to overcome this limitation, we tested other linkers and conjugation methods. We conjugated the FSFG-cys to PEG-diacrylate of varying lengths (700 Da and 10 kDa), to multi-armed PEG-diacrylate, and to maleimide-PEG-acrylate. The decrease in free cysteines following the reaction was verified using Ellman's reagent (Appendix D), indicating that the labeling was successful. However, there was no noticeable difference in transport factor partitioning into these hydrogels.

#### 4.1.4 Free diffusion constant

The final tunable parameter from the binding-diffusion model is the diffusion constant of the transport factor when it is not bound to a Nup, the free diffusion constant  $D_F$ . Decreasing  $D_F$  is predicted to increase a material's selectivity while decreasing the absolute flux of transport factor (Figs. 2.4, 2.5). The free diffusion is predominantly determined by the protein's size and the viscosity of the solution, according to the Stokes-Einstein equation  $D = k_B T / 6\pi\eta R$ , where  $k_B T$  is the thermal energy,  $\eta$  the solution viscosity, and  $R$  the particle radius. The solution viscosity could potentially be increased using a viscous additive such as glycerol; however, these attempts appeared to interfere with the binding of NTF2 and FSFG.

The diffusion of the non-binding 30 kDa protein mCherry was used as a proxy for the free diffusion of similarly-sized NTF2 within the FSFG hydrogels.

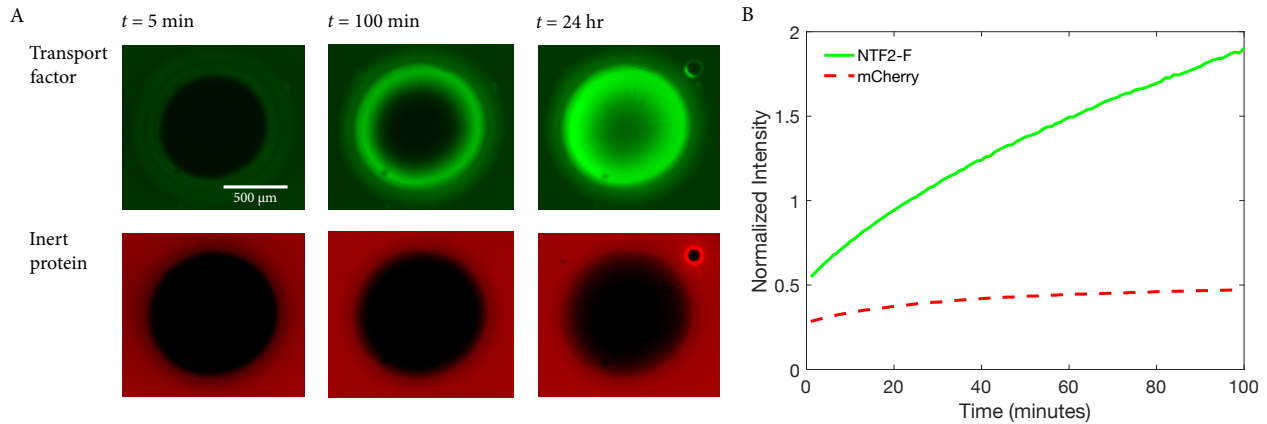
## 4.2 Experimental procedures

The nuclear pore mimics in this dataset were designed with the lessons of Chapter 3 in mind. They consist of hydrogels with the largest average pore size and simplest geometry: a single microliter-scale droplet. While this geometry does not allow for direct measurements of selectivity, the in-gel diffusion constants of both NTF2 and mCherry can be determined and bound diffusion calculated. Two types of experiments were carried out: influx experiments, in which the entry of fluorescent proteins into the hydrogels was monitored, and FRAP experiments, in which a portion of an equilibrated hydrogel was bleached and the recovery observed. Both experiments provide a measurement of the proteins' diffusion constants. These experiments were performed at CU's BioFrontiers Advanced Light Microscopy Core Facility. Thanks go to Joseph Dragavon for much assistance with the microscopy.

### 4.2.1 Hydrogel preparation

Detailed precursor solution recipes are given in Appendix E. For the dataset analyzed in this chapter, we used a precursor solution containing 6% acrylamide and 2 mM LAP as a photoinitiator. FSFG constructs were conjugated to bisacrylamide via their free thiol and lyophilized. Lyophilized FSFG-bis was then resuspended in potassium transport buffer (PTB; 150 mM KCl, 20 mM HEPES, 2 mM MgCl<sub>2</sub>), allowed to sit at room temperature for at least 20 minutes, and added to the precursor solution. After the precursor solution was thoroughly mixed, it was degassed in a vacuum desiccator for 10 minutes and immediately pipetted into a disassembled 400-μm-thick PDMS gasket chamber (Sec. 3.3). Drops between 0.5 and 2 μL were carefully pipetted onto the plastic slide and the chamber assembled around the drops. Typically, each chamber measured a few centimeters on a side and contained a control gel with no Nups as well as one or more Nup-filled gels. The chamber was then illuminated as uniformly as possible with 365 nm light at approximately 200 mW/cm<sup>2</sup> with a ThorLabs M365 LP1 LED. Condensation around the gels resulted from the condensation polymerization reaction, indicative of crosslinking. The chamber was immediately rinsed with at

**Figure 4.2:** Influx image series. (A) A hydrogel whose precursor contained 10 mg/mL FSFG concat-2 was challenged with 20  $\mu$ M NTF2-F and mCherry. The hydrogel shows selective entry of NTF2-F and has largely equilibrated within 24 hours. (B) Fluorescence intensity within hydrogel over time, normalized to reservoir concentration.



least 100  $\mu\text{L}$  of PTB, filled with fresh PTB, and sealed with a PDMS slab and clingwrap. The gels were left to soak at 4°C for at least 12 hours so that any remaining precursor solution and protein could equilibrate with the surrounding reservoir, further reducing the concentration remaining in the gel 10- to 20-fold.

#### 4.2.2 Influx of transport factor and inert protein

After soaking in buffer, the buffer solution was removed by pipette or wicking with a Kimwipe and a fluorescent reservoir solution added. Aspirating the chamber was avoided if possible, as it sometimes disturbed the seal between the gel and the chamber. The reservoir solution contained 20  $\mu\text{M}$  each freshly-thawed NTF2-fluorescein (NTF2-F) and mCherry in PTB. The chamber was resealed after adding the solution. If no influx experiment was planned, the gels were then allowed to equilibrate for 24 hours before FRAP was performed.

When influx experiments were run, they began as soon as possible after loading the reservoir solution. Videos were recorded at 4x magnification on an Olympus IX-81 widefield microscope using FITC (464-500 nm excitation / 516-556 nm emission) and TRITC (532-544 nm excitation / 573-613 nm emission) filter cubes. Exposure times were typically 30-100 ms with 3-8 dB gain.

Videos consisted of 120 frames at one frame per minute. Minimal photobleaching took place over the course of these experiments, as confirmed by tracking the average reservoir intensity over time. After the influx experiment, the chamber was usually stored for equilibration 4°C, protected from light, and a FRAP experiment performed the following day.

Influx experiments on hydrogels containing FSFG show a bright wavefront of NTF2-F slowly progressing into the gel, while mCherry remains largely excluded (Fig. 4.2). This indicates binding of FSFG to NTF2-F but not to mCherry . As expected, mCherry equilibrates more rapidly than does NTF2-F, due to the lack of binding. Influx experiments were analyzed as described in Sec. 4.4.

#### **4.2.3     Fluorescence recovery after photobleaching**

FRAP is typically performed using a confocal microscope, but we were able to bleach the hydrogels using an Olympus IX-81 widefield microscope. The widefield was preferable because the greater depth of field allowed for thicker hydrogel samples, which were easier to fabricate and manipulate. As described above, the hydrogel was first allowed to equilibrate with 20  $\mu$ M NTF2-F and mCherry in PTB. A reference image was taken at 4x magnification in both fluorescence channels. A circular region of the hydrogel approximately 300  $\mu$ m in radius was then photobleached by taking a five-second exposure at 40x magnification using a DAPI (352-402 nm excitation / 417-477 nm emission) filter cube. Following the bleach, the 4x objective was rapidly returned and a time series recorded. Typical series consisted of 15-30 frames taken as rapidly as possible (5-10 s per frame), followed by 30-60 frames taken at a slower rate (1-2 minutes per frame). Total experiment time was 1-4 hours. Typical exposure times were 10 ms for NTF2-F and 40 ms for mCherry, both with a gain of 3 dB.

In order to increase throughput, up to three FRAP experiments were run concurrently by sequentially bleaching and then imaging several locations within a single chamber. This led to a maximum delay time of approximately 35 s between the end of the bleach segment and the beginning of the time series. Delay times were recorded and taken into account in the data processing. Figure 4.4 shows a representative series of images pre- and post-FRAP for both NTF2-F and

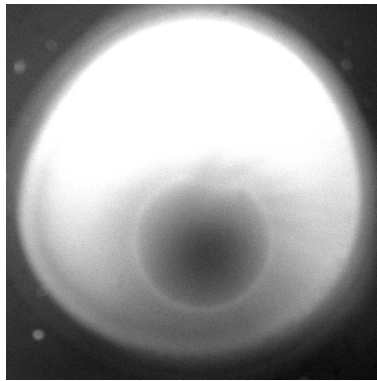


**Figure 4.3:** Bright NTF2-F ring surrounding photobleach spot, 70 minutes after bleaching. This ring often developed in FSFG concat-1 gels. Photo-bleach mask was chosen to be slightly smaller than the ring. FITC channel shown only, with contrast adjusted to make the ring easily visible.

mCherry.

Despite allowing 24 hours for equilibration, the fluorescence intensity across the hydrogel was not always uniform at the beginning of a FRAP experiment. This could be due to slow diffusion into the hydrogels, or to inhomogeneous crosslinking. The center of a hydrogel is more likely to be tightly crosslinked than the edges, as swelling is most inhibited at the center. Gels which were too inhomogeneous to display a clear bleach spot were discarded, but many nonuniform hydrogels were used in the final dataset, with the lack of equilibrium addressed in the data analysis (Sec. 4.5). Smaller hydrogels ( $0.5 \mu\text{L}$  of precursor solution) equilibrated more readily, at the cost of increasing the effect of fluorescent protein exchange with the reservoir, since the bleach spot then covered a significant fraction of the hydrogel. This effect was also taken into account during data analysis.

Many of the FSFG concat-1 hydrogels showed an unusual bright ring in the NTF2-F channel around the photobleach spot which developed slowly after bleaching. Figure 4.3 shows an example. The ring is presumably due to photodamage by bleaching, but it is not clear why the edge of the bleach spot would exhibit increased NTF2-F binding. When hydrogels showed this bright ring, care was taken when drawing the bleach spot mask to exclude the ring entirely.

### 4.3 Analysis of steady-state hydrogel properties

The first step in analyzing the experimental data is to extract key parameters of the hydrogel itself. Both the influx and FRAP experiments rely on steady-state properties of the hydrogel as well as time-dependent ones. These properties include the partition coefficients of transport factors

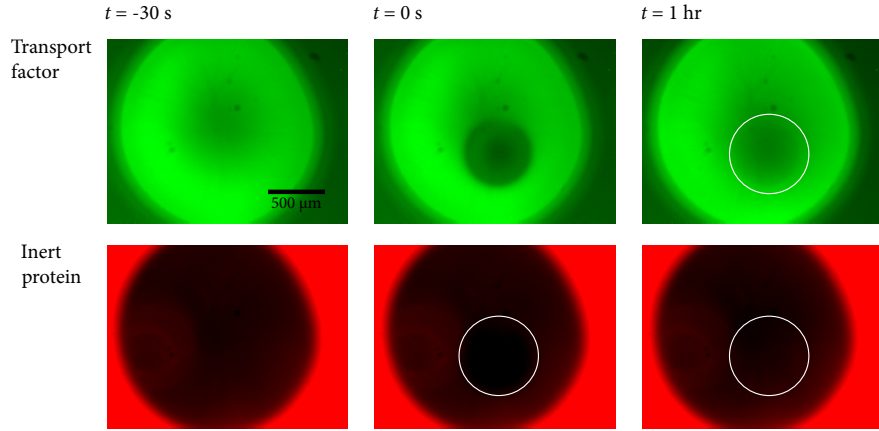


**Figure 4.4:** FRAP image series. NTF2-F (top, green) and mCherry (bottom, red) bleaching and recovery shown separately. Hydrogel precursor contained 10 mg/mL FSFG concat-1. Reservoir contained 20  $\mu\text{M}$  each NTF2-F and mCherry.

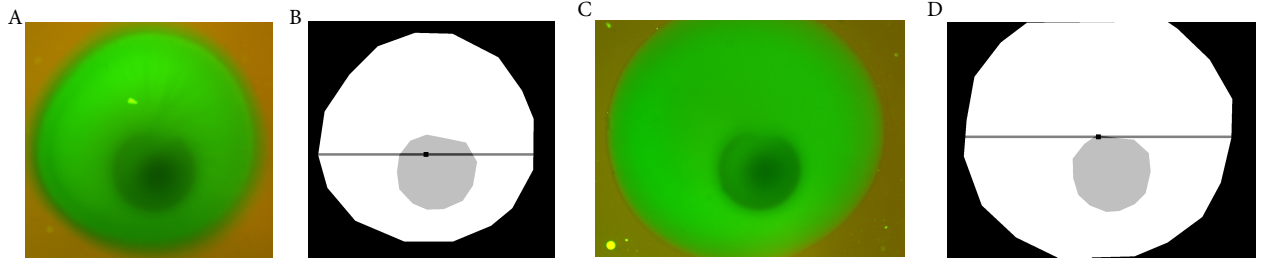
and inert proteins, as well as some properties dependent on the geometry of the hydrogel.

#### 4.3.1 Gel dimension estimates

Although the hydrogels were not perfectly circular, all analysis treated them as circular or nearly so. In total, the analysis made use of a gel's radius, center, perimeter, and area. I began by manually defining two masks: one that covered the entire gel, and one that covered only the bleach spot (Fig. 4.5). The gel area was calculated by summing all of the pixels in the gel mask and scaled using the  $1.58\text{ }\mu\text{m}$  per pixel scale of the Olympus 4x objective. The perimeter was calculated using Matlab's `bperim` function, which takes a binary mask and returns a mask whose only nonzero entries are the original mask's perimeter. Summing over these pixels and scaling provides the gel perimeter. It should be noted that in some cases the full area of the gel was not within the field of view. In these cases, sometimes the partial area in the field of view was used as the area estimate, and sometimes I embedded the gel image in a larger frame and estimated the remaining area when drawing the mask. The following sections indicate which method was used and the mathematical reasoning for the method. However, all perimeter calculations were performed with the estimated full area.

The hydrogel radius was estimated taking the diameter to be the widest row of the gel mask. The widest row was also used to set the  $y$ -coordinate of the gel center, with the  $x$ -coordinate taken to be midway along the non-zero values for that row. As seen in Fig. 4.5, this is a quick and

**Figure 4.5:** Sample hydrogel masks with radius and center calculations. (A) An equilibrated 0.5- $\mu\text{L}$  hydrogel containing FSFG concat-1, immediately post-bleach. (B) The corresponding hydrogel mask (white), bleach spot mask (light gray), calculated gel diameter, and calculated gel center. (C)-(D) A 1- $\mu\text{L}$  hydrogel, showing that the gel is not entirely within the field of view.



relatively crude method, but in almost all cases it works reasonably well. An advantage of this method is that it works even for hydrogels which do not fit in the vertical field of view.

#### 4.3.2 Partition coefficients and fraction of time spent bound

The concentration of NTF2 and mCherry in a flow chamber’s reservoir can be directly controlled, but the partitioning of a protein into the hydrogel depends on the degree to which the presence of the gel sterically excludes the protein, as well as on binding interactions between the gel and protein. When a transport-factor-sized inert protein is present to control for the steric effects, information about the transport factor’s dissociation constant and fraction of time spent bound can be extracted from knowledge of the partition coefficient  $\gamma$ . In particular,  $p_B$ , the fraction of time spent bound, must be calculated in order to determine the bound diffusion coefficient.

As shown in Fig. 4.6A, the partition coefficient is the ratio of a protein’s concentration in a well-equilibrated hydrogel to that in the surrounding reservoir. This quantity is calculated by dividing the average intensity of the gel by that of the portion of the reservoir within the field of view (Fig. 4.6B). If the gel is not fully equilibrated, the partition coefficient can be estimated using a line scan through the reservoir and gel, though this will likely underestimate the true value.

When the system is in chemical equilibrium, the concentration of free transport factor ( $T$ ), free Nup ( $N$ ), and transport factor - Nup complex ( $C$ ) is related to the dissociation constant  $K_D$  by

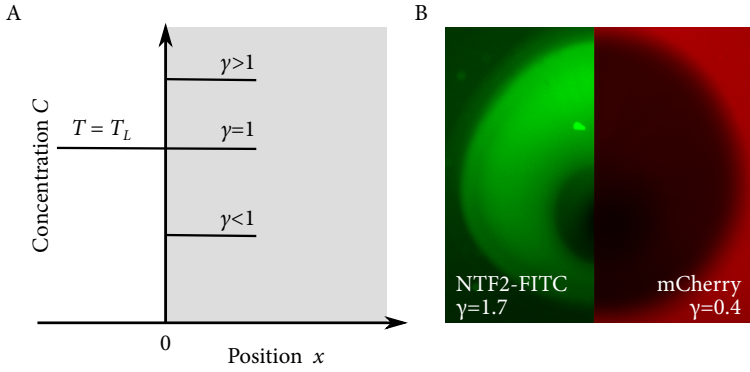


**Figure 4.6:** Partitioning of NTF2 and mCherry into FSFG hydrogel. (A) Partition coefficient  $\gamma$  depends on whether the hydrogel excludes or binds protein. (B) Equilibrated FSFG concat-1 hydrogel (made with 10 mg/mL protein) showing partitioning of  $T_L = 20 \mu\text{M}$  each NTF2-F and mCherry. Contrast adjusted for ease of viewing.

$K_D = NT/C \approx N_t T/C$  in the linear approximation  $N \approx N_t$ . The total tethered Nup concentration, both free and bound, is the constant  $N_t$ . The fraction of transport factors that are bound is then given by

$$p_B = \frac{C}{C + T} = \frac{C}{C + \frac{CK_D}{N_t}} = \frac{1}{1 + \frac{K_D}{N_t}} \quad (4.1)$$

To relate this expression to measurable quantities, write the protein concentrations within the hydrogel in terms of their partition coefficients. The concentrations of the inert protein and the transport factor in the reservoir are equal and given by  $T_0$ . If  $\gamma_T$  is the partition coefficient of the transport factor and  $\gamma_I$  that of the inert protein, then the transport factor concentrations can be expressed as

$$T = \gamma_I T_0 \quad (4.2)$$

$$C = T_T - T = \gamma_T T_0 - \gamma_I T_0 \quad (4.3)$$

The total transport factor concentration within the gel is  $T_T = T + C$  and is a constant. Therefore, within the gel, the chemical equilibrium condition can be expressed as

$$\frac{K_D}{N_t} = \frac{T}{C} = \frac{\gamma_I T_0}{\gamma_T T_0 - \gamma_I T_0} = \frac{\gamma_I}{\gamma_T - \gamma_I} \quad (4.4)$$

Combining Eqns. 4.1 and 4.4, the bound probability can be expressed in terms of the partition coefficients as

$$p_B = \frac{1}{1 + \frac{K_D}{N_t}} = \frac{1}{1 + \frac{\gamma_I}{\gamma_T - \gamma_I}} = 1 - \frac{\gamma_I}{\gamma_T} \quad (4.5)$$

### 4.3.3 Bound-diffusion calculation

Once the observed diffusion constants for NTF2 and mCherry have been calculated, along with the fraction of time spent bound  $p_B$ , the bound diffusion is given straightforwardly by the weighted average

$$D_{\text{obs,TF}} = p_B D_B + (1 - p_B) D_F \quad (4.6)$$

This result assumes Fickian diffusion. In reality the diffusion will be slightly anomalous due to binding and the presence of the hydrogel. However, the binding is highly transient and the hydrogel relatively permeable to proteins of the size of NTF2 and mCherry (Sec. 3.6).

Taking the free diffusion coefficient of the transport factor to be approximately equal to the observed diffusion of the inert protein ( $D_F = D_{\text{obs,I}}$ ), the bound diffusion coefficient of the transport factor is

$$D_B = \frac{D_{\text{obs,TF}} - (1 - p_B) D_{\text{obs,I}}}{p_B} \quad (4.7)$$

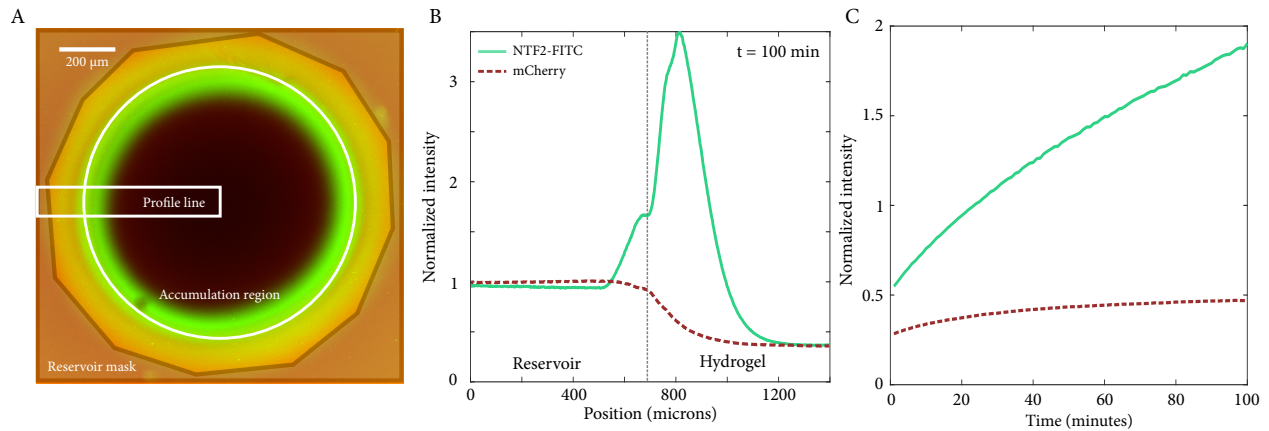
Note that neither the dissociation constant or the total Nup concentration need to be measured independently in order to calculate the bound diffusion constant.

## 4.4 Influx analysis

After recording a time series of fluorescent protein influx into a hydrogel, diffusion constants can be estimated using either a plot of the intensity profile across the gel or a plot of total accumulation within the gel. Figure 4.7 shows an example of each plot. The intensity within the gel is normalized to the average intensity of the reservoir, as calculated using the mask shown in Fig 4.7A. Therefore, each profile trace begins at  $I = 1$  within the reservoir and either dips or rises to the partition coefficient value within the gel. As the gels are not equilibrated, much of the gel interior shows only background fluorescence. Likewise, the average intensity within the hydrogel trends towards the partition coefficient but does not reach it on the time scale of an average experiment.

Analysis of the accumulation and profile curves used the solutions to the diffusion equation described by Mortensen, Okkels, and Bruus [146]. This method assumes that the edge of a

**Figure 4.7:** Intensity profiles and total accumulation within hydrogel as determined from influx time series. (A) Image of an FSFG concat-2 hydrogel whose precursor contained 10 mg/mL protein. Reservoir contains 20  $\mu$ M NTF2-F and mCherry in PTB. Reservoir mask is shown (red polygon) as well as accumulation area and rectangle over which the profile averaging was performed. (B) Normalized intensity profiles as calculated using the box in (A). (C) Normalized average intensity within hydrogel.



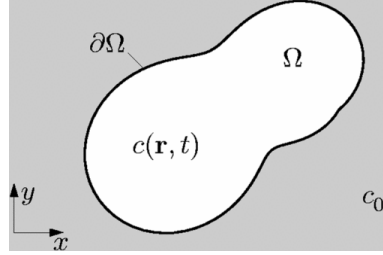


**Figure 4.8:** Geometry used to solve diffusion equation in [146]. The reservoir concentration  $c_0$  fixed the concentration at the edge of the region  $\Omega$ . The concentration  $c(\mathbf{r}, t)$  is determined within  $\Omega$  as a function of position and time.

nearly-circular two-dimensional region is held at a fixed concentration while the interior equilibrates (Fig. 4.8). These boundary conditions correspond to an infinite fluorophore reservoir. Given that our reservoirs are 10-20 times larger than the hydrogel volume, this is a reasonable assumption. In a slight modification, we allow for an arbitrary partition coefficient  $\gamma$  by taking the fixed boundary concentration  $c_0$  to be  $\gamma c_0$ , where  $c_0$  is the fluorescent protein intensity in the reservoir. The assumption of near-circularity is also reasonable.

The two most troublesome restrictions of the Mortensen equations are Fickian diffusion and the homogeneity of the hydrogel. As discussed in Sec. 2.3, the presence of the hydrogel meshwork and binding make diffusion within the hydrogels slightly anomalous. Additionally, despite the improvements made in Chapter 3, the hydrogels probably have nonuniform density to some degree, with the centers most likely being slightly denser than the edges due to differential swelling. The effects of swelling and non-uniform thickness are greatest at the gel edge. Unfortunately, the points at the edge of the gel and earliest in the experiment are the most important to the following fits. As a result, the diffusion constants extracted using the profile and accumulation plots are not reliable. The analysis is presented below nonetheless, as a similar approach was taken in analyzing the FRAP experiments.

#### 4.4.1 Profile analysis

Mortensen et al first define a characteristic timescale for equilibration  $\tau = (\mathcal{A}/\mathcal{P})^2(\pi/4D)$  where  $\mathcal{A}$  and  $\mathcal{P}$  are the area and perimeter, respectively, of the region  $\Omega$ . For a circle  $\mathcal{A}/\mathcal{P} = a/2$ , but this ratio was numerically calculated for the hydrogels (Sec. 4.3.1). For times  $t \ll \tau$ , the

concentration profile as a function of the distance  $r$  from the gel center can be approximated as

$$c(r, t) = c_0 \operatorname{erfc} \left( \frac{r}{\sqrt{4Dt}} \right) \quad (4.8)$$

where  $D$  is the diffusion constant.

Coincidentally, the typical duration of an influx experiment was approximately  $\tau$ , making the short-time approximation questionable throughout most of the time series. We attempted to fit the intensity profile (Fig. 4.9) and obtained fits with fairly low error but with unreliable fit parameters. In addition to the issues of timescale, it was often difficult to determine where the gel edge was located, as well as the value of the partition coefficient. Given these problems, it is not surprising that fits at successive timepoints yielded incompatible values of diffusion constant for both mCherry and NTF2. A similar problem prevented the use of diffusion constants obtained from intensity fits at a fixed position over time (Fig. 4.10).

A more exact solution for  $c(r, t)$  can be written if the gel is assumed to be circular. Mortensen et al quantify the error introduced by small deviations from circularity and find it to be small. Assuming a circular gel, the concentration profile at an arbitrary time  $t$  is given by

$$\frac{c(r, t)}{T_0} = 1 - 2 \sum_{n=0}^{\infty} \frac{J_0(\alpha_n r)}{\alpha_n a J_1(\alpha_n a)} \exp(-\alpha_n D t) \quad (4.9)$$

where  $a$  is the gel radius and  $(\alpha_n a)$  is the  $n$ th zero of the Bessel function of the first kind  $J_0$ .

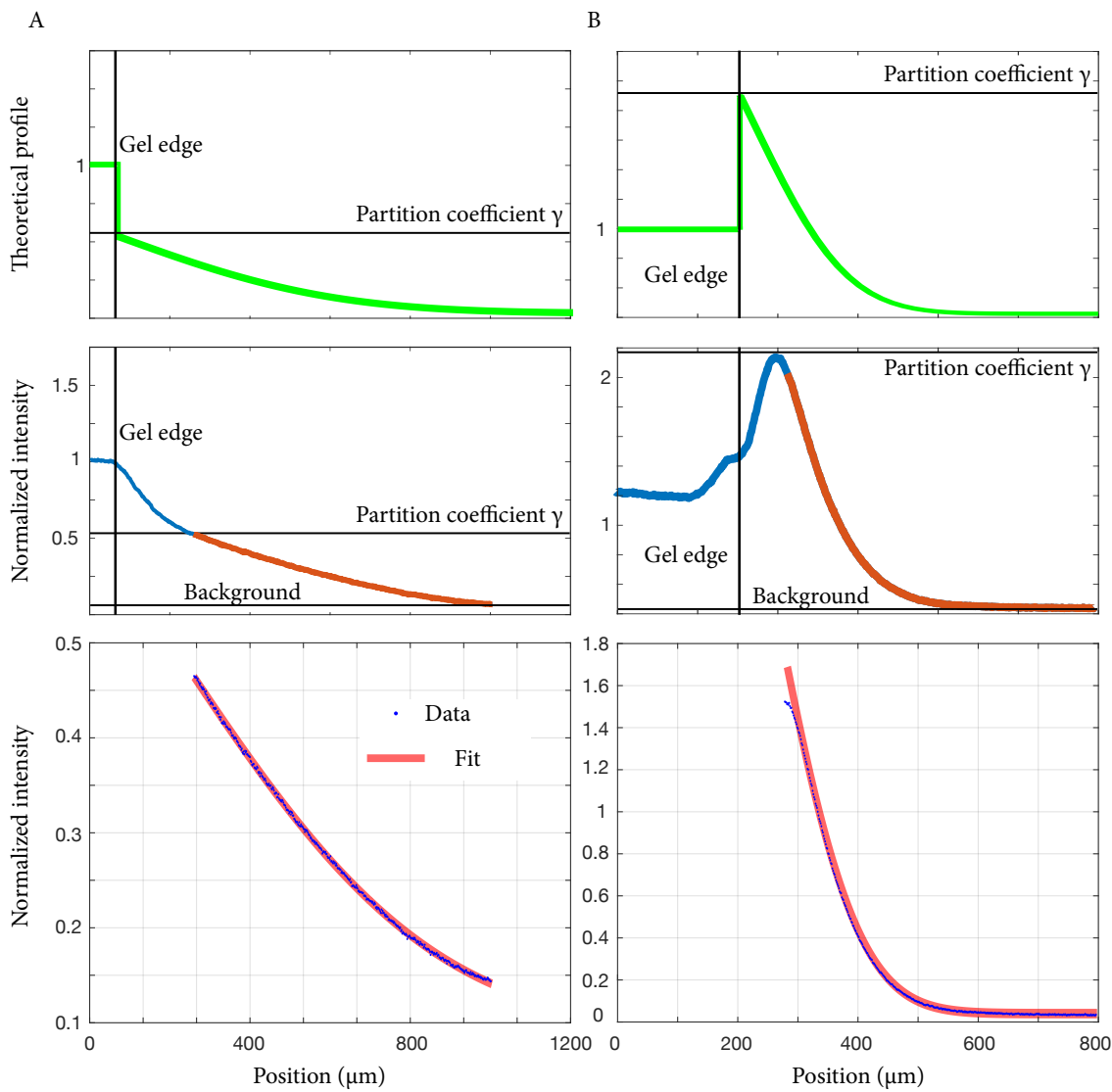
I fit the intensity profiles to Eqn. 4.9 using different numbers of terms  $N$ . For the mCherry curves, the resulting fit parameters tended to converge as  $N$  increased, and the RMSE stabilized. However, neither was true for the NTF2 curves. Increasing values of  $N$  led to steadily decreasing values of diffusion constant, making these fits unreliable.

#### 4.4.2 Accumulation analysis

The total accumulation within the hydrogel can be modeled by integrating the concentration profile over the entire gel. When this is done, the averaged intensity within the hydrogel  $N(t)$  is found to be

$$\frac{N(t)}{N_0} = 1 - \sum_{n=0}^{\infty} \frac{4}{(\alpha_n a)^2} \exp \left( -\frac{(\alpha_n a)^2 \pi t}{16\tau} \right) \quad (4.10)$$

**Figure 4.9:** Fits to Eqn. 4.8 near the beginning of the influx experiment for (A) mCherry and (B) NTF2-Alexa488 intensity profiles. Hydrogel precursor contained 10 mg/mL FSFG-PEGDA 700 Da. Theoretical profiles with a sharp edge are shown in the top panel. The hydrogel intensity profile is shown in the middle panel with the portion used for fitting highlighted in red. Approximate locations of the gel edge, background fluorescence level, and partition coefficient are also shown.



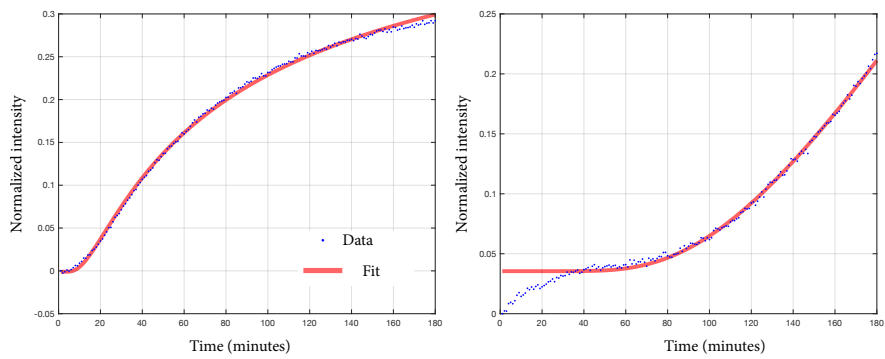


**Figure 4.10:** Fits to Eqn. 4.8 at a fixed point near the gel edge for (A) mCherry and (B) NTF2-Alexa488 intensity profiles. The short-time approximation likely only holds for times  $t \lesssim 20$  minutes. Hydrogel precursor contained 10 mg/mL FSFG-PEGDA 700 Da.

where  $N_0$  is the equilibrium value, here equal to the partition coefficient  $\gamma$  once the intensity has been normalized to that of the reservoir.

Fits to the first 100 terms of Eqn. 4.10 are shown in Fig. 4.11 for mCherry and NTF2. These fits had systematic error, likely for the same reasons that the profile fits did.

While the profile and accumulation data do contain information on the diffusion constants of NTF2 and mCherry, I was unable to extract that information using the influx experiments. The model presented above is in principle a good match to the experimental setup, but the presence of binding and the unpredictable gel-edge effects make it unreliable in practice. The FRAP experiments overcome the problem of edge effects by making use of equilibrated regions deep within the hydrogel.

## 4.5 FRAP analysis

The analysis of the FRAP recovery curves ultimately required a two-dimensional Fourier series solution, but simpler models were tried first and are also presented here.

### 4.5.1 Accounting for photobleaching

Small but noticeable amounts of photobleaching occur over the course of the FRAP experiment. One effective means of correcting for photobleaching is to normalize the intensity of the bleached area to that of the entire gel, including the bleached region. The normalized intensity

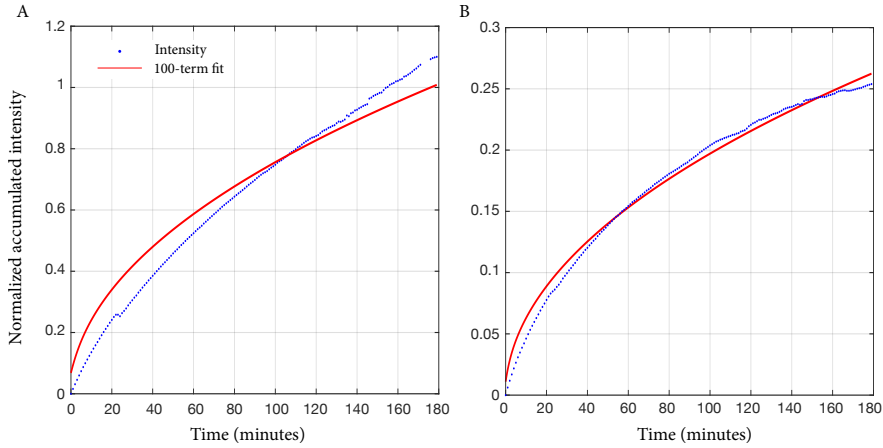


**Figure 4.11:** Accumulation fits to Eqn. 4.10 for (A) mCherry and (B) NTF2-Alexa488. Hydrogel precursor contained 10 mg/mL FSFG-PEGDA 700 Da.

used to fit the recovery curves is given by

$$N(t) = \frac{c_b(t)}{c_g(t)} \quad (4.11)$$

where the average intensity of the bleach spot is  $c_b(t) = C_b(t)/A_b$ . The total intensity within the bleach spot is  $C_b(t)$  and  $A_b$  is the area of the spot as shown in Fig. 4.5. The average intensity of the entire gel  $c_g(t)$  is defined similarly. Using this normalization removes the effects of photobleaching, as verified by simulating recovery data with various photobleaching rates.

#### 4.5.2 No-exchange solution to diffusion equation

The simplest model of fluorescence recovery assumes that the hydrogel is perfectly uniform and equilibrated, that the presence of the gel does not cause anomalous diffusion, and that there is no exchange of fluorescent proteins between the hydrogel and the reservoir during the experiment. Upon making those assumptions, the recovery curve can be fit using a sum of two Bessel functions as described in [68, 142]. The model used in [142] distinguishes between binding affinity regimes; NTF2-FSFG binding is sufficiently transient that it falls into the effective diffusion regime, allowing standard diffusion equations to be used without modification to calculate an effective diffusion constant as described in Sec. 4.3.3. The solution to fluorescence recovery with transient binding (effective diffusion) is given by

$$N(t) = A \exp(-\tau_D/2t) (I_0(\tau_D/2t) + I_1(\tau_D/2t)) + C \quad (4.12)$$

where the diffusion lifetime  $\tau_D$  is related to the effective diffusion constant by  $D = w^2/\tau_D$  if  $w$  is the bleach spot radius.

The amplitude  $A$  and offset  $C$  are related to the bleach depth (given by  $C$ ) and final recovered value (given by  $A + C$ ). Typical bleach depths were 5-10% of the initial intensity and tended to be smaller for mCherry than for NTF2. In principle, the final recovered value reflects the immobile fraction of fluorophore. If there is an immobile fraction, the bleached region will not recover to its initial value. Given the weak binding between NTF2 and FSFG, we do not expect an appreciable immobile fraction of either NTF2 or mCherry. For the most part, the hydrogels appear to recover to their initial value. A few do not, for reasons that are unclear even after accounting for photobleaching.

The no-exchange model fits well to the larger hydrogels and those that are well-equilibrated. Many of the large gels, however, were not fully equilibrated even after a 24-hour incubation with the reservoir solution. The concentration within these gels will change over the course of the experiment as they continue to equilibrate. Smaller hydrogels were quicker to uniformly equilibrate; however, these gels are small enough that exchange of fluorescent proteins with the reservoir is important over the timescale of FRAP recovery. Both of these problems can be accounted for using a more general solution to the diffusion equation.

#### **4.5.3 Fourier series solution to diffusion equation**

To account for exchange of fluorescent proteins with the reservoir, as well as for incomplete equilibration, we need to solve the diffusion equation in a way that allows fluorophores from the reservoir to enter the hydrogel, and vice versa, over the course of the FRAP experiment. This requires a two-dimensional Fourier series solution, which is cumbersome but allows for an accurate description of the concentration profile throughout the entire hydrogel immediately post-bleach. This approach also allows the boundary condition at the edge of the hydrogel to be defined so as to permit exchange with the reservoir.

This analysis begins by numerically calculating the two-dimensional polar Fourier transform

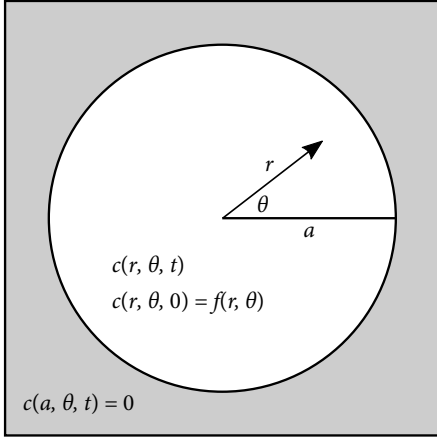


**Figure 4.12:** Geometry for diffusion-equation solution Eqn. 4.13. A circle of radius  $a$  is centered at the origin. The boundary  $r = a$  is held at concentration  $c = 0$  and the interior has initial concentration profile  $f(r, \theta)$ .

of the initial concentration distribution within the gel, decomposing it into a finite number of modes weighted by their contribution to the image. These mode coefficients are then used to create the equation to which the experimentally-measured recovery curve is fit. The fit parameters include the observed diffusion coefficients for NTF2 and mCherry, allowing the bound diffusion constant to be determined as described in Sec. 4.3.3.

Scripts to perform the following calculations are available at <https://github.com/LauraMaguire/image-processing>.

#### 4.5.3.1 Analytic series solution

Mathematically, we need to solve the diffusion equation in a circular region of radius  $a$ , centered at the origin, whose boundary is held at a fixed concentration. The region  $r < a$  has an arbitrary initial concentration distribution  $f(r, \theta)$  which consists of the first post-bleach image (Fig. 4.12). To find the concentration  $c(r, \theta, t)$  for  $r < a$ , we used the Green's function integrals described in [147]. Green's functions describe a system's response to an instantaneous point source. An initial distribution can be built by integrating the Green's function over the region of interest. The correct Green's function must be identified for a particular geometry and set of boundary conditions, but a formal solution is straightforward to write once they have been obtained.

The full solution to the diffusion equation within the hydrogel is given by [147]

$$c(r, \theta, t) = \sum_{\nu=-\infty}^{\infty} \sum_{\alpha=0}^{\infty} \frac{\exp(-D\alpha^2 t) J_{\nu}(\alpha r)}{(J'_{\nu}(\alpha a))^2} \times b_{\nu, \alpha} \int_0^{2\pi} \int_0^a \cos(\nu(\theta - \theta')) J_{\nu}(\alpha r') f(r', \theta') r' dr' d\theta' \quad (4.13)$$

where, as in the previous section,  $(\alpha a)$  are the zeros of  $J_{\nu}$ , and  $b_{\nu, \alpha}$  are normalization constants defined in Sec. 4.5.3.3. Note that the sums run over all positive and negative integer Bessel orders and over all zeros of each Bessel function.

This solution applies to a circle whose boundary is held at  $c = 0$ , so it must be shifted by an offset in order to match the experimental concentration at the boundary. The relevant boundary concentration is just within the hydrogel, not the concentration of the reservoir. The reservoir is assumed to be infinite, in order to maintain the hydrogel edge at its equilibrium concentration, but the concentration of the reservoir itself is irrelevant.

The integral above is difficult to use as written because it contains both primed and unprimed coordinates in the angular term,  $\cos(\nu(\theta - \theta'))$ . The unprimed coordinate can be removed from the integral using the identity

$$\cos(\phi_1 - \phi_2) = \cos \phi_1 \cos \phi_2 + \sin \phi_1 \sin \phi_2$$

The mode coefficients  $C_{\nu, \alpha}$  and  $S_{\nu, \alpha}$  can then be defined as

$$c(r, \theta, t) = \sum_{\nu=-\infty}^{\infty} \sum_{\alpha=0}^{\infty} \frac{\exp(-D\alpha^2 t) J_{\nu}(\alpha r)}{(J'_{\nu}(\alpha a))^2} (C_{\nu, \alpha} \cos(\nu \theta) + S_{\nu, \alpha} \sin(\nu \theta)) \quad (4.14)$$

with

$$C_{\nu, \alpha} = b_{\nu, \alpha} \int_0^{2\pi} \int_0^a \cos(\nu \theta') J_{\nu}(\alpha r') f(r', \theta') r' dr' d\theta' \quad (4.15)$$

$$S_{\nu, \alpha} = b_{\nu, \alpha} \int_0^{2\pi} \int_0^a \sin(\nu \theta') J_{\nu}(\alpha r') f(r', \theta') r' dr' d\theta' \quad (4.16)$$

Now the problem is reduced to determining the mode coefficients by evaluating the integrals.

#### 4.5.3.2 Calculating normalization constants

Before mode coefficients can be calculated using Eqns. 4.15 and 4.16, the normalization constants  $b_{\nu,\alpha}$  must be determined. To find an expression for them, begin with Eqn. 4.14 at  $t = 0$ , when  $c(r, \theta, 0) = f(r, \theta)$ .

$$f(r, \theta) = \sum_{\nu=-\infty}^{\infty} \sum_{\alpha=0}^{\infty} \frac{J_{\nu}(\alpha r)}{(J'_{\nu}(\alpha a))^2} (C_{\nu,\alpha} \cos(\nu\theta) + S_{\nu,\alpha} \sin(\nu\theta)) \quad (4.17)$$

This expression for  $f(r, \theta)$  can be substituted into Eqns. 4.15 and 4.16. Using the cosine coefficients as an example,

$$\begin{aligned} C_{\nu,\alpha} &= b_{\nu,\alpha} \int_0^{2\pi} \int_0^a \cos(\nu\theta') J_{\nu}(\alpha r') \times \\ &\quad \left[ \sum_{\mu=-\infty}^{\infty} \sum_{\beta=0}^{\infty} \frac{J_{\mu}(\beta r')}{(J'_{\mu}(\beta a))^2} (C_{\mu,\beta} \cos(\mu\theta') + S_{\mu,\beta} \sin(\mu\theta')) \right] r' dr' d\theta' \\ C_{\nu,\alpha} &= b_{\nu,\alpha} \sum_{\mu=-\infty}^{\infty} \sum_{\beta=0}^{\infty} \int_0^{2\pi} \int_0^a \cos(\nu\theta') \frac{J_{\nu}(\alpha r') J_{\mu}(\beta r')}{(J'_{\mu}(\beta a))^2} \times \\ &\quad (C_{\mu,\beta} \cos(\mu\theta') + S_{\mu,\beta} \sin(\mu\theta')) r' dr' d\theta' \\ C_{\nu,\alpha} &= b_{\nu,\alpha} \int_0^{2\pi} \int_0^a \frac{J_{\nu}^2(\alpha r')}{(J'_{\nu}(\alpha a))^2} (C_{\nu,\alpha} \cos^2(\nu\theta') + S_{\nu,\alpha} \cos(\nu\theta') \sin(\nu\theta')) r' dr' d\theta' \end{aligned}$$

The integral and sum have been switched and the orthogonality of the basis functions used to collapse the sums. The integral of the  $S_{\nu,\alpha}$  term vanishes, as it is an odd function ( $\cos(\nu\theta') \sin(\nu\theta')$ ) integrated over all  $\theta'$ . Similarly, the  $C_{\nu,\alpha}$  term drops from the sine coefficient integral. The remaining term gives

$$C_{\nu,\alpha} = b_{\nu,\alpha} \int_0^{2\pi} \int_0^a \frac{J_{\nu}^2(\alpha r')}{(J'_{\nu}(\alpha a))^2} C_{\nu,\alpha} \cos^2(\nu\theta') r' dr' d\theta'$$

or finally

$$\frac{1}{b_{\nu,\alpha}} = \int_0^{2\pi} \int_0^a \frac{J_{\nu}^2(\alpha r') \cos^2(\nu\theta')}{(J'_{\nu}(\alpha a))^2} r' dr' d\theta' \quad (4.18)$$

So long as the integral is truly over the entire circle  $r < a$ , this constant is the same for both  $C_{\nu,\alpha}$  and  $S_{\nu,\alpha}$ . In that case, Eqn. 4.18 gives  $b_{\nu,\alpha} = 2/\pi a^2$  for every mode.

However, in many cases, it is not possible to numerically integrate over the entire gel, as seen in Fig. 4.5D. All numerical integrals are instead over the gel mask, which encompasses as much of

the gel as fits into the field of view. The value of this mask is one within the gel and zero outside, so it serves to define the limits of numerical integration. Denoting the area covered by this mask as  $\Omega$ , the normalization constants for  $C_{\nu,\alpha}$  and  $S_{\nu,\alpha}$ , respectively, are

$$1/b_{\nu,\alpha}^C = \int_{\Omega} \frac{J_{\nu}^2(\alpha r') \cos^2(\nu\theta')}{(J'_{\nu}(\alpha a))^2} r' dr' d\theta' \quad (4.19)$$

$$1/b_{\nu,\alpha}^S = \int_{\Omega} \frac{J_{\nu}^2(\alpha r') \sin^2(\nu\theta')}{(J'_{\nu}(\alpha a))^2} r' dr' d\theta' \quad (4.20)$$

Likewise, the numerical integrals in Eqns. 4.15 and 4.16 are more precisely written

$$C_{\nu,\alpha} = b_{\nu,\alpha}^C \int_{\Omega} \cos(\nu\theta') J_{\nu}(\alpha r') f(r', \theta') r' dr' d\theta' \quad (4.21)$$

$$S_{\nu,\alpha} = b_{\nu,\alpha}^S \int_{\Omega} \sin(\nu\theta') J_{\nu}(\alpha r') f(r', \theta') r' dr' d\theta' \quad (4.22)$$

The degree to which the resulting coefficients deviate from the ideal case of a perfect circle can be roughly quantified by the ratio  $b_{\nu,\alpha}/(2/\pi a^2) = \pi a^2 b_{\nu,\alpha}/2$ . For small hydrogels, which entirely fit into the field of view, these values range from 1.01 to 1.03, signifying deviations of up to 3%. Large hydrogels whose top and bottom were cut from the field of view had deviations of up to 10%. However, using Eqns. 4.19 and 4.20 instead of the uniform mode weighting  $b_{\nu,\alpha} = 2/\pi a^2$  should compensate for the irregular area of integration.

#### 4.5.3.3 Calculating mode coefficients

For every hydrogel, every Bessel order  $\nu$ , and every Bessel zero  $\alpha$ , mode coefficients were calculated numerically. The polar coordinates  $(r, \theta)$  were converted to Cartesian  $(x, y)$  and a sum taken over all the pixels of the initial post-bleach image  $f(x, y)$ , using the hydrogel mask to set the limits. The center of the coordinate system was set at the center of the gel and the value of the gel radius  $a$  calculated as described in Sec. 4.3.1. Before the sum was calculated, the average intensity of the equilibrated portions of the hydrogel was subtracted from the entire image, effectively setting the equilibrium concentration at  $c = 0$  as required by the series solution. For well-equilibrated gels, a pre-bleach image of the entire gel was used to determine the average equilibrium concentration.

For gels which were not fully equilibrated, a mask was defined which contained only the equilibrated portions, and that mask was used to calculate the average concentration.

The sum was scaled using the area represented by each pixel (using the scale  $1.58 \mu\text{m}/\text{pixel}$ ) and normalized using the weighting constants  $b_{\nu,\alpha}$ . The final values of  $C_{\nu,\alpha}$  and  $S_{\nu,\alpha}$  were stored in two arrays for use in constructing the equation to which the experimental data was fit.

#### 4.5.3.4 Reconstruction of initial image

To verify the mode coefficients, I reconstructed the initial post-bleach image from which they were calculated. The image was reconstructed by numerically integrating Eqn. 4.17 using a similar method to that discussed in the previous section. The area outside the gel mask was not reconstructed. Figure 4.13 shows the resulting reconstructions as the number of terms in the series increases. The relative magnitudes of those terms are shown in Fig. 4.14. The reconstruction is adequate for our purposes by the time  $N_\nu = 20$  and  $N_\alpha = 20$ , i.e. twenty Bessel orders and twenty zeros are used. Note that the Bessel orders are given by  $\nu = -10, -9, \dots, 0, \dots, 8, 9$ . A coefficient array of this size allowed a dataset of 43 hydrogels to be entirely processed and fit in approximately 24 hours on a desktop computer; larger coefficient arrays would require the use of a computing cluster.

#### 4.5.3.5 Fitting recovery curves

Once the mode coefficients had been calculated, a fit string was constructed using the full series equation Eqn. 4.14 and fed into the Matlab curve fitter. Careful thought was required to ensure that the model was treated in the same way as the experimental data.

To begin, the mode coefficients were used to predict the average intensity of the bleach spot at each time point. Since all the time dependence in each term is contained in one decaying exponential, the average value of the bleach spot could be determined by integrating over the bleach spot:

$$\bar{c}_{\text{bleach}}(D, t) = \frac{1}{A_B} \sum_{\nu=-\infty}^{\infty} \sum_{\alpha=0}^{\infty} \exp(-D\alpha^2 t) \int_{\Omega_B} \frac{J_\nu(\alpha r)}{(J'_\nu(\alpha a))^2} (C_{\nu,\alpha} \cos(\nu\theta) + S_{\nu,\alpha} \sin(\nu\theta)) dA \quad (4.23)$$

**Figure 4.13:** Reconstruction of initial concentration distribution. Reservoir is masked and not included. (A) Heatmap of original image with average equilibrated gel intensity set to zero. (B) Reconstruction using two Bessel orders ( $N_\nu = 2$ ) and two zeros ( $N_\alpha = 2$ ) in each order. (C-E) Reconstructions with  $N_\nu = N_\alpha = 4, 10$ , and  $20$ .

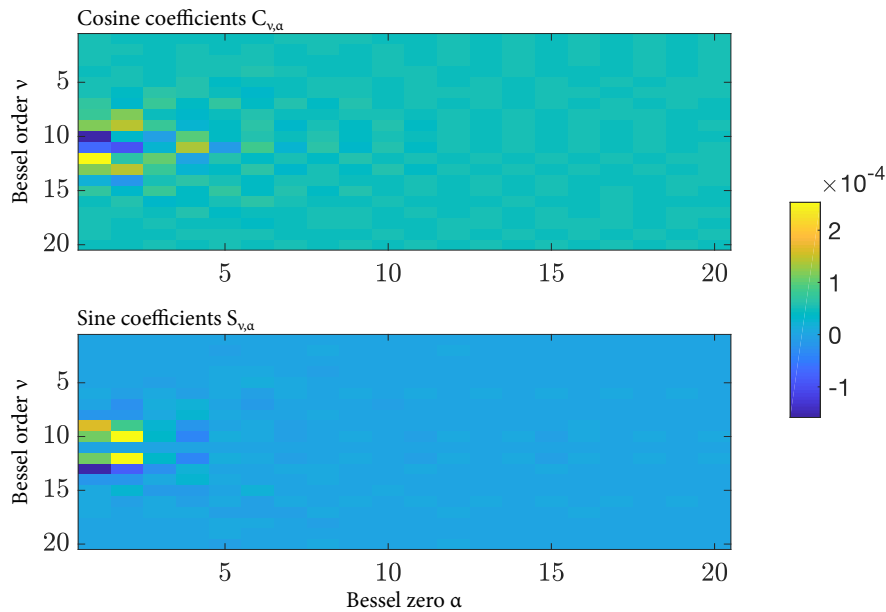
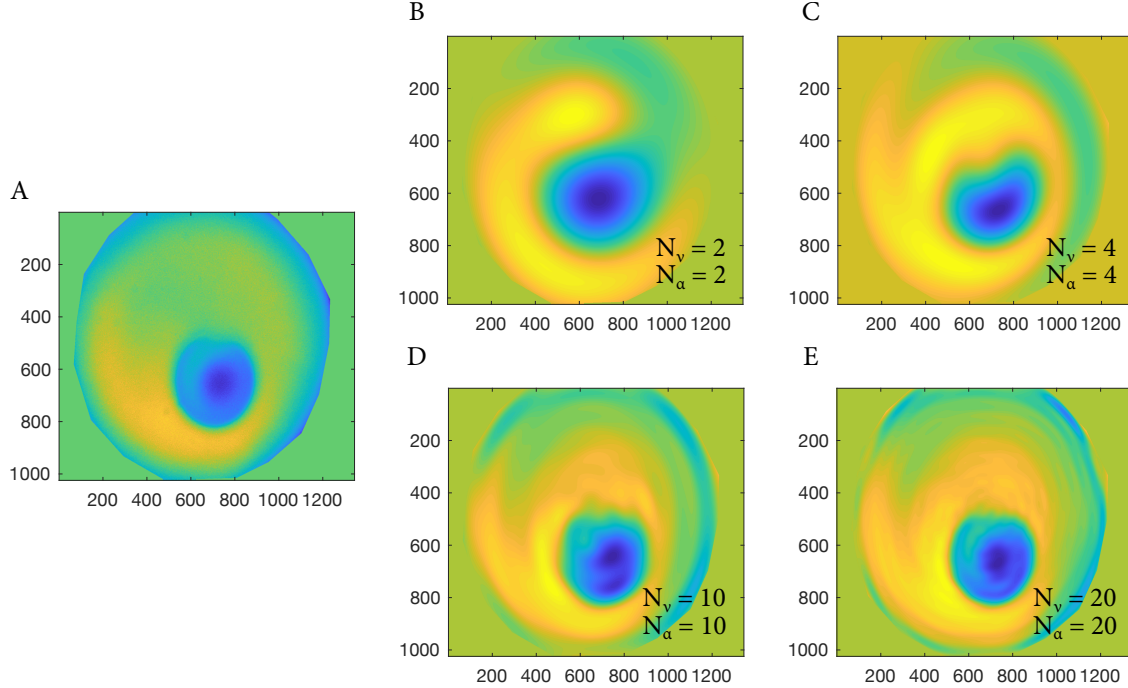
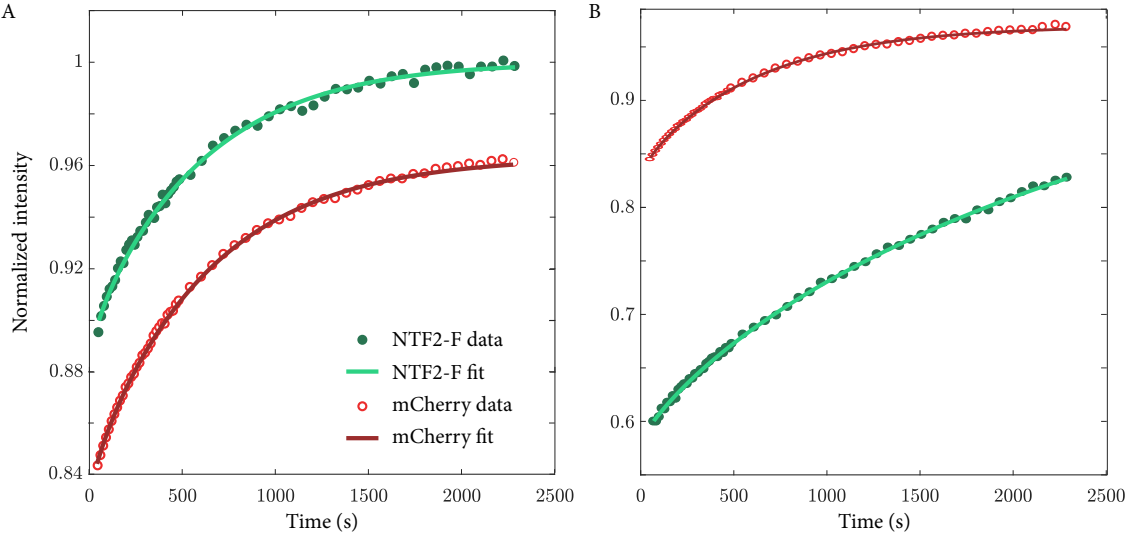


**Figure 4.14:** Heatmap of cosine and sine mode coefficients  $C_{\nu,\alpha}$  and  $S_{\nu,\alpha}$  for the reconstruction shown in Fig. 4.13E. Values are shown for each Bessel order  $\nu$  and each zero  $\alpha$ .

**Figure 4.15:** Fits using the series expansion Eqn. 4.13. (A) NTF2-F and mCherry recovery curves for a no-Nup hydrogel. (B) NTF2-F and mCherry recovery curves for a hydrogel whose precursor contained 10 mg/mL FSFG concat-1.



where  $\Omega_B$  is the region defined by the bleach-spot mask and  $A_B$  is its total area. The Bessel function derivative  $J'_\nu$  was computed using the identity

$$J'_\nu(x) = \frac{1}{2} (J_{\nu-1}(x) - J_{\nu+1}(x))$$

The average intensity of the entire gel, including the bleach spot, was determined in the same way, using the hydrogel mask instead of the bleach-spot mask. Both results were formatted as strings of sums, containing numerical values wherever possible as well as the diffusion constant parameter  $D$  (units of  $\mu\text{m}^2/\text{s}$ ) and the time variable  $t$ , measured in seconds.

Once these strings were created, the equilibrium concentration value  $T_0$  was added back to both of them, and their ratio was taken, in order to mimic the data processing in Sec. 4.5.1. Mathematically, this gave a normalized string of

$$f(D, t) = \frac{\bar{c}_{\text{bleach}}(D, t) + T_0}{\bar{c}_{\text{gel}}(D, t) + T_0} \quad (4.24)$$

At this point, I checked the normalization by simulating data using the value of  $D$  calculated from the no-exchange analysis in Sec. 4.5.2. Often the simulated data matched the experiment to within 10%, but further fit parameters were needed in order to fit the data well. Ultimately, the

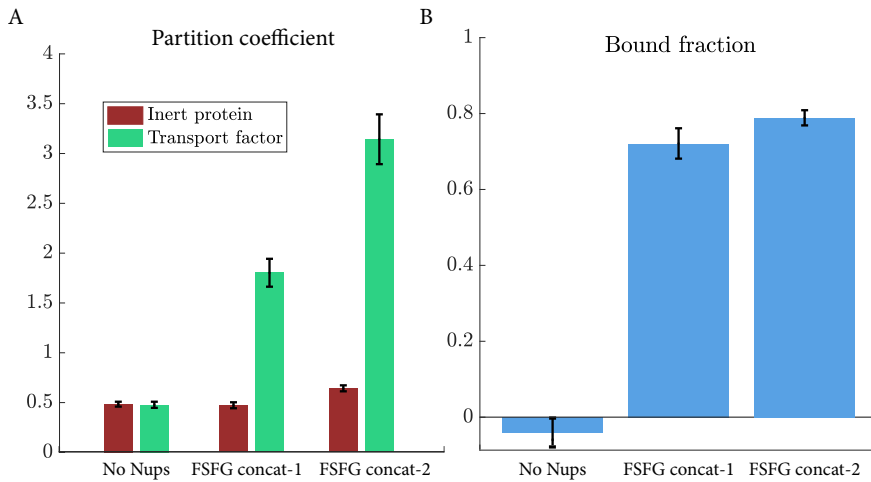


**Figure 4.16:** (A) Partition coefficients for NTF2-F and mCherry in each of the three experimental conditions. (B) Fraction of NTF2-F bound as calculated using Sec. 4.3.2. All errors are standard error of the mean.

function to which the data were fit was

$$g(c_1, c_2, D, t) = c_1 f(D, t) + c_2 \quad (4.25)$$

where  $c_1$  and  $c_2$  reflect the bleach depth and final recovered concentration similarly to  $A$  and  $C$  in Sec. 4.5.2. Their values are less important than that of the diffusion constant  $D$ .

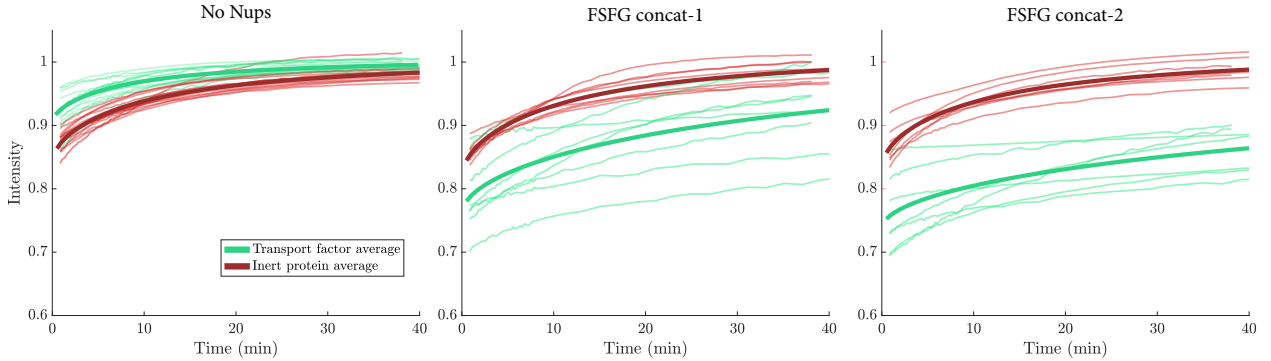
Fits such as those shown in Fig. 4.15 were typical results. Values for  $c_1$  and  $c_2$  were of order unity, except for a few fits that were clearly incorrect and were omitted from the final dataset.

## 4.6 Results

In all, FRAP analysis was performed on 34 hydrogels: 15 no-Nup gels, 12 created from a precursor solution containing 10 mg/mL FSFG concat-1, and 7 containing FSFG concat-2 with 20 mg/mL protein in the precursor solution.

The partition coefficients for NTF2-F and mCherry are shown in Fig. 4.16 along with the corresponding fraction bound. As expected, the partition coefficients NTF2-F and mCherry are very similar in the no-Nup hydrogels, while the NTF2-F partition coefficient increases for FSFG hydrogels due to binding. The FSFG concat-2 hydrogels show a slightly higher fraction bound than the FSFG concat-1 gels. We measured the final tethered Nup concentration to be roughly equal at  $\sim 1$  mg/mL in both types of gels, although the method used was not reliable (Sec. 4.1.3). If the concentration is in fact the same between the FSFG concat-1 and concat-2 hydrogels and

**Figure 4.17:** FRAP recovery curves for (A) no-Nup, (B) FSFG concat-1, and (C) FSFG concat-2 hydrogels. All curves are shown for both NTF2-F and mCherry. Dark lines are averaged curves. Data are normalized so that pre-bleach intensity is one.



the fraction bound is higher in the FSFG concat-2 gels, NTF2 must bind more strongly to FSFG concat-2 than to FSFG concat-1. This would contradict work which measured approximately the same binding affinity for both constructs [27]. The crowded, confined environment of the Nup-filled hydrogel might be responsible for any change in binding affinity between FSFG concat-1 and concat-2. However, the measurements of the tethered Nup concentration are not precise enough to rule out similar binding affinities for FSFG concat-1 and FSFG concat-2.

Figure 4.17 shows normalized recovery curves for all hydrogels in the dataset. In addition to the normalization described in Sec. 4.5.1, these curves were also scaled so that the pre-bleach average bleach spot intensity was one. Dark curves show the average NTF2 and mCherry recovery curves for each condition. The most obvious difference between conditions is the greater bleach depth for NTF2-F in FSFG hydrogels. Bleach depth stays roughly constant for mCherry between conditions.

Next, the observed diffusion constants for NTF2-F and mCherry were calculated using the Fourier series model. Mean values for each of the experimental conditions are shown in Fig. 4.18 along with calculated bound diffusion constants, computed from the observed diffusion constants as described in Sec. 4.3.3. The observed diffusion for NTF2-F and mCherry was roughly equal in the no-Nup hydrogels, but NTF2-F has a much lower diffusion constant in the FSFG conditions,

due to binding.

Both the FSFG concat-1 and concat-2 hydrogels showed a non-zero bound diffusion coefficient. We measured  $D_B = 5.6 \pm 2.3 \mu\text{m}^2/\text{s}$  for FSFG concat-1 gels and  $D_B = 5.2 \pm 3.2 \mu\text{m}^2/\text{s}$  for FSFG concat-2 gels. Two-tailed t-tests were conducted with the null hypothesis that  $D_B = 0$ . For FSFG concat-1, the resulting p-value was  $p = 0.025$ ; for FSFG concat-2, it was  $p = 0.13$ . There is no distinguishable difference between  $D_B$  for FSFG concat-1 and FSFG concat-2, which may be due to the lack of sensitivity in our measurements.

We also predicted the value of  $D_B$  we would expect from our tethered diffusion model (Sec. 2.2.1). Assuming all bound diffusion comes from tethered diffusion, we can write the bound diffusion constant in terms of the polymer properties of the tethered Nup as

$$D_B = \frac{D_F L_c \ell_p k_{\text{off}}}{L_c \ell_p k_{\text{off}} + 3D_F} = \frac{D_F}{1 + 3 \frac{D_F}{D_P}} \quad (4.26)$$

where  $D_P = L_c \ell_p k_{\text{off}}$ ,  $k_{\text{off}}$  is the off-rate constant,  $L_c$  is the Nup contour length, and  $\ell_p$  is the Nup persistence length. We used the observed mCherry diffusion constant as a proxy for  $D_F$ . The contour lengths for FSFG concat-1 and concat-2 are known: FSFG concat-1 is 124 amino acids in length, or 50 nm, and FSFG concat-2 is twice that, approximately 100 nm. The persistence length of disordered proteins is around 1 nm [120].

We first tried to use published data for the off-rate constant for NTF2 and both FSFG constructs [27]. The published data showed  $K_D = 545 \mu\text{M}$  for FSFG concat-1; for FSFG concat-2,  $K_D = 395 \mu\text{M}$ . However, combining these values of  $K_D$  with our measurements of the partition coefficients as in Eqn. 4.5 leads to estimates of the tethered Nup concentration  $N_t$  which are not compatible with our hydrogels. As discussed in Sec. 4.1.3, we do not have a definitive measurement of  $N_t$ , but it is almost certainly much lower than the concentration in the precursor solution. Even assuming, as an upper bound, that the tethered concentration is equal to the precursor Nup concentration, the maximum possible value for  $N_t$  is 10 mg/mL for the FSFG concat-1 hydrogels and 20 mg/mL for FSFG concat-2. The above published  $K_D$  values lead to an estimate of 25 mg/mL tethered FSFG concat-1 and 23 mg/mL tethered FSFG concat-2, higher than the concentration

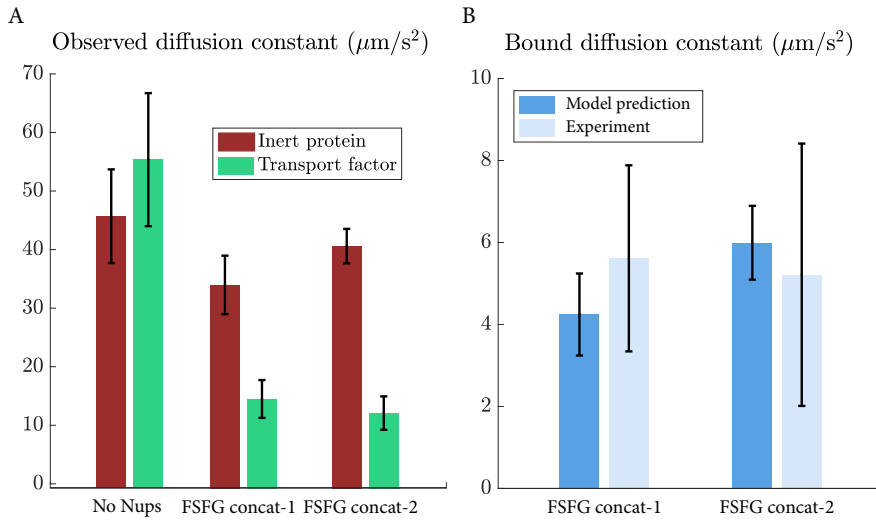


**Figure 4.18:** (A) Observed diffusion constant for NTF2-F and mCherry in each of the three experimental conditions. (B) Calculated values of the bound diffusion constant  $D_B$  for NTF2-F in the FSFG hydrogels. All errors shown are standard error of the mean.

that was put into the precursor solution.

Therefore, instead of using the published data, we calculated a predicted  $D_B$  value assuming the maximum possible tethered Nup concentration:  $N_t = 10 \text{ mg/mL}$  for FSFG concat-1 and  $N_t = 20 \text{ mg/mL}$  for FSFG concat-2. The mean value of the predictions is shown in Fig. 4.18B. For FSFG concat-1 hydrogels, the predicted bound diffusion constant is  $D_B = 4.3 \pm 1.0 \mu\text{m}^2/\text{s}$ ; for FSFG concat-2 gels this value is  $D_B = 6.0 \pm 0.9 \mu\text{m}^2/\text{s}$ . The predicted values agree well with the experimentally-measured values of  $D_B = 5.6 \pm 2.3 \mu\text{m}^2/\text{s}$  for FSFG concat-1 and  $D_B = 5.2 \pm 3.2 \mu\text{m}^2/\text{s}$  for FSFG concat-2. Full datasets are shown in Appendix H.

If, as very rough measurements of the tethered Nup concentration suggest, both types of hydrogel had a similar mass density of Nups ( $\sim 1 \text{ mg/mL}$ ), then the higher NTF2 partition coefficients observed in FSFG concat-2 gels would imply tighter binding of NTF2 to FSFG concat-2 than to concat-1. If the on-rate is diffusion limited for both constructs, FSFG concat-2 would necessarily have a lower off-rate. In our tethered diffusion model, the bound diffusion constant is predicted to increase when the Nup contour length increases but decrease when the off-rate decreases (Eqn. 4.26). In particular, if the affinity is indeed changing between the two Nup conditions, the net result of the two effects would not be possible to predict without knowledge of the change in off-rate constant  $k_{\text{off}}$ .

#### 4.7 Discussion

Our goal was to create a material in which we could measure and test the properties of bound diffusion. These results suggest that we can indeed measure non-zero bound diffusion, although there is no measurable difference between Nups of different lengths and valencies. More subtle effects would be measurable if the fraction of transport factor bound ( $p_B$ ) increased, as then the contribution of bound diffusion to the observed diffusion would become more prominent. The most straightforward way of increasing the fraction bound is to increase the concentration of tethered Nups within the gel, a task which has proven difficult. However, this dataset still provides a check on the predictions of our model.

Remarkably, the simple model of tethered diffusion described in Chapter 2 yields a prediction which is in agreement with the experimentally-observed bound diffusion constant in FSFG concat-1 hydrogels. This result suggests that the flexible nature of the Nups is indeed important to bound diffusion within our hydrogel nuclear pore mimics. Non-zero bound diffusion was measured for two values of Nup length, in both the FSFG concat-1 and FSFG concat-2 hydrogels.

If a more precise method of measuring the tethered Nup concentration could be developed in the future, we would be able to say more definitively whether the binding affinity of NTF2 changes with the Nup length in the crowded and confined environment of the hydrogels. We would also be able to probe the effects of changing the concentration of FG motifs independently of the chain length, by incorporating long Nups with a lower density of FG motifs along their length. Experimentally controlling the model's parameters such as hopping rate, binding affinity, and free diffusion constant has proven difficult, but it would be interesting to test our model's predictions when those parameters are varied. The hydrogel nuclear pore mimics discussed in this chapter do not reproduce the selectivity properties of nuclear transport, nor are they intended to. However, they do provide a platform from which to measure bound diffusion. For both Nup lengths tested, we measured non-zero values of bound diffusion in agreement with our tethered-diffusion model. This represents a first step towards understanding the effect of bound diffusion on selective biofilters.

## Chapter 5

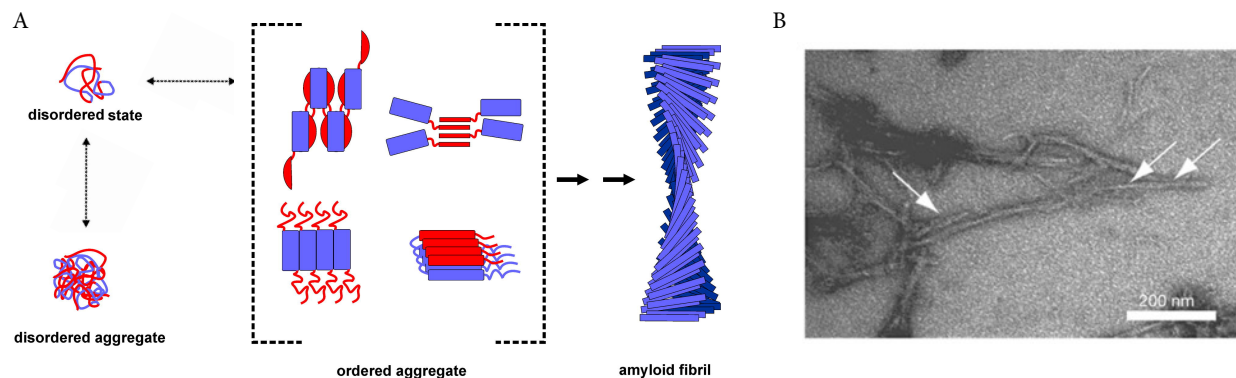
### FG Nup aggregation under crowded conditions

While our bound-state diffusion model of selectivity is general enough to apply to many biofilters, we have been using the nuclear pore in particular as inspiration. We predict that its selective properties arise from the continued mobility of transport factors while bound to FG Nups. One mechanism of bound-state diffusion arises from the flexible, tether-like nature of the disordered Nups. Such a mechanism is possible whether the Nups form a polymer brush or a transient hydrogel, so long as they remain sufficiently dynamic.

The exact conformation of Nups within the nuclear pore is unknown, due to the difficulty in imaging such a disordered system. Some Nups, such as Nsp1, aggregate in buffer to form hydrogel structures [49–51], although evidence suggests it does not aggregate in the cellular environment [11]. Other Nups can form phase-separated liquid droplets [112]. Nup153 forms amyloid fibrils *in vitro* (Fig. 5.1B) at a rate which is increased by the addition of inert crowders [148]. Amyloid structures, as shown in Fig. 5.1A, are long chains of stacked  $\beta$  sheets which are much less flexible and dynamic than individual disordered proteins, potentially limiting the effectiveness of the tethered bound diffusion of transport factors. Amyloid fibrils are commonly formed by disordered proteins upon aggregation and are often implicated in disease [149]. On the other hand, simulations and atomic force microscopy (AFM) data suggest that Nups in the nuclear pore remain highly dynamic [12,14].

We decided to test the aggregation behavior of a fragment of Nsp1 known as FG124, described in Sec. 3.4 and Appendix F. This 124-amino-acid peptide contains eight FG motifs and is known to aggregate in buffer over the course of several hours. However, in-cell NMR shows it to remain

**Figure 5.1:** Aggregation of FG Nups into amyloid fibrils. (A) Schematic of possible aggregation states of a disordered protein, including disordered aggregates, intermediate amyloid-like states, and fibrils composed of stacked  $\beta$  sheets. Rectangles denote secondary structure. Figure adapted from [149]. (B) Negative-staining electron micrograph of amyloid fibrils consisting of the human Nup153 FG domain. Arrows indicate characteristic twists of the fibrils. Figure adapted from [148].



disordered inside bacterial cells [11]. Given the disparity in aggregation behavior under these different conditions, we wanted to determine whether we could encourage or suppress aggregation and amyloid formation with our choice of crowding agents.

While the simplicity of studying aggregation of FG124 in buffer alone is appealing, the nuclear pore is a very different environment. Cells are extremely crowded with proteins, nucleic acids, and other macromolecules. Macromolecules may fill up to 30% of a cell's volume [150]. Crowding can have strong effects on a protein's behavior, sometimes in surprising ways. Furthermore, crowding effects can differ depending on whether the crowders are inert, interacting, compact, extended, and so on. Generally speaking, crowding seems to increase the rate of aggregation of disordered proteins, but this is by no means universal [148, 150–153]. The presence of small crowders tends to encourage proteins to take on compact conformations due to the excluded volume effect, which in the case of IDPs often leads to aggregation. However, the viscosity changes due to crowding may inhibit the formation of aggregates [154, 155]. Crowding with proteins capable of nonspecific interactions has been shown to inhibit the partitioning of IDPs into phase-separated liquid droplets [156]. Other important but not well-understood factors include crowder structure and interactions, agitation or its absence, and the presence of an air-water interface [150, 152].

We studied FG124 aggregation in the presence of various crowding agents, both inert and nonspecifically interacting, using a number of techniques. The kinetics were probed with a fluorescence aggregation assay, which showed significant differences between crowders. Two inert crowders, poly(ethylene glycol) and polyvinylpyrrolidone, were chosen for further NMR and fluorescence spectroscopy. The results do not have a clear interpretation but suggest that the presence and type of crowding agent is indeed affecting the local chemical environment of the peptide's residues, including its phenylalanines. Given the importance of the FG repeats to Nup cohesive-ness and transport factor binding, this could have implications for the optimal conditions under which to study Nup behavior *in vitro*.

### 5.1 Fluorescence time courses

To probe the aggregation kinetics of FG124, we incubated samples in the presence of crowders and thioflavin T (ThT), a dye which is sensitive to the presence of amyloids. Over the course of several hours, FG124 aggregated and the fluorescence intensity from ThT increased. After recording the intensity at 10-minute intervals, we plotted sigmoidal aggregation curves for the samples, as shown in Fig. 5.2. These curves show a lag phase while the aggregates are nucleating, followed by a growth phase of rapid aggregation, ending in a plateau phase. We recorded timecourses for multiple crowders, including inert crowders as well as nonspecifically binding ones, and analyzed the resulting aggregation parameters. Poly(ethylene glycol) (PEG) and polyvinylpyrrolidone (PVP) were chosen as representative inert crowders. Cell lysate was used to imitate the cellular environment and test the effect of nonspecific interactions on FG124 aggregation. Finally, serine was used as a crowder as previous work demonstrated that it caused Nup153 to aggregate more quickly [148]. Many of the timecourse experiments were performed by Sophie Reskin and Paul Marchando, and Sophie also took part in the analysis.

Thioflavin T is a dye that grows much brighter when bound to amyloids. Upon binding, its absorption maximum shifts from 385 nm to 450 nm and its emission maximum from 445 nm to 482 nm [157]. Although ThT is a more reliable indicator of amyloids than other fluorescence methods,

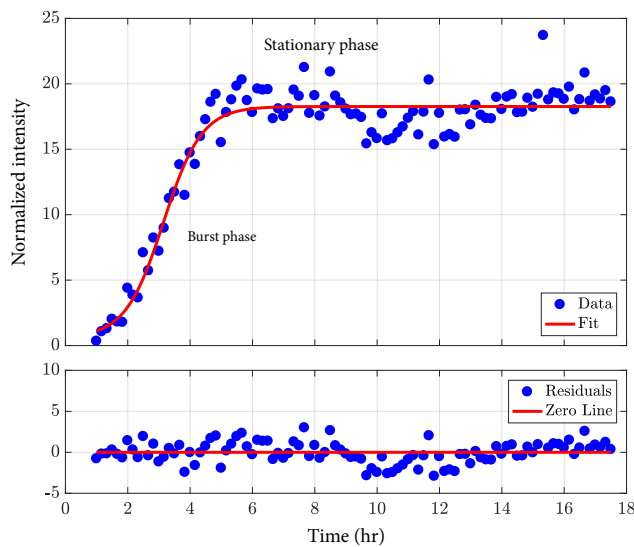


**Figure 5.2:** Sample sigmoid fit to FG124 aggregation timecourse with 13% w/v PEG. Burst phase and stationary phase are shown; lag phase took place before data collection began. Fit is to Eqn. 5.1.

notably Congo red stain, it suffers from reproducibility problems. There is no consensus on the mechanism of ThT binding to amyloids. Some proposed mechanisms rely on the presence of ThT micelles, which form above a critical concentration of about 4  $\mu\text{m}$ , while other work advocates for avoiding micelles [158, 159]. There is some evidence that amyloid fibrils can adsorb to the plastic surface of a multiwell plate, decreasing ThT fluorescence intensity as the fibrils mature [160]. Often in our timecourse experiments, the ThT fluorescence did reach a maximum and then decrease. The fluorescence intensity also depends on the sample viscosity, an effect which we noticed in our timecourses [161]. Despite these challenges, thioflavin T is the most reliable dye for detecting the process of amyloid formation.

### 5.1.1 Methods

#### 5.1.1.1 Buffers

Potassium transport buffer (PTB) (150 mM KCl, 20 mM HEPES, 2 mM  $\text{MgCl}_2$ ) was used for all timecourse and NMR samples.

### 5.1.1.2 FG124 preparation

His-tagged FG124 was expressed in *E. coli* in the plasmid pRSF. Cultures were grown in LB and induced at 37°C for 2-4 hr with 1 mM IPTG at OD 0.6-0.8. Periplasmic matrix was removed prior to lysis. Cells were then lysed via sonication and FG124 was purified using TALON cobalt resin (Appendix C). All purification buffers were PTB with 7M guanidine hydrochloride (GuHCl) and 1:1000 protease inhibitor cocktail (PIC). The elution buffer also contained 250 mM imidazole.

### 5.1.1.3 Timecourse preparation

Stocks of PEG (avg. MW 20 kDa, Sigma, Bio-Ultra) and PVP (avg. MW 40 kDa, Sigma) in PTB were prepared at 20 or 40% w/v; L-serine (EMD Millipore Calbiochem) stocks were prepared at 30% w/v. PEG and serine were at pH 7; PVP was pH 7 or pH 5. Lyophilized lysate was prepared by homogenizing and centrifuging BL21 DE3 Gold cells. The supernatant was lyophilized in a decomposing 25 mM ammonium bicarbonate buffer and resuspended in PTB to the desired concentration when needed. A 10 mM stock solution of ThT in PTB was prepared and filtered no more than a week before the timecourse, stored at room temperature and protected from light. Immediately prior to starting the timecourse, FG124 was desalted into PTB to remove the imidazole and GuHCl. Samples were promptly prepared containing the appropriate percentage of crowder, a final concentration of 0.3-2.5 mg/mL FG124, and 200 μM ThT. All samples in the same timecourse had the same concentration of FG124, including the buffer sample, which contained no crowding agent. Blanks were prepared with crowding agent and ThT, but no FG124. Samples were pipetted into black, flat-bottomed, clear-bottomed 96-well plates with 150 μL per replicate. Each sample yielded four to six replicates. Only one blank replicate was used per condition. One negative control and corresponding blank were prepared per timecourse containing 7M GuHCl and no crowding agent but using the same protein sample as all other conditions. Each well contained a 3mm-diameter glass or Teflon bead. The plate was sealed with a PCR seal. The fluorescence was measured from the bottom at 10-minute intervals with an excitation wavelength of 450 nm, emission

wavelength of 482 nm, and 5 nm bandwidth using a Safire II plate reader. The plate shook orbitally at high speed between measurements and was held at a temperature of 30°C. The time between desalting and beginning the plate reader measurements was typically about an hour; the time of desalting was taken as  $t = 0$  for the purposes of calculating lag time. In parallel with the sample preparation, the concentration of the desalted FG124 was measured with a BCA assay. Sophie Reskin helped to optimize this assay, making extensive use of [162].

#### 5.1.1.4 Timecourse analysis

After carrying out the aggregation timecourse, the data were normalized and fit to a sigmoid function in order to extract aggregation lifetimes and lag times.

The data were first normalized to the blanks, which contained crowding agents but no protein. In nearly all cases, the blank intensity remained steady over time, as expected. In those cases, the mean blank intensity was subtracted from the corresponding data. In cases where the blank intensity changed over time, it was subtracted pointwise from the data.

Then the normalized curves were fit to a sigmoid given by

$$I(t) = C + \frac{A}{1 + \exp(-k(t - T_{1/2}))} \quad (5.1)$$

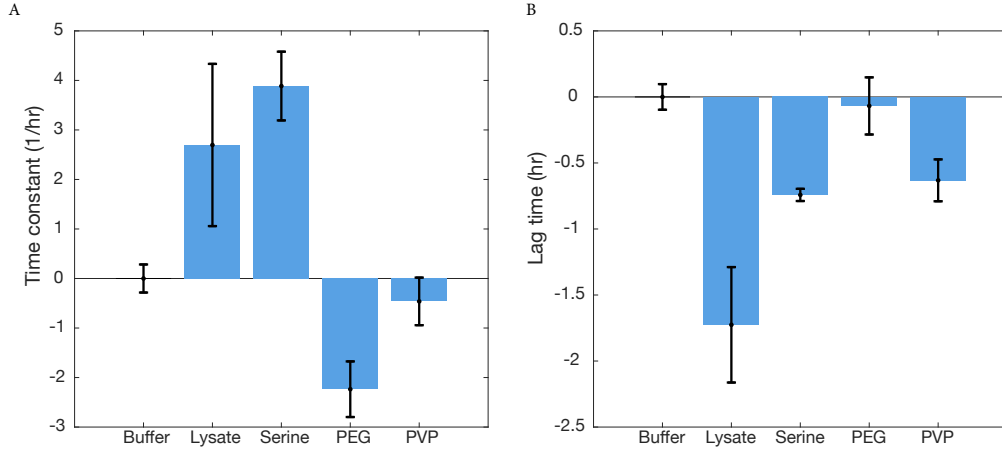
where  $I(t)$  is the normalized fluorescence intensity as a function of time (Fig. 5.2). The aggregation dynamics are described by the rate  $k$  and the half-time  $T_{1/2}$ , which reflects the time needed for the intensity to reach half of its asymptotic value. More descriptive than the half-time is the lag time  $T_l$ , calculated as

$$T_l = T_{1/2} - \frac{2}{k} \quad (5.2)$$

and representing the duration of the lag phase [163]. The lag time here is defined as the intersection of the tangent line of maximum slope of the growth phase with the flat background signal of the lag phase.

The offset  $C$  and final amplitude  $A$  are less meaningful in this context, and less reliable. The offset should in principle be  $C = 1$ , as the fluorescence of the sample and its blank should be equal

**Figure 5.3:** (A) Aggregation rates and (B) lag times for all crowding agents, normalized to the no-crowding condition. Crowder concentrations were 19% w/v serine, 13% PEG, 13% PVP, and approximately 10 mg/mL lysate. Lysate concentration varied somewhat between experiments. Error bars are standard error of the mean.



before aggregation has begun. Experimentally,  $C \sim 1\text{-}2$ , reaching a maximum near  $C = 10$  for a few sample conditions. While this may have been because sample aggregation had already begun, the long lag times of those conditions do not support that interpretation. It is possible that the presence of the unaggregated protein caused a change in baseline fluorescence through an unknown mechanism.

The plateau phase asymptotes to an intensity given by  $I_\infty = C + A$ . We found significant variation in  $I_\infty$  for the same condition between timecourses, and the relative magnitudes of different conditions also varied between timecourses. As seen in previous ThT studies, higher viscosity tended to result in higher values of  $I_\infty$ . Therefore, we do not consider  $I_\infty$  in our analysis, leaving the aggregation rate  $k$  and lag time  $T_\ell$  as parameters of interest.

Next we normalized once again to account for differences between timecourses. It was impossible to hold the FG124 concentration exactly fixed between timecourses. Final protein concentration varied between 0.3 and 2.5 mg/mL. Within each timecourse, we averaged the fit parameters for all replicates of FG124 in buffer only and subtracted that average from each replicate of each crowding condition.

### 5.1.2 Results

The mean fit parameters and number of replicates for each crowder condition are shown in Table 5.1 and Fig. 5.3. For both the aggregation rate  $k$  and lag time  $T_\ell$ , a one-factor ANOVA rejected at the  $p = 0.05$  level the null hypothesis that there was no difference between the means. Two-tailed t-tests were then run comparing all conditions shown in Fig. 5.3. The resulting  $p$ -values were below 0.05 except for those comparing no crowder to PVP (rate), no crowder to PEG (lag time), and serine to PVP (lag time). All  $p$ -values are reported in Appendix I.

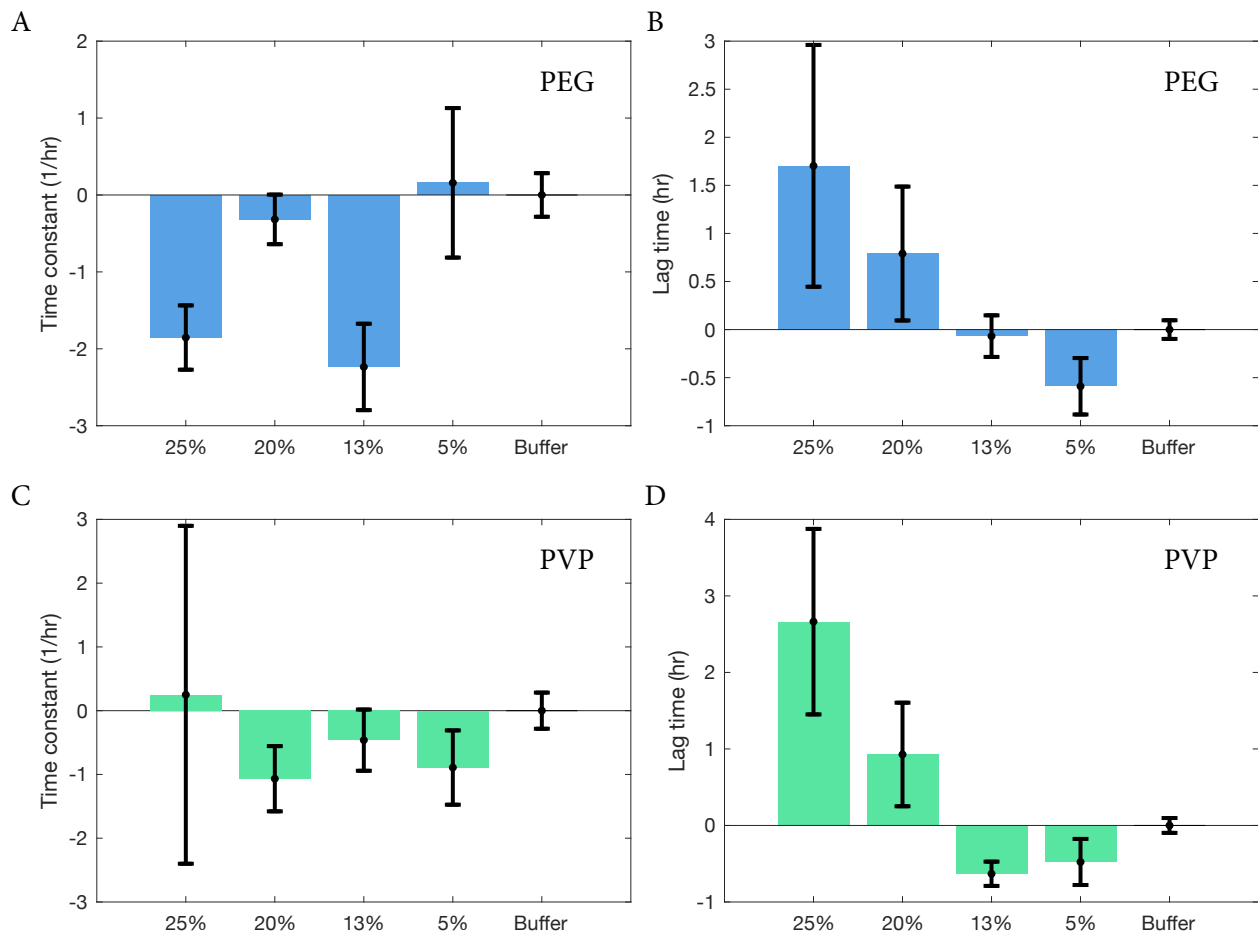
Several timecourses were run without crowders at varying pH. Table 5.2 shows the resulting fit parameters, given as lifetime  $\tau = 1/k$  and lag time  $T_\ell$ . Six replicates were run of each pH condition. One-way ANOVAs fail to reject the null hypothesis at the  $p = 0.05$  level, suggesting that FG124 aggregation is not affected by pH in the range 5-8.

Two crowders, PEG and PVP, warranted special attention. These inert crowders are commonly used interchangeably, but the results of timecourses containing 13% PEG or PVP suggest that they may in fact affect FG124 differently (Fig. 5.3). In order to investigate any differences between PEG and PVP, timecourses were run with varying crowder concentrations and analyzed as before. Mean parameter values are shown in Fig. 5.4. Statistics are given in Appendix I but do not strongly suggest differences between varying concentrations within the same crowder.

**Table 5.1:** Mean aggregation rate and lag time for all crowding agents, normalized to no-crowder condition. Number of replicates is  $N$ . Errors are standard errors of the mean.

Condition	Rate $k$ (1/hr)	Lag time $T_\ell$ (hr)	$N$
No crowder	$0 \pm 0.3$	$0 \pm 0.1$	32
Lysate	$2.7 \pm 1.6$	$-1.7 \pm 0.4$	16
Serine (19%)	$3.7 \pm 0.7$	$-0.7 \pm 0.05$	28
PEG (25%)	$-1.9 \pm 0.4$	$1.7 \pm 1.3$	7
PEG (20%)	$-0.3 \pm 0.3$	$0.8 \pm 0.7$	7
PEG (13%)	$-2.2 \pm 0.6$	$-0.07 \pm 0.2$	31
PEG (5%)	$0.2 \pm 1.0$	$-0.6 \pm 0.3$	7
PVP (25%)	$0.2 \pm 2.6$	$2.7 \pm 1.2$	7
PVP (20%)	$-1.1 \pm 0.5$	$0.9 \pm 0.7$	6
PVP (13%)	$-0.5 \pm 0.5$	$-0.6 \pm 0.2$	32
PVP (5%)	$-0.9 \pm 0.6$	$-0.5 \pm 0.3$	7

**Figure 5.4:** Aggregation rates and lag times for varying PEG and PVP concentrations, normalized to the no-crowding condition. Error bars are standard error of the mean.



### 5.1.3 Discussion

The results of the FG124 aggregation timecourses were difficult to interpret. The reproducibility of thioflavin T fluorescence assays is notoriously poor, and many timecourses were run with high variability in results. Results became more reproducible once the protocol was modified to include a glass or Teflon bead in each well, which seemed to assist with mixing during the shaking incubation between time points. Only data taken after this change are included in this dataset.

The results indicate changes in both lag time and aggregation lifetime of FG124 as a result of changing crowder conditions. The origin and magnitude of these changes is unclear. We chose to target the crowders PEG and PVP for further investigation. These crowders, while typically treated as interchangeable, behaved differently during the fluorescence timecourses (Fig. 5.3). When added to FG124 at a final concentration of 13% w/v, PEG reduced the aggregation rate below that of the no-crowder condition while PVP did not. Conversely, the lag time of the PEG condition remained approximately that of the no-crowder condition, but the lag time of the PVP condition decreased.

It is possible that the differences in aggregation time between PEG and PVP come from changes in viscosity. The two samples do have widely different viscosity, as measured by Steve Whitten. A 13% PEG solution in PTB has a dynamic viscosity of 15.87 mPa s, while that of a 13% PVP solution in PTB is 7.34 mPa s. Studies on aggregation of insulin or  $\alpha$  synuclein show varying effects of viscosity. Increasing viscosity has been shown to increase the lag time and decrease the aggregation rate [154, 155]. However, other studies suggest that the behavior is nonmonotonic depending on viscosity and the aggregation propensity of the protein [153, 164]. While 13% PEG and PVP solutions have significantly different viscosities, both fall into what Munishkina et al.

**Table 5.2:** FG124 aggregation lifetime and lag time with varying pH. Each condition run with 6 replicates in PTB buffer. Errors are standard errors of the mean.

pH	Lifetime $\tau$ (hr)	Lag time $T_\ell$ (hr)
5	$0.34 \pm 0.09$	$6.8 \pm 0.1$
6	$0.35 \pm 0.12$	$6.2 \pm 0.2$
7	$0.38 \pm 0.14$	$6.8 \pm 0.4$
8	$0.50 \pm 0.14$	$6.6 \pm 0.2$

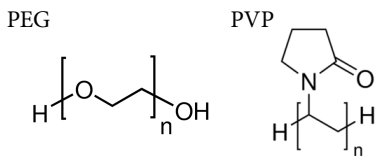


**Figure 5.5:** Chemical structures of PEG and PVP (Sigma).

characterize as the “high concentration” regime where fibrillation rate is expected to decrease [164]. The trends shown in Fig. 5.4 roughly agree with the hypothesis that crowding effects decrease lag time and increase aggregation rate for moderate crowder concentrations but have the opposite effect as viscosity effects begin to dominate.

To further probe the origin of the differences in aggregation, we recorded NMR spectra for FSFG and fluorescence spectra for FG124 and FSFG in crowded PEG and PVP solutions.

## 5.2 Fluorescence spectra

An obvious structural difference between PEG and PVP as inert crowders is the presence of an aromatic ring in PVP (Fig. 5.5). The phenylalanines of FG124 also possess an aromatic ring, making ring-stacking or other interactions with PVP more likely. As the phenylalanines are also key to transport factor binding, it is important to understand their interactions with crowders. The presence of the ring itself makes fluorescence spectroscopy a natural choice for probing the differences between PEG and PVP as crowders. While protein fluorescence is typically dominated by tryptophan and then tyrosine fluorescence, these amino acids are absent from both FG124 and FSFG, leaving phenylalanine with the strongest fluorescent signal. Fluorescence spectra were therefore collected near phenylalanine’s emission maximum from both fresh and aggregated FG124 in PEG or PVP.

### 5.2.1 Methods

#### 5.2.1.1 Sample preparation

FG124 was purified as described above and in Appendix C and stored in PTB with 7M GuHCl. Immediately before use, 130  $\mu\text{L}$  of 520  $\mu\text{M}$  FG124 was desalted with a Zeba spin desalting

column to remove the GuHCl. The resulting stock was used in the crowder samples, which had a final concentration of 340  $\mu\text{M}$  FG124.

#### 5.2.1.2 Fluorescence spectra

Fluorescence spectra were recorded using a Photon Technology International QM-6 fluorimeter. High concentrations of crowder were not possible due to background fluorescence, so samples containing 340  $\mu\text{M}$  FG124 along with 5% w/v PEG or PVP were tested, along with FG124 in PTB only. Blanks consisting of crowder only, buffer only, water, and FSFG in buffer were measured as well. FG124 samples were tested before aggregation (within two hours of GuHCl removal), allowed to incubate at room temperature overnight without shaking, and tested again after aggregation. FG124 samples were visibly cloudy after overnight incubation.

A micro quartz UV cuvette with approximately 12  $\mu\text{L}$  sample volume was used for all spectra. Between runs, the cuvette was rinsed three times with ethanol and five times with deionized water, and the exterior gently blotted with ethanol. When aggregated FG124 was used, it was necessary to first rinse the cuvette with 7M GuHCl, soak in 7M GuHCl for five minutes, and then follow the cleaning procedure above.

The fluorimeter was set to 4 nm excitation and emission slits and an excitation wavelength of 240 nm. Emission spectra were recorded at 1 nm intervals and automatically averaged over two runs. The PMT detector was set to 1000 V.

#### 5.2.1.3 Data processing

Data were normalized by averaging over two separate spectra and subtracting the appropriate blank spectrum containing the relevant crowder and buffer but no protein.

### 5.2.2 Results

Unfortunately, both PEG and PVP presented obstacles to the collection of UV fluorescence spectra. As shown in Fig. 5.6A, PEG displayed a prominent fluorescence peak centered at 320 nm.

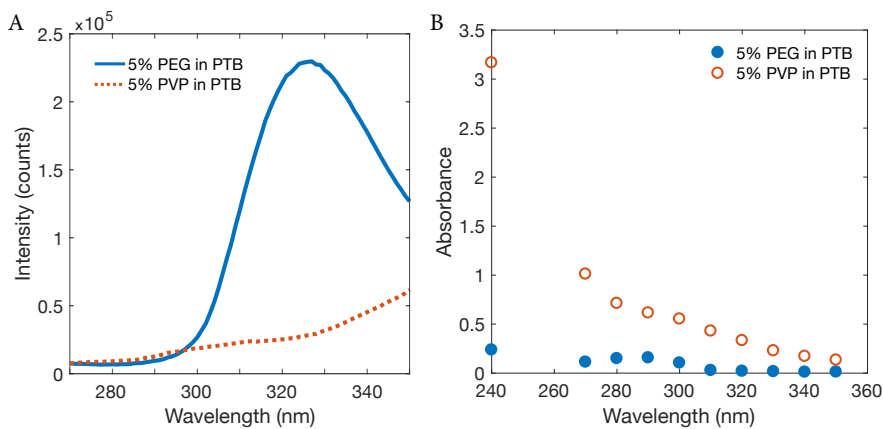


**Figure 5.6:** (A) Fluorescence spectrum of 5% w/v PEG and 5% w/v PVP in PTB. Normalized by subtracting PTB spectrum. (B) Absorbance spectrum of same samples. Measured on a SpectraMax spectrophotometer in a cuvette with a 1 cm path length. Normalized by subtracting PTB absorbance.

This may have been due to impurities in the PEG source, despite using the high-purity BioUltra brand from Sigma. At low PEG concentrations, this peak was still small compared to that of FG124 (Fig. 5.8B) and could be subtracted from the signal. However, the PEG peak limited the maximum concentration of crowder to 5%. PVP, on the contrary, did not display a large peak within the region of interest, but its absorbance is quite high from 240-280 nm (Fig. 5.6B). The high PEG absorbance suppresses the fluorescence signal from FG124 (Fig. 5.8C). While higher crowder concentrations might be expected to produce more dramatic effects on the FG124 fluorescence spectrum, the limit of 5% w/v does serve to minimize any viscosity effects.

Figure 5.7 compares the phenylalanine peaks in FSFG concat-1, fresh and aggregated FG124, and pure phenylalanine in water from [165]. The peak shifts slightly toward longer wavelengths as the data progress from pure phenylalanine to FSFG to fresh and aggregated FG124. Additionally, a shoulder develops at longer wavelengths.

Fresh and aggregated FG124 samples are compared in Figs. 5.8 and 5.9. The PEG sample showed the largest difference upon aggregation, both in peak height and location. In both crowder conditions, but not in the buffer condition, a small peak appears in the aggregated FG124 near 310 nm.

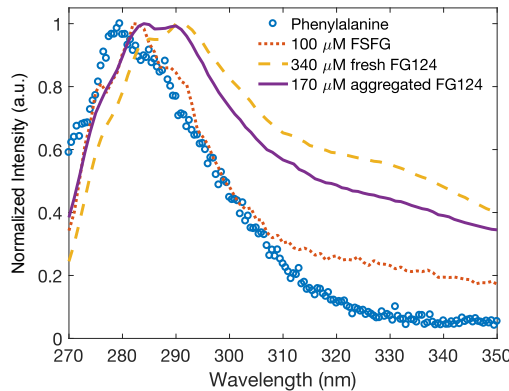


**Figure 5.7:** Fluorescence spectra of FSFG concat-1, FG124, and pure phenylalanine in water [165]. Excitation wavelength is 240 nm for all samples. Buffer spectra are subtracted from FSFG and FG124 traces, and all data are normalized to a maximum of one.

**Figure 5.8:** Fluorescence spectra of fresh and aggregated FG124 in crowded conditions: (A) PTB buffer only, (B) 5% w/v PEG, (C) 5% w/v PVP. All data normalized by subtracting appropriate blank.

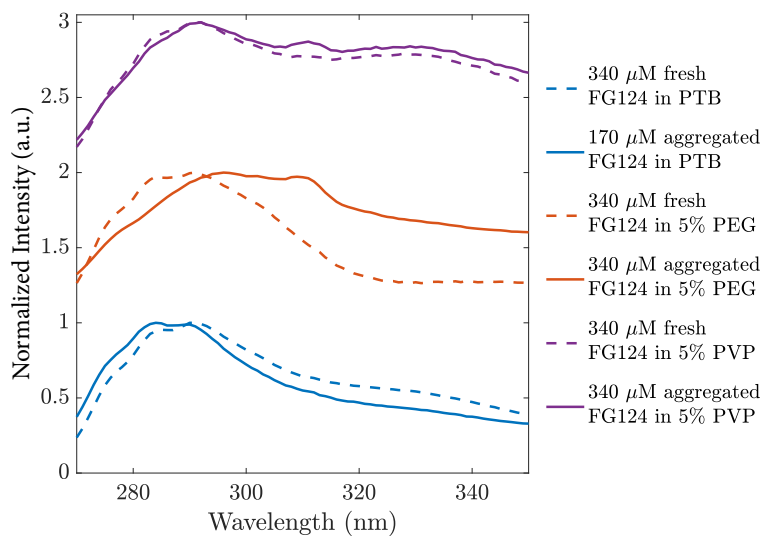
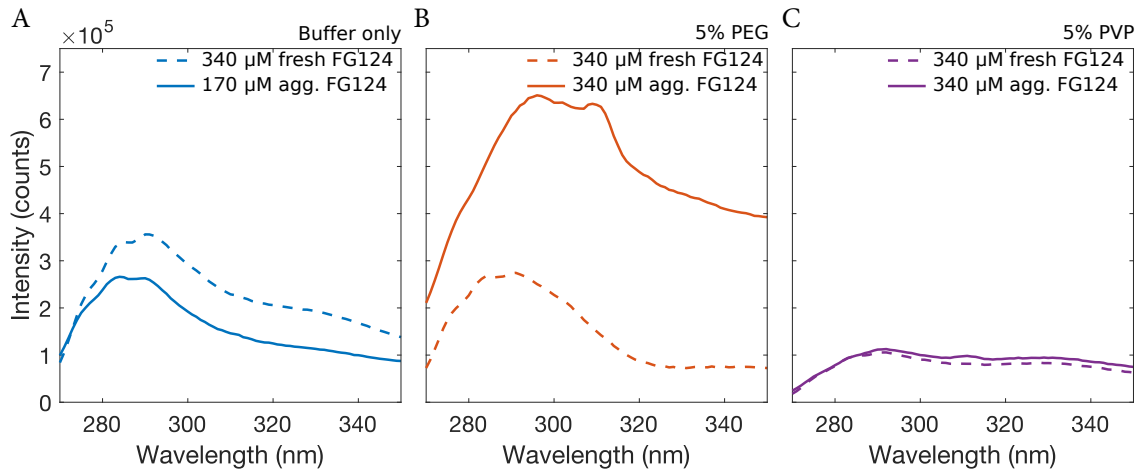


**Figure 5.9:** FG124 fluorescence comparison between 5% w/v PEG, 5% w/v PVP, and no crowder. All data normalized by subtracting appropriate blank and the resulting data are normalized to a maximum of one. Traces are offset for visual clarity.

### 5.2.3 Discussion

The fluorescence spectra of proteins can in principle be used to extract many types of information, from the properties of the environment in which its aromatic residues are located to protein folding and ligand binding [166]. This information comes from the many electronic states of the aromatic rings, which are often sensitive to the local environment and whose changes can cause shifts in fluorescence spectra. Of the three aromatic residues, tryptophan, with its double ring, dominates a protein's fluorescence, followed by tyrosine. Phenylalanine fluorescence is only measurable in the uncommon proteins which contain neither tryptophan or tyrosine. Fortunately, FSFG and FG124 contain no aromatic residues except for phenylalanine. The importance of those phenylalanine residues to binding both transport factors and other FG repeats makes them an interesting target for study by fluorimetry.

Given the rarity of detectable phenylalanine fluorescence in proteins, little literature exists interpreting its spectral shifts. That being the case, we can make an analogy to the tryptophan literature in broad strokes. The complex electronic states of tryptophan give rise to a number of designated spectral classes, as shown in Fig. 5.10. While very few proteins display any one of these classes in their pure form, the spectrum generally becomes redshifted when the tryptophan residue is surrounded by an increasingly hydrophilic environment [166, 167]. It is not clear that a similar shift should hold true in detail for phenylalanine, but it seems likely that changes in local chemical environment could lead to shifts in its emission spectrum as well. The emergence of the smaller redshifted peaks in the spectra of the aggregated FSFG in crowded conditions, but not in the buffer sample (Fig. 5.9), could well mean that the phenylalanines are interacting differently with the crowding agents. In order to further investigate differences in the environment of the phenylalanines in crowded conditions, we next measured their relaxation rates using NMR.

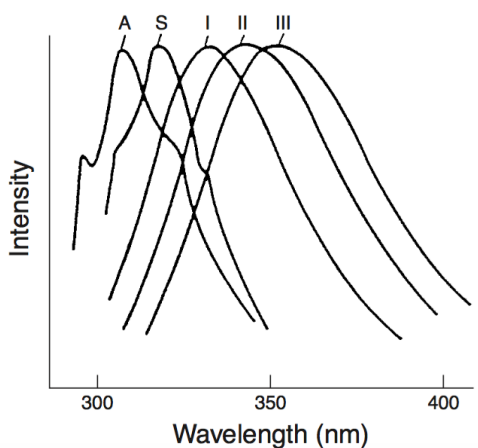


**Figure 5.10:** Qualitative depiction of spectral classes of tryptophan fluorescence. The classes correspond to differing solvent environments, with more hydrophilic environments generally being redshifted. Figure from [166].

### 5.3 NMR relaxation measurements

NMR uses the magnetic relaxation of unpaired spins, found in atoms such as  $^1\text{H}$ ,  $^{15}\text{N}$ , and  $^{13}\text{C}$  to probe the local chemical environment of those spins. When applied to isotopically labeled proteins, NMR can provide information on protein-protein interactions, structure, and relaxation rates. Measurements of the longitudinal ( $R_1$ ) and transverse ( $R_2$ ) relaxation rates of each residue give information about the relaxation of individual spins and the time for the collection of spins in a sample to go out of phase with each other, respectively. In particular,  $R_2$  increases when a residue is interacting strongly with its environment.

Kathryn Wall measured the relaxation rates of FSFG in 13% w/v PEG or PVP. While ideally FG124 would be used, its propensity towards aggregation makes NMR experiments, which take several hours at a minimum, impossible. Despite its differences in aggregation behavior, FSFG is a useful proxy in this case. FSFG and FG124 are of similar lengths, derived from the Nup Nsp1, and contain similar number of FG motifs (6 FSFG motifs and 8 varied FG motifs, respectively) (Appendix F). Given that we expect the crowders to particularly affect the phenylalanines, results from FSFG are likely a good estimate of FG124 behavior as well.

### 5.3.1 Methods

Isotopically-labeled, his-tagged  $^{15}\text{N}$  FSFG was expressed in BL21DE3 Gold cells in the pRSF plasmid (Kan resistant). Cells were grown in 1 L LB after inoculation with 1:500 preculture until reaching an OD<sub>600</sub> of 0.6-0.8. Cells were then pelleted by centrifuging for 10 minutes at 4000g and resuspended in a total of 1 L M9 salts pH 7.4 (10x M9 salts: 62 g/L Na<sub>2</sub>HPO<sub>4</sub>, 30 g/L KH<sub>2</sub>PO<sub>4</sub>, 5 g/L NaCl). After washing, cells were pelleted, resuspended in 1 L M9 minimal media with  $^{15}\text{N}$  ammonium chloride, and induced with 1 mM IPTG for 2-4 hours. The periplasmic matrix was then removed and the FSFG purified as described in Appendix C.

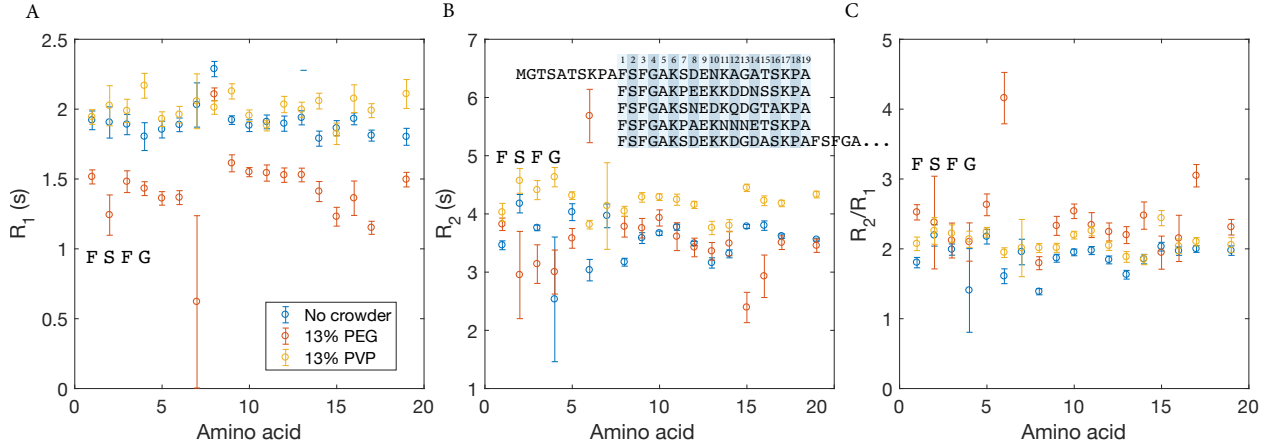
The NMR samples contained 13% w/v of either PEG or PVP, 140  $\mu\text{M}$  FSFG  $^{15}\text{N}$ , 10% D<sub>2</sub>O, 1% 15 mM TSP, and 1% 1mM DSS in PTB. Total sample volume was 336  $\mu\text{L}$ . Ideally the protein concentration would have been at least 300  $\mu\text{M}$ , but the presence of the crowders reduced the available volume for protein. An identical sample containing no crowders was also prepared.

NMR experiments were run by Kathryn Wall on an Inova 600 MHz. Using the standard  $^{15}\text{N}$ -HSQC experiment from the Varian BioPac, the parameter `relaxT` was adjusted for the measurement of  $T_1$  and  $T_2$  relaxation parameters. For measurement of  $T_1$ , `relaxT` was arrayed (0, 0.1, 0.2, 0.3, 0.4, 0.5, 0.6, 0.7, 0.8, 0.9 ms). For the measurement of  $T_2$ , `relaxT` was arrayed (0.01, 0.03, 0.05, 0.07, 0.09, 0.11, 0.13, 0.15, 0.17, 0.19, 0.21, 0.23, 0.25 ms). The data were processed using standard scripts in NMRPipe, and analyzed using CCPNmr Analysis software.

### 5.3.2 Results

Figure 5.11 shows the relaxation rates  $R_1$  and  $R_2$  of FSFG in 13% PEG, 13% PVP, or PTB without a crowder, along with the ratio  $R_2/R_1$ . Due to the disordered nature of FSFG, many peaks in the NMR spectra overlap. Amino acids of the same type experience less difference in their average local chemical environment than they would in an ordered protein, with the result that a single peak often corresponds to several amino acids. This effect is particularly pronounced for the FSFG motif itself, in which the six repeated motifs are almost entirely collapsed to four peaks, one

**Figure 5.11:** Relaxation rates for FSFG in 13% PEG, 13% PVP, or PTB only. The 19-amino-acid quasi-repeating unit that begins with the FSFG motif has been averaged over the first five repeats as shown. Experiments performed by Kathryn Wall. (A) Longitudinal relaxation rate  $R_1$ , (B) transverse relaxation rate  $R_2$ , (C) Ratio  $R_2/R_1$ .



for each residue of the sequence. The sole exception is the phenylalanine closest to the N-terminal, which has a peak distinct from the others. Therefore, we broke the sequence of the FSFG peptide into quasi-repeating segments, each 19 amino acids in length, which begin with an FSFG motif and contain the hydrophilic linker which separates it from the next FSFG (Fig. 5.11B, inset). The errors in  $R_1$  and  $R_2$  are given by the weighted average of the fit errors for the unique peaks that are being averaged [168]. The errors of the ratio  $R_2/R_1$  were propagated from  $R_1$  and  $R_2$  errors.

There are noticeable differences between the crowded conditions and buffer condition, which are likely due to a combination of viscosity effects and differences in interactions with the crowders. Surprisingly, the systemic differences in rates do not all correspond to viscosity changes. For example, the PVP sample has the highest  $R_1$  and  $R_2$  values overall, despite having an intermediate viscosity. The  $R_1$  values are significantly lower for the PEG sample than the other two, which also is not obviously explained by viscosity changes.

### 5.3.3 Discussion

There are noticeable differences between the relaxation rates in 13% PEG, 13% PVP, and without crowders whose source is not obvious. In addition to varying the crowding agent, the

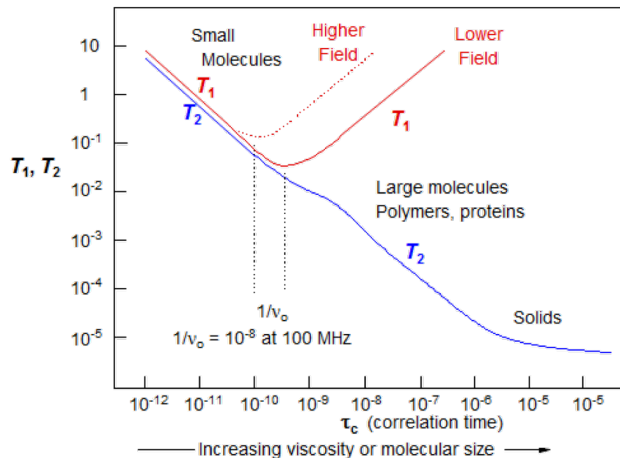


**Figure 5.12:** Approximate dependence of relaxation times  $T_1$  and  $T_2$  on solvent viscosity. Figure from [169].

viscosity varies from sample to sample, with buffer having the lowest and PEG the highest viscosity. Some differences in the rates are likely due to the change in viscosity, while others may be due to differences in the peptide's interaction with the crowders. As mentioned above, PVP shows the highest relaxation rates overall despite having an intermediate viscosity. On the other hand, the ratio  $R_2/R_1$  generally shows higher rates for PEG, then for PVP, with the lowest rates belonging to the buffer-only sample.

The typical behavior of relaxation times (with  $T_1 = 1/R_1$  and  $T_2 = 1/R_2$ ) as a function of viscosity is shown in Fig. 5.12 [169]. As viscosity increases, the transverse relaxation time  $T_2$  decreases monotonically. However, the longitudinal relaxation time  $T_1$  begins by decreasing, reaches a turnaround point, and increases afterwards. The location of the turnaround point  $\tau_0$  is related to the strength of the NMR magnetic field expressed as a frequency  $\nu_0$  by  $\tau_0 = 1/\nu_0$ . For the 600 MHz instrument used in these experiments,  $\tau_0 \approx 1 \times 10^{-9}$  s. Given that the measured rates are on the order of 1 s,  $T_1$  is likely in the region where it should decrease with increasing viscosity. In addition, the viscosities span an order of magnitude from buffer (1 mP s) to 13% PEG (15 mP s), and would be expected to produce a comparably large change in relaxation rates. Instead, the rates change by approximately 25% at most, and the PEG sample shows the lowest relaxation rates and therefore the largest relaxation times. Overall, the relaxation rates show features that are not obviously explained by changes in sample viscosity and may be due to differences in their interactions with the crowding agents.

#### 5.4 Conclusions

We used several methods to investigate FG Nup aggregation in crowded conditions, focusing on FG124 as a representative peptide. All methods indicate that there are indeed differences in aggregation and the resulting chemical environments depending on the presence and type of crowder. The aggregation timecourses pointed to differences between most of the crowders tested, and between PEG and PVP in particular. Since PEG and PVP are often used interchangeably as inert crowders, we pursued these differences using fluorimetry and NMR. Both reinforced the idea that there are in fact differences between FG124 behavior in these crowders. The fluorescence spectra of the aggregated FG124 in particular suggests that the phenylalanines behave differently in crowded conditions than in buffer only. Since FG repeats are involved not only to binding transport factors for selective transport, but also in forming transient crosslinks with other FG Nups, our results indicate that great care should be taken in determining what conditions to use to study Nups *in vitro*.

## Chapter 6

### Conclusions and future directions

Living systems contain many examples of selective filters which control the transport of all manner of macromolecules. In this work, we studied biofilters which allow rapid transport of highly specific targets, counterintuitively relying on binding interactions to promote rather than hinder flux. These filters often contain similar features, such as transient, multivalent binding and binding to flexible, dynamic tethers. In order to understand the presence of these features, we approached the problem through both modeling and experiment. Bound-state diffusion proved to be a key parameter for selectivity. While the theory and experimental setup were based on nuclear transport, they were not designed to exactly reproduce the nuclear pore, but to be applicable to a wider variety of biofilters.

We created a minimal model of the nuclear pore, containing very little beyond the diffusion of transport factors and their binding to FG Nups. Interestingly, even this highly simplified model was able to reproduce the selectivity properties of the nuclear pore, predicting that binding could increase the flux of a protein through this material up to 300-fold over the flux of an identical inert protein. The simplicity of our model made the key parameter clear: we could not reproduce the selectivity of the nuclear pore without allowing bound-state diffusion, that is, assuming that bound Nup - transport factor complexes were mobile within the pore. Plausible mechanisms of bound diffusion in the nuclear pore include tethered diffusion arising from the disordered, flexible nature of the Nups, and inter-chain hopping of the transport factor due to its binding multivalency.

We modeled both of these mechanisms and found that they allow for significant bound mobility and therefore high selectivity. These mechanisms may also be at work in other highly-specific, high-throughput biofilters.

After developing the minimal model of selectivity, we began developing a synthetic biofilter inspired by the nuclear pore with which to experimentally probe the effect of bound-state diffusion on selectivity. In order to capture the key features of selectivity, we designed hydrogels containing peptide tethers derived from FG Nups. The transport factor NTF2 served as a test protein whose diffusion we could compare with a similarly-size but nonbinding counterpart. Fluorescence recovery after photobleaching (FRAP) was used to determine the effective diffusion constants of both NTF2 and an inert protein, from which the bound diffusion constant was calculated. We measured a non-zero bound diffusion constant that is consistent with the predictions of our model, and tested the effect of varying Nup length on bound-state diffusion.

Additionally, we probed the aggregation behavior of an FG-Nup-derived peptide in several crowded conditions. We used a fluorescent aggregation assay as well as NMR and fluorimetry to investigate differences in the aggregated state between crowding conditions, and found that even inert crowders which are widely used interchangeably show differences in the local chemical environments of the peptide.

Although a true hydrogel-based selective biofilter proved challenging to design, our nuclear-pore-inspired material can be used to measure the bound-state diffusion of proteins. This parameter is likely important to a variety of problems involving rapid transport of highly-selective proteins. The model and biomaterials developed here could be used to investigate these systems more generally in the future. This work suggests that bound-state diffusion, particularly when resulting from transient, multivalent binding, may help explain a number of unusual biological filters.

## 6.1 Future directions

It would be interesting to apply our model of bound-state diffusion to other selective biofilters, particularly those like the ones described in Chapter 1, which share similarities with the nuclear

pore. One question which we are well-positioned to investigate using both our theoretical model and experimental setup is particle diffusion in mucus [76,82]. As described in Sec. 1.2.1, the mucus barrier in the lungs is an obstacle to drug delivery, because nanoparticles tend to get trapped in this barrier, which is constantly being cleared and replaced. Our bound-state diffusion model of flux through a barrier could be used to describe nanoparticles which interact with the mucus layer, particularly if we modify it to include a flux representing the clearance of mucus. It is currently not clear whether drug delivery is better accomplished with particles designed to bind to mucins or to avoid interactions [75,78]. Our model predicts that the flux of nanoparticles through the mucus layer will be higher with binding but only if the binding mechanism permits high mobility of the bound complex. A first step towards testing our model is measuring the diffusion of nanoparticles in mucus, an experiment that could be done using the flow chambers developed in Chapter 3. It would likely be possible to use both the model and experimental systems with only minor modifications to investigate nanoparticle diffusion and drug delivery through mucus barriers.

Another system with striking similarities to our bound-diffusion model of selectivity is the speed-stability paradox of transcription factor and DNA damage repair proteins that target specific sites on DNA (Sec. 1.2.2). In the case of the DNA damage repair protein poly(ADP-ribose) polymerase 1 (PARP1) in particular, PARP1 binds even intact chromatin with micromolar affinity, but it moves to the sites of DNA damage with a diffusion constant only an order of magnitude less than its diffusion in water [95,96]. If there is truly only negligible free PARP1 in the nucleus, and it is almost entirely bound to DNA, then all diffusion to sites of damage must be bound diffusion. Given the high diffusion constant measured, we might then expect to see evidence of the mechanisms which we think give rise to bound diffusion in the nuclear pore complex: multivalent binding and tethered diffusion.

Indeed, PARP1 contains four DNA binding domains and has been shown to possess a “hopping” mechanism to move between stands while bound [95]. Furthermore, recent unpublished data from Johannes Rudolph and the Luger group suggest that PARP1 may dimerize while bound to intact DNA searching for damage. Previous work has also indicated that PARP1 may dimerize,

though the context and extent of dimerization is unclear [170, 171]. At first glance, our model predicts that dimerization could increase the bound diffusion constant, provided it increases the rate of hopping between strands. Multivalent binding appears to be important to PARP1 diffusion in several ways. Tethered diffusion is also a plausible mechanism in this case, as there is evidence that chromatin is dynamic and could act as a flexible tether [123, 126]. Naive calculations which use only our tethered diffusion model and do not allow hopping are consistent with the calculated off-rate from intact DNA (Sec 2.4.1).

Finally, it is interesting that PARP1 binding to DNA is another example of a highly multivalent system, with several binding sites on each PARP1 and many on each DNA strand, for which *in vivo* affinity measurements are very difficult. Even affinity measurements to intact DNA as opposed to damaged are difficult to carry out *in vitro*, as most DNA *in vitro* is damaged somehow. This situation reminds me of the similar historical difficulty in measuring Nup - transport factor affinities, and the way that the field's understanding of the mechanisms of nuclear transport evolved as those measured values improved. If the problem of binding affinity in the nuclear pore is any indication, I would not be surprised to find that future calculations of PARP1's affinity for intact DNA show weaker binding than is currently accepted.

The similarities between the nuclear pore and PARP1 diffusion are fascinating, as is the problem of diffusion through a mucus barrier, and our model of selectivity is well-positioned to offer insight into all of these. While ideas of bound-state diffusion are already present in all of these fields, I think our model has particular value in clarifying why bound-state diffusion can lead to unusual selective filters and in suggesting practical mechanisms with which to engineer systems with bound diffusion. There are a surprisingly high number of examples of selective biofilters which use binding to increase flux, and our model provides new insight into how they might accomplish this remarkable task.

## Bibliography

- [1] B. L. Timney, B. Raveh, R. Mironksa, J. M. Trivedi, S. J. Kim, D. Russel, S. R. Wente, A. Sali, and M. P. Rout. Simple rules for passive diffusion through the nuclear pore complex. *J Cell Biol*, 215(1):57–76, October 2016.
- [2] V. N. Uversky. A decade and a half of protein intrinsic disorder: Biology still waits for physics. *Protein Science*, 22(6):693–+, June 2013. WOS:000319422500001.
- [3] P. E. Wright and H. J. Dyson. Intrinsically disordered proteins in cellular signalling and regulation. *Nature Reviews Molecular Cell Biology*, 16(1):18–29, January 2015.
- [4] I. V. Aramburu and E. A. Lemke. Floppy but not sloppy: Interaction mechanism of FG-nucleoporins and nuclear transport receptors. *Seminars in Cell & Developmental Biology*, 68:34–41, August 2017.
- [5] M. M. Babu, R. van der Lee, N. S. de Groot, and J. Gsponer. Intrinsically disordered proteins: Regulation and disease. *Current Opinion in Structural Biology*, 21(3):432–440, June 2011.
- [6] C. P. Brangwynne, P. Tompa, and R. V. Pappu. Polymer physics of intracellular phase transitions. *Nature Physics*, 11(11):899–904, November 2015.
- [7] M. Beck and E. Hurt. The nuclear pore complex: Understanding its function through structural insight. *Nature Reviews Molecular Cell Biology*, 18(2):73–89, February 2017.
- [8] S. S. Patel, B. J. Belmont, J. M. Sante, and M. F. Rexach. Natively Unfolded Nucleoporins Gate Protein Diffusion across the Nuclear Pore Complex. *Cell*, 129(1):83–96, April 2007.
- [9] C. Strambio-De-Castillia, M. Niepel, and M. P. Rout. The nuclear pore complex: Bridging nuclear transport and gene regulation. *Nature Reviews Molecular Cell Biology*, 11(7):490–501, July 2010.
- [10] L. J. Terry and S. R. Wente. Flexible Gates: Dynamic Topologies and Functions for FG-Nucleoporins in Nucleocytoplasmic Transport. *Eukaryotic Cell*, 8(12):1814–1827, December 2009.
- [11] L. E. Hough, K. Dutta, S. Sparks, D. B. Temel, A. Kamal, J. Tetenbaum-Novatt, M. P. Rout, and D. Cowburn. The molecular mechanism of nuclear transport revealed by atomic-scale measurements. *eLife*, 4:e10027, September 2015.

- [12] Y. Sakiyama, A. Mazur, L. E. Kapinos, and R. Y. H. Lim. Spatiotemporal dynamics of the nuclear pore complex transport barrier resolved by high-speed atomic force microscopy. *Nature Nanotechnology*, 11(8):719–723, August 2016.
- [13] L.-C. Tu and S. M. Musser. Single Molecule Studies of Nucleocytoplasmic Transport. *Biochimica et biophysica acta*, 1813(9):1607–1618, September 2011.
- [14] R. Moussavi-Baygi and M. R. K. Mofrad. Rapid Brownian Motion Primes Ultrafast Reconstruction of Intrinsically Disordered Phe-Gly Repeats Inside the Nuclear Pore Complex. *Scientific Reports*, 6, July 2016.
- [15] R. L. Schoch, L. E. Kapinos, and R. Y. H. Lim. Nuclear transport receptor binding avidity triggers a self-healing collapse transition in FG-nucleoporin molecular brushes. *Proceedings of the National Academy of Sciences of the United States of America*, 109(42):16911–16916, October 2012.
- [16] J. Yamada, J. L. Phillips, S. Patel, G. Goldfien, A. Calestagne-Morelli, H. Huang, R. Reza, J. Acheson, V. V. Krishnan, S. Newsam, A. Gopinathan, E. Y. Lau, M. E. Colvin, V. N. Uversky, and M. F. Rexach. A bimodal distribution of two distinct categories of intrinsically disordered structures with separate functions in FG nucleoporins. *Molecular & cellular proteomics: MCP*, 9(10):2205–2224, October 2010.
- [17] D. Ando, R. Zandi, Y. W. Kim, M. Colvin, M. Rexach, and A. Gopinathan. Nuclear Pore Complex Protein Sequences Determine Overall Copolymer Brush Structure and Function. *Biophysical Journal*, 106(9):1997–2007, May 2014.
- [18] M. Tagliazucchi, O. Peleg, M. Kroeger, Y. Rabin, and I. Szleifer. Effect of charge, hydrophobicity, and sequence of nucleoporins on the translocation of model particles through the nuclear pore complex. *Proceedings of the National Academy of Sciences of the United States of America*, 110(9):3363–3368, February 2013. WOS:000315841900039.
- [19] B. Zeitler and K. Weis. The FG-repeat asymmetry of the nuclear pore complex is dispensable for bulk nucleocytoplasmic transport *in vivo*. *The Journal of Cell Biology*, 167(4):583–590, November 2004.
- [20] L. A. Strawn, T. Shen, N. Shulga, D. S. Goldfarb, and S. R. Wente. Minimal nuclear pore complexes define FG repeat domains essential for transport. *Nature Cell Biology*, 6(3):197–206, March 2004.
- [21] S. W. Kowalczyk, L. Kapinos, T. R. Blosser, T. Magalhães, P. van Nies, R. Y. H. Lim, and C. Dekker. Single-molecule transport across an individual biomimetic nuclear pore complex. *Nature Nanotechnology*, 6(7):433–438, July 2011.
- [22] T. Jovanovic-Talisman, J. Tetenbaum-Novatt, A. S. McKenney, A. Zilman, R. Peters, M. P. Rout, and B. T. Chait. Artificial nanopores that mimic the transport selectivity of the nuclear pore complex. *Nature*, 457(7232):1023–1027, February 2009.
- [23] B. Pyhtila and M. Rexach. A Gradient of Affinity for the Karyopherin Kap95p along the Yeast Nuclear Pore Complex. *Journal of Biological Chemistry*, 278(43):42699–42709, October 2003.

- [24] D. Gilchrist, B. Mykytka, and M. Rexach. Accelerating the Rate of Disassembly of Karyopherin-Cargo Complexes. *Journal of Biological Chemistry*, 277(20):18161–18172, May 2002.
- [25] J. Tetenbaum-Novatt, L. E. Hough, R. Mironcka, A. S. McKenney, and M. P. Rout. Nucleocytoplasmic Transport: A Role for Nonspecific Competition in Karyopherin-Nucleoporin Interactions. *Molecular & Cellular Proteomics : MCP*, 11(5):31–46, May 2012.
- [26] S. Milles, D. Mercadante, I. V. Aramburu, M. R. Jensen, N. Banterle, C. Koehler, S. Tyagi, J. Clarke, S. L. Shammas, M. Blackledge, F. Gräter, and E. A. Lemke. Plasticity of an Ultrafast Interaction between Nucleoporins and Nuclear Transport Receptors. *Cell*, 163(3):734–745, October 2015.
- [27] R. Hayama, S. Sparks, L. M. Hecht, K. Dutta, J. M. Karp, C. M. Cabana, M. P. Rout, and D. Cowburn. Thermodynamic characterization of the multivalent interactions underlying rapid and selective translocation through the nuclear pore complex. *Journal of Biological Chemistry*, 293(12):4555–4563, 2018.
- [28] T. Jovanovic-Talisman and A. Zilman. Protein Transport by the Nuclear Pore Complex: Simple Biophysics of a Complex Biomachine. *Biophysical Journal*, 113(1):6–14, July 2017.
- [29] L. E. Kapinos, B. Huang, C. Rencurel, and R. Y. H. Lim. Karyopherins regulate nuclear pore complex barrier and transport function. *J Cell Biol*, page jcb.201702092, September 2017.
- [30] S. H. Yoshimura and T. Hirano. HEAT repeats – versatile arrays of amphiphilic helices working in crowded environments? *J Cell Sci*, 129(21):3963–3970, November 2016.
- [31] Y. M. Chook and K. E. Süel. Nuclear import by karyopherin-*Bs*: Recognition and inhibition. *Biochimica et Biophysica Acta (BBA) - Molecular Cell Research*, 1813(9):1593–1606, September 2011.
- [32] L. E. Kapinos, R. L. Schoch, R. S. Wagner, K. D. Schleicher, and R. Y. H. Lim. Karyopherin-Centric Control of Nuclear Pores Based on Molecular Occupancy and Kinetic Analysis of Multivalent Binding with FG Nucleoporins. *Biophysical Journal*, 115(12):2512, December 2018.
- [33] K. D. Schleicher, S. L. Dettmer, L. E. Kapinos, S. Pagliara, U. F. Keyser, S. Jeney, and R. Y. H. Lim. Selective transport control on molecular velcro made from intrinsically disordered proteins. *Nature Nanotechnology*, 9(7):525–530, July 2014.
- [34] L. E. Kapinos, R. L. Schoch, R. S. Wagner, K. D. Schleicher, and R. Y. Lim. Karyopherin-Centric Control of Nuclear Pores Based on Molecular Occupancy and Kinetic Analysis of Multivalent Binding with FG Nucleoporins. *Biophysical Journal*, 106(8):1751–1762, April 2014.
- [35] D. Görlich, N. Panté, U. Kutay, U. Aebi, and F. R. Bischoff. Identification of different roles for RanGDP and RanGTP in nuclear protein import. *The EMBO Journal*, 15(20):5584–5594, October 1996.
- [36] M. Stewart. Molecular mechanism of the nuclear protein import cycle. *Nature Reviews. Molecular Cell Biology*, 8(3):195–208, March 2007.

- [37] K. Ribbeck, G. Lipowsky, H. M. Kent, M. Stewart, and D. Görlich. NTF2 mediates nuclear import of Ran. *The EMBO Journal*, 17(22):6587–6598, November 1998.
- [38] R. Bayliss, K. Ribbeck, D. Akin, H. M. Kent, C. M. Feldherr, D. Görlich, and M. Stewart. Interaction between NTF2 and xFxFG-containing nucleoporins is required to mediate nuclear import of RanGDP 1. *Journal of Molecular Biology*, 293(3):579–593, October 1999.
- [39] K. Ribbeck and D. Görlich. Kinetic analysis of translocation through nuclear pore complexes. *The EMBO Journal*, 20(6):1320–1330, March 2001.
- [40] J. P. Siebrasse and R. Peters. Rapid translocation of NTF2 through the nuclear pore of isolated nuclei and nuclear envelopes. *EMBO Reports*, 3(9):887–892, September 2002.
- [41] N. I. Kiskin, J. P. Siebrasse, and R. Peters. Optical Micowell Assay of Membrane Transport Kinetics. *Biophysical Journal*, 85(4):2311–2322, October 2003.
- [42] G. J. Stanley, A. Fassati, and B. W. Hoogenboom. Biomechanics of the transport barrier in the nuclear pore complex. *Seminars in Cell & Developmental Biology*, 68:42–51, August 2017.
- [43] K. E. Knockenhauer and T. U. Schwartz. The Nuclear Pore Complex as a Flexible and Dynamic Gate. *Cell*, 164(6):1162–1171, March 2016.
- [44] A. Paradise, M. K. Levin, G. Korza, and J. H. Carson. Significant proportions of nuclear transport proteins with reduced intracellular mobilities resolved by fluorescence correlation spectroscopy. *Journal of molecular biology*, 365(1):50–65, January 2007.
- [45] W. Yang and S. M. Musser. Nuclear import time and transport efficiency depend on importin  $\beta$  concentration. *The Journal of Cell Biology*, 174(7):951–961, September 2006.
- [46] T. Dange, D. Grünwald, A. Grünwald, R. Peters, and U. Kubitscheck. Autonomy and robustness of translocation through the nuclear pore complex: A single-molecule study. *The Journal of Cell Biology*, 183(1):77–86, 2008.
- [47] U. Kubitscheck, D. Grünwald, A. Hoekstra, D. Rohleider, T. Kues, J. P. Siebrasse, and R. Peters. Nuclear transport of single molecules. *The Journal of Cell Biology*, 168(2):233–243, January 2005.
- [48] M. Elbaum. Polymers in the Pore. *Science*, 314(5800):766–767, November 2006.
- [49] S. Frey, R. P. Richter, and D. Görlich. FG-Rich Repeats of Nuclear Pore Proteins Form a Three-Dimensional Meshwork with Hydrogel-Like Properties. *Science*, 314(5800):815–817, November 2006.
- [50] S. Frey and D. Görlich. A Saturated FG-Repeat Hydrogel Can Reproduce the Permeability Properties of Nuclear Pore Complexes. *Cell*, 130(3):512–523, August 2007.
- [51] C. Ader, S. Frey, W. Maas, H. B. Schmidt, D. Görlich, and M. Baldus. Amyloid-like interactions within nucleoporin FG hydrogels. *Proceedings of the National Academy of Sciences*, 107(14):6281–6285, June 2010.

- [52] M. Kim, W. G. Chen, J. W. Kang, M. J. Glassman, K. Ribbeck, and B. D. Olsen. Artificially Engineered Protein Hydrogels Adapted from the Nucleoporin Nsp1 for Selective Biomolecular Transport. *Advanced materials* (Deerfield Beach, Fla.), 27(28):4207–4212, July 2015.
- [53] T. Bickel and R. Bruinsma. The Nuclear Pore Complex Mystery and Anomalous Diffusion in Reversible Gels. *Biophysical Journal*, 83(6):3079–3087, December 2002.
- [54] C. Gu, A. Vovk, T. Zheng, R. D. Coalson, and A. Zilman. The Role of Cohesiveness in the Permeability of the Spatial Assemblies of FG Nucleoporins. *Biophysical Journal*, 116(7):1204–1215, April 2019.
- [55] M. P. Rout, J. D. Aitchison, A. Suprapto, K. Hjertaas, Y. Zhao, and B. T. Chait. The Yeast Nuclear Pore Complex Composition, Architecture, and Transport Mechanism. *The Journal of Cell Biology*, 148(4):635–652, February 2000.
- [56] R. Y. H. Lim, U. Aebi, and B. Fahrenkrog. Towards reconciling structure and function in the nuclear pore complex. *Histochemistry and Cell Biology*, 129(2):105–116, February 2008.
- [57] R. S. Wagner, L. E. Kapinos, N. J. Marshall, M. Stewart, and R. Y. H. Lim. Promiscuous Binding of Karyopherin $\beta$ 1 Modulates FG Nucleoporin Barrier Function and Expedites NTF2 Transport Kinetics. *Biophysical Journal*, 108(4):918–927, February 2015.
- [58] R. Zahn, D. Osmanović, S. Ehret, C. A. Callis, S. Frey, M. Stewart, C. You, D. Görlich, B. W. Hoogenboom, and R. P. Richter. A physical model describing the interaction of nuclear transport receptors with FG nucleoporin domain assemblies. *eLife*, 5:e14119, April 2016.
- [59] A. Vovk, C. Gu, M. G. Opferman, L. E. Kapinos, R. Y. Lim, R. D. Coalson, D. Jasnow, and A. Zilman. Simple biophysics underpins collective conformations of the intrinsically disordered proteins of the Nuclear Pore Complex. *eLife*, 5:e10785, May 2016.
- [60] A. E. Nasrabad, D. Jasnow, A. Zilman, and R. D. Coalson. Precise control of polymer coated nanopores by nanoparticle additives: Insights from computational modeling. *Journal of Chemical Physics*, 145(6):064901, August 2016. WOS:000381680300043.
- [61] J. S. Mincer and S. M. Simon. Simulations of nuclear pore transport yield mechanistic insights and quantitative predictions. *Proceedings of the National Academy of Sciences of the United States of America*, 108(31):E351–358, August 2011.
- [62] A. Zilman, S. D. Talia, B. T. Chait, M. P. Rout, and M. O. Magnasco. Efficiency, Selectivity, and Robustness of Nucleocytoplasmic Transport. *PLOS Computational Biology*, 3(7):e125, July 2007.
- [63] L.-C. Tu, G. Fu, A. Zilman, and S. M. Musser. Large cargo transport by nuclear pores: Implications for the spatial organization of FG-nucleoporins. *The EMBO journal*, 32(24):3220–3230, December 2013.
- [64] J. Tetenbaum-Novatt, L. E. Hough, R. Mironksa, A. S. McKenney, and M. P. Rout. Nucleocytoplasmic Transport: A Role for Nonspecific Competition in Karyopherin-Nucleoporin Interactions. *Molecular & Cellular Proteomics : MCP*, 11(5):31–46, May 2012.

- [65] A. Zilman. Effects of Multiple Occupancy and Interparticle Interactions on Selective Transport through Narrow Channels: Theory versus Experiment. *Biophysical Journal*, 96(4):1235–1248, February 2009.
- [66] A. Zilman, S. D. Talia, T. Jovanovic-Talisman, B. T. Chait, M. P. Rout, and M. O. Magnasco. Enhancement of Transport Selectivity through Nano-Channels by Non-Specific Competition. *PLOS Computational Biology*, 6(6):e1000804, June 2010.
- [67] B. L. Timney, J. Tetenbaum-Novatt, D. S. Agate, R. Williams, W. Zhang, B. T. Chait, and M. P. Rout. Simple kinetic relationships and nonspecific competition govern nuclear import rates in vivo. *J Cell Biol*, 175(4):579–593, November 2006.
- [68] Y. J. Yang, D. J. Mai, T. J. Dursch, and B. D. Olsen. Nucleopore-Inspired Polymer Hydrogels for Selective Biomolecular Transport. *Biomacromolecules*, September 2018.
- [69] A. N. Ananth, A. Mishra, S. Frey, A. Dwarkasing, R. Versloot, E. van der Giessen, D. Görlich, P. Onck, and C. Dekker. Spatial structure of disordered proteins dictates conductance and selectivity in nuclear pore complex mimics. *eLife*, 7:e31510, February 2018.
- [70] S. Frey and D. Görlich. FG/FxFG as well as GLFG repeats form a selective permeability barrier with self-healing properties. *The EMBO Journal*, 28(17):2554–2567, September 2009.
- [71] A. K. Friedman and L. A. Baker. Synthetic hydrogel mimics of the nuclear pore complex display selectivity dependent on FG-repeat concentration and electrostatics. *Soft Matter*, 12(47):9477–9484, November 2016.
- [72] P. D. E. Fisher, Q. Shen, B. Akpinar, L. K. Davis, K. K. H. Chung, D. Baddeley, A. Saric, T. J. Melia, B. W. Hoogenboom, C. Lin, and C. P. Lusk. A Programmable DNA Origami Platform for Organizing Intrinsically Disordered Nucleoporins within Nanopore Confinement. *ACS nano*, January 2018.
- [73] T. Carlson, J. Lock, and R. Carrier. Engineering the Mucus Barrier. *Annual Review of Biomedical Engineering*, 20(1):197–220, 2018.
- [74] A. Popov, L. Schopf, J. Bourassa, and H. Chen. Enhanced pulmonary delivery of fluticasone propionate in rodents by mucus-penetrating nanoparticles. *International Journal of Pharmaceutics*, 502(1):188–197, April 2016.
- [75] A. F. L. Schneider and C. P. R. Hackenberger. Fluorescent labelling in living cells. *Current Opinion in Biotechnology*, 48:61–68, December 2017.
- [76] J. Witten and K. Ribbeck. The particle in the spider’s web: Transport through biological hydrogels. *Nanoscale*, May 2017.
- [77] S. K. Lai, Y.-Y. Wang, K. Hida, R. Cone, and J. Hanes. Nanoparticles reveal that human cervicovaginal mucus is riddled with pores larger than viruses. *Proceedings of the National Academy of Sciences*, 107(2):598–603, January 2010.
- [78] S. K. Lai, J. S. Suk, A. Pace, Y.-Y. Wang, M. Yang, O. Mert, J. Chen, J. Kim, and J. Hanes. Drug carrier nanoparticles that penetrate human chronic rhinosinusitis mucus. *Biomaterials*, 32(26):6285–6290, September 2011.

- [79] N. A. Peppas and P. A. Buri. Surface, interfacial and molecular aspects of polymer bioadhesion on soft tissues. *Journal of Controlled Release*, 2:257–275, November 1985.
- [80] Y. Shang, K. Inthavong, and J. Tu. Development of a computational fluid dynamics model for mucociliary clearance in the nasal cavity. *Journal of Biomechanics*, 85:74–83, March 2019.
- [81] J. C. Lay, M. R. Stang, P. E. Fisher, J. R. Yankaskas, and W. D. Bennett. Airway retention of materials of different solubility following local intrabronchial deposition in dogs. *Journal of Aerosol Medicine: The Official Journal of the International Society for Aerosols in Medicine*, 16(2):153–166, 2003.
- [82] J. M. Newby, I. Seim, M. Lysy, Y. Ling, J. Huckaby, S. K. Lai, and M. G. Forest. Technological strategies to estimate and control diffusive passage times through the mucus barrier in mucosal drug delivery. *Advanced Drug Delivery Reviews*, 124:64–81, January 2018.
- [83] X. Huang, J. Chisholm, J. Zhuang, Y. Xiao, G. Duncan, X. Chen, J. S. Suk, and J. Hanes. Protein nanocages that penetrate airway mucus and tumor tissue. *Proceedings of the National Academy of Sciences*, 114(32):E6595–E6602, August 2017.
- [84] P. Mastorakos, A. L. da Silva, J. Chisholm, E. Song, W. K. Choi, M. P. Boyle, M. M. Morales, J. Hanes, and J. S. Suk. Highly compacted biodegradable DNA nanoparticles capable of overcoming the mucus barrier for inhaled lung gene therapy. *Proceedings of the National Academy of Sciences*, 112(28):8720–8725, July 2015.
- [85] B. Porsio, E. F. Craparo, N. Mauro, G. Giannona, and G. Cavallaro. Mucus and Cell-Penetrating Nanoparticles Embedded in Nano-into-Micro Formulations for Pulmonary Delivery of Ivacaftor in Patients with Cystic Fibrosis. *ACS Applied Materials & Interfaces*, 10(1):165–181, January 2018.
- [86] B. C. Tang, M. Dawson, S. K. Lai, Y.-Y. Wang, J. S. Suk, M. Yang, P. Zeitlin, M. P. Boyle, J. Fu, and J. Hanes. Biodegradable polymer nanoparticles that rapidly penetrate the human mucus barrier. *Proceedings of the National Academy of Sciences of the United States of America*, 106(46):19268–19273, November 2009.
- [87] L. Mirny, M. Slutsky, Z. Wunderlich, A. Tafvizi, J. Leith, and A. Kosmrlj. How a protein searches for its site on DNA: The mechanism of facilitated diffusion. *Journal of Physics A: Mathematical and Theoretical*, 42(43):434013, October 2009.
- [88] J. Iwahara and Y. Levy. Speed-stability paradox in DNA-scanning by zinc-finger proteins. *Transcription*, 4(2):58–61, March 2013.
- [89] S. E. Halford. An end to 40 years of mistakes in DNA–protein association kinetics? *Biochemical Society Transactions*, 37(2):343–348, April 2009.
- [90] B. Raveh, J. M. Karp, S. Sparks, K. Dutta, M. P. Rout, A. Sali, and D. Cowburn. Slide-and-exchange mechanism for rapid and selective transport through the nuclear pore complex. *Proceedings of the National Academy of Sciences*, 113(18):E2489–E2497, May 2016.
- [91] M. Doucette and G. M. Clore. Global jumping and domain-specific intersegment transfer between DNA cognate sites of the multidomain transcription factor Oct-1. *Proceedings of the National Academy of Sciences*, 105(37):13871–13876, September 2008.

- [92] S. E. Halford, A. J. Welsh, and M. D. Szczelkun. Enzyme-mediated DNA looping. *Annual Review of Biophysics and Biomolecular Structure*, 33:1–24, 2004.
- [93] L. Zandarashvili, A. Esadze, D. Vuzman, C. A. Kemme, Y. Levy, and J. Iwahara. Balancing between affinity and speed in target DNA search by zinc-finger proteins via modulation of dynamic conformational ensemble. *Proceedings of the National Academy of Sciences*, 112(37):E5142–E5149, September 2015.
- [94] M. V. Sukhanova, S. Abrakhi, V. Joshi, D. Pastre, M. M. Kutuzov, R. O. Anarbaev, P. A. Curmi, L. Hamon, and O. I. Lavrik. Single molecule detection of PARP1 and PARP2 interaction with DNA strand breaks and their poly(ADP-ribosyl)ation using high-resolution AFM imaging. *Nucleic Acids Research*, 44(6):e60–e60, April 2016.
- [95] J. Rudolph, J. Mahadevan, P. Dyer, and K. Luger. Poly(ADP-ribose) polymerase 1 searches DNA via a ‘monkey bar’ mechanism. *eLife*, 7:e37818, August 2018.
- [96] J. Mahadevan, J. Rudolph, A. Jha, J. W. Tay, J. Dragavon, E. M. Grumstrup, and K. Luger. Q-FADD: A mechanistic approach for modeling the accumulation of proteins at sites of DNA damage by free diffusion. *bioRxiv*, page 373043, July 2018.
- [97] M. Feric, N. Vaidya, T. S. Harmon, D. M. Mitrea, L. Zhu, T. M. Richardson, R. W. Krizwicki, R. V. Pappu, and C. P. Brangwynne. Coexisting Liquid Phases Underlie Nucleolar Subcompartments. *Cell*, 165(7):1686–1697, June 2016.
- [98] N. Shiina. Liquid- and solid-like RNA granules form through specific scaffold proteins and combine into biphasic granules. *Journal of Biological Chemistry*, 294(10):3532–3548, August 2019.
- [99] A. E. Posey, A. S. Holehouse, and R. V. Pappu. Chapter One - Phase Separation of Intrinsically Disordered Proteins. In E. Rhoades, editor, *Methods in Enzymology*, volume 611 of *Intrinsically Disordered Proteins*, pages 1–30. Academic Press, January 2018.
- [100] J. Wang, J.-M. Choi, A. S. Holehouse, H. O. Lee, X. Zhang, M. Jahnel, S. Maharana, R. Lemaitre, A. Pozniakovsky, D. Drechsel, I. Poser, R. V. Pappu, S. Alberti, and A. A. Hyman. A Molecular Grammar Governing the Driving Forces for Phase Separation of Prion-like RNA Binding Proteins. *Cell*, 174(3):688–699.e16, July 2018.
- [101] A. Catalano and D. H. O’Day. Evidence for nucleolar subcompartments in Dictyostelium. *Biochemical and Biophysical Research Communications*, 456(4):901–907, January 2015.
- [102] D. H. O’Day. Proteins of the Nucleolus of Dictyostelium discoideum: Nucleolar Compartmentalization, Targeting Sequences, Protein Translocations and Binding Partners. *Cells*, 8(2):167, February 2019.
- [103] S. Jain, J. R. Wheeler, R. W. Walters, A. Agrawal, A. Barsic, and R. Parker. ATPase-Modulated Stress Granules Contain a Diverse Proteome and Substructure. *Cell*, 164(3):487–498, January 2016.
- [104] L. Ristroph, A. J. Bergou, G. J. Berman, J. Guckenheimer, Z. J. Wang, and I. Cohen. Dynamics, Control, and Stabilization of Turning Flight in Fruit Flies. In S. Childress, A. Hosoi, W. W. Schultz, and J. Wang, editors, *Natural Locomotion in Fluids and on Surfaces*,

- The IMA Volumes in Mathematics and Its Applications, pages 83–99. Springer New York, 2012.
- [105] A. C. Noel and D. L. Hu. Cats use hollow papillae to wick saliva into fur. *Proceedings of the National Academy of Sciences*, 115(49):12377–12382, December 2018.
  - [106] S. J. Gerbode, J. R. Puzy, A. G. McCormick, and L. Mahadevan. How the Cucumber Tendril Coils and Overwinds. *Science*, 337(6098):1087–1091, August 2012.
  - [107] J. Pulupa, M. Rachh, M. D. Tomasini, J. S. Mincer, and S. M. Simon. A coarse-grained computational model of the nuclear pore complex predicts Phe-Gly nucleoporin dynamics. *The Journal of General Physiology*, page jgp.201711769, September 2017.
  - [108] S. Pagliara, S. L. Dettmer, and U. F. Keyser. Channel-facilitated diffusion boosted by particle binding at the channel entrance. *Physical Review Letters*, 113(4):048102, July 2014.
  - [109] A. R. Lowe, J. H. Tang, J. Yassif, M. Graf, W. Y. Huang, J. T. Groves, K. Weis, and J. T. Liphardt. Importin- $\beta$  modulates the permeability of the nuclear pore complex in a Ran-dependent manner. *eLife*, 4:e04052, March 2015.
  - [110] W. Yang, J. Gelles, and S. M. Musser. Imaging of single-molecule translocation through nuclear pore complexes. *Proceedings of the National Academy of Sciences of the United States of America*, 101(35):12887–12892, August 2004.
  - [111] M. Stefferson. Dynamics of Crowded and Active Biological Systems. *Physics Graduate Theses & Dissertations*, January 2018.
  - [112] H. B. Schmidt and D. Görlich. Nup98 FG domains from diverse species spontaneously phase-separate into particles with nuclear pore-like permselectivity. *eLife*, 4:e04251, January 2015.
  - [113] D. Frenkiel-Krispin, B. Maco, U. Aebi, and O. Medalia. Structural Analysis of a Metazoan Nuclear Pore Complex Reveals a Fused Concentric Ring Architecture. *Journal of Molecular Biology*, 395(3):578–586, January 2010.
  - [114] T. Maimon, N. Elad, I. Dahan, and O. Medalia. The Human Nuclear Pore Complex as Revealed by Cryo-Electron Tomography. *Structure*, 20(6):998–1006, June 2012.
  - [115] F. Cardarelli and E. Gratton. In Vivo Imaging of Single-Molecule Translocation Through Nuclear Pore Complexes by Pair Correlation Functions. *PLOS ONE*, 5(5):e10475, May 2010.
  - [116] R. Y. H. Lim, B. Fahrenkrog, J. Köser, K. Schwarz-Herion, J. Deng, and U. Aebi. Nanomechanical Basis of Selective Gating by the Nuclear Pore Complex. *Science*, 318(5850):640–643, October 2007.
  - [117] S. Milles and E. A. Lemke. Mapping Multivalency and Differential Affinities within Large Intrinsically Disordered Protein Complexes with Segmental Motion Analysis. *Angewandte Chemie International Edition*, 53(28):7364–7367, July 2014.
  - [118] J. Howard. *Mechanics of Motor Proteins and Cytoskeleton*. Sinauer Associates, 1st edition, 2001.
  - [119] M. Doi and S. F. Edwards. *The Theory of Polymer Dynamics*. Clarendon Press, 1988. Google-Books-ID: dMzGyWs3GKcC.

- [120] V. Receveur-Bréchot and D. Durand. How Random are Intrinsically Disordered Proteins? A Small Angle Scattering Perspective. *Current Protein & Peptide Science*, 13(1):55–75, February 2012.
- [121] R. Blackwell, C. Edelmaier, O. Sweezy-Schindler, A. Lamson, Z. R. Gergely, E. O’Toole, A. Crapo, L. E. Hough, J. R. McIntosh, M. A. Glaser, and M. D. Betterton. Physical determinants of bipolar mitotic spindle assembly and stability in fission yeast. *Science Advances*, 3(1):e1601603, January 2017.
- [122] W. A. McGuinness, N. Malachowa, and F. R. DeLeo. Vancomycin Resistance in Staphylococcus aureus. *The Yale Journal of Biology and Medicine*, 90(2):269–281, June 2017.
- [123] T. Nozaki, R. Imai, M. Tanbo, R. Nagashima, S. Tamura, T. Tani, Y. Joti, M. Tomita, K. Hibino, M. T. Kanemaki, K. S. Wendt, Y. Okada, T. Nagai, and K. Maeshima. Dynamic Organization of Chromatin Domains Revealed by Super-Resolution Live-Cell Imaging. *Molecular Cell*, 67(2):282–293.e7, July 2017.
- [124] M. Kruithof, F.-T. Chien, A. Routh, C. Logie, D. Rhodes, and J. van Noort. Single-molecule force spectroscopy reveals a highly compliant helical folding for the 30-nm chromatin fiber. *Nature Structural & Molecular Biology*, 16(5):534–540, May 2009.
- [125] D. Norouzi and V. B. Zhurkin. Dynamics of Chromatin Fibers: Comparison of Monte Carlo Simulations with Force Spectroscopy. *Biophysical Journal*, 115(9):1644–1655, November 2018.
- [126] K. Maeshima, S. Ide, K. Hibino, and M. Sasai. Liquid-like behavior of chromatin. *Current Opinion in Genetics & Development*, 37:36–45, April 2016.
- [127] S. Hihara, C.-G. Pack, K. Kaizu, T. Tani, T. Hanafusa, T. Nozaki, S. Takemoto, T. Yoshimi, H. Yokota, N. Imamoto, Y. Sako, M. Kinjo, K. Takahashi, T. Nagai, and K. Maeshima. Local Nucleosome Dynamics Facilitate Chromatin Accessibility in Living Mammalian Cells. *Cell Reports*, 2(6):1645–1656, December 2012.
- [128] T. Nozaki, K. Kaizu, C.-G. Pack, S. Tamura, T. Tani, S. Hihara, T. Nagai, K. Takahashi, and K. Maeshima. Flexible and dynamic nucleosome fiber in living mammalian cells. *Nucleus*, 4(5):349–356, September 2013.
- [129] S. Chatani, T. Gong, B. A. Earle, M. Podgórski, and C. N. Bowman. Visible-Light Initiated Thiol-Michael Addition Photopolymerization Reactions. *ACS Macro Letters*, 3(4):315–318, April 2014.
- [130] D. P. Nair, M. Podgórski, S. Chatani, T. Gong, W. Xi, C. R. Fenoli, and C. N. Bowman. The Thiol-Michael Addition Click Reaction: A Powerful and Widely Used Tool in Materials Chemistry. *Chemistry of Materials*, 26(1):724–744, January 2014.
- [131] B. D. Fairbanks, M. P. Schwartz, C. N. Bowman, and K. S. Anseth. Photoinitiated polymerization of PEG-diacrylate with lithium phenyl-2,4,6-trimethylbenzoylphosphinate: Polymerization rate and cytocompatibility. *Biomaterials*, 30(35):6702–6707, December 2009.
- [132] D. Bartolo, G. Degré, P. Nghe, and V. Studer. Microfluidic stickers. *Lab on a Chip*, 8(2):274–279, January 2008.

- [133] J. S. Paustian, R. N. Azevedo, S.-T. B. Lundin, M. J. Gilkey, and T. M. Squires. Microfluidic Microdialysis: Spatiotemporal Control over Solution Microenvironments Using Integrated Hydrogel Membrane Microwindows. *Physical Review X*, 3(4), November 2013.
- [134] J. Yin, P. D. Straight, S. M. McLoughlin, Z. Zhou, A. J. Lin, D. E. Golan, N. L. Kelleher, R. Kolter, and C. T. Walsh. Genetically encoded short peptide tag for versatile protein labeling by Sfp phosphopantetheinyl transferase. *Proceedings of the National Academy of Sciences*, 102(44):15815–15820, November 2005.
- [135] C. Chaillan-Huntington, P. J. G. Butler, J. A. Huntington, D. Akin, C. Feldherr, and M. Stewart. NTF2 monomer-dimer equilibrium1. *Journal of Molecular Biology*, 314(3):465–477, November 2001.
- [136] N. Annabi, J. W. Nichol, X. Zhong, C. Ji, S. Koshy, A. Khademhosseini, and F. Dehghani. Controlling the porosity and microarchitecture of hydrogels for tissue engineering. *Tissue Engineering Part B: Reviews*, 16(4):371–383, 2010.
- [137] T. Brunette, F. Parmeggiani, P.-S. Huang, G. Bhabha, D. C. Ekiert, S. E. Tsutakawa, G. L. Hura, J. A. Tainer, and D. Baker. Exploring the repeat protein universe through computational protein design. *Nature*, 528(7583):580–584, December 2015.
- [138] P.-S. Huang, G. Oberdorfer, C. Xu, X. Y. Pei, B. L. Nannenga, J. M. Rogers, F. DiMaio, T. Gonen, B. Luisi, and D. Baker. High thermodynamic stability of parametrically designed helical bundles. *Science*, 346(6208):481–485, October 2014.
- [139] S. De and D. Robinson. Polymer relationships during preparation of chitosan–alginate and poly-l-lysine–alginate nanospheres. *Journal of Controlled Release*, 89(1):101–112, April 2003.
- [140] M. Bruchet and A. Melman. Fabrication of patterned calcium cross-linked alginate hydrogel films and coatings through reductive cation exchange. *Carbohydrate Polymers*, 131:57–64, October 2015.
- [141] M. A. Masuelli. Dextrans in Aqueous Solution. Experimental Review on Intrinsic Viscosity Measurements and Temperature Effect. *Journal of Polymer and Biopolymer Physics Chemistry*, 1(1):13–21, January 2013.
- [142] B. L. Sprague, R. L. Pego, D. A. Stavreva, and J. G. McNally. Analysis of Binding Reactions by Fluorescence Recovery after Photobleaching. *Biophysical Journal*, 86(6):3473–3495, June 2004.
- [143] J. Wu, N. Shekhar, P. P. Lele, and T. P. Lele. FRAP Analysis: Accounting for Bleaching during Image Capture. *PLOS ONE*, 7(8):e42854, August 2012.
- [144] M. Kang, C. A. Day, E. DiBenedetto, and A. K. Kenworthy. A Quantitative Approach to Analyze Binding Diffusion Kinetics by Confocal FRAP. *Biophysical Journal*, 99(9):2737–2747, November 2010.
- [145] M. Kang, C. A. Day, A. K. Kenworthy, and E. DiBenedetto. Simplified equation to extract diffusion coefficients from confocal FRAP data. *Traffic (Copenhagen, Denmark)*, 13(12):1589–1600, December 2012.

- [146] N. A. Mortensen, F. Okkels, and H. Bruus. Universality in edge-source diffusion dynamics. *Physical Review E*, 73(1), January 2006.
- [147] H.S. Carslaw and J.C. Jaeger. *Conduction of Heat in Solids*. Clarendon Press, Oxford, 2 edition, 1959.
- [148] S. Milles, K. Huy Bui, C. Koehler, M. Eltsov, M. Beck, and E. A. Lemke. Facilitated aggregation of FG nucleoporins under molecular crowding conditions. *EMBO Reports*, 14(2):178–183, February 2013.
- [149] T. R. Jahn and S. E. Radford. Folding versus aggregation: Polypeptide conformations on competing pathways. *Archives of Biochemistry and Biophysics*, 469(1):100–117, January 2008.
- [150] L. Breydo, K. D. Reddy, A. Piai, I. C. Felli, R. Pierattelli, and V. N. Uversky. The crowd you're in with: Effects of different types of crowding agents on protein aggregation. *Biochimica et Biophysica Acta (BBA) - Proteins and Proteomics*, 1844(2):346–357, February 2014.
- [151] L. Breydo, A. E. Sales, T. Frege, M. C. Howell, B. Y. Zaslavsky, and V. N. Uversky. Effects of Polymer Hydrophobicity on Protein Structure and Aggregation Kinetics in Crowded Milieu. *Biochemistry*, 54(19):2957–2966, May 2015.
- [152] C. F. Lee, S. Bird, M. Shaw, L. Jean, and D. J. Vaux. Combined Effects of Agitation, Macromolecular Crowding, and Interfaces on Amyloidogenesis. *Journal of Biological Chemistry*, 287(45):38006–38019, February 2012.
- [153] A. Magno, A. Caflisch, and R. Pellarin. Crowding Effects on Amyloid Aggregation Kinetics. *The Journal of Physical Chemistry Letters*, 1(20):3027–3032, October 2010.
- [154] M. Sleutel, A. E. S. Van Driessche, W. Pan, E. K. Reichel, D. Maes, and P. G. Vekilov. Does Solution Viscosity Scale the Rate of Aggregation of Folded Proteins? *The Journal of Physical Chemistry Letters*, 3(10):1258–1263, May 2012.
- [155] S. Saha, A. Sharma, and S. Deep. Differential influence of additives on the various stages of insulin aggregation. *RSC Advances*, 6(34):28640–28652, 2016.
- [156] D. S. W. Protter, B. S. Rao, B. Van Treeck, Y. Lin, L. Mizoue, M. K. Rosen, and R. Parker. Intrinsically Disordered Regions Can Contribute Promiscuous Interactions to RNP Granule Assembly. *Cell Reports*, 22(6):1401–1412, February 2018.
- [157] M. M. Picken and G. A. Herrera. Thioflavin T Stain: An Easier and More Sensitive Method for Amyloid Detection. In M. M. P. M. FASN, A. D. M.D, and G. A. H. M.D, editors, *Amyloid and Related Disorders*, Current Clinical Pathology, pages 187–189. Humana Press, 2012.
- [158] R. Khurana, C. Coleman, C. Ionescu-Zanetti, S. A. Carter, V. Krishna, R. K. Grover, R. Roy, and S. Singh. Mechanism of thioflavin T binding to amyloid fibrils. *Journal of Structural Biology*, 151(3):229–238, September 2005.
- [159] M. Groenning. Binding mode of Thioflavin T and other molecular probes in the context of amyloid fibrils—current status. *Journal of Chemical Biology*, 3(1):1–18, August 2009.

- [160] A. N. Murray, F. L. Palhano, J. Bieschke, and J. W. Kelly. Surface adsorption considerations when working with amyloid fibrils in multiwell plates and Eppendorf tubes. *Protein Science*, 22(11):1531–1541, November 2013.
- [161] A. I. Sulatskaya, A. A. Maskevich, I. M. Kuznetsova, V. N. Uversky, and K. K. Turoverov. Fluorescence Quantum Yield of Thioflavin T in Rigid Isotropic Solution and Incorporated into the Amyloid Fibrils. *PLoS ONE*, 5(10), 2010.
- [162] L. Giehm and D. E. Otzen. Strategies to increase the reproducibility of protein fibrillization in plate reader assays. *Analytical Biochemistry*, 400(2):270–281, May 2010.
- [163] P. Arosio, T. P. J. Knowles, and S. Linse. On the lag phase in amyloid fibril formation. *Physical Chemistry Chemical Physics*, 17(12):7606–7618, March 2015.
- [164] L. A. Munishkina, E. M. Cooper, V. N. Uversky, and A. L. Fink. The effect of macromolecular crowding on protein aggregation and amyloid fibril formation. *Journal of Molecular Recognition*, 17(5):456–464, September 2004.
- [165] S. Prahl. Phenylalanine. <https://omlc.org/spectra/PhotochemCAD/html/073.html>, 1995.
- [166] A. S. Ladokhin. Fluorescence Spectroscopy in Peptide and Protein Analysis. In R. A. Meyers, editor, *Encyclopedia of Analytical Chemistry*, page a1611. John Wiley & Sons, Ltd, Chichester, UK, October 2000.
- [167] L. Serrano-Andrés and B. O. Roos. Theoretical Study of the Absorption and Emission Spectra of Indole in the Gas Phase and in a Solvent. *Journal of the American Chemical Society*, 118(1):185–195, January 1996.
- [168] J. Taylor. *An Introduction to Error Analysis*. University Science Books, 2nd edition, 1997.
- [169] H. Reich. 8-TECH-1 Relaxation in NMR Spectroscopy. <https://www.chem.wisc.edu/areas/reich/nmr/08-tech-01-relax.htm>, 2018. University of Wisconsin.
- [170] E. Pion, G. M. Ullmann, J.-C. Amé, D. Gérard, G. de Murcia, and E. Bombarda. DNA-Induced Dimerization of Poly(ADP-ribose) Polymerase-1 Triggers Its Activation. *Biochemistry*, 44(44):14670–14681, November 2005.
- [171] M. Altmeyer, S. Messner, P. O. Hassa, M. Fey, and M. O. Hottiger. Molecular mechanism of poly(ADP-ribosyl)ation by PARP1 and identification of lysine residues as ADP-ribose acceptor sites. *Nucleic Acids Research*, 37(11):3723–3738, June 2009.
- [172] T. Canal and N. A. Peppas. Correlation between mesh size and equilibrium degree of swelling of polymeric networks. *Journal of Biomedical Materials Research*, 23(10):1183–1193, 1989.
- [173] M. B. Mellott, K. Searcy, and M. V. Pishko. Release of protein from highly cross-linked hydrogels of poly(ethylene glycol) diacrylate fabricated by UV polymerization. *Biomaterials*, 22(9):929–941, May 2001.
- [174] A. Datta. Characterization of polyethylene glycol hydrogels for biomedical applications. *LSU Master's Theses*, January 2007.

## Appendix A

### Predicted selectivity of nuclear pore mimics

Nup fragment	Nup concentration	Molecule	MW	Partition coeff.	Diffusion coeff. in gel	Diffusion coeff. free	$K_D$	$D_B$	$D_B/D_F$	$S$	$S$ with partition coeff.	10x	Notes
Nsp1 (2-601)	3 mM	IBB-MBP-mEGFP-ImpB MBP-mCherry	510 kD 70 kD	100 0.16	0.17 $\mu\text{m}^2/\text{s}$	4.03 $\mu\text{m}^2/\text{s}$	4.8 $\mu\text{M}$	0.17 $\mu\text{m}^2/\text{s}$	0.04	42	50		[70]
Nup57 (1-223)-Nup49 (1-246)	3.7 mM	IBB-MBP-mECFP-ImpB MBP-mCherry	510 kD 70 kD	400 0.15	0.1 $\mu\text{m}^2/\text{s}$	2.7 $\mu\text{m}^2/\text{s}$	1.4 $\mu\text{M}$	0.1 $\mu\text{m}^2/\text{s}$	0.04	69	45		[70]
Nup57 (1-223)-Nsp1 (2-601)-Nup49 (1-246)	1.7 mM	IBB-MBP-mEGFP-ImpB MBP-mCherry	510 kD 70 kD	350 0.1	0.24 $\mu\text{m}^2/\text{s}$	4.03 $\mu\text{m}^2/\text{s}$	0.48 $\mu\text{M}$	0.24 $\mu\text{m}^2/\text{s}$	0.06	38	16		[70]
Nsp1 (2-175)	3.0 mM	IBB-MBP-mEGFP-ImpB MBP-mCherry	510 kD 70 kD	100 3	0.04 $\mu\text{m}^2/\text{s}$	12.1 $\mu\text{m}^2/\text{s}$	90 $\mu\text{M}$	0.04 $\mu\text{m}^2/\text{s}$	0.003	1.4	4.3		[51]
Nsp1 (2-601)	3.0 mM	IBB-MBP-mEGFP-ImpB MBP-mCherry	510 kD 70 kD	60 0.4	0.22 $\mu\text{m}^2/\text{s}$	6.94 $\mu\text{m}^2/\text{s}$	20 $\mu\text{M}$	0.22 $\mu\text{m}^2/\text{s}$	0.03	15	40		[51]
Nsp1 (1-601)	2.2 mM	IBB-Redstar-ImpB IBB-Redstar	530 kD 150 kD	1000 0.3	0.1 $\mu\text{m}^2/\text{s}$	0.2 $\mu\text{m}^2/\text{s}$	0.66 $\mu\text{M}$	0.1 $\mu\text{m}^2/\text{s}$	0.5	230	100		[50]
Nsp1 (1-601)	2.2 mM	GFP-ImpB IBB-Redstar	124 kD 150 kD	100 0.3	0.1-0.2 $\mu\text{m}^2/\text{s}$	0.2 $\mu\text{m}^2/\text{s}$	6.6 $\mu\text{M}$	0.1-0.2 $\mu\text{m}^2/\text{s}$	0.5-1	210-250	230-240		[50]
Nsp1 (1-601)	2.2 mM	GFP-ImpB acRedStar	124 kD 117 kD	100 0.05	0.1-0.2 $\mu\text{m}^2/\text{s}$	0.2-1 $\mu\text{m}^2/\text{s}$	1.1 $\mu\text{M}$	0.1-0.2 $\mu\text{m}^2/\text{s}$	0.1-1	94-260	53-130		[50]
P - Nsp1 (274-601) - P *	4.4 mM	IBB-MBP-mEGFP-ImpB IBB-MBP-mEGFP	510 kD 100 kD	7 0.9	2.78 $\mu\text{m}^2/\text{s}$	16.0 $\mu\text{m}^2/\text{s}$	560 $\mu\text{M}$	2.42 $\mu\text{m}^2/\text{s}$	0.15	5.3	25		[52]

**Table A.1:** Predicted selectivity of FG Nup hydrogels in previous work. We took partition and diffusion coefficients from tables in references or calculated them using concentration plots. We determined the dissociation constant  $K_D$  from the partition coefficient of the binding species ( $P_B$ ) and non-binding species ( $P_N$ ) and the Nup concentration  $N_t$  using  $K_D \approx (P_I/P_B)N_t$ . Note that the measured  $P_B$  is an underestimate of the true partition coefficient. We estimated the bound diffusion coefficient from the in-gel (effective) diffusion coefficient ( $D_{\text{eff}}$ ) and the probability of the binding species being bound ( $p_b \approx 1 - K_D/N_t$ ) using  $D_B = p_b D_{\text{eff}}$  (Sec. 4.3.2). We used the reaction-diffusion equations discussed in Sec. 2.1 to estimate the selectivity. Because partition coefficient estimates were lower bounds, we also calculated selectivity assuming that the reported partition coefficients were 10% of their actual value. P - Nsp1 (274-601) - P \* refers to a fusion between Nsp1 (274-601) and a pentameric coiled-coil P which facilitates the aggregation of the Nsp1 domain into hydrogels. See [52].

## Appendix B

### Calculation of PEG hydrogel pore size

The following equation was used to estimate pore size in a 10 wt % PEG hydrogel with 20-kDa 8-armed PEG-norbornene and 1-kDa PEG-dithiol crosslinker [172].

$$\frac{1}{M_c} = \frac{2}{M_n} - \frac{\left(\frac{\bar{v}}{v_1}\right) (\ln(1 - v_{2,s} + v_{2,s} + \chi v_{2,s}^2))}{v_{2,r} \left( \left(\frac{v_{2,s}}{v_{2,r}}\right)^{1/3} - \frac{1}{2} \left(\frac{v_{2,s}}{v_{2,r}}\right) \right)} \quad (\text{B.1})$$

with:

The average molecular weight between crosslinks as  $M_c$ .

The average polymer molecular weight before crosslinking  $M_n = 20$  kDa.

The specific volume of polymer  $\bar{v} = 0.8$  cm<sup>3</sup>/g for 1.5K PEG.

The molar volume of the swelling agent  $v_1 = 18$  g/mol for water.

The Flory PEG-water interaction parameter  $\chi = 0.4$  [173].

The polymer volume fraction before swelling  $v_{2,r} = 0.10$  for a 10 wt % hydrogel.

The polymer volume fraction after swelling  $v_{2,s} = (\rho_p(\frac{Q_m}{\rho_s} + \frac{1}{\rho_p}))^{-1}$  [174] with:

The solvent density  $\rho_s = 1$  g/cm<sup>3</sup> for water.

The polymer density  $\rho_p = 1.2$  g/cm<sup>3</sup> for 20-kDa PEG (Santa Cruz Biotech).

The mass ratio of solvent to polymer  $Q_m = 9$ .

This calculation gives  $M_c \approx 210$  Da as the average molecular weight between crosslinks. The

mesh size  $\xi$  can be estimated using [172]

$$\xi = v_{2,s}^{-1/3} \ell \left( \frac{2M_c}{M_r} \right)^{1/2} c_n^{1/2} \quad (\text{B.2})$$

with:

The carbon-carbon bond length  $\ell = 1.54 \text{ \AA}$ .

The molecular weight of the repeating polymer unit  $M_r = 67 \text{ Da}$  for PEG.

The “characteristic ratio” for PEG  $c_n \approx 4$ .

The result is an estimated mesh size on the order of 1 nm.

## Appendix C

### Protein expression and purification

#### C.1 Purification of his-tagged protein with metal affinity column

Most proteins used in this work contain a C-terminal 6x histidine tag. These proteins can be purified using a cobalt or nickel affinity column. Proteins purified with this protocol include all Nup variants (FSFG, FG124, etc.), NTF2, mCherry, and GFP. This protocol is designed for the purification of one 0.5-L cell pellet. If running more than one column at once, adjust the total buffer volumes accordingly.

This protocol is used for all Nup variants. For FSFG variants, use the urea concentrations noted in the buffer table. For FG124 purifications, use 7M guanidine hydrochloride in all buffers (including elution) instead of urea. Always make urea and guanidine hydrochloride solutions the same day they will be used. **Do not use urea, guanidine hydrochloride, or other denaturants when purifying ordered proteins.**

To prevent aggregation, BME must be used for any protein that has been labeled with two cysteines. **Do not use BME if not necessary; any BME solutions must be disposed of as hazardous waste.**

Add the protease inhibitor cocktail (PIC) stock in DMSO immediately before using the buffer. PIC has a lifetime of about 30 minutes in aqueous solution. Store all buffers on ice before use. Incubations should be done at 4°C, but the column can be used at room temperature.

**Figure C.1:** Buffer guide for cobalt or nickel affinity column purifications.

Buffer	Use (and volume)	Composition
Lysis Buffer	for cell lysis (15 mL)	Buffer of choice 1x (15** mL) 1:1000 PIC (15uL) (8M Urea) (7.2 g) (3mM BME) (3 uL)
Wash I	for wash I (20 mL)	Buffer of choice 1x (20** mL) 1:1000 PIC (20uL) (3M Urea) (4 g) (3mM BME) (4uL)
Wash II <b>*the imidazole is optional; can be useful for removing junk bound to column</b>	for wash II (20 mL)	Buffer of choice 1x (20** mL) 1:1000 PIC (20 uL) (10mM Imidazole) (.013 g) (3mM BME) (4uL)
Elutions	20 mL total	Buffer of choice 1x (20** mL) 1:1000 PIC (20uL) <b>250mM Imidazole (.32 g)</b> (3mM BME) (4uL)
Handy Molecular Weights	Imidazole: 68.08 g/mol Urea: 60.06 g/mol BME: 14.3 M GuHCl: 95.53 g/mol	**Bring up to volume with buffer. Will not need full 20- <u>25mL</u> if using urea

- (1) Remove the periplasmic matrix, if not already done (Sec. C.2).
- (2) Lyse the cells. Add 15 mL of lysis buffer to thawed 0.5-L pellet. Resuspend pellet by pipetting up and down or vortexing and then lyse with Qsonica sonicator. Keep solution on ice. Sonicate for at least two minutes total, in 30 s on, 59 s off pulses. Power delivered to sample should be at least 20 W. Centrifuge resulting lysate for at least 15 mins on top speed of Marathon centrifuge to pellet cellular debris.
- (3) Prepare the metal-affinity column. Gently resuspend the resin into a slurry by slowly turning the bottle. The beads will be crushed if shaken vigorously. Into a disposable plastic column, pipette enough slurry to contain 3.5-4 mL of beads once the storage buffer has drained out (typically 6-8 mL of slurry, if beads and buffer are stored in a one-to-one mixture). Equilibrate the column by running 5-10x the bed volume (25-50 mL) of buffer through the column. Do not let the column run dry at any point in the purification.
- (4) Add supernatant to column and nutate for one hour at 4°C.
- (5) Drain the column. Add wash I buffer and nutate at 4°C for 10 minutes.
- (6) Drain the column. Add wash II buffer, nutate at 4°C for 10 minutes, and drain.
- (7) Elute and collect the protein. Three elution methods can be used:
  - (a) *Fractional elution:* Prepare a row of eppendorfs. Add 5-10 mL elution buffer to open column and catch the draining liquid in fractions with 0.5-1.0 mL (8-16 drops) per eppendorf. Do not let the column dry. After all elutions are completed, use the Bradford test to pool the fractions with similar protein concentrations. **The Bradford test is unreliable for Nup variants and batch elution should be used.** Fractional elution gives the highest protein concentration and should be used where possible.
  - (b) *Batch elution:* Add a bed volume of elution buffer to column and let drain to remove

waste buffer from column. Watch resin color change carefully so as not to lose protein.

Add 3-5 mL of elution buffer and collect flow-through.

- (c) *Nutated elution:* Add 5-10 mL of elution buffer to sealed column and nutate for 10-30 minutes. Collect flow-through.

Early elutions should be fractional or batch elutions.

- 9) Clean and store the column. Run 5 bed volumes of 20 mM MES hydrate, 300 mM NaCl, pH 5 buffer through the column, then 5 bed volumes DI water. Store 1:1 in 20% ethanol.

## C.2 Periplasmic matrix removal (PPMR)

The periplasmic matrix (PPM) contains proteases and debris that bind to metal affinity columns. Removing the PPM before protein purification significantly increases the yield of his-tagged disordered proteins.

**Note:** Keep both solutions on ice. Resuspension of pellets should be done by gently pipetting up and down and swirling the tubes. Do not vortex to resuspend. Rough treatment of the cells may lyse them.

- (1) Spin down cell culture at 4000g (Sorvall centrifuge, GSA rotor) for 10 minutes at 4°C.
- (2) Resuspend pellets in at least 50 mL cold SHE buffer (20% sucrose, 50mM HEPES, 1mM EDTA pH 7.9) per liter of culture. Keep tubes on ice.
- (3) Spin down for 10 minutes at 4000g at 4°C.
- (4) Resuspend pellets in at least 50 mL cold 5mM MgSO<sub>4</sub> per liter of culture.
- (5) Incubate tubes on ice for 10 minutes.
- (6) Spin down for 10 minutes at 2500g at 4°C.
- (7) Proceed to purification or flash-freeze tubes in liquid nitrogen and store in ultra-low freezer.

### C.3 Lyophilization

Lyophilization refers to freeze-drying proteins. It's a good way to store a known mass of protein before resuspension in hydrogel precursor solution. All lyophilization in this work was done using a Labconco freeze dry system. Lyophilization concentrates any salts in the sample buffer. Therefore, whenever possible, a decomposing buffer should be used. A 25 mM ammonium bicarbonate buffer was used for all lyophilized Nup variants. This buffer decomposes into carbon dioxide, ammonia, and water when lyophilized or above 36°C.

- (1) Dialyze sample into 25 mM ammonium bicarbonate if possible.
- (2) Perform a BCA to quantify the protein concentration in the sample. Prepare eppendorf aliquots that contain the desired mass of protein (usually 100 or 200  $\mu\text{g}$ ).
- (3) Cover the aliquots with parafilm and use a needle to punch a hole in the covering.
- (4) Flash-freeze the aliquots.
- (5) Follow lyophilizer instructions. Keep samples frozen and load as quickly as possible to avoid thawing. Ensure that the vacuum is below  $50 \times 10^{-3}$  mBar.
- (6) Leave aliquots on lyophilizer at least 12 hours.
- (7) Remove aliquots from lyophilizer. Remove parafilm and close eppendorfs. Store with desiccant in ultra-low freezer.

## Appendix D

### Bis-labeling Nup fragments for incorporation into acrylamide hydrogels

Before FSFG-cys or any other cys-labeled Nup variant can be tethered to an acrylamide hydrogel, it needs to be labeled with bisacrylamide or PEG-DA. This protocol describes the labeling procedure for either chemical group. The cysteines must be fully reduced for the labeling to occur. No BME, TCEP, or other reducing agent can be present in the reaction mixture. FSFG and other disordered peptides form disulfide bonds within minutes of being removed from reducing agents, so begin the reaction as quickly as possible after reducing. This protocol was developed with the help of Benjamin Fairbanks. Following labeling, the extent of labeling can be quantified using an Ellman's reagent assay.

#### D.1 Bis-labeling reaction protocol

- (1) Begin with a stock of at least 1 mg/mL FSFG with a terminal cysteine in PBS pH 7.8. Typical reactions use 1 mL of approximately 2 mg/mL FSFG.
- (2) Equilibrate an equal volume of immobilized TCEP resin slurry in a disposable 5-mL column which can be spun in a conical tube. Refer to Thermo-Pierce product reference sheet for resin volume and nutation time if necessary. Equilibrate with 20-30 bed volumes of PBS pH 7.8 using gravity, then spin at 2300g for 10 s to remove remaining buffer.
- (3) Immediately add the FSFG stock and nutate at 4°C for 1 hour.

- (4) Prepare a conical tube with 40  $\mu\text{L}$  of triethanolamine (TEA, in fume hood) and 50  $\mu\text{L}$  2% bisacrylamide solution. This will lead to a 10-fold molar excess of bisacrylamide over protein and 300 mM TEA in the final reaction mixture. Place column in prepared conical tube and spin down 1000 rpm for 1 minute.
- (5) Immediately vortex thoroughly. Nutate at room temperature for 30 minutes.
- (6) Dialyze into 25 mM ammonium bicarbonate buffer to remove excess bisacrylamide and prepare for lyophilizing.
- (7) Perform a BCA to quantify protein concentration. Prepare 100 or 200  $\mu\text{g}$  aliquots, freeze, and lyophilize. Store lyophilized protein with a desiccant in ultra-low freezer.

## D.2 Ellman's reagent assay protocol

This protocol was taken from Thermo-Fisher's protocol and modified for a microwell plate. Due to the rapid disulfide bond formation of FSFG, the reactants must be mixed very rapidly once reducing agent is removed.

- (1) Equilibrate 80  $\mu\text{L}$  TCEP resin slurry in each of two disposable 1-mL spin columns which can be spun in an eppendorf centrifuge. Refer to Thermo-Pierce product reference sheet for resin volume and nutation time if necessary. Equilibrate with 20-30 bed volumes of PBS pH 7.8 using gravity, then spin at 2300g for 10 s to remove remaining buffer.
- (2) Add 80  $\mu\text{L}$  of bis-labeled FSFG in 25 mM ammonium bicarbonate to one column and a known concentration of unlabeled FSFG-cys (as a control) in 25 mM ammonium bicarbonate to the other. Nutate for two hours.
- (3) While incubation proceeds, prepare the reaction buffer (0.1 M sodium phosphate buffer, pH 8.0, with 1 mM EDTA) and the Ellman's reagent solution (ERS, 4 mg/mL Ellman's reagent in reaction buffer).

- (4) Prepare a 96-well plate with wells containing 1.8  $\mu\text{M}$  ERS and 29.5  $\mu\text{M}$  reaction buffer. Prepare wells for the FSFG-bis and FSFG-cys samples but do not add the protein until everything has been prepared. Prepare a well containing ERS, reaction buffer, and 68  $\mu\text{L}$  of 25 mM ammonium bicarbonate buffer. Finally, prepare a well containing ERS, reaction buffer, and 68  $\mu\text{L}$  of unlabeled FSFG cys of a known concentration that has not been reduced.
- (5) Spin down both columns of TCEP solution at 2300g for 30 s in an eppendorf centrifuge and collect the flow-through. Very rapidly, add 68  $\mu\text{L}$  of flow-through to the appropriate wells and mix by pipetting up and down.
- (6) Incubate plate at room temperature for 15 minutes.
- (7) Measure the absorbance at 412 nm using a plate reader.
- (8) Calculate labeling efficiency. Use the buffer well's absorbance to blank the absorbance of the reduced FSFG-cys sample and the labeled FSFG sample. Divide the blanked absorbance of the labeled sample by that of the reduced FSFG-cys sample and subtract the resulting ratio from 1. The unreduced FSFG sample is not directly used but is a good check on the results.

## Appendix E

### Hydrogel precursor solutions

This appendix contains details of hydrogel precursor solutions. Lyophilized protein should be resuspended in the buffer component of the precursor solution and incubated at room temperature for at least 20 minutes before adding the other components. No-Nup control gels simply omit the protein. Precursor solutions must be degassed for 10 minutes and promptly polymerized. All solutions containing photoinitiator must be protected from light at all times. Mix under red light only. Prepare precursor solutions immediately before use.

#### E.1 PEG hydrogel precursor recipes

All PEG hydrogels were 10 wt % PEG with and 0.5 thiol-ene ratio. For more accurate pipetting, stock solutions were designed to be combined in equal volumes (Table E.2).

**Table E.1:** PEG hydrogel precursor stocks

Component	Concentration	Buffer
20-kDa PEG-norbornene	438 $\mu\text{g}/\mu\text{L}$	Water
1-kDa PEG-dithiol crosslinker	45 $\mu\text{g}/\mu\text{L}$	Water
8-kDa PEG-dithiol crosslinker	360 $\mu\text{g}/\mu\text{L}$	Water
Irgacure 2959	2 mM	Water
LAP	2 mM	Water
TCEP	4 mM	4x PTB

## E.2 Acrylamide hydrogel precursor recipes

The monomer and crosslinker were bought premixed from BioRad (acrylamide/bisacrylamide 30% 29:1) but potentially could be prepared in different ratios and mixed separately. Any additional components, such as dextran or photoinhibitor, should be made into a stock with PTB and used instead of the buffer component in the recipe. Acrylamide hydrogels were mostly crosslinked with LAP photoinitiator, but sometimes with the APS/TEMED chemical crosslinking system. Results of several APS/TEMED concentrations in a 6% acrylamide precursor solution are shown in Table E.5.

**Table E.2:** Sample precursor soution recipe (10 wt % PEG, 10 mg/mL nominal Nup concentration)

Stock	Amount
20-kDa PEG-norbornene	2.5 $\mu$ L
1-kDa PEG-dithiol crosslinker	2.5 $\mu$ L
Irgacure 2959	2.5 $\mu$ L
TCEP in 4x PTB	2.5 $\mu$ L
Lyophilized FSFG-cys	100 $\mu$ g

**Table E.3:** Acrylamide hydrogel precursor stocks

Component	Concentration	Buffer
Acrylamide monomer	30%	Premixed
Bisacrylamide crosslinker	1%	Premixed
LAP	20 mM	Water
APS	10% w/v	PTB
TEMED	1% w/v	PTB
PTB buffer	1x	PTB

**Table E.4:** Sample precursor soution recipe (6% final acrylamide concentration)

Stock	Amount
Premixed acrylamide/bis	2 $\mu$ L
LAP	1 $\mu$ L
PTB	7 $\mu$ L
Lyophilized FSFG-cys	100 $\mu$ g

**Table E.5:** APS/TEMED chemical crosslinking tests

APS concentration	TEMED concentration	Degas time (min)	Results
1%	0.5%	0	Gelled in under 10 s.
0.1%	0.5%	0	Gelled in 5 minutes.
0.1%	0.1%	5	Gelled in 5 minutes (while degassing).
0.1%	0.1%	0	Gelled in 10 minutes.
0.1%	0.05%	0	Did not gel.
0.1%	0.05%	5	Gelled in 10 minutes.

## Appendix F

### Protein and peptide sequences

**Table F.1:** Protein and peptide sequences

Description	Notes	Sequence
FSFG his	(‘FSFG concat-1’)	MGTSATSKPAFSFGAKSDENKAGATSKPA FSFGAKPEEKDDNSSKPAFSFGAKSN EDKQDGTAKPAFSFGAKPAEKNNNET SKPAFSFGAKSDEKKDGDASKPAFSF GAKPDENKASATSKPASHHHHHH
cys FSFG his		MGCTSATSKPAFSFGAKSDENKAGATSKPA FSFGAKPEEKDDNSSKPAFSFGAKSNED KQDGTAKPAFSFGAKPAEKNNNETSKPA FSFGAKSDEKKDGDASKPAFSFGAKPDEN KASATSKPASHHHHHH

Continued on next page

**Table F.1 – continued from previous page**

Description	Notes	Sequence
cys FSFG cys his	Aggregates unless kept in reducing agent.	MGCTSATSKPAFSFGAKSDENKAGATSKPA FSFGAKPEEKDDNSSKPAFSFGAKSNED KQDGTAKPAFSFGAKPAEKNNNETSKPA FSFGAKSDEKKDGDASKPAFSFGAKPDEN KACATSKPASHHHHHH
ybbR FSFG cys his	Most often used for hydrogel experiments; ybbR tag is intended for site-specific labeling but not used in the hydrogel experiments.	MGDSLEFIASKLATSATSKPAFSFGAKSDEN KAGATSKPAFSFGAKPEEKDDNSSKPA FSFGAKSNEDKQDGTAKPAFSFGAK PAEKNNNETSKPAFSFGAKSDEKKDGDAS KPAFSFGAKPDENKACATSKPASHHHHHH
ybbR FSFG concat-2 cys his		MGDSLEFIASKLATSATSKPAFSFGAKSDEN KAGATSKPAFSFGAKPEEKDDNSSKPA FSFGAKSNEDKQDGTAKPAFS FGAKPAEKNNNETSKPAFSFGA KSDEKKDGDASKPAFSFGAKP DENKASATSKPASATSKPAFS FGAKSDENKAGATSKPAFSF GAKPEEKDDNSSKPAFSFGAKSNED KQDGTAKPAFSFGAKPAEKNNNET SKPAFSFGAKSDEKKDGDASKPAFSF GAKPDENKACATSKPASHHHHHH

Continued on next page

**Table F.1 – continued from previous page**

Description	Notes	Sequence
ybbR FSFG concat- 3 cys his	Did not express well in my hands.	MGDSLEFIASKLATSATS KPAFSFGAKSDEN KAGATSKPAFSFGAKPEEKK DDNSSKPAFSFGAKSNEDKQDGTAK PAFSFGAKPAEKNNNETSKPAFSF GAKSDEKKDG DASKPAFSFGAKPD ENKASATSKPASATSKPAFSFGAKS DENKAGATSKPAFSFGAKPEEKKDDN SSKPAFSFGAKSNEDKQDGTAKPAFSF GAKPAEKNNNETSKPAFSFGAKSDEKK DGDASKPAFSFGAKPDENKASATSKPA SATSKPAFSFGAKSDENKAGATSKPAFS FGAKPEEKKDDNSSKPAFSFGAKSNEDKQ DGTA KPAFSFGAKPAEKNNNETSKPAF SFGAKSDEKKDG DASKPAFSFGAKPDEN KACATSKPASHHHHHH
ybbR SSSG cys his	Nonbinding control.	MGDSLEFIASKLATSATS KPAASSSGAKSDEN KAGATSKP ASSSGAKPEEKKDDNSSKPA SSSGAKSNEDKQDGTAKP ASSSGAK PAEKNNNETSKP ASSSGAKSDEKKDG DAS KPASSSGAKPDENKACATSKPASLEHHH HHH

Continued on next page

**Table F.1 – continued from previous page**

Description	Notes	Sequence
FG124 his	Aggregates unless kept in denaturant	MAPNNTNNANSSITPAFGSNNTGNTAFGN SNPTSNVFGSNNSTNTFGSNSAGT SLFGSSSAQQTKSNGTAGGNT FGSSSLFNNSTNSNTTKPAFGGLNFGGGN NTTPSSTGNANTSNNLFGATASHHHHHH
cys FG124 his	Aggregates unless kept in denaturant.	MGCTSAPNNTNNANSSITPAFGSNNTGN TAFGNSNPTSNSNVFGSNNSTNT FGSNSAGTSLFGSSAQQTKSNGTAGGNT FGSSSLFNNSTNSNTTKPAFGGLNFGGGN NTTPSSTGNANTSNNLFGATASHMHHH HHH
NTF2 his	Wild-type yeast NTF2.	MALDFNTLAQNFTQFYYNQFDTDRSQLGN LYRNESMLTFETSQLQGAKDIVEKLVS LPFQKVQHRITTLDAQPASPNGDVLVMIT GDLLIDEEQNPQRFSQVFHLIPDGN SYYVFNDIFRLNYSAAHHHHH
Pho4	Nuclear localization sequence.	KVDKLGGSGSANKVTKNKSNSSPYLNKRR GKPGPDSLE
Spo12	Nuclear localization sequence.	KVDKLGGSGKSTSNLKSSHTTSNLVKKT FKRDLLQDPKRKLQLQQRFASPTDR LVSPCSLKLE

## Appendix G

### Dye-labeling protocols

The following protocols were used to label proteins with various fluorophores. Dyes should always be stored in the ultra-low freezer in anhydrous DMSO. Labeled proteins should be aliquoted within 24 hours of labeling and stored in the ultra-low freezer until just before use. These protocols were adapted from Thermo-Fisher amine and cysteine labeling protocols with help from Eric Verbeke and Annette Erbse.

If better efficiency is needed, the next improvement would be to carry out the protocols in a glove bag under nitrogen.

#### G.1 Labeling NTF2 with fluorescein-NHS

- (1) Resuspend lyophilized fluorescein-NHS at 100 mg/mL in anhydrous DMSO in the dark-room. Discard the remaining DMSO aliquot. Make 100- $\mu$ L aliquots of dye solution. Store with desiccant in ultra-low freezer, protected from light.
- (2) Mix NTF2 in PTB pH 7.0 and 100 mg/mL fluorescein-NHS in DMSO with around 15-fold molar excess dye. Several other buffers can be used as well (see Thermo protocol). A typical labeling reaction used 0.5 mL of 16 mg/mL NTF2 and 18.6  $\mu$ L dye stock mixed in an Eppendorf with an Eppendorf stir bar.
- (3) Incubate mixture, stirring, protected from light, at room temperature for one hour.

- (4) Equilibrate TALON cobalt resin with PTB in a column that can be spun in a centrifuge. TALON resin has a stated capacity of 5-15 mL protein per mL resin. Using significantly more than needed can lead to nonspecific binding of free dye. A typical reaction required 1.6 mL of the resin slurry. Equilibrate with at least 10 bed volumes PTB.
- (5) Cap column and add reaction mixture. Nutate at 4°C for one hour, protected from light.
- (6) Allow column to drain and wash with approximately 100 bed volumes of PTB, protected from light as best as possible. Occasionally cap column and resuspend resin to remove free dye from column cap and sides. Test flow-through using UV light to ensure that no dye is visible by the end of the wash. Resin should still be bright yellow.
- (7) Spin column at 160g for one minute to remove remaining wash buffer. Immediately cap and elute with 1 mL of 300 mM imidazole in PTB. Nutate 4°C for half an hour and collect elution. Resin should return to pink.
- (8) Dialyze elution against PTB to remove imidazole. No more than 24 hours after labeling, aliquot and freeze labeled NTF2.
- (9) Run a sample of labeled NTF2 on a native PAGE gel along with a sample of fluorescein-NHS. Use the Typhoon to compare the concentration of free dye to labeled protein in the protein sample.

## **G.2 Labeling NTF2 with Alexa Fluor 488 - SDP or FSFG with Alexa Fluor 647 - SDP**

- (1) Resuspend lyophilized Alexa Fluor 488 at 10 mg/mL in anhydrous DMSO in the darkroom. Discard the remaining DMSO aliquot. Make 10- $\mu$ L aliquots of dye solution. Store with desiccant in ultra-low freezer, protected from light.
- (2) Mix NTF2 in 0.1 M sodium bicarbonate buffer and 10 mg/mL fluorescein-NHS in DMSO. A typical labeling reaction used 200  $\mu$ L of 16 mg/mL NTF2 and 20  $\mu$ L dye stock mixed in

an Eppendorf with an Eppendorf stir bar.

- (3) Incubate mixture, stirring, protected from light, at room temperature for one hour.
- (4) Equilibrate TALON cobalt resin with PTB in a column that can be spun in a centrifuge. TALON resin has a stated capacity of 5-15 mL protein per mL resin. Using significantly more than needed can lead to nonspecific binding of free dye. Equilibrate with at least 10 bed volumes PTB.
- (5) Cap column and add reaction mixture. Nute at 4°C for one hour, protected from light.
- (6) Allow column to drain and wash with approximately 100 bed volumes of PTB, protected from light as best as possible. Occasionally cap column and resuspend resin to remove free dye from column cap and sides. Test flow-through using UV light to ensure that no dye is visible by the end of the wash. Resin should still be bright yellow.
- (7) Spin column 2300g for 20 s to remove remaining wash buffer. Immediately cap and elute with 300  $\mu$ L of 500 mM imidazole in PTB. Nute 4°C for half an hour and collect elution. Resin should return to pink.
- (8) Dialyze elution against PTB to remove imidazole. No more than 24 hours after labeling, aliquot and freeze labeled NTF2.
- (9) Run a sample of labeled NTF2 on a native PAGE gel along with a sample of fluorescein-NHS. Use the Typhoon to compare the concentration of free dye to labeled protein in the protein sample.

### G.3 Labeling NTF2-cys with Alexa Fluor 488 - maleimide

- (1) Resuspend lyophilized Alexa Fluor 488 at 10 mg/mL in anhydrous DMSO in the darkroom. Discard the remaining DMSO aliquot. Make 10- $\mu$ L aliquots of dye solution. Store with desiccant in ultra-low freezer, protected from light.

- (2) Mix protein in PTB pH 7.0 and 50  $\mu$ M TCEP (with no other reducing agent present) and 10 mg/mL dye in DMSO. Typical amounts were 50  $\mu$ L of 100  $\mu$ M NTF2-cys into 50  $\mu$ L dye stock.
- (3) Incubate mixture, stirring, protected from light, at room temperature for two hours.
- (4) Equilibrate TALON cobalt resin with PTB in a column that can be spun in a centrifuge. TALON resin has a stated capacity of 5-15 mL protein per mL resin. Using significantly more than needed can lead to nonspecific binding of free dye. Equilibrate with at least 10 bed volumes PTB.
- (5) Cap column and add reaction mixture. Nutate at 4°C for one hour, protected from light.
- (6) Allow column to drain and wash with approximately 100 bed volumes of PTB, protected from light as best as possible. Occasionally cap column and resuspend resin to remove free dye from column cap and sides. Test flow-through using UV light to ensure that no dye is visible by the end of the wash. Resin should still be bright yellow.
- (7) Spin column 2300g for 20 s to remove remaining wash buffer. Immediately cap and elute with 300  $\mu$ L of 500 mM imidazole in PTB. Nutate 4°C for half an hour and collect elution. Resin should return to pink.
- (8) Dialyze elution against PTB to remove imidazole. No more than 24 hours after labeling, aliquot and freeze labeled NTF2.
- (9) Run a sample of labeled NTF2 on a native PAGE gel along with a sample of fluorescein-NHS. Use the Typhoon to compare the concentration of free dye to labeled protein in the protein sample.

## Appendix H

### Hydrogel nuclear pore mimic dataset

This appendix gives the parameters calculated for each hydrogel in the FRAP dataset, organized by FSFG condition. The predicted values for bound diffusion constant  $D_B$  and bound to free diffusion ratio  $D_B/D_F$  assume that the only mechanism of bound diffusion is tethered diffusion, so that

$$\frac{D_B}{D_F} = \frac{L_c \ell_p k_{\text{off}}}{L_c \ell_p k_{\text{off}} + 3D_F}$$

The parameters used are given in Fig. H.1. The  $K_D$  values are average values from [27]. The on-rate  $k_{\text{on}}$  is assumed to be diffusion-limited. Diffusion constants have units of  $\mu\text{m}^2/\text{s}$ . Partition coefficients ( $\gamma$ ) and fraction of NTF2 bound ( $p_B$ ) are unitless.

	FSFG concat-1	FSFG concat-2
$L_c (\text{aa})$	124	248
$L_c (\text{m})$	4.96E-08	9.92E-08
Length per aa (m)	4.00E-10	4.00E-10
$\ell_p (\text{m})$	1.00E-09	1.00E-09
$K_D (\text{M})$	0.000545	0.000395
$k_{\text{on}} (\text{M}^{-1} \text{s}^{-1})$	1.00E+09	1.00E+09
$k_{\text{off}} (\text{s}^{-1})$	5.45E+05	3.95E+05

**Figure H.1:** Parameters used to predict the bound diffusion constant for NTF2-F in FSFG hydrogels. Binding data is from [27].

**Figure H.2:** Measured and calculated values for no-Nup hydrogels.

	Dataset index	Experiment ID	$D_{\text{obs}}$ NTF2	$D_{\text{obs}}$ mCherry	$\gamma$ NTF2	$\gamma$ mCherry	$p_B$
	1 '19-1-3_1'		41.6	26.7	0.64	0.52	0.19
	4 '19-2-6_1'		68.7	71.2	0.57	0.52	0.10
	7 '19-2-6_7'		25.3	26.4	0.52	0.52	-0.01
	10 '19-2-6_13'		177.3	126.3	0.60	0.69	-0.16
	13 '19-2-6_19'		72.0	71.5	0.66	0.61	0.07
	18 '19-2-12_7'		33.1	25.8	0.44	0.47	-0.08
	20 '19-2-12_11'		100.1	68.1	0.42	0.49	-0.16
	24 '19-2-15_1'		26.8	26.5	0.21	0.30	-0.45
	25 '19-2-15_7'		31.2	27.6	0.40	0.42	-0.05
	26 '19-2-15_13'		74.8	61.4	0.48	0.45	0.06
	28 '19-2-15_19'		10.9	15.2	0.42	0.42	-0.01
	30 '19-2-19_1'		37.8	32.0	0.53	0.52	0.02
	31 '19-2-19_7'		18.3	15.6	0.39	0.42	-0.07
	33 '19-2-19_19'		40.8	44.2	0.44	0.41	0.06
	41 '19-2-21_19'		82.9	57.9	0.45	0.47	-0.04
<b>Mean</b>			<b>56.10</b>	<b>46.44</b>	<b>0.48</b>	<b>0.48</b>	<b>-0.04</b>
<b>Standard deviation</b>			42.52	29.94	0.11	0.09	0.15
<b>Standard error of the mean</b>			<b>11.36</b>	<b>8.00</b>	<b>0.03</b>	<b>0.02</b>	<b>0.04</b>

**Figure H.3:** Measured and calculated values for FSFG concat-1 hydrogels. Predicted  $D_B$  calculated assuming 10 mg/mL tethered FSFG concat-1.

	Dataset index	Experiment ID	$D_{\text{obs}}$ NTF2	$D_{\text{obs}}$ mCherry	$\gamma$ NTF2	$\gamma$ mCherry	$p_B$	$D_B$	Predicted $D_B$
	2 '19-1-3_3'		29.0	49.1	2.06	0.54	0.74	21.84	3.66
	5 '19-2-6_3'		7.2	41.9	1.89	0.46	0.76	-3.91	3.29
	8 '19-2-6_9'		13.9	22.9	1.31	0.54	0.59	7.71	5.76
	11 '19-2-6_15'		13.4	36.1	1.53	0.42	0.72	4.76	3.77
	14 '19-2-6_21'		20.2	46.0	1.77	0.41	0.77	12.48	3.10
	16 '19-2-12_3'		12.5	22.3	1.77	0.56	0.69	7.95	4.12
	19 '19-2-12_9'		10.9	41.4	1.63	0.47	0.71	-1.51	4.09
	21 '19-2-12_13'		42.4	70.4	1.03	0.63	0.38	-2.78	14.25
	27 '19-2-15_15'		10.0	19.4	1.65	0.36	0.78	7.41	2.68
	32 '19-2-19_15'		4.8	35.9	2.20	0.39	0.82	-1.82	2.22
	34 '19-2-19_21'		7.4	20.2	1.84	0.36	0.81	4.28	2.36
	39 '19-2-21_15'		11.0	10.9	2.95	0.46	0.84	10.96	1.72
<b>Mean</b>			<b>15.23</b>	<b>34.71</b>	<b>1.80</b>	<b>0.47</b>	<b>0.72</b>	<b>5.62</b>	<b>4.25</b>
<b>Standard deviation</b>			<b>10.71</b>	<b>16.55</b>	<b>0.48</b>	<b>0.09</b>	<b>0.13</b>	<b>7.52</b>	<b>3.33</b>
<b>Standard error of the mean</b>			<b>3.23</b>	<b>4.99</b>	<b>0.14</b>	<b>0.03</b>	<b>0.04</b>	<b>2.27</b>	<b>1.00</b>

**Figure H.4:** Measured and calculated values for FSFG concat-2 hydrogels. Predicted  $D_B$  calculated assuming 20 mg/mL tethered FSFG concat-2.

	Dataset index	Experiment ID	$D_{\text{obs}}$ NTF2	$D_{\text{obs}}$ mCherry	$\gamma$ NTF2	$\gamma$ mCherry	$p_B$	$D_B$	Predicted $D_B$
	6	'19-2-6_5'	12.78184	44.56024563	3.23	0.70	0.78	4.04	6.24
	9	'19-2-6_11'	10.307	43.18354162	2.82	0.66	0.77	0.24	5.86
	12	'19-2-6_17'	8.353138	30.91040114	3.24	0.50	0.85	4.22	4.12
	17	'19-2-12_5'	9.398679	42.56939841	4.41	0.67	0.85	3.49	4.29
	22	'19-2-12_15'	26.73285	39.71193071	2.64	0.68	0.74	22.25	9.74
	23	'19-2-12_17'	16.29925	53.36041486	2.89	0.73	0.75	3.88	7.77
	35	'19-2-19_23'	5.88424	34.98831302	2.78	0.57	0.80	-1.54	3.87
	Mean		<b>12.82</b>	<b>41.33</b>	<b>3.14</b>	<b>0.64</b>	<b>0.79</b>	<b>5.22</b>	<b>5.99</b>
	Standard deviation		6.97	7.21	0.60	0.08	0.04	7.83	2.17
	Standard error of the mean		<b>2.85</b>	<b>2.94</b>	<b>0.25</b>	<b>0.03</b>	<b>0.02</b>	<b>3.20</b>	<b>0.89</b>

## Appendix I

### FG124 aggregation condition p-values

**Table I.1:** Aggregation rate  $k$  p-values for all crowding agents, two-tailed t-test.

	10 mg/mL cell lysate	19% w/v serine	13% PEG	13% PVP
No crowder	0.031	$1.2 \times 10^{-6}$	$6.6 \times 10^{-4}$	0.41
10 mg/mL cell lysate	N/A	0.44	0.0010	0.022
19% w/v serine	N/A	N/A	$4.4 \times 10^{-9}$	$2.2 \times 10^{-6}$
13% PEG	N/A	N/A	N/A	0.019

**Table I.2:** Lag time  $T_\ell$  p-values for all crowding agents, two-tailed t-test.

	10 mg/mL cell lysate	19% w/v serine	13% PEG	13% PVP
No crowder	$5.4 \times 10^{-6}$	$1.4 \times 10^{-8}$	0.77	0.0012
10 mg/mL cell lysate	N/A	0.0051	0.00041	0.0060
19% w/v serine	N/A	N/A	0.0052	0.53
13% PEG	N/A	N/A	N/A	0.039

**Table I.3:** Aggregation rate  $k$  p-values for PEG (% w/v) , two-tailed t-test. A one-way ANOVA rejected the null hypothesis with  $p = 0.0024$ .

	20%	13%	5%	0%
25%	0.0063	0.6167	0.0007	0.8344
20%	N/A	0.0131	0.7539	0.0815
13%	N/A	N/A	0.1196	0.6508
5%	N/A	N/A	N/A	0.0681

**Table I.4:** Lag time  $T_\ell$  p-values for PEG (% w/v) , two-tailed t-test. A one-way ANOVA rejected the null hypothesis with  $p = 0.0102$ .

	20%	13%	5%	0%
25%	0.0071	0.0412	0.7726	0.0221
20%	N/A	0.5377	0.0206	0.1012
13%	N/A	N/A	0.1322	0.0927
5%	N/A	N/A	N/A	0.2833

**Table I.5:** Aggregation rate  $k$  p-values for PVP (% w/v) , two-tailed t-test. A one-way ANOVA failed to reject the null hypothesis.

	20%	13%	5%	0%
25%	0.8521	0.1327	0.4104	0.1880
20%	N/A	0.6607	0.6530	0.6815
13%	N/A	N/A	0.5991	0.8283
5%	N/A	N/A	N/A	0.6902

**Table I.6:** Lag time  $T_\ell$  p-values for PVP (% w/v) , two-tailed t-test.

	20%	13%	5%	0%
25%	$4.7 \times 10^{-5}$	0.0133	0.0012	0.0628
20%	N/A	0.2586	$8.6 \times 10^{-6}$	0.0272
13%	N/A	N/A	0.0018	0.0709
5%	N/A	N/A	N/A	0.6774